Microstructural evolution of silicate immiscible liquids in solidifying ferrobasalts

Victoria Claire Honour

Department of Earth Sciences

University of Cambridge

Jesus College

September 2019

This thesis is submitted for the degree of

Doctor of Philosophy

Declaration

This thesis is the result of my own work and includes nothing which is the outcome of work done in collaboration except where specifically indicated in the text.

It is not substantially the same as any that I have submitted, or, is being concurrently submitted for a degree or diploma or other qualification at the University of Cambridge or any other University or similar institution. I further state that no substantial part of my thesis has already been submitted, or, is being concurrently submitted for any such degree, diploma or other qualification at the University of Cambridge or any other University or similar institution.

The total length does not exceed the 275 numbered page limit for the Degree Committee of Earth Sciences, including 225 pages of text, appendices, illustrations and bibliography.

Victoria Claire Honour

Microstructural evolution of silicate immiscible liquids in solidifying ferrobasalts

Victoria Claire Honour

Evidence of silicate liquid immiscibility in ferrobasalts is provided by co-existing Fe- and Si-rich melt inclusions and Fe-rich droplets dispersed in the Si-rich glassy mesostasis of rapidly cooled rocks. Crucially, the different physical properties of these unmixed liquids mean that they may migrate and separate within a granular medium, forming chemically distinct accumulations. I combine experiments, geochemistry, image analysis and field observations to better quantify the physical behaviour of emulsions in ferrobasaltic magmas.

Quantification of the microstructural evolution of an emulsion in ferrobasaltic experiments shows that the Fe-rich liquid forms homogeneously nucleated droplets dispersed in an immiscible Si-rich liquid, together with droplets heterogeneously nucleated on plagioclase, magnetite, and pyroxene. Heterogeneous nucleation is likely promoted by localised compositional heterogeneities around growing crystals. The equilibrium wetting angle of Fe-rich droplets on both plagioclase and magnetite increases with decreasing temperature. Droplet coarsening occurs by diffusion-controlled growth (including Ostwald ripening), with an insignificant contribution from coalescence. The experimental observations are scaled to infer that in magma bodies < ~10 m in size, gravitationally-driven segregation of immiscible Fe-rich droplets is unlikely to be significant. The same concepts are investigated using natural samples with preserved immiscible textures found in tholeiitic basaltic glass from Hawaii (USA), the Snake River Plain (USA), and the Laki eruption (Iceland). High-resolution imaging, electron probe microanalysis, and atom probe tomography are combined to examine the role played by compositional boundary layers in promoting unmixing around growing crystals at melt-crystal interfaces. The effects of cooling rate on silicate liquid immiscibility microstructure are studied using basaltic dykes from Northeast England, coupled with simple 1D thermal models. The size of Fe-rich droplets within a continuous silicic phase is found to increase with decreasing cooling rate. At the even slower cooling rate of the Skaergaard Intrusion, field, whole rock and petrographic observations of late-stage immiscible segregations show that complete segregation of unmixed liquids on the metre scale is feasible; therefore, timescales of cooling are shown to be a key factor in immiscible liquid separation.

Microstructural evolution of silicate immiscible liquids in solidifying ferrobasalts

Evidence of silicate liquid immiscibility in ferrobasalts is provided by co-existing Fe- and Si-rich melt inclusions (e.g. Fischer et al., 2016; Jakobsen et al., 2005; Jakobsen et al., 2011; Luais, 1987; Roedder and Weiblen, 1970c) and Fe-rich droplets dispersed in the Si-rich glassy mesostasis of rapidly cooled rocks (e.g. De, 1974; Philpotts, 1982; Philpotts and Doyle, 1980). The physical behaviour of these immiscible liquids in a crystal mush may play an important role in the evolution of mafic intrusions (e.g. Holness et al., 2011; VanTongeren and Mathez, 2012; Zhou et al., 2013). Crucially, the different physical properties of these unmixed liquids mean that they may migrate and separate within a granular medium, forming chemically distinct accumulations. I combine experiments, geochemistry, image analysis and field observations to better quantify the physical behaviour of emulsions in ferrobasaltic magmas.

Quantification of the microstructural evolution of an immiscible basaltic emulsion in ferrobasaltic experimental charges shows that the Fe-rich liquid forms homogeneously nucleated droplets dispersed in an immiscible Si-rich liquid, together with droplets heterogeneously nucleated on plagioclase, magnetite, and pyroxene. Heterogeneous nucleation is likely promoted by localised compositional heterogeneities around growing crystals. The equilibrium wetting angle of Fe-rich droplets on both plagioclase and magnetite increases with decreasing temperature. Droplet coarsening occurs by diffusion-controlled growth (including Ostwald ripening), with an insignificant contribution from coalescence. The experimental observations are scaled to infer that in magma bodies < ~10 m in size, gravitationally-driven segregation of immiscible Fe-rich droplets is unlikely to be significant. The same concepts are investigated using natural samples with preserved immiscible textures found in tholeiitic basaltic glass from Hawaii (USA), the Snake River Plain (USA), and the Laki eruption (Iceland), to examine the onset of unmixing in natural samples, its relationship to crystal growth and the evolution of an emulsion in a crystal mush. High-resolution imaging, electron probe microanalysis, and atom probe tomography are combined to examine the role played by compositional boundary layers in promoting unmixing around growing crystals at melt-crystal interfaces. The effects of cooling rate on the microstructure of unmixed immiscible silicate liquids are studied through detailed microstructural investigations of Paleogene basaltic dykes from Northeast England, coupled with simple 1D thermal models. The size of unmixed Fe-rich droplets within a continuous silicic phase is strongly related to the cooling rate by a power law, with droplet diameter increasing with decreasing cooling rate.

Layered intrusions provide an insight into the geochemical evolution of magmas, increasing our understanding of processes operating in solidifying mushes in the shallow crust (O'Driscoll and VanTongeren, 2017). The well-exposed Skaergaard Intrusion of East Greenland offers a perhaps unparalleled example of closed-system behaviour and uninterrupted fractionation of ferrobasaltic magma. The intrusion preserves a variety of structures interpreted as a record of the behaviour of late-stage evolved liquids, such as gabbroic pegmatites, dendritic anorthosites, and melanogranophyres. Striking associations of irregular Si-rich and Fe-rich segregations are interpreted as the remains of unmixed immiscible liquids. Previous studies of these late-stage features have been limited to particular localities in the intrusion. A more comprehensive investigation, building on recent quantification of the thickness of the mushy layer on the chamber floor, shows that the morphological and compositional variations in the late-stage structures are linked to the physical properties of the crystal mush and the progressive chemical evolution of the bulk magma. The late-stage structures are podiform in thick mush and planar in thin mush. Gabbroic pegmatites are spatially associated with paired Si-rich and Fe-rich segregations. The physical properties of the mush control the movement of the late-stage interstitial liquids, with implications for our understanding of the rheology of mafic sub-volcanic mush and the mechanisms of melt segregation. The compositions of the paired segregations are consistent with experimental evidence for the compositional evolution down the silicate liquid binodal. Complete separation of the mafic- and felsic-rich segregations is observed on the metre scale; therefore, time scales of cooling are shown to be a key factor in unmixed liquid separation.

“It is more fun to talk with someone who doesn't use long, difficult words but rather short, easy words like "What about lunch?”

A. A. Milne, Winnie-the-Pooh

I dedicate this thesis to my family

– thank you.

With love

Acknowledgements

A big thank you to my supervisor, Marian Holness – your honesty, support and guidance throughout my PhD have been invaluable. I have learnt a tremendous amount from working with you and your supervision has been instrumental in my development as a scientist. Thank you to Bernard Charlier (University of Liège, Belgium), Michael Stock, Sandra Piazolo (University of Leeds), John Maclennan, and Jerome Neufeld; our discussions and time working together have always been thought provoking, highly useful and enjoyable. I am incredibly grateful for your kindness in going above and beyond when I needed guidance. I would also like to thank Troels Nielsen (GEUS), George Bergantz (University of Washington, USA), Madeleine Humphreys (University of Durham), Michael Carpenter, Olivier Namur (KU Leuven, Belgium), Joseph Paulsen (Syracuse University) and Zoja Vukmanovic for advice, support and timely conversations. I am very thankful for samples loaned to me by the Sedgwick Museum, University of Cambridge; Roz Helz (USGS), Marlon Jean (University of Alaska Anchorage) and Bernard Charlier; as well as fieldwork locality advice from Brian Young and the late Henry Emeleus; these were vital for several chapters. Many thanks also to Penny Wieser, Simon Matthews and Nick Barber for proof reading and providing helpful discussions and comments on various chapters.

A big thanks to the Skaergaard fieldwork team for a fabulous summer in Greenland, Sam Weatherley (TEK), Brendan Dyck (Simon Fraser University, Canada), Gautier Nicoli, Jens Andersen (Camborne School of Mines, University of Exeter), and Marian. You made it a truly memorable six weeks exploring and working on such an iconic geological locality. The science we achieved and the camp environment we had are testaments to you all, and living in the Arctic for a month was just spectacular. I am indebted to Iris Buisman and Giulio Lampronti, your help, guidance and tutoring on the SEM and electron probe was invaluable – as well as the plentiful political discussions! Thanks also to Robin Clarke, Martin Walker, and Nic Odling (University of Edinburgh) for patience and support with my many rocks during sample preparation. Additional thanks to Nic for running my XRF analyses, and to Ty Prosa and Isabelle Martin at CAMECA for the atom probe tomography work.

This research has been funded by the Natural Environmental Research Council. Additional grants from Jesus College, the Cambridge Philosophical Society and the Geological Society of London have helped enhance the opportunities I have had during my PhD, for which I am incredibly grateful.

Nothing helps power you through a particularly chewy thesis section like some good music, and over the course of the last 6 months I have developed a new found (and unexpected) appreciation of deep house and 70s glam rock… cheers Bowie (amongst others!).

The various occupants of M10 have been a constant source of fun, laughter and encouragement; many thanks to Madeleine Ploy-Bohin, Peter Scott, Charlotte Jackson and Nick Barber. Thanks also to the wonderful co-demonstrators from 1A and ESB labs, Katy Relph, Hal Bradbury, Alec Hutchings, Kieran Gilmore, and Matt Ball; demonstrating with you all, week-in, week-out over the years has been extremely entertaining. A huge thanks to the many friends with whom coffee, chats, and lots of cake have been shared over the course of this PhD – you know who you are, and your friendship, support and smiles have kept me sane over the years!

And finally, an immense thank you to Mum, Dad, and Abigail for your unwavering support, encouragement, eccentric chat, and refreshing perspectives! Coming back to the farm is always such a wonderful, grounding indulgence. I never say it enough, but I could never have done all this without you. Thank you for everything.

CONTENTS

1 SILICATE LIQUID IMMISCIBILITY

1.1 Introduction

Interest in silicate liquid immiscibility has waxed and waned over the last century. Daly (1914) suggested it as a mechanism by which magmas could differentiate; however, Bowen (1928) rejected this, arguing: "In no case has any petrologist advocating this process been able to point out exactly how it [silicate liquid immiscibility] is to be applied to any particular series of rocks". The debate over the role of immiscibility in magmatic differentiation resurfaced after the serendipitous discovery of glassy immiscible products in the Apollo-11 lunar basalt samples (collected 50 years ago last month). Over the last decade, significant petrological and experimental advances have rapidly developed our understanding of unmixing in tholeiitic magmas (e.g. Charlier and Grove, 2012; Hou et al., 2018; Jakobsen et al., 2011; Veksler et al., 2007). The process of immiscibility is now commonly invoked to explain the formation of metallic cores in terrestrial planets, magmatic sulfide deposits, carbonatites, and magmatic-hydrothermal systems (e.g. Thompson et al., 2007; Veksler, 2004; Wahl and Militzer, 2015).

Silicate liquid immiscibility has been directly observed in melt inclusions with co-existing Fe- and Si-rich inclusions in the same mineral (e.g. Fischer et al., 2016; Jakobsen et al., 2005; Jakobsen et al., 2011; Luais, 1987; Roedder and Weiblen, 1970c), and as Fe-rich droplets dispersed in Si-rich glass in the mesostasis of rapidly cooled silicate liquids (e.g. De, 1974; Philpotts, 1982; Philpotts and Doyle, 1980). The physical behaviour of these immiscible liquids in a crystal mush may play an important role in the evolution of mafic magmas, particularly if there is relative movement between the two liquids (e.g. Holness et al., 2011; VanTongeren and Mathez, 2012; Zhou et al., 2013).

This thesis seeks to explore the physical behaviour of immiscible silicate liquids and to develop an understanding of the kinetic controls on the onset of unmixing, coarsening of the emulsion, separation of the conjugate liquids, and ultimately to identify how such immiscible liquids migrate through a crystal mush. These concepts require investigation over a variety of length-scales and cooling rates. Hence, this thesis encompasses observations from nano-scale petrography to kilometre-scale field observations, with cooling rates varying between rapidly cooled experiments to a slowly cooled intrusion.

1.2 Structure of thesis

The thesis is divided into four studies (Chapters 2–5), each dealing with unmixing processes at a range of cooling rates.

1.2.1 Chapter 1

This chapter provides an overview of the theoretical background to silicate liquid immiscibility – the common theme investigated throughout this thesis. I discuss the conditions under which unmixing may occur, detail experimental work on element partitioning, and the mechanisms of unmixing. I outline several case studies with a range of cooling rates to illustrate how silicate liquid immiscibility has been directly and indirectly inferred in natural samples.

1.2.2 Chapter 2

Chapter 2 details an experimental study of emulsion microstructural evolution with decreasing temperature in a ferrobasalt. Combining image analysis with geochemistry I investigate the nucleation (homogeneous and heterogeneous) and coarsening of Fe-rich droplets dispersed in an immiscible Si-rich liquid. I examine the wetting angles of Fe-rich liquids on different crystals phases and assess several microstructures that may be indicative of crystallisation in the presence of an unmixed liquid. Overall, the implications for gravitationally-driven segregations of immiscible liquids are discussed.

1.2.3 Chapter 3

In Chapter 3 a detailed microstructural investigation of three basaltic dykes from Northeast England are combined with a simple theoretical model to produce a quantitative relationship between the size of unmixed Fe-rich droplets and the cooling rate of basalt. The crystallisation regime of the dykes and the potential growth mechanism of Fe-rich droplets are also proposed.

1.2.4 Chapter 4

I present the results and interpretations of geochemical and microstructural analyses on basaltic samples from the Kīlauea Iki lava lake (Hawaii, USA), Laki eruption (Iceland) and Snake River Plain lava flow (USA). Records of compositional boundary layers forming around growing plagioclase crystals highlight a kinetic control on unmixing of a basaltic composition. Novel analytical techniques, including the first use of atom probe tomography (APT) on basaltic glass, are used to investigate such features.

1.2.5 Chapter 5

I discuss background information on the Skaergaard Intrusion (Greenland), focusing on the late-stage segregations identified within the intrusion. I detail observations of the late-stage segregations from my fieldwork on the intrusion, with a focus on their interaction with the surrounding gabbro. I present a geochemical and petrological investigation of the late-stage segregations looking at the major and trace element whole rock geochemistry and plagioclase mineral chemistry. I discuss the migration of late-stage liquids within the layered series alongside a model for unmixing and segregation of late-stage liquids within granular media.

1.2.6 Chapter 6

Chapter 6 is split into three parts. First, the main findings of each study are summarised. Second, these findings are placed into context and their broader implications for magma unmixing and ultimately segregation of two immiscible liquids are discussed. Finally, I outline areas for future research into unmixing processes.

1.3 Principles of unmixing

Liquid immiscibility, or phase separation, is a well recorded phenomenon in glass-forming binary and multicomponent silicate systems (e.g. James, 1975; Roedder, 1978; Shelby, 2005). Whether phase separation occurs is driven by thermodynamics and is determined by the Gibbs free energy (ΔG) of the system (equation 1.1). If mixing two phases yields a lower free energy (ΔG_m) at constant pressure and temperature, the mixture will remain homogeneous; if separation of two phases yields a lower ΔG_m at constant pressure and temperature then the mixture will unmix to reach equilibrium, if kinetically feasible (e.g. James, 1975; Shelby, 2005). Wood and Hess (1980) showed that phase separation arises from the conflict between enthalpy (ΔH) and entropy (ΔS) in minimising Gibbs free energy:

$$\Delta G = \Delta H - T\Delta S \qquad \textit{(equation 1.1)}$$

At higher temperatures (T) there is greater chemical disorder and so the entropy contribution is greater: a more random distribution of cations minimises the free energy of the mixture (Wood and Hess, 1980). At lower temperatures, the enthalpy term dominates as $T\Delta S$ becomes smaller. Consequently, to minimise the ΔG, the mixture splits into two coexisting phases (Fig. 1.1a): one weakly polymerised with a low SiO_2 content and abundant network modifying cations (the Fe-rich liquid), the other highly polymerised, rich in SiO_2 and with abundant network forming cations (the Si-rich liquid). Generally, the Fe-rich end member is enriched in Fe, Ti, Mg, Ca, P and Mn and the Si-rich end member is enriched in Si, Al, Na and K.

Network forming cations are small, highly charged cations, with coordination numbers (the number of ions surrounding the cation) ≤4 in silicate liquids and solids. The most abundant network forming cation in tholeiitic systems is Si^{4+}. Network modifying cations have ionic radii >87.2 pm, with coordination numbers ≥5 (Hudon and Baker, 2002). This group includes cations such as the rare earth elements (REE), Th^{4+}, U^{4+}, and some alkali and alkaline earth elements. Cations greater in size than Si^{4+} (26 pm), but smaller than 87.2 pm, with multiple co-ordination numbers (named amphoteric cations) are an important group for tholeiitic liquids and include Al^{3+}, Mg^{2+}, Ti^{4+}, Zn^{2+}, and Mn^{2+}.

At the atomic level, unmixing results from Coulombic forces (Hess, 1995). Coulombic forces are the forces holding ions together and in ionic solids these are electrostatic. In the oxide-silica systems the size of the miscibility gap increases non-linearly (Hudon and Baker, 2002) with the ionic

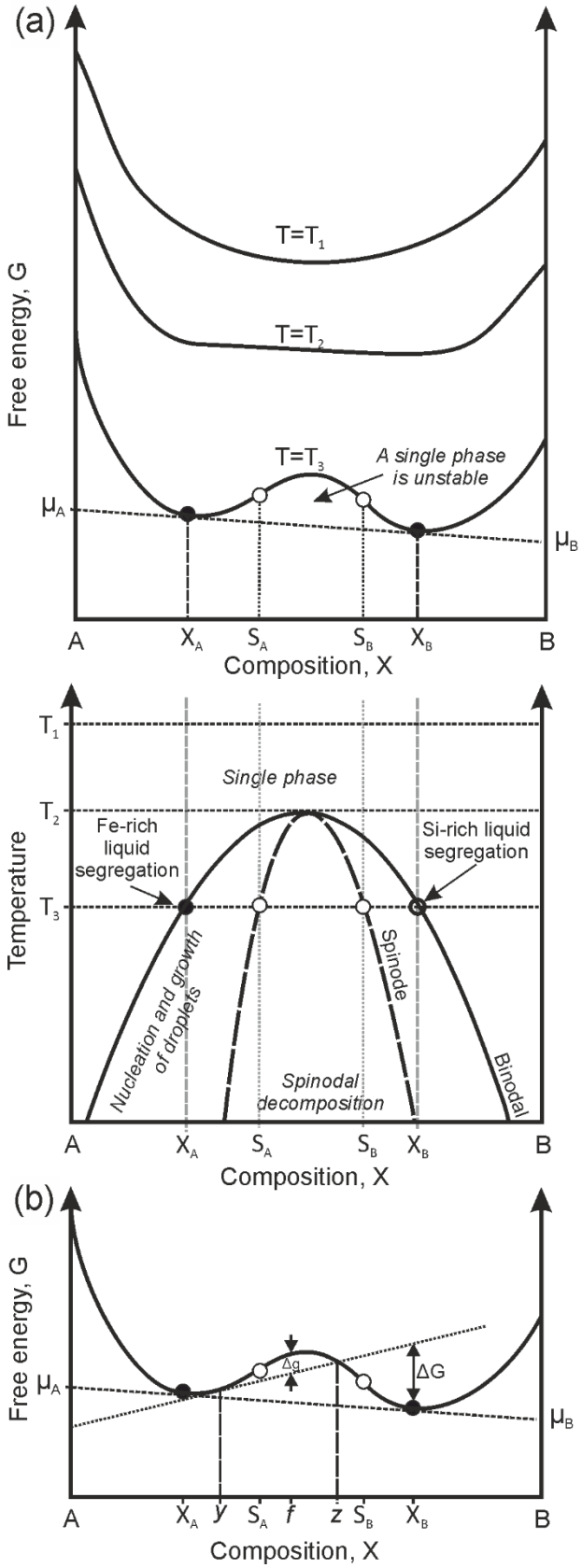

Figure 1.1. A schematic binary system showing (a) Gibbs free energy (G) versus composition (X) for different temperatures (T_1 to T_3), defining a binodal and spinodal in temperature-composition space. X_A and X_B are equilibrium compositions of unmixed, immiscible liquids. μ_A and μ_B are chemical potentials of the liquids A and B. S_A and S_B are the inflexion points that define the spinodal. (b) Free energy (G) versus composition (X), showing the driving force and the barrier for nucleation.

potential of the network modifying cations (ionic potential is defined as Z/r; where Z is the cation charge and r is the cation radius). Consequently, Hudon and Baker (2002) proposed that there is a structural control on silicate liquid immiscibility as determined by the network modifying cation radius. The charge of any network modifying cation is poorly shielded due to the configuration of the electron shells, and consequently Coulombic repulsion builds up between cations, promoting phase separation. Notably, Hudon and Baker (2002) showed that miscibility gaps are larger for trivalent cations, such as V^{3+}. Amphoteric cations with 4-fold coordination numbers have covalently bonded cation-oxygen pairs surrounded by an electron cloud, which shields the positive charge of the nuclei and so reduces the repulsion from other amphoteric cations (Hudon et al., 2004). This results in minimal phase separation. Cations with greater than 4-fold coordination numbers are bonded to 5 or more (relatively) distant oxygens via bonds with a strong ionic character, which results in a weaker shielding effect and so greater repulsion between cations, widening any miscibility gap (Hudon et al., 2004).

The miscibility gap is defined in temperature-composition (T-X) space by the binodal curve (Fig. 1.2): the region on a T-X phase diagram below which it is energetically favourable for a single-phase liquid to unmix. The interaction between the binodal and the liquidus of a given liquid determines the stability of the miscibility gap (e.g. Biggar, 1979; Freestone, 1979; Philpotts and Doyle, 1980; Philpotts, 1979). If the binodal lies above the liquidus, the miscibility gap is stable. At the binodal-liquidus intersection, two immiscible liquids and solid phases exist (Fig. 1.3). If the binodal lies beneath the liquidus then the miscibility gap will be metastable (Philpotts, 1979; Veksler and Charlier, 2015). The presence of a subliquidus miscibility gap distorts the liquidus surface (Fig. 1.3b) and so limits the development of intermediate compositions (Charlier and Grove, 2012; Freestone and Powell, 1983). The distinction between metastable and stable liquid immiscibility ultimately affects the scale of the unmixing process, the potential for segregation of the two immiscible liquids, and therefore the capability of the process to produce large-scale magma differentiation. If metastable, the process of unmixing remains highly localised.

Below the binodal, the spinodal defines the T-X space in which there are no thermodynamic barriers to unmixing (the spinodal is defined by the Gibbs free energy curve having a $d^2y/dx^2 = 0$; Fig. 1.2) and infinitesimally small fluctuations in composition and density grow spontaneously by uphill diffusion, leading to unmixing (Cahn, 1961). Below the spinode the interface between the two unmixed phases is characterised by low amplitude concentration differences that sharpen with time (James, 1975).

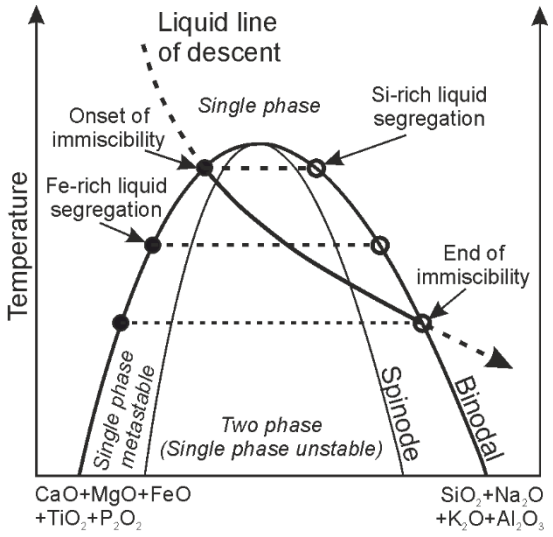

Figure 1.2. A sketch after Charlier and Grove (2012); Philpotts and Ague (2009) showing the liquid line of descent through a silicate liquid immiscibility field, as defined by the binodal.

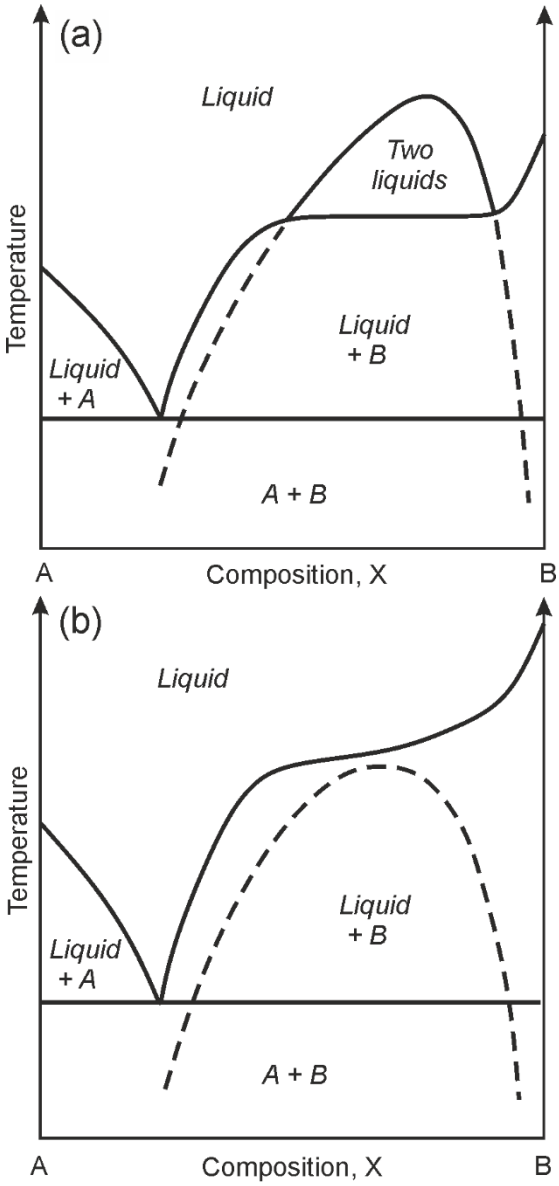

Figure 1.3. Schematic binary showing (a) a stable two-liquid field with an extension to metastable conditions below the liquidus; and (b) metastable unmixing below the liquidus, note the flattening of the liquidus above the metastable binodal, following Freestone (1978); Veksler and Charlier (2015).

1.4 Onset of silicate liquid immiscibility and the size of the miscibility gap

Liquid composition, crystallisation temperature and pressure, crystallisation order, cooling rate, and oxygen fugacity all affect the stability, shape, size, and apex of the miscibility gap (e.g. Charlier and Grove, 2012; Dixon and Rutherford, 1979; Philpotts and Doyle, 1983; Roedder, 1951; Veksler et al., 2007; Visser and Van Groos, 1979b). Prior work on constraining the miscibility field has chiefly focused on dry tholeiitic magma compositions. Below, I outline the existing studies investigating

silicate liquid immiscibility in tholeiitic systems, as well as the limited literature on hydrous- and alkaline-rich systems.

1.4.1 Dry tholeiitic compositions

Bowen (1928) rejected the idea of immiscibility as a large-scale magma differentiation process, arguing that the known immiscibility field in the fayalite-SiO_2 system existed at a temperature too high (greater than 1689°C) to be of relevance to igneous petrologists. The debate was reopened with the discovery by Roedder (1951) of the low temperature (below 1100°C) immiscibility field in the fayalite-leucite-silica system at atmospheric pressure. In recent years, experiments on liquid immiscibility in ferrobasalts have progressively increased in complexity from five-component systems (e.g. Greig, 1927; Greig, 1928; Naslund, 1976; Roedder, 1951; Visser and Koster Van Groos, 1976) to basaltic systems (e.g. Charlier and Grove, 2012; Charlier et al., 2013; Hou and Veksler, 2015; Philpotts, 1976; Philpotts, 1979; Veksler et al., 2008b).

The temperature of unmixing differs between static and dynamic (centrifuge) experiments. Static experiments conducted at one-atmosphere with a rapid quench have constrained the apex of the binode surface to 1025°C for equilibrium ferrobasaltic compositions (Charlier and Grove, 2012). The centrifuge experiments of Veksler et al. (2007) sought to establish if silicate liquid immiscibility could occur in ferrobasalts at high temperatures (>1100°C), as unmixing of a ferrobasalt prior to 50% crystallisation (at 1070–1100°C) has greater significance for large-scale magma differentiation. In the centrifuge experiments, droplets of Fe-rich liquid were produced but there were no examples of clearly defined liquids (in equilibrium) separated by a meniscus (Charlier, 2015). The results and implications of Veksler et al. (2007) experiments have been debated (McBirney, 2008; Morse, 2008a; Philpotts, 2008; Veksler et al., 2008a). Philpotts (2008) suggested the unmixing formed as the liquid line of descent crossed below a sub-liquidus binodal and so was metastable. Further experimental evidence for a stable two-liquid field in a ferrobasaltic system at 1150–1200°C was presented by Hou and Veksler (2015). Their experiments (mixing, rather than unmixing experiments) produced an Fe-rich liquid at 1150°C with a composition of 53–56 wt.% SiO_2 and 15–18 wt.% FeO. This is a more silica-rich composition than produced by static experiments drop quenched at 1020°C, which have 30–50 wt.% SiO_2 and 18–32 wt.% FeO (approximating to a pyroxenitic composition; Charlier and Grove, 2012).

Previously, it was thought that extreme iron enrichment (i.e. >19 wt.% FeO) was a necessary condition for the onset of unmixing (Dixon and Rutherford, 1979; Philpotts and Doyle, 1983). A single experiment by Philpotts and Doyle (1983) reported an FeO of 15.4 wt.% prior to unmixing. Subsequently, experiments by Charlier and Grove (2012), using starting compositions between 46–56 wt.% SiO_2 and 12–18 wt.% FeO, have shown that extreme iron enrichment is not inherently required to reach the silicate liquid immiscibility field. Rather, silicate liquid immiscibility can develop during iron depletion (i.e. <19 wt.% FeO) and post-crystallisation of Fe–Ti oxides (Charlier and Grove, 2012).

The cooling rate of a liquid affects the crystallisation order of the major phases (Grove and Bence, 1979), which in turn affects the development of an iron depleted or enriched liquid line of descent. This impacts the size and shape of the miscibility gap. The miscibility gap is expanded by higher concentrations of TiO_2 in the liquid (Bogaerts and Schmidt, 2006; Charlier and Grove, 2012; Ryerson and Hess, 1978; Visser and Van Groos, 1979b; Watson, 1976). Higher P_2O_5 concentrations increase the modal plagioclase/pyroxene ratio, which promotes iron enrichment during magma differentiation (Toplis et al., 1994). Unmixing is also promoted by elevated concentrations of Na_2O, K_2O, Cr, and REE (Charlier and Grove, 2012; Watson, 1976), whereas the substitution of MgO for FeO reduces the miscibility gap (Naslund, 1976). Likewise, increasing the concentration of CaO and Al_2O_3 in the liquid stabilises a single-liquid field (Cygan and Koster van Groos, 1978).

Pressure causes competing expansion and contraction effects on the miscibility gap. There is a trade-off between the pressure effects on the stability of the liquidus phases and the response to pressure of the cations in the system (Hudon et al., 2004). High pressure expands the stability field of augite, reducing the relative volume of plagioclase in the assemblage, as olivine, augite, and plagioclase crystallise in closer mass proportions, and hence early iron enrichment of the liquid is inhibited (Grove and Baker, 1984; Grove et al., 1992; Villiger et al., 2006; Villiger et al., 2004). This effect is compound as plagioclase crystallisation affects the concentration of elements which expand the silicate liquid immiscibility field. For example, after plagioclase saturation but before oxide saturation, TiO_2 concentrations in the remaining melt increase rapidly; lower volumes of plagioclase crystallisation therefore reduces the expansion of the immiscibility gap normally attributed to TiO_2. In systems dominated by network modifier cations (e.g. Ca^{2+}), pressure has a minimal effect on the miscibility gap due to their high coordination numbers at atmospheric pressure i.e. they have a compact arrangement and so are not very compressible (Hudon et al., 2004). For systems dominated by amphoteric cations, increasing pressure results in the miscibility gap expanding, as the cations with 4-fold coordination adopt more compact arrangements by increasing their coordination number, which decreases their charge shielding (Durben and Wolf, 1991; Farber and Williams, 1992; Hudon et al., 2004; Kubicki et al., 1992; Williams and Jeanloz, 1988; Yarger et al., 1995). This is true for both Fe^{2+} and Fe^{3+}, at higher pressures they will adopt a 6-fold coordination number expanding the Fe miscibility gap (Hudon et al., 2004). On balance, lower pressure conditions are more favourable for the development of silicate liquid immiscibility (Hudon et al., 2004; Visser and Van Groos, 1979a).

Oxygen fugacity (fO_2) specifies the redox state of the system, which influences the stability and size of the silicate liquid immiscibility field (Philpotts and Doyle, 1983). At atmospheric pressures there is no pure FeO or Fe_2O_3 liquid; any liquid contains both ferric and ferrous Fe in a ratio depending on fO_2. A high Fe_2O_3/FeO ratio (due to high fO_2) causes an expansion of the silicate liquid immiscibility field in the system $KAlSi_3O_8$-FeO-Fe_2O_3-SiO_2 (Naslund, 1983). Oxygen fugacity also influences the stability and first appearance of Fe–Ti oxides (Toplis and Carroll, 1995). High fO_2 promotes magnetite

crystallisation, which inhibits iron enrichment in the bulk liquid. Consequently, at high fO_2 there is a trade-off between miscibility gap expansion and the stabilisation of magnetite causing iron depletion. Toplis and Carroll (1996) investigated the differentiation of ferrobasalts in open and closed oxygen systems, concluding that closed systems better promote silicate liquid immiscibility.

Overall, anhydrous, low-pressure fractional crystallisation is the most favourable condition for unmixing during differentiation. Examples of silicate liquid immiscibility occurring in dry tholeiitic compositions are provided in section 1.8 and 1.9.

1.4.2 Hydrous tholeiitic compositions

H_2O behaves as an incompatible element, increasing in concentration in the bulk liquid with progressive fractionation. At the surface, tholeiitic basalts typically have low water contents (<0.1 wt.% H_2O for primitive MORB; Danyushevsky (2001)). Increasing the H_2O content of a basaltic melt suppresses plagioclase crystallisation relative to other crystallising phases and promotes Fe-Ti oxide crystallisation (Botcharnikov et al., 2008; Sisson and Grove, 1993); this inhibits iron enrichment in the remaining liquid and shifts the liquid line of descent to a calc-alkaline trend. Charlier and Grove (2012) illustrate the decreasing apex temperature of the binodal as a function of the increasing water content during differentiation of a tholeiitic basalt at low pressures. Charlier (2019 pers. comm.) further updated this schematic, highlighting how higher H_2O concentrations also enlarge the two-liquid field (Fig. 1.4). In contrast, at high pressure (200 MPa) H_2O, in isolation or combined with P, S or F, increases the apex temperature and compositional range of the miscibility gap at fO_2 equal to the nickel-nickel oxide and magnetite-hematite buffers (Lester et al., 2013). Overall, they conclude that liquid-phase separation may be stable in some H_2O-rich silicate magmas at pressures >200 MPa. Unmixing was shown to occur experimentally at 100MPa, with elevated fO_2 and H_2O by Hou et al. (2018) at 1000-1040°C.

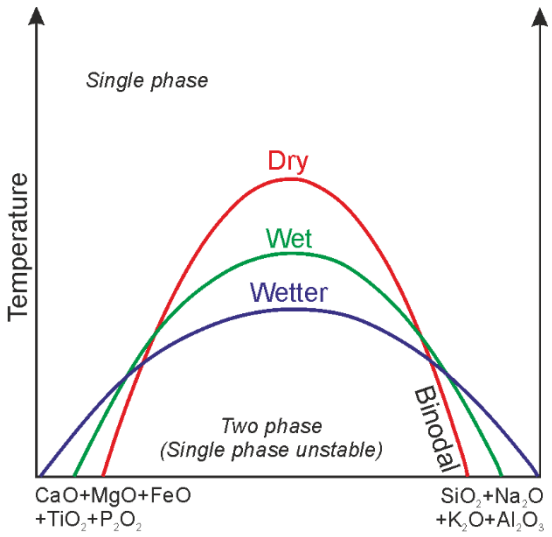

Figure 1.4. Schematic illustration of the potential effect of increasing water content during differentiation of a tholeiitic basalt on the silicate liquid immiscibility field (Charlier 2019 pers. comm.). Increasing water content depresses the binodal apex, but expands the compositional range of the field.

1.4.3 Alkaline compositions

Philpotts (1976) suggests that in alkaline rocks the onset of silicate liquid immiscibility is early enough for the process to be important in large-scale magma differentiation, whereas in tholeiitic magmas the increase in incompatible elements (e.g. Na_2O and K_2O), does not occur in sufficient concentrations to

promote unmixing until the last stages of differentiation. Similar to tholeiitic melts, Freestone (1978) demonstrated that the addition of TiO_2 and P_2O_5 in the silica-fayalite-leucite pseudo-ternary system causes the two-liquid field to expand.

1.5 Mechanisms of unmixing

Unmixing of a cooling liquid can occur by: (1) nucleation of droplets of the volumetrically minor phase, as determined by the initial liquid's composition as it intersects the binodal (Fig. 1.2). In this case, nucleation is limited by thermodynamic and kinetic barriers (Fig. 1.5a). (2) spontaneous spinodal decomposition if the liquid experiences a large, (near-) instantaneous undercooling (Cahn, 1961). There are no thermodynamic barriers to spinodal decomposition; however, there will be kinetic limitations (Fig. 1.5b).

A reduction in Gibbs free energy, driven by the chemical potential difference (Fig. 1.1a) promotes unmixing. However, prior to nucleation of a stable droplet, small compositional fluctuations (as shown by *f* in Fig. 1.1b) in the homogenous liquid produce an increase in free energy (as shown by Δg in Fig. 1.1b; James (1975)). This is a thermodynamic barrier to liquid-liquid unmixing. Any small compositional fluctuation must develop beyond composition z (Fig. 1.1b) for the free energy to decrease and the thermodynamic barrier to be overcome.

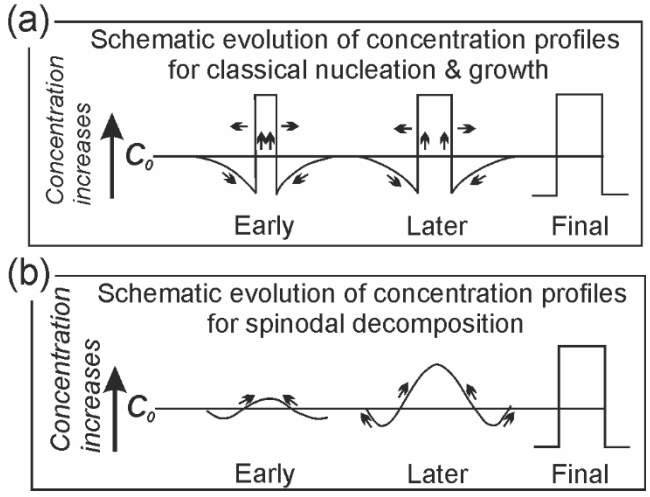

Figure 1.5. The schematic evolution of element concentration profiles for (a) nucleation and growth below a binodal; and (b) spinodal decomposition below a spinode, following Findik (2012).

Nucleation of the minor phase can occur via homogenous or heterogeneous nucleation (Fig. 1.6). Homogeneous nucleation occurs in the interior of a uniform phase and is the formation of a new phase solely from compositional fluctuations within the existing phase (Abraham, 2012; Kalikmanov, 2013). Heterogeneous nucleation utilises pre-existing surfaces as nucleation sites; an example of this is dust, which can serve as a heterogeneous nucleation centre for water condensation in the atmosphere.

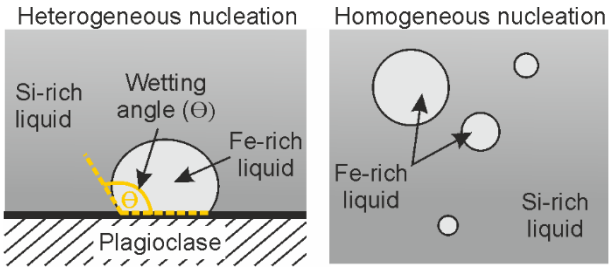

Figure 1.6. A schematic cartoon defining heterogeneous and homogeneous nucleation. Heterogeneous droplets are defined as droplets in contact with a solid phase. Homogeneous droplets are defined as droplets not in contact with any solid phase. The cartoons illustrate the case where the Fe-rich liquid is the minor phase and the Si-rich liquid is the continuous phase.

Classical nucleation theory assumes that the critical radius of a homogeneously nucleated droplet determines the fate of the droplet (e.g. Abraham, 2012). The critical radius denotes the maximum free energy required for the formation of a stable droplet. This free energy is the sum of two terms (Fig. 1.7a): (1) the bulk free energy, which scales with volume and is always negative; and (2) the interfacial energy of the droplet (defined by the surface tension between the interface and its surroundings), which is positive and scales with droplet surface area. Heterogeneous nucleation is more common than homogeneous nucleation as the nucleation barrier is proportional to the surface area of the nucleus. For heterogeneous nucleation this is smaller because part of the boundary is on the surface of a crystal (Fig. 1.7b). Kinetic barriers to nucleation of an immiscible liquid arise from material transport and dynamics (Veksler and Charlier, 2015), and are affected by parameters such as: diffusion rates, viscosity, interfacial tension, and wetting angles between the immiscible liquids and the solids (see section 1.6).

Post-nucleation, the evolution (and hence size) of an immiscible droplet can be controlled by factors operating either in isolation or simultaneously: coalescence, kinetic growth and equilibration (e.g. processes such as Ostwald ripening and growth driven by widening of the binodal during cooling). Martin and Kushiro (1991) found that cooling rate affects the size of immiscible droplets, with droplet size decreasing as cooling rate increases.

Kinetic barriers limit the nucleation and growth of immiscible droplets (Veksler and Charlier, 2015), so while Fe-rich and Si-rich liquids have different physical properties that theoretically should promote separation (see section 1.6), the feasibility of large-scale segregation of two unmixing liquids in natural systems needs to be proven. Current work on the kinetics of silicate liquid immiscibility in natural magmas is still limited (Martin and Kushiro, 1991; Veksler et al., 2008b; Veksler et al., 2010). Veksler and Charlier (2015) explicitly state that further work is required to better understand "the nucleation, growth and potential segregation of immiscible melts".

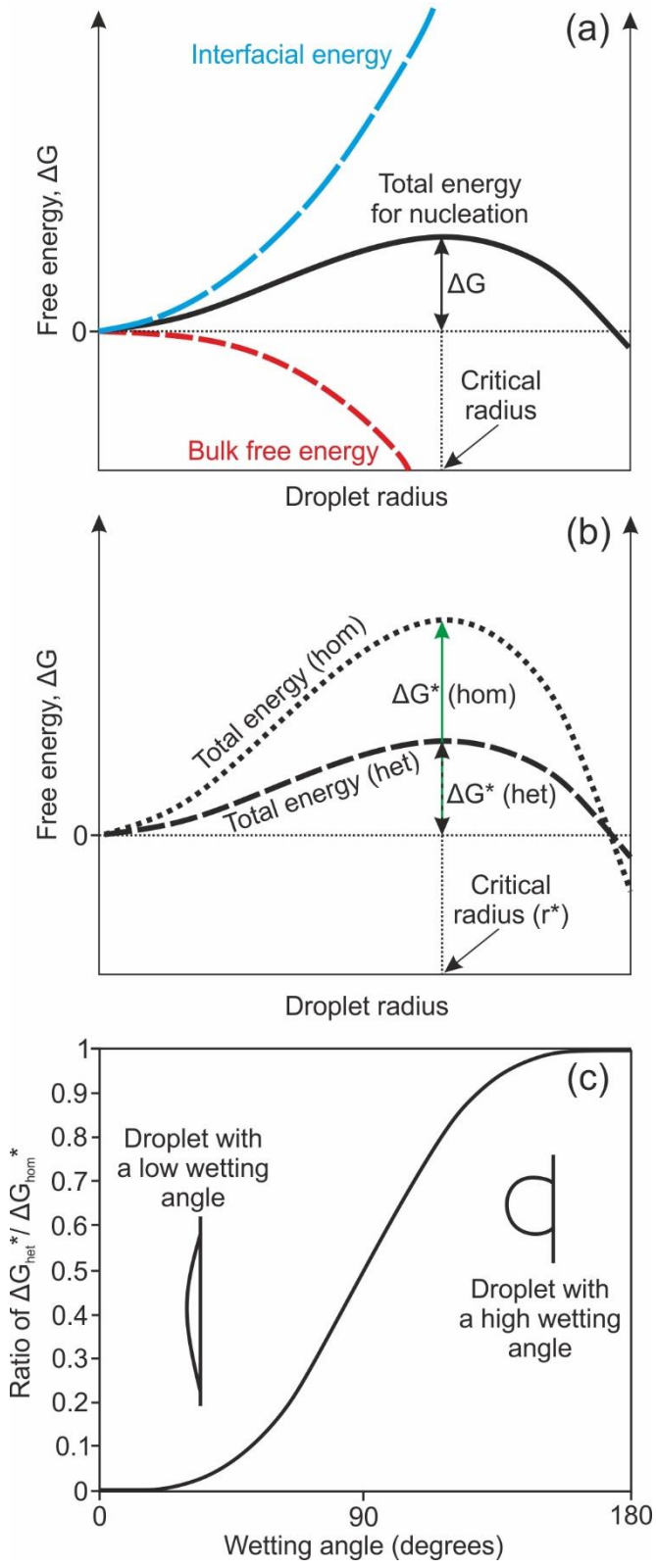

Figure 1.7. A schematic determination of (a) the critical radius size, required for the nucleation of a stable droplet; (b) the differing energy (ΔG*) required for the formation of a stable droplet by homogeneous (hom) nucleation compared to heterogeneous (het) nucleation (e.g. Abraham, 2012); (c) the effect of the ratio of the differing energy required for heterogeneous nucleation compared to homogeneous nucleation versus wetting angle following.

1.6 Physical properties of immiscible melts

1.6.1 Density contrasts

The two immiscible liquids have different compositions and so different densities; the Fe-rich liquid is denser than the Si-rich liquid. The densities of the two liquids will vary depending on the composition of the system. As an approximation, an Fe-rich liquid is typically >2.9 g/cm^3, increasing in density at lower temperatures (between 1050°C to 955°C), while the density of a Si-rich liquid is typically <2.6 g/cm^3 decreasing in density at lower temperatures (as calculated from glass compositions from ferrobasaltic unmixing experiments – see Chapter 2). As a comparison, the density of basalt is typically 2.7–2.8 g/cm^3 (e.g. Stolper and Walker, 1980), while the density of anorthosites is <2.8 g/cm^3 (e.g. Cawthorn and Ashwal, 2009).

1.6.2 Viscosity contrasts

Viscosity is a measure of a liquid's internal resistance to flow; the more polymerised the liquid, the higher the viscosity. The degree of polymerisation of a silicate liquid can be expressed by the parameter: NBO/T, where NBO = number of non-bridging oxygen and T = tetrahedrally coordinated network former cations (Mysen and Richet, 2018). A value of NBO/T = 0 indicates complete polymerisation (e.g. quartz), whereas NBO/T = 4 indicates isolated oxygen tetrahedrons.

The Fe-rich liquid has a lower viscosity than the Si-rich liquid for any given temperature. Viscosities for Fe-rich liquids range from 10^4 Pa.s to 10^3 Pa.s, decreasing with decreasing temperature, while for Si-rich liquids the viscosity ranges from 10^4 Pa.s to 10^7 Pa.s, increasing with decreasing temperature between 1050°C to 955°C (Honour et al., 2019). For the Si-rich liquid NBO/T values are typically <1 (representing a high degree of polymerisation) and Fe-rich liquid NBO/T values range from 1-2 (representing a lower degree of polymerisation) (e.g. Charlier and Grove, 2012; Hamann et al., 2013; Honour et al., 2019). The differing viscosities will affect the separation and migration of the two unmixed liquids.

1.6.3 Interfacial tension

Veksler et al. (2010) measured the interfacial tension between two immiscible liquids resulting from unmixing in the K_2O-FeO-Fe_2O_3-Al_2O_3-SiO_2 system. They showed that the interfacial tension increases with decreasing temperature as the immiscible liquids become more dissimilar in composition. The interfacial tension values were low, ranging from 5-16 mN/m for an Fe-rich liquid nucleating droplets in a continuous Si-rich liquid (Veksler et al., 2010). Droplet nucleation is easier at low interfacial tensions. Furthermore, a low interfacial tension between the immiscible droplets and the continuous phase reduces coarsening rates of the resultant silicate emulsion (James, 1975; Veksler et al., 2010); this will impede the gravitational separation of the immiscible liquids (Veksler and Charlier, 2015). The unmixed liquids in experimental charges typically separate with sharp interfaces (Charlier and

Grove, 2012; Dixon and Rutherford, 1979; Longhi, 1990; Philpotts and Doyle, 1983). Diffuse interfaces in ferrobasaltic experiments have been attributed to slow chemical diffusion (Hou and Veksler, 2015).

1.6.4 Wetting angles

The wetting angle is defined as the angle, conventionally measured through the liquid, where a liquid interface meets a solid. It quantifies the wettability of a solid by a liquid. Wetting angles for an unmixed liquid are a function of the interfacial energy balance between the two liquids and their substrate (i.e. the solid), and are therefore controlled by the compositions of the three phases (e.g. Yablonovitch and Gmitter, 1984). This is expressed in the Young equation:

$$\gamma_{XL1} - \gamma_{XL2} - \gamma_{L1L2}\cos\Theta_c = 0 \qquad \textit{(equation 1.2)}$$

where X is the interfacial energy of the attachment surface, L1 denotes the interfacial energy of the minor liquid phase forming the droplet, L2 denotes the interfacial energy of the major liquid phase, and Θ_C denotes the wetting angle as measured from the crystal surface through the wetting liquid (Young, 1805). Wetting angles control the immiscible liquid morphology and connectivity where in contact with the solid fraction and affect the coarsening and migration of the unmixed liquids within the crystal mush.

The surface area of the droplet decreases as the wetting angle decreases. This geometrical effect reduces the barrier to heterogeneous nucleation and hence results in faster nucleation on surfaces with smaller wetting angles (Sear, 2007). Smaller wetting angles occur when the compositions of the crystal surface and the wetting liquid are more similar (Young, 1805), i.e. the ΔG_{het} required is lower and so the ratio of $\Delta G_{het}^*/\Delta G_{hom}^*$ is lower (Fig. 1.7c).

1.7 Partition coefficients between two immiscible phases

Element partitioning is defined by Nernst's Partition law (1891): "when a solute is taken up with two immiscible liquids, in both of which the solute is soluble, the solute distributes itself between the two liquids in such a way that the ratio of its concentration in the two liquid phases is constant at a given temperature provided the molecular state of the distributed solute is the same in both the phases". Element partitioning between two immiscible silicate liquids is primarily a function of temperature, pressure, redox conditions and composition (Schmidt et al., 2006; Veksler et al., 2006; Watson, 1976).

Liquid-liquid Nernst partition coefficients are typically expressed as

$$D_i = C_i^{Lfe}/C_i^{Lsi} \qquad \textit{(equation 1.3)}$$

where i is the element of interest, C^{Lfe} is the concentration in the Fe-rich liquid, and C^{Lsi} is the concentration in the Si-rich liquid. There is a close relationship between the ionic potential of an element

(Z/r; see section 1.3) and the liquid-liquid partition coefficient (Hudon and Baker, 2002). Elements with wider miscibility gaps for silicate-oxide binary systems (e.g. network modifying cations) have partition coefficients (D_i) >1 and preferentially partition into the Fe-rich liquid (Hudon and Baker, 2002; Schmidt et al., 2006; Veksler et al., 2006). Trivalent cations and REEs have the highest partition coefficients of all elements. In contrast, Si^{4+} and K^+ have partition coefficients <1 and preferentially partition into the Si-rich liquid. Cs, Rb and Sb have the lowest partition coefficients (Veksler and Charlier, 2015), the former two are network modifiers with low ionic potentials while the latter is a network former. Na^+ and Al^{3+} have partition coefficients very close to 1, with approximately equal concentrations in each liquid (Fig. 1.8).

Bogaerts and Schmidt (2006) showed that in the unmixing Fe_2SiO_4–$KAlSi_3O_8$–SiO_2–CaO–MgO–TiO_2–P_2O_5 system, the relationship between the partition coefficients for the network modifying cations (e.g. Fe^{2+}, Ca^{2+}, and Mg^{2+}) and the NBO/T of the Si-rich liquid is best described by a negative power law. Consequently, the more polymerised a Si-rich liquid (i.e. smaller values of NBO/T), the higher the partition coefficient into the Fe-rich liquid. This trend is also observed in unmixed natural glasses (Philpotts, 1976; Philpotts, 1982) and unmixing experiments on natural basaltic compositions (e.g. Dixon and Rutherford, 1979; Longhi, 1990; Rutherford et al., 1974; Ryerson and Hess, 1978). Bogaerts and Schmidt (2006) suggest that the major element partition coefficients are controlled chiefly by the degree of liquid polymerisation.

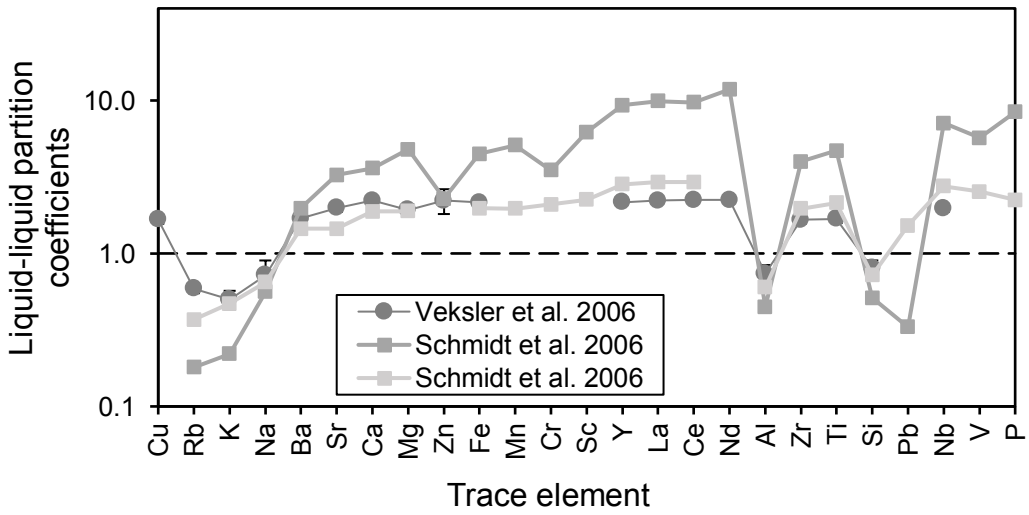

Figure 1.8. Experimentally determined partition coefficients between an Fe-rich and Si-rich immiscible liquid, defined as $D_i = C_i^{Lfe}/C_i^{Lsi}$, where i is the element of interest, C^{Lfe} is the concentration in the Fe-rich liquid, and C^{Lsi} is the concentration in the Si-rich liquid. Data from Schmidt et al. (2006); Veksler et al. (2006). The dark grey squares present experimental sample Z10, while the light grey squares present sample Z18a from Schmidt et al. (2006).

1.8 Liquid immiscibility in rapidly cooled rocks

In rapidly cooled igneous rocks, unmixing is typically a late-stage process affecting the interstitial liquid on a relatively local scale, such as droplets of one crystalline or glassy phase dispersed in another crystalline or glassy phase (e.g. Philpotts, 1976). Here I give an overview of the microstructures that are preserved following rapid cooling after unmixing in the interstices of a crystal mush.

1.8.1 Emulsion microstructures

There is both terrestrial and extra-terrestrial evidence of silicate liquid immiscibility within tholeiitic and alkali rocks in the geological record. Incontrovertible evidence for immiscibility requires two distinct compositions of glass droplets preserved within each other (Roedder and Weiblen, 1970b). Liquid immiscibility occurring along an iron depleted, silica enriched liquid line of descent is recorded by the presence of Fe-rich sub-spherical, crystal-free droplets (of varying diameters up to ~50 μm, generally about 1–2 μm) of brownish, variably devitrified, high refractive index glass within a groundmass of light brown to colourless glass (De, 1974; Philpotts, 1982; Roedder and Weiblen, 1970a). Fe-rich droplets are observed to be either isolated within the mesostasis and/or attached to crystal faces (Fig. 1.6), with a predominant affinity for plagioclase and pyroxene (Luais, 1987; Roedder and Weiblen, 1970a; Sensarma and Palme, 2013). Liquid immiscibility occurring along an iron enriched, silica depleted liquid line of descent is recorded by the presence of Si-rich droplets dispersed within an Fe-rich continuous phase.

Comparatively few studies have investigated the kinetics of silicate liquid immiscibility in natural magmas. Nucleation kinetics will locally affect unmixing in the interstices of a crystal mush. Greater supersaturation is required for nucleation in a small pore compared to a larger one, i.e. greater undercooling is required for nucleation in progressively smaller pores (Bigg, 1953; Cahn, 1980; Holness and Sawyer, 2008; Putnis and Mauthe, 2001; Scherer, 1999). This has implications for the homogeneous nucleation of immiscible droplets in the interstices of solidifying liquids. Philpotts (1978) suggests that at slower cooling rates, Fe-rich droplets preferentially nucleate on phases most similar to their composition and structure (e.g. pyroxene), while at rapid cooling rates Fe-rich droplets nucleate on plagioclase due to slow diffusion of elements. Luais (1987) and Philpotts (1978) attributed the preferred alignment of melt inclusions in plagioclase to the entrapment of a liquid rich in plagioclase incompatible elements at the growing crystal face. This suggests that the kinetics of crystal growth may have significant implications for the onset of silicate liquid immiscibility.

Martin and Kushiro (1991) combined experiments with the study of a tholeiitic basaltic dyke to determine the effect of cooling rate on droplet coarsening in the dyke. They identified that droplet size increases at slower cooling rates. Similarly in pillow lavas, droplet size increases with distance from the margin (Luais, 1987; Mével, 1975). On shorter experimental timescales, Veksler et al. (2008b);

(2010) showed that a fine-scale emulsions can be stable for a significant time i.e. it can have a very low coarsening rate. Such a stable emulsion could have significant effects on magma dynamics due to the differing physical properties of the two liquids.

1.8.2 Preservation in the geological record

Key evidence supporting basaltic liquid unmixing was found in the mesostasis of Apollo 11 lunar mare rocks, in which Si-rich droplets were dispersed in an Fe-rich phase (Roedder and Weiblen, 1970a; Roedder and Weiblen, 1970b). Study of the Apollo 11 lunar rocks paved the way for further microstructural studies on silicate liquid immiscibility (e.g. De, 1974; Philpotts, 1976). Tholeiitic basalts are the most common rock type preserving evidence of liquid immiscibility in the mesostasis, i.e. late-stage unmixing (Philpotts, 1978; Philpotts, 1979). Interstitial unmixing is observed within a variety of lava flows, on different scales. Examples include: high alumina olivine tholeiites from Hat Creek, California and Fuji, Japan (Anderson and Gottfried, 1971; Fujii et al., 1980); tholeiitic dykes from the northeast of England (Philpotts, 1982); olivine basalts from Hawaii (Philpotts, 1982); tholeiitic basalts from Nova Scotia, Canada (Kontak et al., 2002); and the Deccan Trap basalts (De, 1974). Silicate liquid immiscibility has also been observed in glass from meteorite impacts; including the Wabar crater in Saudi Arabia (Hamann et al., 2013), the Reis suevite in Germany (Oberdorfer, 1904), and Libyan desert glass (Pratesi et al., 2002). This is by no means an exhaustive list of studies on unmixing in interstitial liquids, but provides an indication of the wide range of natural examples of unmixing. Undoubtedly there are many more unreported (or unrecognised) grain-scale occurrences of the process.

Droplets are rarely preserved in older rocks due to glass devitrification. However, features attributed to unmixing in older rapidly cooled rocks include Fe-rich relict crystalline structures with pyroxene-like compositions, often with attached small magnetite crystals (Luais, 1987; Philpotts, 1978; Philpotts, 1979; Sensarma and Palme, 2013).

1.9 Liquid immiscibility in plutonic environments

Establishing if unmixing occurred in intrusions is difficult, as intrusive rocks are the fractional crystallisation products of the relevant eutectic for the bulk and interstitial liquids (Veksler and Charlier, 2015). If the two immiscible liquids did not segregate, there would be minimal traces of unmixing in the crystallised rocks as the two immiscible liquids would crystallise the same assemblages and the solidified products of the emulsion would be indistinguishable from the products of a homogeneous liquid with the same bulk composition. However, microstructural features have been suggested to record evidence of late-stage unmixing and two-phase separation within the residual liquids of solidifying gabbroic cumulates (e.g. Holness et al., 2011; Humphreys, 2011), and unmixing has been proposed as a mechanism for large-scale magma differentiation based on melt inclusions and whole

rock geochemistry – provided unmixing occurs early enough during crystallisation (e.g. Jakobsen et al., 2011; Namur et al., 2012; VanTongeren and Mathez, 2012; Veksler et al., 2007). Examples of large-scale and interstitial unmixing raise important questions pertaining to an emulsion's physical behaviour (e.g. nucleation, coarsening and migration).

A variety of approaches have been used in an attempt to identify whether the liquid line of descent of an intrusion crossed the silicate liquid immiscibility field. Pairs of compositionally different, but simultaneously trapped, melt inclusions (one Fe-rich, the other Si-rich) provide direct evidence of an emulsion in the liquid during mineral growth. Such melt inclusions in cumulus apatite have been analysed to irrefutably show evidence of silicate liquid immiscibility in the Skaergaard Intrusion (Jakobsen et al., 2005); the Sept Iles intrusion (Charlier et al., 2011); and the Upper Zone of the Bushveld Complex (Fischer et al., 2016; VanTongeren, 2018). Other authors have used geochemical datasets to infer that unmixing occurred, for example the presence of bimodal whole rock compositions in the Sept Iles intrusion (Namur et al., 2012), and bimodal patterns of trace element compositions such as REEs in apatite in the Bushveld Complex (VanTongeren and Mathez, 2012).

There is not necessarily a need to form fully segregated immiscible layers to significantly affect material transport and post-cumulus crystallisation in an intrusion (Veksler and Charlier, 2015). Even if the bulk magma is compositionally far from the miscibility gap, the interstitial liquid in the crystal mush may become sufficiently fractionated to unmix (Holness et al., 2011). If significant two-phase separation occurs in the immiscible interstitial liquid, the cumulus phases of the mush will be in local disequilibrium with the immediately adjacent liquid. Consequently, the migration of segregated immiscible liquids within the cumulate pile can be documented by inter-cumulus reactive microstructures and trace element mineral chemistry, e.g. TiO_2 in plagioclase (Holness et al., 2011; Humphreys, 2011).

Since the 1970s, immiscibility on the liquid line of descent has been hypothesised and debated for many intrusions, including: Skaergaard, Greenland (McBirney, 1975); Nain Complex, Labrador (Wiebe, 1979); Mull, Scotland (Philpotts, 1982); Duluth Complex, Minnesota (Ripley et al., 1998); Bjerkreim-Sokndal Intrusion, Norway (Wilson and Overgaard, 2005); Upper Zone of the Bushveld Complex, South Africa (Cawthorn, 2013; Fischer et al., 2016; VanTongeren and Mathez, 2012; VanTongeren, 2018); and Sept Iles, Canada (Namur et al., 2012; Namur et al., 2011). Below I outline the evidence for unmixing in several mafic layered intrusions that have helped shape the recent debate.

1.9.1 Skaergaard Intrusion, East Greenland

While the Skaergaard Intrusion has been influential in the silicate liquid immiscibility debate, here I present only a brief overview: a more detailed background summary of the Skaergaard is presented in Chapter 5 together with new observations of liquid unmixing in the intrusion.

Holgate (1954) first hypothesised that the ferrobasaltic bulk magma in the Skaergaard Intrusion split into two immiscible conjugates from the behaviour of "quartzose xenoliths" in basic igneous magmas. Subsequently, field evidence of Si-rich pods and lenses in the upper reaches of the intrusion have been cited as evidence of immiscible Si-rich liquid segregations (e.g. McBirney, 1989; McBirney and Nakamura, 1974; Naslund, 1984; Stewart and DePaolo, 1990). More recently, coexisting Si-rich and Fe-rich inclusions in cumulus apatite provided direct evidence of an emulsion in the bulk magma as the cumulus grains crystallised (Jakobsen et al., 2005). Studies investigating the liquid line of descent also demonstrate the occurrence of liquid immiscibility in the bulk magma (McBirney, 1975; McBirney and Nakamura, 1974; Veksler et al., 2007; Veksler et al., 2008a).

A variety of petrological and geochemical studies indicate the presence of intercumulus unmixing in the middle to upper reaches of the intrusion. This has been argued from the presence of reactive intercumulus microstructures including mafic symplectites, fish-hook pyroxenes, polycrystalline olivine rims on cumulus phases and serrated grain boundaries (Holness et al., 2011). Mineral chemistry (specifically TiO_2 in plagioclase) has been used to constrain the spatial distribution and differential migration of interstitial immiscible liquids within the Skaergaard Intrusion (Humphreys, 2011). Overall, the debate surrounding silicate liquid immiscibility in Skaergaard is not whether unmixing occurred, but rather, when (e.g. Holness et al., 2011; Jakobsen et al., 2005; McBirney and Nakamura, 1974; McBirney and Naslund, 1990; Veksler et al., 2007; Veksler et al., 2008a).

1.9.2 Sept Iles Intrusion, Canada

The Sept Iles layered intrusion (some 80 km in diameter) crystallised from a ferrobasaltic bulk magma (Namur et al., 2015b) that followed a tholeiitic liquid line of descent, with two major magma influxes (Namur et al., 2010). Charlier et al. (2011); and Namur et al. (2012) suggest, based on the bimodal bulk-rock compositions of the ferrogabbros, that unmixing was a significant differentiation process during the crystallisation of one of the three megacyclic units of the Layered Series. The physical separation of the Fe-rich and Si-rich liquids resulted in the formation of alternating bands of leucocratic and melanocratic gabbros on the 5-20 m scale, with the melanocratic bands comprising major P-Ti-Fe deposits. Evidence for unmixing is further supported by co-existing Fe-rich and Si-rich melt inclusions in apatite, which have a homogenisation temperature of 1100–1060°C (Charlier et al., 2011), implying unmixing occurred below this temperature interval. The stratigraphic distribution of particular symplectite structures (attributed to a reaction between cumulus primocrysts and an Fe-rich immiscible liquid following loss of the buoyant Si-rich conjugate (Holness et al., 2011)) are also used to suggest that unmixing occurred during progressive crystallisation (Namur et al., 2012).

1.9.3 Bushveld Complex, South Africa

The Rustenburg Suite of the Bushveld Complex, is the largest layered intrusion on Earth, covering over 66,000 km^2 and comprising mafic-ultramafic gabbroic cumulates, overlain by granites (Eales and

Cawthorn, 1996; Wager and Brown, 1968). The cumulates formed in an open system with multiple magma mixing and replenishment events (Cawthorn, 2015). There is a close association between oxide-rich and phosphate-rich layers in the Complex. A number of different processes have been proposed for the origin of this layering, ranging from dynamic processes of crystallisation of a boundary layer and periodic overturn (Tegner et al., 2006), to silicate liquid immiscibility (e.g. VanTongeren and Mathez, 2012). Reynolds (1985); Von Gruenewaldt (1993) suggested that the oxide-phosphate layering in the upper third of the Bushveld Complex formed from an immiscible Fe-rich liquid based on textural and compositional relations. Sharp changes in the concentration of REE in apatite have been used to infer intrusion-wide segregation in the upper third of the Complex (VanTongeren and Mathez, 2012). However, Cawthorn (2013) disputed the conclusions drawn from the apatite REE patterns (VanTongeren and Mathez, 2012) and instead suggested that the apatite geochemistry formed as a result of the trapped liquid shift effect, whereby cumulus crystals re-equilibrated with an evolved interstitial liquid. Incomplete separation of two immiscible conjugates in the upper third of the Bushveld Complex is hypothesised by Fischer et al. (2016) based on the compositions of apatite melt inclusions. Fischer et al. (2016); and Yuan et al. (2017) suggested that the partial segregation of immiscible liquids in the crystal mush could form the cyclic melanocratic (oxide-phosphate layers) to leucocratic layering observed in the upper third of the Bushveld Complex.

In the Rustenburg Suite are Fe-rich ultramafic pegmatites. These are dominated by ferro-augite, olivine, magnetite and ilmenite. The coarse-grained isolated bodies have a variety of forms, including tubes, discs and complex branching morphologies that cut the stratigraphy (Cawthorn et al., 2000; Reid and Basson, 2002; Scoon and Mitchell, 1994; Viljoen and Scoon, 1985). They range from metres to a few kilometres in scale and have sharp contacts with the host gabbro. The whole rock composition of these Fe-rich pegmatites is analogous to the composition of an Fe-rich immiscible liquid, leading to suggestions that they formed from unmixing and replacement of anorthosites (Reid and Basson, 2002; Scoon and Mitchell, 1994). However, the nature of the processes forming these pegmatitic bodies is controversial (Veksler and Charlier, 2015). Further occurrences of such bodies are presented in Chapter 5.

1.9.4 Stillwater Complex, Montana, USA

The Stillwater Complex is a mafic-ultramafic layered intrusion, with significant mineral deposits, that formed in an open system, with multiple magma injections (McCallum et al., 1980). A major feature of the Complex is the presence of anorthosite sheets, each several hundred meters thick (Hess and Smith, 1960; Raedeke, 1982). Cumulus plagioclase from the anorthosite sheets host crystallised multiphase melt inclusions, which contain traces of Fe-rich liquids. Consequently, it has been suggested that either the anorthosite sheets crystallised from a Si-rich immiscible liquid, or that immiscibility occurred in compositional boundary layers around the crystallising plagioclase (Loferski and Arculus, 1993).

1.10 Implications for Ore Deposits

Silicate liquid immiscibility has potential implications for the formation of ore deposits, specifically Fe-Ti-P ores in layered intrusions (e.g. Von Gruenewaldt, 1993), and by extension Kiruna-type or iron oxide-apatite (IOA) deposits. The origin of these ore bodies is controversial and has been attributed to both magmatic and hydrothermal processes (Chen et al., 2010; Dare et al., 2015; Frietsch, 1978; Hildebrand, 1986; Jonsson et al., 2013; Knipping et al., 2015; Nystroem and Henriquez, 1994). In particular, silicate liquid immiscibility and the subsequent segregation of an Fe–P-rich immiscible liquid from a Si-rich liquid is often invoked to explain the formation of Fe-rich melts (Chen et al., 2010). These conclusions are based on the coexistence of two glass compositions in the matrix and in the melt inclusions of the phenocrysts. Until recently, there has been a lack of experimental evidence for unmixing at conditions suitable for IOA formation. However, Hou et al. (2018) performed experiments at magmatic reservoir conditions relevant to most subvolcanic IOA deposits (i.e. at 100 MPa, 1000–1040 °C, elevated fO_2 and H_2O) and showed that liquid immiscibility is the key process in their formation. This has significance for the future refinement of models for IOA deposits (Hou et al., 2018).

2 MICROSTRUCTURAL EVOLUTION OF SILICATE IMMISCIBLE LIQUIDS IN FERROBASALTIC EXPERIMENTS

A version of this chapter is published as:

Honour, V.C., Holness, M.B., Partridge, J.L. and Charlier, B., 2019. Microstructural evolution of silicate immiscible liquids in ferrobasalts. Contributions to Mineralogy and Petrology, 174(9): 77.

I prepared the samples and planned the experimental set-up. Charlier, B. ran the experiments. I undertook the subsequent analyses. The Matlab script used for image analysis was developed in collaboration with Partridge, J.L., who is a co-author on the manuscript. Data processing and interpretation of the results were my own work.

Co-authors and reviewers have provided comments on the manuscript.

2.1 Introduction

Co-existing Fe- and Si-rich melt inclusions (e.g. Fischer et al., 2016; Jakobsen et al., 2005; Jakobsen et al., 2011; Luais, 1987; Roedder and Weiblen, 1970c) and Fe-rich droplets dispersed in Si-rich glassy mesostasis in rapidly cooled natural examples (e.g. De, 1974; Philpotts, 1982; Philpotts and Doyle, 1980), provide evidence of immiscibility in ferrobasaltic liquid. The physical behaviour of these immiscible liquids in a crystal mush may play an important role in the evolution of mafic intrusions, particularly if there is relative movement of the two liquids (e.g. Holness et al., 2011; VanTongeren and Mathez, 2012; Zhou et al., 2013).

Published experimental work on liquid immiscibility in ferrobasalts has primarily assessed the conditions (e.g. temperature, pressure, composition, fO_2) under which unmixing occurs, evolving in experimental complexity from five-component systems (e.g. Naslund, 1976; Visser and Koster Van Groos, 1976) to complex multiphase systems that more closely replicate basaltic liquids (e.g. Charlier and Grove, 2012; Hou et al., 2018; Hou et al., 2017; Hou and Veksler, 2015; Veksler et al., 2008b). There is little corresponding work on the microstructural evolution of systems containing immiscible liquids, despite its importance in controlling mass transport and large-scale chemical fractionation.

Veksler et al. (2010) measured the interfacial tension between co-existing Fe-rich and Si-rich unmixed liquids and showed that, as expected, it increases with decreasing temperature as the liquids become more dissimilar in composition. The unmixed liquids in experimental charges are observed to separate with either sharp or diffuse interfaces (Charlier and Grove, 2012; Dixon and Rutherford, 1979; Hou and Veksler, 2015; Longhi, 1990; Philpotts and Doyle, 1983; Veksler et al., 2008b). The diffuse interfaces have been attributed to slow chemical diffusion (Hou and Veksler, 2015). Cooling rate affects the size

of the immiscible Fe-rich droplets and the extent of coarsening (Martin and Kushiro, 1991). The differential flow of the two immiscible liquids in a porous medium, driven by density differences, has been investigated in fluid dynamical models (Dufek, 2016; Hassanizadeh, 2016), but these models do not account for any control on liquid migration through a crystal mush by the effect of emulsion coarsening, or different wetting properties of the two liquids (about which little is known, despite the importance of wetting angle in sintering and grain boundary formation (German et al. 2009)).

What is currently missing is a systematic, quantitative study of the kinetics of unmixing and microstructural evolution of immiscible liquids in basaltic systems. Here, I report the results of an experimental study designed to address this gap in our understanding with some comparisons to natural samples. Anhydrous one-atmosphere crystallisation experiments on ferrobasaltic compositions were conducted, in which unmixing manifests by the separation of Fe-rich droplets in a continuous Si-rich phase. I analysed the resultant microstructures to provide insights into the processes controlling the physical behaviour of unmixing and coarsening of immiscible liquids in a crystal mush. Using backscatter electron images on 2D slices through the experimental charges, I quantified the wetting angles of Fe-rich droplets on crystal phases, produced droplet size distributions (DSDs), and linked these textural characteristics to the spatial distribution and composition of the Fe-rich droplets.

2.2 Experimental methods and analytical procedures

2.2.1 Starting materials

I chose a sample of monzonitic composition from the Sept Iles Intrusion (Quebec, Canada), sample 03-41, that has been studied by Namur et al. (2011) and Charlier and Grove (2012) (Table 2.1). The sample originally contained 165 ppm Ce, 103 ppm Y and 786 ppm Zr. I doped the starting composition to reach 1000 ppm for these elements and also for Rb; the former three elements preferentially partition into an immiscible Fe-rich liquid, whereas the latter preferentially partitions into an immiscible Si-rich liquid (Veksler et al., 2006).

Data I obtained from microstructural analysis of seven experimental charges produced by Charlier and Grove (2012) are also presented in this study. These charges have starting compositions of sample 03-41 from the Sept Iles Intrusion (Canada; experiments: SI-5, SI-8, SI-9) and an intermediate basalt from the Mull Tertiary volcano (Scotland; experiments: M-9, M-5, M-6, M-7; Table 2.1). Both localities preserve evidence of immiscibility (Charlier et al., 2011; Namur et al., 2012; Philpotts, 1982).

2.2.2 Experimental techniques

Anhydrous one-atmosphere experiments were performed using a GERO HTRV 70-250/18 vertical tube furnace at the University of Liège, Belgium. The starting materials were suspended in the hot spot of the furnace (ca. 5 cm with a temperature within ± 1°C). The sample temperature was measured using a

$Pt–Pt_{90}Rh_{10}$ thermocouple calibrated to the melting points of Ag and Au. The experimental charge was prepared on a 0.2 mm iron–platinum alloy loop, which I previously annealed with 11 wt.% Fe added by electroplating to prevent Fe loss to the alloy during the experiment (Grove, 1982). The oxygen fugacity in the alumina tube was controlled using mixtures of high-purity CO and CO_2 flushed from bottom to top. Bronkhorst gas flow controllers were used to control the flow rate at 0.12 cm/s. The furnace tube, the water-cooled flange, and the gas connections form a gas-tight system. The oxygen fugacity was monitored using a zirconium dioxide oxygen sensor and was kept at the QFM buffer. Prior to experiments some sample pellets were heated to 1104°C at QFM while others were heated in a muffle furnace in air to 1150°C (see section 2.3.5.5 for implications), both sets were quenched in air.

Table 2.1. Compositions of starting materials (wt.%) (Charlier and Grove, 2012; Philpotts and Philpotts, 2005)

	Sept Iles	**Mull**	**Kīlauea Iki lava lake**	**Cohassett flood-basalt flow**
No. of analyses	15	17 (Charlier & Grove, 2012)	45	Whole rock XRF (Philpotts & Philpotts, 2005)
SiO_2	57.91	54.9	54.22	53.4
TiO_2	2.07	2.40	3.99	1.67
Al_2O_3	14.78	13.40	12.55	13.81
FeO	10.57	14.40	11.88	11.7
MnO	0.09	0.19	0.19	0.2
MgO	2.16	3.35	3.62	5.2
CaO	4.69	6.36	6.94	8.9
Na_2O	4.51	2.31	2.87	2.6
K_2O	2.64	1.45	1.60	1.2
P_2O_5	0.78	0.92	0.91	0.2
Total	100.20	99.68	98.78	98.88
Mg#	26.5	29.0	21.5	28.6

The experimental run conditions are detailed in Table 2.2. Nine experimental charges were cooled at 1°C/h to different temperatures and quenched in water (Fig. 2.1). Pre-quench temperatures of the experimental charges ranged from 1150˚C to 955˚C. An additional six samples were cooled at 1°C/h and then held isothermally at 1021°C or 1000°C for up to 158 h or 182 h respectively. These experiments, which I describe as "isothermal" for simplicity, were quenched in water after different dwell times (at 1021°C: t_{12} = 12 h, t_{40} = 40 h, t_{158} = 158 h; at 1000°C: t_{18} = 18 h, t_{62} = 62 h, t_{182} = 182 h). Experiments were held at 1100°C prior to cooling to ensure equilibration at QFM. Unless described as experimental charges that were subjected to an isothermal dwell time, the temperatures used to describe

the experimental charges are the pre-quench temperatures, after 1°C/h cooling with no time spent isothermally.

Table 2.2. Experimental conditions and phases present; gl glass, pl plagioclase, ol olivine, aug augite, pig pigeonite, il ilmenite, tmt titanomagnetite, mt magnetite, wht whitlockite; italicised final temperatures denote experiments prepared @ QFM.

Run	Starting temperature (°C)	Final temperature (°C)	Time (h)	Cooling method	Starting preparation	Phases present
VIC08	1100	1050	74	1°C/h	Melted to 1150C - muffle furnace	gl, pl, aug, pig, mt
VIC06	1100	*1030*	94	1°C/h	Melted to 1104°C @ QFM	gl Si, gl Fe, pl, ol, aug, pig, tmt, mt
VIC08	1100	1025	99	1°C/h	Melted to 1150C - muffle furnace	gl Si, gl Fe, pl, aug, pig, mt, wht
VIC08	1100	1010	114	1°C/h	Melted to 1150C - muffle furnace	gl Si, gl Fe, pl, aug, pig, mt, wht
VIC06	1100	*1010*	114	1°C/h	Melted to 1104C @ QFM	gl Si, gl Fe, pl, ol, aug, pig, mt, wht
VIC07	1100	1005	119	1°C/h	Melted to 1150C - muffle furnace	gl Si, gl Fe, pl, aug, pig, mt, wht
VIC09	1100	1000	124	1°C/h	Melted to 1150C - muffle furnace	gl Si, gl Fe, pl, aug, mt, wht
VIC09	1100	980	144	1°C/h	Melted to 1150C - muffle furnace	gl Si, gl Fe, pl, aug, pig, mt, wht
VIC09	1100	955	169	1°C/h	Melted to 1150C - muffle furnace	gl Si, gl Fe, pl, aug, pig, mt, wht
VIC10	1100	1021	115	Isothermal	Melted to 1150C - muffle furnace	gl Si, gl Fe, pl, aug, pig, mt. wht
VIC10	1100	1021	143	Isothermal	Melted to 1150C - muffle furnace	gl Si, gl Fe, pl, aug, pig, mt, wht
VIC10	1100	1021	261	Isothermal	Melted to 1150C - muffle furnace	gl Si, gl Fe, pl, aug, pig, mt, wht
VIC06	1100	*1000*	142	Isothermal	Melted to 1104°C @ QFM	gl Si, gl Fe, pl, ol, aug, pig, mt, wht
VIC07	1100	1000	186	Isothermal	Melted to 1150C - muffle furnace	gl Si, gl Fe, pl, aug, pig, mt, wht
VIC07	1100	1000	306	Isothermal	Melted to 1150C - muffle furnace	gl Si, gl Fe, pl, aug, pig, mt, wht

2.2.3 Natural samples

I chose two well-characterised natural examples of liquid immiscibility for preliminary microstructural comparisons with the experiments, based on their similarities in composition and temperature history to the experiments (Table 2.1): 1) the 1976 drill core from the Kīlauea Iki lava lake in Hawaii, USA (e.g. Helz, 1980); and 2) the Cohassett flood-basalt flow, Hanford, Washington, USA (e.g. Philpotts and Philpotts, 2005).

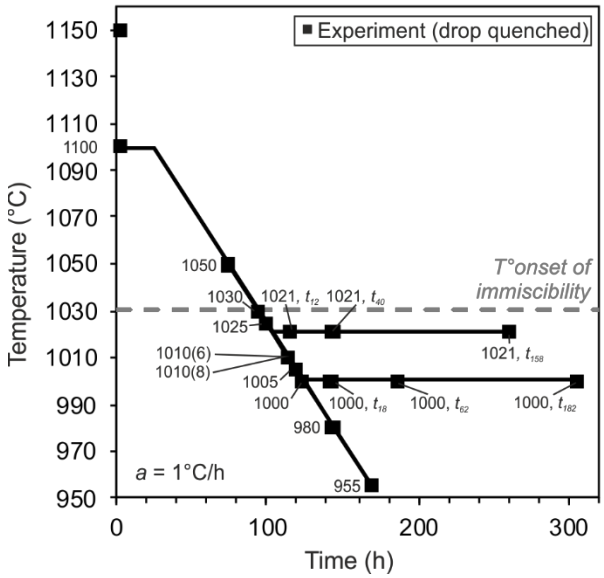

Figure 2.1 Temperature-time paths for experimental runs with a constant cooling rate (Table 2.2). There is a variable duration along a final isothermal plateau for two different experiments held at different temperatures (1000°C and 1021°C). The duration (in hours; Z) that each experiment was held at for that temperature are indicated by t_Z. a = the cooling rate of the experiments.

2.2.4 Analyses

The experimental charges were split and mounted in epoxy. The charges were analysed using a Quanta FEG 650 F SEM at the Department of Earth Sciences, University of Cambridge, using a 10 kV beam at spot 3, with a 30 μm aperture and a working distance of 10 mm. This provided semi-quantitative mineral compositions, element energy dispersive X-ray spectroscopy (EDS) maps and back-scatter electron (BSE) imagery (Fig. 2.2a-d). Images (3072 x 2048 pixels in size) were collected from transects across each experiment, with a dwell time of 20 μs.

The area of each Fe-rich droplet, and the number of droplets, were quantified from BSE images using *Matlab R2017b*. The smallest effective droplet diameter that could be resolved for image analysis was 0.25 μm. There are two types of Fe-rich droplet (Fig. 1.6): attached droplets are in contact with a crystal phase, whereas isolated droplets are (at least in the 2D plane of the image) surrounded by glass (Fig. 2.2e-f). I measured attached droplets and isolated droplets separately. The effective diameters of all Fe-rich droplets (as viewed in 2D) were calculated from their area, assuming a circular shape. The true, 3D, distribution of droplet sizes was calculated using *CSDCorrections1.6* (Higgins, 2000), assuming a spherical shape and using a logarithmic base 2 scale to calculate bin sizes.

The wetting angle of Fe-rich droplets in contact with plagioclase, magnetite and pyroxene was determined from populations of >25 apparent wetting angles per experimental charge, using *CorelDRAW X7* to measure the angle from the crystal surface through the Fe-rich droplet in BSE images (Fig. 2.2f) (Mungall and Su, 2005; Rotenberg et al., 1983). Measurements were taken for both sides of

each droplet, and all discernible attached droplets in each image were measured. The median of a population of at least 25 measurements of apparent (2D) angles is within a few degrees of the true (3D) angle (Riegger and Van Vlack, 1960). I determined the 95% confidence intervals for the true (3D) angle following Stickels and Hucke (1964).

Following the methodology outlined by Holness (2014), the 'fit ellipse' function in *ImageJ* software was used to calculate plagioclase apparent aspect ratios from measurements of the long and short axes of a minimum of 250 plagioclase grains per sample, from BSE images. In each image, all discernible plagioclase grains were measured. I use the parameter AR, defined as the average apparent aspect ratio of plagioclase as viewed in thin section (e.g. Boorman et al., 2004; Holness et al., 2017a); this can be used as a measure of grain shape with no associated assumptions about the range of 3D shapes (c.f. Higgins, 1994), and changes systematically with cooling rate (Holness, 2014). The 95% confidence intervals for AR were calculated using bootstrap sampling. Average apparent plagioclase grain sizes were quantified using the long axis of a minimum of 250 plagioclase grains, for which the length was determined using the perimeter function in *ImageJ* software.

Mineral and glass compositions were measured using a CAMECA SX-100 electron microprobe with five WDS spectrometers at the Department of Earth Sciences, University of Cambridge. The instrument uses PeakSight software with ZAF correction. Appropriate natural and synthetic primary standards were used. The glass analyses were run at 15 kV, 4 nA with a defocused 10 μm, 5 μm and 2 μm beam. Regardless of the beam size, 40 analyses of natural and synthetic glasses (Basalt glass Makaopuhi Lava Lake HI NMNH 113498-1 A-99; and Corning Glass Reference 'D' NMNH 117218-3) had standard deviations of 0.5 wt.% or less for all elements (Appendix Table 2.A). Na and Si were analysed on peak for 10 s; Al for 20 s; K, Ca, Mg and Fe for 30 s; Mn and Ti for 40 s, and P, Y, Zr and Ce for 60 s. Mineral compositions were analysed at 15 kV, 10 nA with a focused beam; Na and Si were analysed for 10s on peak, Al for 20 s, Ca, Mg, K, Ti and Mn for 30 s, and Fe for 40 s. Relevant mineral and glass secondary standards were run at regular intervals to check for precision and reproducibility. The experimental phase composition analyses generally had standard deviations below 1 wt.%. Analyses were normalised to an internal standard (Basalt glass Makaopuhi Lava Lake HI NMNH 113498-1 A-99 and fayalite, Rockport, NMNH 85276) for consistency between runs. The mineral phases were analysed on their rims. Analyses of Fe-rich immiscible droplets were challenging due to the typically small area presented (<25 μm^2), together with the unknown 3D droplet shape creating uncertainty about the electron beam interaction volume (this was modelled using *Casino v2.48* software (Drouin et al., 2007)). Hence, while each droplet was analysed in its apparent centre, there may have been a component of mixing with the surrounding Si-rich conjugate.

Electron backscatter diffraction (EBSD) data were collected to obtain crystallographic orientations of pyroxene, titanomagnetite and whitlockite, at the Department of Earth Sciences, University of

Cambridge, using a Quanta FEG 650 F SEM. Data collection, indexing, analysis of electron backscatter diffraction patterns, EBSD maps and pole figures were processed by *Bruker Esprit 2.1* software and the MTEX Toolbox run in *Matlab R2017b*.

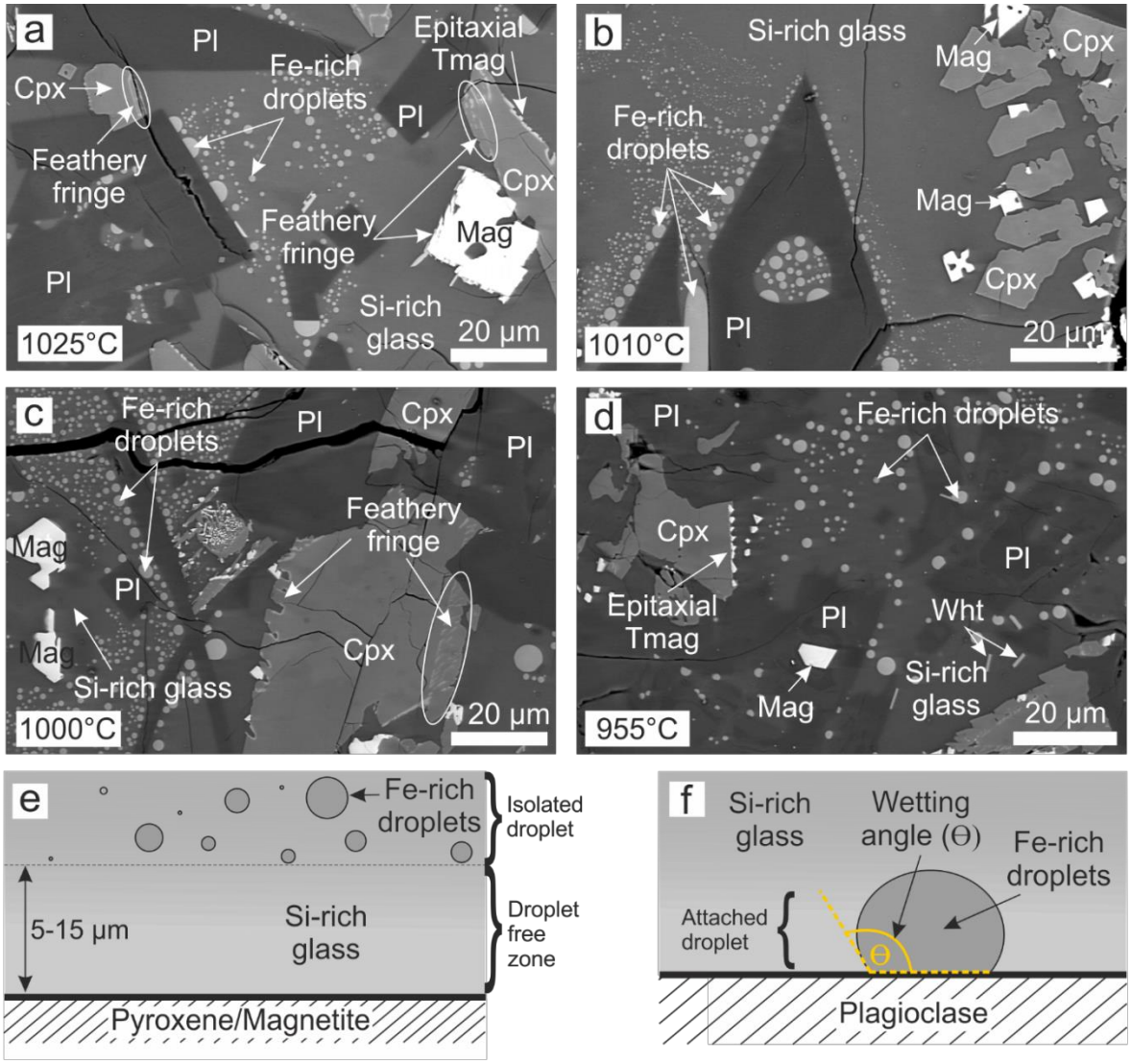

Figure 2.2 Backscatter electron (BSE) images of the experimental charges at different temperatures with constant cooling of 1°C/h. (a) Fe-rich droplets, at 1025°C, are attached to plagioclase and isolated in the interstitial Si-rich glass. Note the feathery fringes on the pyroxene and magnetite. (b) Fe-rich droplets at 1010°C, with bigger attached droplets than isolated droplets. The isolated droplets preferentially surround the plagioclase grains, avoiding the mafic phases. (c) Immiscibility at 1000°C with Fe-rich droplets situated close to plagioclase, and a droplet-free zone around pyroxene and magnetite. (d) The Fe-rich droplets are uniformly distributed at 955°C. (e) A cartoon depicting the difference in size and frequency of attached versus isolated Fe-rich droplets. (f) A cartoon illustrating the apparent wetting angle of an Fe-rich droplet on a crystal face. Mineral abbreviations after Whitney and Evans (2010).

2.3 Results

2.3.1 Phase composition

Glass, plagioclase, augite and pigeonite are the major phases in each experimental charge, with accessory magnetite, whitlockite (a calcium phosphate) and rare dendritic ilmenite and olivine (Table 2.2). Phase compositions are presented in the Appendix Table 2.B. At 1030°C and below, the glass comprises Fe-rich droplets dispersed within a continuous Si-rich phase (Fig. 2.2). Due to volatile loss in the anhydrous one-atmosphere experiments, whitlockite crystallises instead of apatite, with a similar arrival point on the liquidus (Tollari et al., 2006). At a constant cooling rate of 1˚C/h, and with no isothermal dwell time, the volume of the solid fraction increases with decreasing temperature: for example, the experimental charge quenched at 955°C has a solid fraction of 57% (in 2D cross-section).

Given a constant cooling rate of 1˚C/h, plagioclase An# (mol.%) evolves from An_{48} at a temperature of 1100°C to An_{29} at 955°C; the plagioclase grains are normally zoned. In the same temperature interval, the Mg# (mol.%) of augite and pigeonite decreases from 46 to 42 and from 56 to 54, respectively. In the experiments in which olivine is present (Table 2.2), the forsterite number (mol.%) was 49 at 1030°C, decreasing to 48 at 1010°C and 43 at 1000°C after 18 h dwell time at 1000°C (t_{18}).

The "isothermal" experiments were cooled at a constant rate of 1˚C/h, and then held at 1021°C and 1000°C for 158 h and 182 h respectively. The experimental charges contain glass, plagioclase, augite and pigeonite as the major phases, with accessory magnetite and whitlockite. Olivine is present in the experimental charge t_{18} at 1000°C. Bulk crystallinity (with the solid component dominated by plagioclase) increases with isothermal dwell time, and with decreasing isothermal dwell temperature: from 28% at 1021°C t_{12} to 32% at t_{158}; and from 30% at 1000°C t_{18} to 37% at t_{182}. The average plagioclase An# (mol.%) decreases as isothermal dwell time increases: at 1021°C from An_{37} at t_{12}, to An_{35} at t_{158}, and at 1000°C from An_{40} at t_{18}, to An_{37} at t_{182}. Augite Mg# decreases with increased dwell time.

2.3.2 Microstructure

2.3.2.1 The silicate liquid immiscibility binodal

The term 'binodal' describes the field of liquid immiscibility - the region on a phase diagram below which it is energetically favourable for a single liquid phase to unmix. Unmixing of a cooling liquid commonly occurs simultaneously with crystal growth and can occur by nucleation of droplets of the volumetrically minor phase. Such nucleation is limited by thermodynamic and kinetic barriers. Alternatively, unmixing can occur by spontaneous spinodal decomposition if the liquid experiences a large, (near-) instantaneous undercooling (Cahn, 1961). There are no thermodynamic barriers to spinodal decomposition; however, there will be kinetic limitations. The typical microstructure indicative of spinodal decomposition is "a highly inter-connected fat spaghetti-like structure which contrasts with the separated growing blobs associated with nucleation and growth" (Elliott, 1989).

2.3.2.2 Immiscible liquids

In the experimental charge quenched at 1030°C, Fe-rich droplets are concentrated in the interstices of skeletal plagioclase. In the experimental charges quenched at, or below 1025°C, Fe-rich droplets are widely distributed (Fig. 2.2a), either isolated in the continuous Si-rich glass, or attached to crystal surfaces. Fe-rich droplets preferentially attach to plagioclase, but at temperatures <1005°C they are also commonly attached to magnetite and pyroxene.

A single plagioclase face can have many attached Fe-rich droplets, ranging in diameter from sub-micron to 10 μm (as measured in 2D). The number and/or size of the attached Fe-rich droplets does not correlate with plagioclase grain size; however, crystal faces with large attached droplets (>6 μm diameter) tend to be associated with fewer, small, attached droplets. Close to the top of the binodal (e.g. 1025°C), single large Fe-rich droplets are commonly attached to the fastest growth faces of the plagioclase (i.e. those faces perpendicular to (010)). At lower temperatures (1010°C to 955°C), the Fe-rich droplets show no consistent preference for any particular crystal face, regardless of the nature of the substrate. Mafic crystals rarely have multiple attached droplets. Instead, the crystal faces may be covered by a single droplet with a low apparent wetting angle.

Isolated Fe-rich droplets vary from sub-micron to 10 μm in diameter (viewed in 2D). Rare examples of droplet coalescence are preserved (Fig. 2.3). Isolated droplets in experimental charges run at temperatures <1005°C are larger on average than attached droplets. The spatial distribution of isolated droplets in the experimental charges is highly heterogeneous, with large droplet-free volumes (>20 μm^2 in 2D), contrasting with abundant droplets in semi-enclosed regions surrounded by plagioclase (Fig. 2.2b). A 5–15 μm wide Fe-rich droplet-free zone often surrounds pyroxene, oxide and whitlockite. Furthermore, there is commonly a 2–4 μm wide droplet-free boundary zone between droplets attached to plagioclase grains and droplets isolated in the surrounding Si-rich glass (Fig. 2.2b). The Fe-rich droplets become more uniformly dispersed in the Si-rich glass with longer isothermal dwell times.

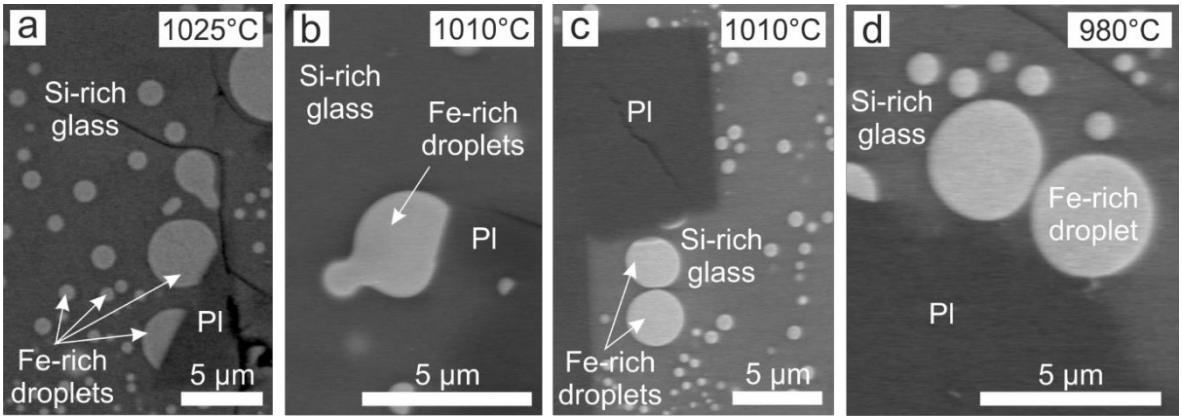

Figure 2.3 Fe-rich droplet coalescence (a) and (b); near droplet coalescence (c) and (d).

2.3.2.3 Pyroxene

The pyroxene grains display two main features (Fig. 2.2): (1) epitaxial growth of titanomagnetite on planar faces, observed at 1050°C and below; and (2) feathery fringes, 1–3 µm wide, observed at 1025°C and below. These feathery fringes comprise a marginal growth structure of crystalline, approximately oval, inclusions along the margins of the pyroxene grains, defining the euhedral core of the grain, and generally with a consistent shape orientation. They are found on any crystal face and are comprised chiefly of a mineral phase dominated by P and Ca, with a crystalline diffraction pattern most consistent with that of whitlockite. The whitlockite has a preferred orientation relationship with respect to each augite crystal face; however, this does not appear to consistently correlate with particular crystal faces of either whitlockite or augite. Features (1) and (2) are found on the same grain, but never on the same crystal face (Fig. 2.2c). Hammer et al. (2010) report a similar epitaxial relationship between clinopyroxene and titanomagnetite, with one of the symmetrically equivalent {110} faces of titanomagnetite aligned with the clinopyroxene (010) face. The clinopyroxene-titanomagnetite epitaxial relationship and the feathery fringes are also visible in natural samples from the Cohassett lava flow, USA (Fig. 2.4a).

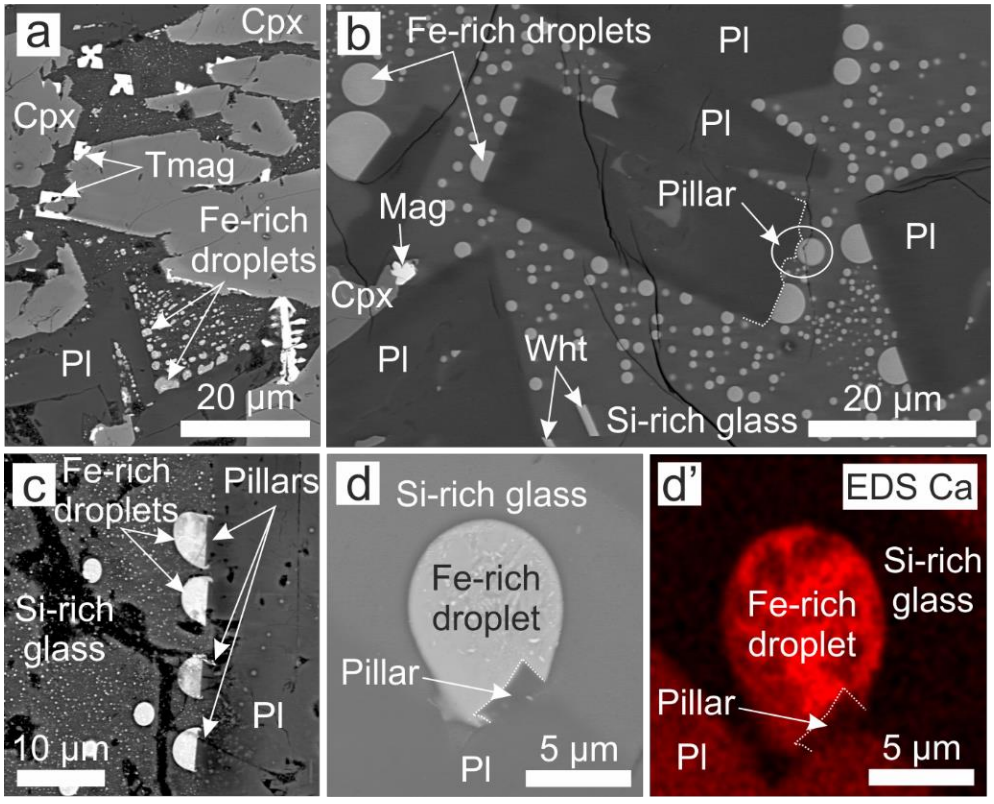

Figure 2.4 Microstructures in BSE images from (a) the Cohassett flow, USA, showing epitaxial growth of titanomagnetite along planar pyroxene faces and feathery fringes on pyroxene. (b) from the experiments: plagioclase laths with pillar structures along crystal faces, enclosed by an attached Fe-rich droplet of slightly larger diameter than the pillar. (c) from the Cohassett flow: pillar structures, enclosed by Fe-rich droplets on plagioclase. (d) from the Kīlauea Iki lava lake: a pillar structure enclosed by an Fe-rich droplet on plagioclase; (d') a Ca EDS map of image (d).

2.3.2.4 Plagioclase

In experimental charges quenched at 1010°C and 1000°C, plagioclase laths develop pillar structures along crystal faces perpendicular to [001] that protrude 2–5 μm outward into the surrounding glass (the interstitial glass is >45 modal % of the experimental charge). The pillars (first described by Philpotts (1981b)) are 3–7 μm wide, and are each enclosed by an attached Fe-rich droplet of slightly larger diameter (Fig. 2.4b). Several pillars may be present on a single plagioclase crystal face, giving a crenulated appearance to the plagioclase edge, analogous to medieval castle battlements. Plagioclase pillars are also present in samples from the entablature of the Cohassett lava flow, USA (Fig. 2.4c), and in the upper crust of the Kīlauea Iki lava lake, Hawaii, USA (Fig. 2.4d). In the Kīlauea Iki samples, the pillars are observed in samples quenched (by water during drilling) at 1017°C; this is comparable to the temperature of the experimental charges showing this microstructure. In my experimental charges and the natural samples, the pillars are more albitic than the substrate plagioclase (Fig. 2.4d') and the contact between the two compositional regions is sharp.

Overall, plagioclase grain sizes increase with decreasing temperature (Table 2.3). Plagioclase growth rates were calculated assuming a constant cooling rate of 1°C/h from the time when the experimental charge reached 1050°C (when plagioclase starts nucleating) to when it was quenched (Fig. 2.1), and using the maximum observed long axis of the plagioclase grains as viewed in the 2D images. Calculated plagioclase growth rates range from 1.39×10^{-10}–2.32×10^{-10} m/s (Table 2.3).

Table 2.3 Plagioclase apparent sizes and growth rates. Italicised values denote those experiments prepared @ QFM (see Table 2.2).

Run	Final temp (°C)	No. plag	Min size (μm)	Max size (μm)	Av size (μm)	Aspect Ratio (AR)	Growth rate (max) m/s	Growth rate (av) m/s	Plag modal %
VIC08	1050	285	3.19	60.92	13.83	1.80	2.29E-10	5.19E-11	16
VIC06	*1030*	*273*	*9.65*	*513.09*	*78.97*	*4.68*	*1.52E-09*	*2.33E-10*	*27*
VIC08	1025	397	3.95	82.66	19.60	2.34	2.32E-10	5.50E-11	32
VIC08	1010	295	3.92	57.00	20.10	2.18	1.39E-10	4.90E-11	29
VIC06	*1010*	*267*	*7.59*	*431.84*	*83.11*	*3.96*	*1.05E-09*	*2.03E-10*	*27*
VIC07	1005	333	3.24	72.20	17.62	2.38	1.69E-10	4.11E-11	31
VIC09	1000	269	6.35	90.01	26.08	2.11	2.02E-10	5.84E-11	35
VIC09	980	371	5.81	76.99	22.80	2.12	1.49E-10	4.40E-11	36
VIC09	955	460	4.04	100.18	22.19	2.34	1.65E-10	3.65E-11	43

Regardless of the temperature on quenching, plagioclase aspect ratios in my experimental charges are constant at ~2.1 (Table 2.3), with the exception of those in the charges that were not prepared in the muffle furnace (Table 2.2). These charges have a higher plagioclase aspect ratio of 4.3 and a faster plagioclase growth rate of 1.05×10^{-9}–1.52×10^{-9} m/s (Table 2.3). There is no relationship between the prevalence and size of Fe-rich droplets, and either plagioclase aspect ratio, grain size or growth rate.

2.3.2.5 Magnetite

Below 1025°C, magnetite locally develops feathery fringes, analogous to the pyroxene marginal growth structures, on at least two, but not all, of the intersected crystal faces (Fig. 2.2a). The elongated oval-shaped grains in the fringe are whitlockite. Feathery fringes are also visible on magnetite in natural samples from the Cohassett lava flow, USA. Fe-rich droplets wet the surface of magnetite with a low wetting angle against the sharply defined planar growth face of the magnetite (Table 2.4). Fe-rich droplets do not wet a surface with a feathery fringe. At lower temperatures (<1005°C), Fe-rich droplets commonly wet magnetite grains, which tend to form clusters and are commonly associated with tabular grains of whitlockite.

2.3.3 Glass compositions

2.3.3.1 Constant cooling experiments

In experimental charges quenched above 1030°C (i.e. above the binodal), the glass phase has relatively constant major element concentrations (Appendix Table 2.B). Minor incompatible elements such as ZrO_2, Y_2O_3 and P_2O_5, increase in concentration in the glass as crystallisation progresses. For example, P_2O_5 concentrations in the glass rose from 0.8 wt.% at 1150°C to 1.2 wt.% at 1050°C. With the onset of unmixing apparent at 1030°C, the Si-rich glass SiO_2 concentration increases down-temperature from 57 wt.% to 70 wt.% at 955°C: the opposite trend is observed for FeO, which decreases in concentration in the Si-rich glass at lower temperatures. Similarly, ZrO_2, Y_2O_3 and P_2O_5 concentrations decrease in the Si-rich glass (Ce_2O_3 concentrations were below EPMA detection). The P_2O_5 concentration decreases from 1.3 wt.% at 1030°C, to 0.5 wt.% at 955°C. Crystallisation and unmixing occur simultaneously: the onset of unmixing coincides with the onset of whitlockite crystallisation, and the observed decrease in P_2O_5 concentration in the Si-rich glass is thus a consequence of both whitlockite crystallisation and the unmixing of an Fe-rich liquid.

The FeO concentration of those Fe-rich droplets large enough to be analysed by EPMA increases steadily from 22 to 24 wt.% as the temperature decreases from 1025°C to 955°C. Likewise, ZrO_2, Ce_2O_3 and P_2O_5 concentrations increase in the (larger) Fe-rich droplets: P_2O_5 concentrations rise from 5.7 wt.% at 1025°C to 11.7 wt.% at 955°C. Over the same temperature interval, SiO_2 concentration in the Fe-rich droplets decreases from 38 to 29 wt.%.

I plot the glass composition data as a function of NBO/T (where NBO is the number of non-bridging oxygens, T is the tetrahedrally coordinated network forming cations: Si + Al + P + Ti). This can be used as a measure of the degree of polymerisation in silicate melts (Mysen, 1983). The NBO/T for Fe-rich droplets increases with decreasing temperature; conversely, the NBO/T for the Si-rich phase decreases. Thus, the immiscibility field expands with decreasing temperature (Fig. 2.5). The density of the Si-rich melt, with the composition of the Si-rich glass, (calculated according to Bottinga and Weill (1970)) decreases from 2.6 to 2.4 g/cm^3 over an experimental temperature drop of 1025°C to 955°C. The density

of Fe-rich melt, with the composition of the Fe-rich glass, increases from 2.9 to 3.0 g/cm^3 over the same 70°C interval (Appendix Table 2.B). The calculated viscosity (Giordano et al., 2008) for liquids with the composition of the Si-rich glass increases from 10^4 Pa.s at 1050°C to 10^7 Pa.s at 955°C. The calculated viscosity for the corresponding Fe-rich liquid remains relatively constant as temperature decreases, with a viscosity ranging from 10^4 Pa.s to 10^3 Pa.s (Appendix Table 2.B).

Table 2.4. Wetting angle (WA) measurements of the Fe-rich droplets attached to mineral phases for the experiments presented here; and measurements collected from experiments with a Mull and Sept Iles starting composition from the study of Charlier and Grove (2012). Italicised values denote those experiments prepared @ QFM (see Table 2.2).

Run	Final temp (°C)	Dwell time (h)	Plag median WA (°)	No. of WA	-ve 2σ	+ve 2σ	Oxide median WA (°)	No. of WA	-ve 2σ	+ve 2σ
Experiments from this study										
VIC06	*1030*	*0*	*81*	*29*	*12*	*8*	-	-	-	-
VIC08	1025	0	93	196	2	2	-	-	-	-
VIC08	1010	0	101	112	3	3	24	21	11	2
VIC06	*1010*	*0*	*121*	*143*	*2*	*2*	*25*	*6*	5	14
VIC07	1005	0	115	122	4	5	-	-	-	-
VIC09	1000	0	118	210	3	3	23	38	4	3
VIC09	980	0	125	121	3	3	26	40	2	2
VIC09	955	0	127	221	3	2	33	29	5	7
VIC10	1021	12	112	119	5	4	-	-	-	-
VIC10	1021	40	108	189	2	5	-	-	-	-
VIC10	1021	158	114	85	1	2	-	-	-	-
VIC06	*1000*	*18*	*118*	*168*	*1*	*2*	*23*	*14*	*7*	*3*
VIC07	1000	62	121	141	2	2	20	44	2	3
VIC07	1000	182	119	101	3	4	20	30	8	8
Sept Iles experiments (experimental details in Charlier & Grove, 2012)										
SI-5	1006	96	118	54	2	6	-	-	-	-
SI-8	963	48	120	83	2	3	-	-	-	-
SI-9	938	72	123	105	1	2	-	-	-	-
Mull experiments (experimental details in Charlier & Grove, 2012)										
M-9	1020	64	74	122	3	3	-	-	-	-
M-5	1005	92	81	103	3	2	-	-	-	-
M-6	963	48	86	108	1	2	-	-	-	-
M-7	938	72	91	56	3	3	-	-	-	-

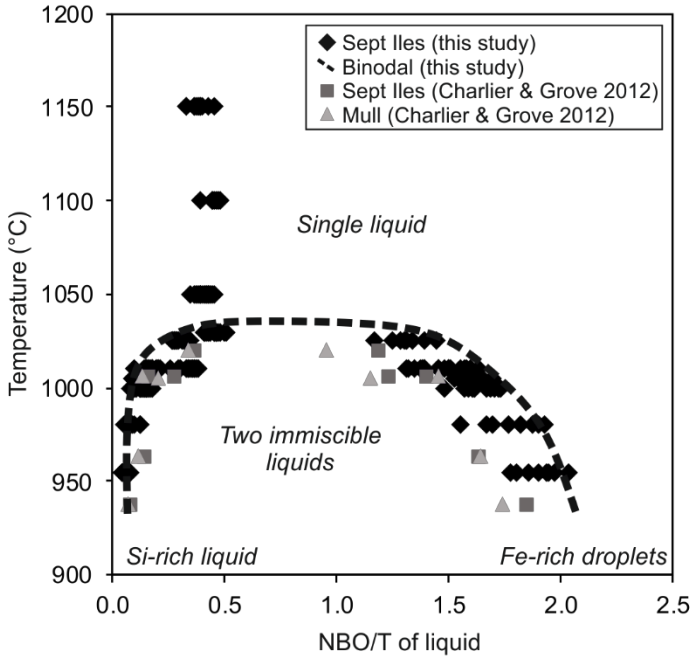

Figure 2.5 Temperature as a function of the degree of polymerisation (NBO/T, T = Si + Al + P + Ti), the dashed line represents the maximum compositional space where these experiments show evidence of unmixing. As a comparison, immiscible liquid analyses are plotted from Charlier and Grove (2012) for Sept Iles and Mull compositions.

2.3.3.2 Isothermal experiments

The SiO_2 concentration in the Si-rich glass increases from 66 to 69 wt.% over the 146 h that the experimental charges were held at 1021°C; and from 66 to 71 wt.% over the 164 h the charges were held at 1000°C. FeO concentrations in the Si-rich glass decrease with longer isothermal dwell times, from 7.0 to 4.7 wt.% FeO between experimental charges t_{12} and t_{158} at 1021°C; and from 7.5 to 4.1 wt.% FeO between experimental charges t_{18} and t_{182} at 1000°C. Consequently, the NBO/T values for the Si-rich glass decrease as dwell time increases.

Conversely, the NBO/T and Mg# of the Fe-rich droplets increase with isothermal dwell time, as does the concentration of P_2O_5, Ce_2O_3 and ZrO_2. The concentration of P_2O_5 increases by 50% over 146 h, from 8.9 wt.% to 13.3 wt.%, in experimental charges held at 1021°C prior to quenching, and 148% over 164 h, from 5.9 wt.% to 14.6 wt.%, in experimental charges held at 1000°C. The SiO_2 concentration of the Fe-rich droplets decreases with dwell time; there is a faster rate of decrease in the experimental charges held at the 1000°C isothermal plateau compared to those held at 1021°C.

2.3.4 Wetting angles

The population of measured apparent wetting angles of the Fe-rich liquid on plagioclase is typically unimodal (Fig. 2.6), with the exception of the experiment quenched at 1030°C, which is bimodal.

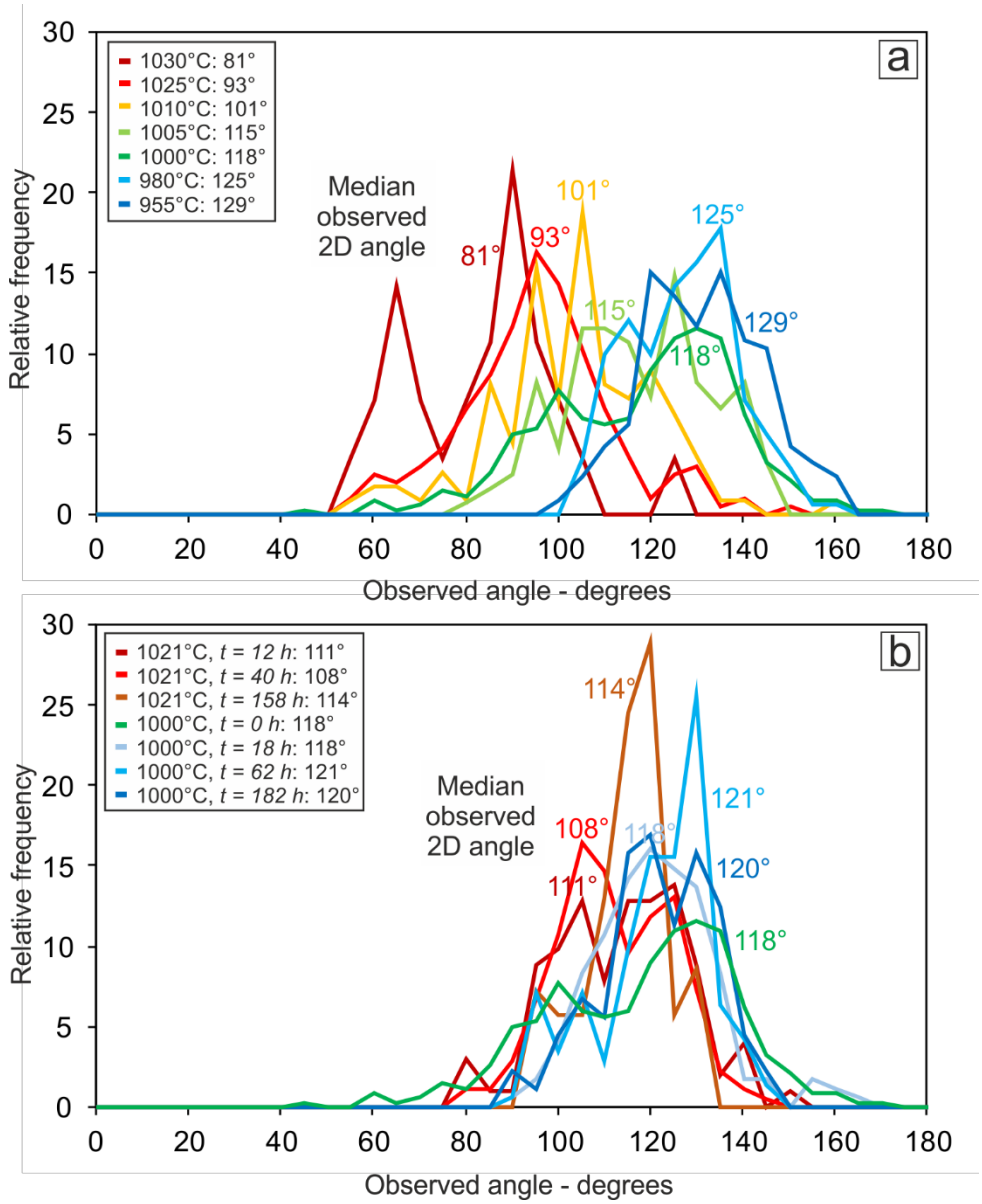

Figure 2.6 Frequency plots showing the populations of apparent wetting angle measurements for experimental charges that have undergone (a) constant cooling; (b) constant cooling and then were held isothermally at 1021°C between t_{12} to t_{158} and at 1000°C between t_{18} to t_{182}.

The 3D wetting angle (determined as the median of the population of 2D apparent wetting angles) increases as the temperature decreases from 93° ± 2° at 1025°C to 127° ± 3° at 955°C (Table 2.4, Fig. 2.7a). The largest wetting angle is associated with the lowest NBO/T value of the surrounding Si-rich phase and the highest NBO/T value of the Fe-rich phase, i.e. when the continuous phase is most polymerised and the Fe-rich phase is least polymerised (Fig. 2.7b). The wetting angles do not vary as a function of increasing isothermal dwell time prior to quenching (Fig. 2.7c).

The wetting angle of Fe-rich droplets on oxides is constant at ~24° between 1030–1005°C, increasing to 33° ± 6° at 955°C. While the number of wetting angle measurements of Fe-rich droplets on pyroxene were insufficient to provide a statistically robust median value, the measurements obtained suggest

angles between 23–32° over the temperature range 1025°C to 980°C. Additional wetting angle measurements were made on the Charlier and Grove (2012) experimental charges with a Mull and Sept Iles starting composition (Table 2.4); these corroborate the trends from my experiments.

2.3.5 Nucleation kinetics

2.3.5.1 Volume of immiscible liquid

In experimental charges that were continuously cooled (1°C/h) and then quenched, the proportion of Fe-rich droplets in the glass increases and then decreases relative to the continuous Si-rich phase with decreasing temperature. At 1025°C the Fe-rich droplets comprise 5 vol.% of the total glass; at 1000°C they comprise 7 vol.%; and at 955°C they comprise 4 vol.% (Table 2.5). This trend follows that of the relative percentages of the two phases calculated from the asymmetric silicate liquid immiscibility binodal (Fig. 2.5). In experimental charges with longer isothermal dwell times, the proportion of Fe-rich glass decreases.

2.3.5.2 Droplet size distribution: constant cooling evolution

A preliminary evaluation of the size and number of Fe-rich droplets as a function of temperature after cooling at a constant rate can be made by inspecting Fig. 2.2. The number density of Fe-rich droplets (as viewed in 2D, combining both attached and isolated droplets) decreases between 1025°C and 955°C, from 72 to 33 Fe-rich droplets per mm^2 of glass (Table 2.5). There is little variation in the number of

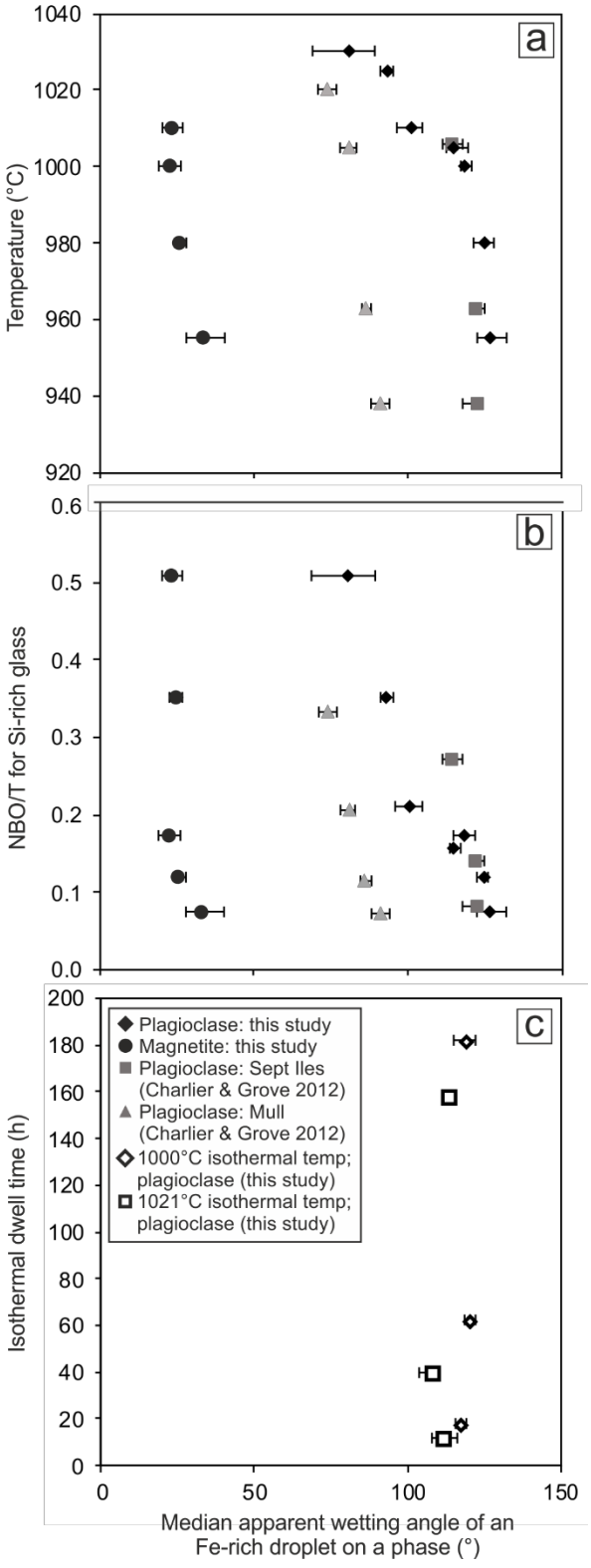

Figure 2.7 Wetting angle for the Fe-rich immiscible liquid plotted against (a) temperature; (b) NBO/T for the Si-rich liquid, where T = Si + Al + P + Ti, which represents the degree of polymerisation of the surrounding liquid; (c) wetting angle for the Fe-rich droplets on plagioclase plotted against dwell time (h).

attached droplets over the investigated temperature interval, whereas the number of isolated droplets decreases.

During constant cooling from the onset of unmixing to 1000°C, attached droplets have a larger average effective diameter, as viewed in 2D (d_{AT}), than isolated droplets (d_{IS}) (Fig. 2.8 and 2.9). The d_{IS} increases with decreasing temperature, from 0.78 to 0.98 µm. Below 1000°C, isolated and attached droplets have comparable average effective diameters (Table 2.5).

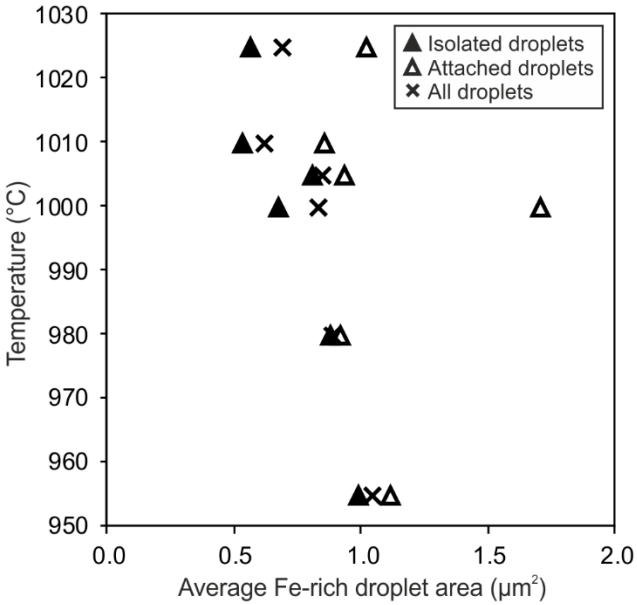

Figure 2.8 The average area of Fe-rich droplets (µm^2) plotted against temperature for experiments that underwent constant cooling at 1°C/h.

The droplet size distributions (DSD) for attached Fe-rich droplets at different temperatures have a constant maximum number density and a constant droplet diameter at that maximum number density (d_{AT}*; Fig. 2.9a). The range of d_{AT} is <1 µm to 22 µm. With decreasing temperature, the gradient of the DSDs for attached droplets remains constant. For isolated droplets, the maximum number density decreases with decreasing temperature, simultaneously with an increase in the droplet diameter at that maximum number density (d_{AT}*). The d_{AT} and d_{IS} is within bin size error of d_{AT}* and d_{IS}*. Between 1025°C and 1005°C, the d_{IS} range is 0.5–3 µm. At lower temperatures, this doubles to 6.5 µm (Fig. 2.9b). The DSDs for isolated droplets have a steeper gradient to larger droplet sizes (for each experimental charge) than the DSDs for attached droplets. Nevertheless, as temperature decreases, the gradient of the isolated droplet DSDs decreases.

2.3.5.3 Droplet size distribution: isothermal evolution

The number density of all Fe-rich droplets (normalised to modal glass) decreases as the dwell time at constant temperature increases (Table 2.5). In detail, the number density of isolated Fe-rich droplets decreases with a significantly steeper gradient than attached Fe-rich droplets.

At shorter dwell times, the DSDs for Fe-rich droplets have a wider range of droplet diameters (Fig. 2.10); 0.25–>10 µm for d_{AT} and 0.25–6 µm for d_{IS}. These ranges halve for experimental charges with isothermal dwell times longer than 150 h. The attached droplets have a constant maximum number density and the droplet diameter at the maximum number density (d_{AT}*) is relatively consistent (Fig. 2.10). The exception is a decrease in maximum number density of attached Fe-rich droplets in the experimental charge t_{158}, which was quenched at 1021°C. The DSDs have a positive slope for $d_{IS} < d_{IS}$*;

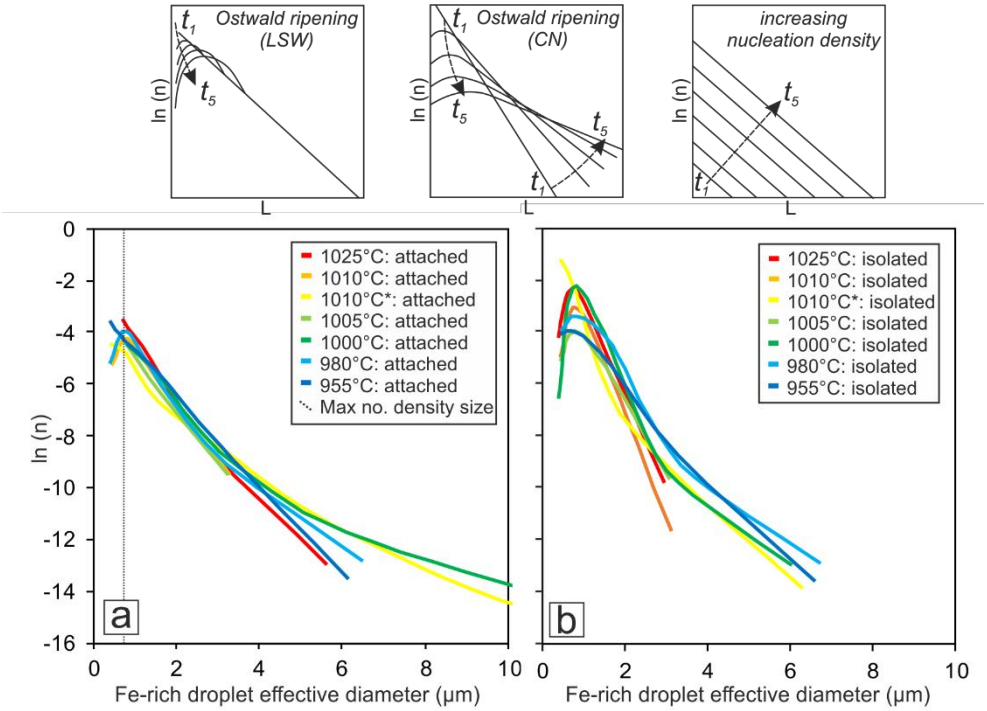

Figure 2.9 Droplet size distribution (DSDs) for experiments that have undergone constant cooling at 1°C/h. (a) DSDs for Fe-rich droplets attached to plagioclase. (b) DSDs for Fe-rich droplets not in contact with a crystal phase in the 2D view (isolated). 1010°C* indicates that this experimental charge underwent different preparation to the other experiments (Table 2.2). The insets are theoretical dispersions of crystal size distributions after Higgins (2002); and Marsh (1988): LSW theory (Lifshitz and Slyozov, 1961; Wagner, 1961) assumes a particle's coarsening rate is independent of its surroundings; the "communicating neighbours" (CN) theory (DeHoff, 1991) assumes only particles in close proximity affect the other's evolution.

Table 2.5 Fe-rich droplet size distributions. d_{IS} = isolated Fe-rich droplet diameter; d_{AT} = attached Fe-rich droplet diameter. $(D_{4,3}/D_{3,2})$ is the ratio of the Fe-rich droplet volume-weighted mean diameter versus the surface-weighted mean diameter, following Farr et al. (2017).

Final Temp (°C)	Dwell time (h)	Modal glass %	Droplets/mm² of glass	Mean d_{IS} (μm)	Mean d_{AT} (μm)	Max d_{IS} (μm)	Max d_{AT} (μm)	Density change (kg/m³)	$\frac{D\,4,3}{D\,3,2}$
1030	0	66	2	0.48	0.49	0.92	0.64	-	-
1025	0	54	72	0.78	1.01	3.55	4.23	420	1.13
1010	0	57	37	0.76	0.91	2.24	3.80	510	1.09
1010	0	59	70	0.54	1.18	4.03	22.26	400	1.46
1005	0	55	23	0.91	0.96	3.79	3.51	560	1.17
1000	0	53	75	0.85	1.18	6.47	9.06	530	1.21
980	0	47	47	0.96	0.91	5.76	5.75	590	1.19
955	0	43	33	0.98	1.00	4.51	4.62	640	1.21
1021	12	63	20	0.85	0.89	3.26	4.73	470	1.14
1021	40	61	39	0.72	1.07	3.3	5.91	490	1.17
1021	158	53	6	0.69	1.01	1.84	3.26	510	1.11
1000	18	60	80	0.63	0.97	5.87	9.38	480	1.50
1000	62	54	38	0.85	1.00	7.76	5.42	590	1.54
1000	182	50	21	0.81	0.95	3.22	3.45	580	1.09

where d_{IS}* is the isolated droplet diameter at the maximum number density. For the isolated Fe-rich droplets, the maximum number density decreases in the experimental charges held for an increasing dwell time at both temperatures. The d_{IS}* is constant for experimental charges $t_{12} - t_{158}$ held at 1021°C, while for $t_{18} - t_{182}$, held at 1000°C, the d_{IS}* doubles from 0.4 µm at t_{18} to 0.8 µm at t_{182}. The gradient of the isolated DSDs is steeper than that of the attached DSDs for all experimental charges regardless of isothermal dwell time or quench temperature.

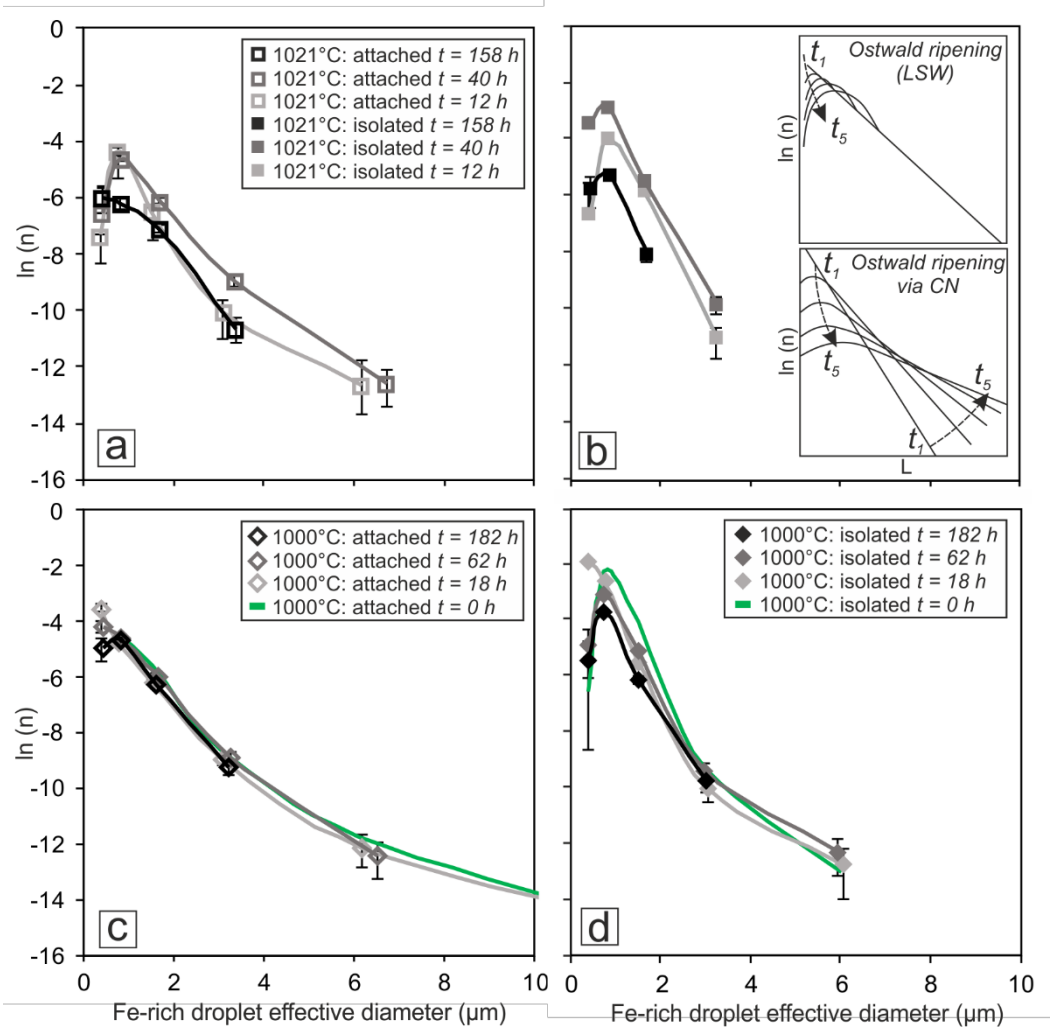

Figure 2.10 Droplet size distribution (DSDs) for experimental charges that have been held isothermally. (a) DSDs for Fe-rich droplets attached to plagioclase held at 1021°C between t_{12} to t_{158}. (b) DSDs for isolated Fe-rich droplets in the 2D view, held at 1021°C between t_{12} to t_{158}. (c) DSDs for Fe-rich droplets attached to plagioclase held at 1000°C between t_{18} to t_{182}. (d) DSDs for isolated Fe-rich droplets in the 2D view, held at 1000°C between t_{18} to t_{182}. For comparison in (c-d), the attached and isolated DSDs for the experiment quenched at 1000°C with no isothermal dwell time are plotted. The insets are theoretical dispersions of crystal size distributions after Higgins (2002); and Marsh (1988).

2.3.5.4 The location of nucleation of immiscible droplets

Isolated Fe-rich droplets are volumetrically more significant than attached Fe-rich droplets in the experimental charges with no isothermal dwell time. The number of potential sites for heterogeneous nucleation of Fe-rich droplets on plagioclase grains is a function of the area of plagioclase surfaces but

as modal plagioclase increases from 27% at 1030°C to 43% at 955°C, the ratio of the total area of isolated/attached Fe-rich droplet also increases, while the ratio of the numbers of isolated/attached Fe-rich droplets decreases. There is a positive correlation between the ratio of isolated/attached Fe-rich droplet *areas* and the wetting angle of Fe-rich droplets on plagioclase for angles >90° (Fig. 2.11a). When the wetting angle is <90°, there is a negative correlation between the wetting angle on plagioclase and the ratio of isolated/attached Fe-rich droplet *areas*, as shown by the experiments with a Mull composition. The ratio of isolated/attached Fe-rich droplet *numbers* decrease with decreasing quenching temperature for the Mull composition experiments.

The ratio of isolated/attached Fe-rich droplets in terms of both *area* and *number* decreases in experimental charges held for longer isothermal dwell times prior to quenching (i.e. more droplets are attached at longer dwell times; Fig. 2.11b). The gradient decrease is steeper for experimental charges held isothermally at 1021°C compared to 1000°C.

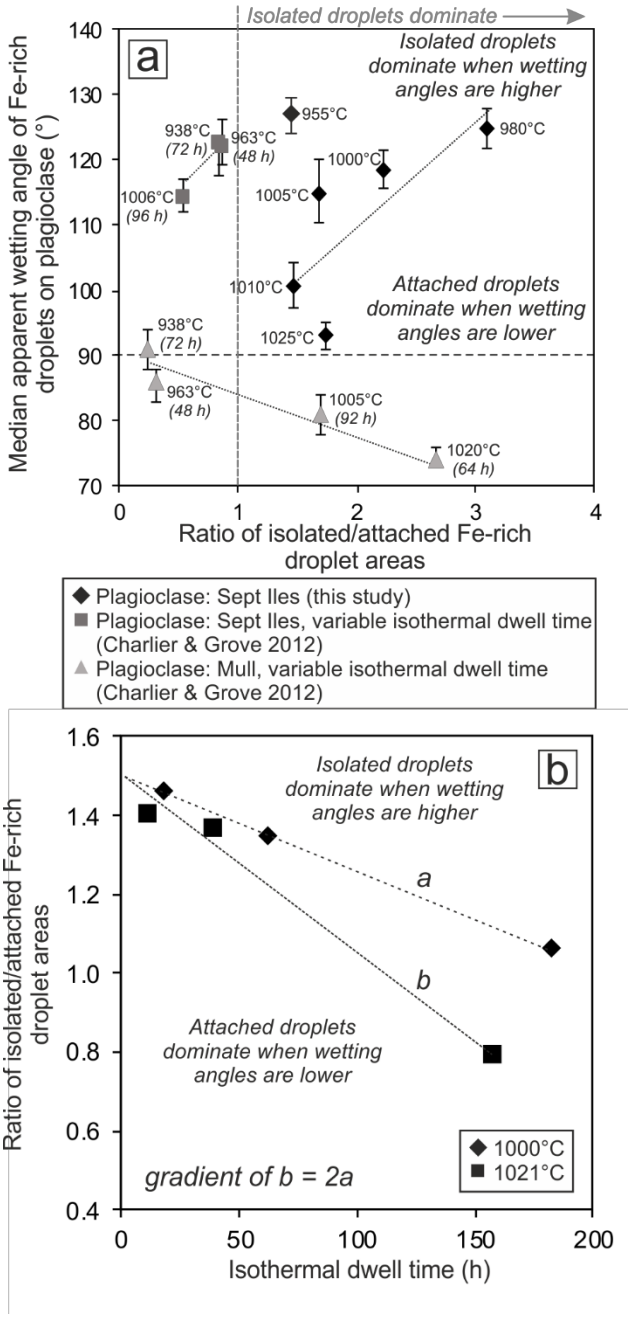

Figure 2.11 (a) The ratio of isolated/attached Fe-rich droplet areas plotted against the wetting angle of Fe-rich droplets on plagioclase for these experiments, and Charlier and Grove (2012) experiments using a Sept Iles and Mull composition. (b) the ratio of isolated/attached Fe-rich droplet areas plotted against dwell time (h).

2.3.5.5 Influence of the super-liquidus history on droplet nucleation and growth

The effect of the initial thermal history above the liquidus was explored with two experiments quenched at 1010°C: one being part of the experimental run VIC08 (herein referred to as 1010(8)) and the other being part of the experimental run VIC06 (herein referred to as 1010(6)) (Table 2.2). Both experimental charges underwent a constant cooling rate of 1°C/h, with no dwell time before quenching, but the immiscibility microstructures differ. The preparation of the two charges was different prior to

commencement of the constant cooling rate experiments (Table 2.2): experimental run 1010(8) was heated to 1150°C in a muffle furnace in air, whereas experimental run 1010(6) was heated to 1104°C at QFM. Experiment 1010(6) contains an order of magnitude more Fe-rich droplets than experiment 1010(8), with the majority of droplets smaller than 1 μm^2 (as viewed in 2D). In experiment 1010(8) the majority of droplets are smaller than 2 μm^2 (Table 2.5). The plagioclase aspect ratio in experiment 1010(6) is 4.0, (the crystals are dendritic) while in experiment 1010(8) the aspect ratio is 2.2, consistent with the other experimental charges that were prepared in the muffle furnace (Table 2.3). Hence, experimental preparation has an influence on nucleation and growth rates (see section 2.4.1.3).

2.4 Discussion

2.4.1 Nucleation processes: homogeneous or heterogeneous?

2.4.1.1 Onset of Unmixing

At the onset of silicate liquid unmixing, isolated Fe-rich droplets dominate. The narrow size distribution of the Fe-rich droplets, and their (apparent) isolation in the continuous Si-rich liquid, are consistent with a short interval of (homogeneous) nucleation. Homogeneous nucleation is likely promoted by the small compositional difference between the immiscible liquids which leads to a low energy interface between the two liquids (Veksler et al., 2010).

2.4.1.2 Droplet nucleation as the binodal widens

At lower temperatures, the compositional difference between the two immiscible liquids increases (Fig. 2.5), increasing the energy of the interface separating the two phases (Veksler et al., 2010). As temperature decreases, isolated droplets remain abundant suggesting that homogeneous nucleation remains important; however, the number of isolated droplets decreases with decreasing temperature, simultaneously with increasing average droplet size.

At temperatures 10–20°C below the onset of unmixing, the undercooling is relatively small. In isothermal experiments held at 1010°C (after constant cooling at 1°C/h), the number of isolated Fe-rich droplets decreases (likely due to coarsening – see later), but there is no increase in the nucleation density (as shown by the DSDs, Fig. 2.10), even after an isothermal dwell time greater than 150 h.

Small degrees of undercooling make it energetically favourable to nucleate droplets heterogeneously on crystal faces. Plagioclase is the dominant phase for heterogeneous nucleation of the Fe-rich liquid (Fig. 2.12). This is perhaps surprising because Fe-rich liquids are more likely to wet a mafic phase (e.g. Holness, 2006; Jakobsen et al., 2005; Philpotts, 1977; Vukmanovic et al., 2018) as shown by my wetting angle measurements. Kinetic processes must therefore play a role. I suggest the Fe-rich liquid distribution in the quenched experiments is controlled by the creation of compositional boundary layers (CBL) around the growing grains (Zellmer et al., 2016): compositional boundary layers adjacent to

plagioclase will be enriched in Fe, Ti, Mg, and P, promoting unmixing and heterogeneous nucleation of Fe-rich droplets. Conversely, any compositional boundary layer developing around growing grains of whitlockite will be depleted in P, thus decreasing the size of the silicate liquid immiscibility field in composition space (Bogaerts and Schmidt, 2006; Charlier and Grove, 2012; Visser and Van Groos, 1979b), and inhibiting unmixing in the adjacent liquid. While there is no obvious control by temperature, with the density of heterogeneously nucleated Fe-rich droplets on plagioclase crystal faces being constant in experiments with continuous cooling (as shown by DSDs, Fig. 2.9), a further factor might be the nature of the underlying structure of the crystal surface, with the plagioclase surface providing a particularly favourable substrate (e.g. Pleše et al., 2018).

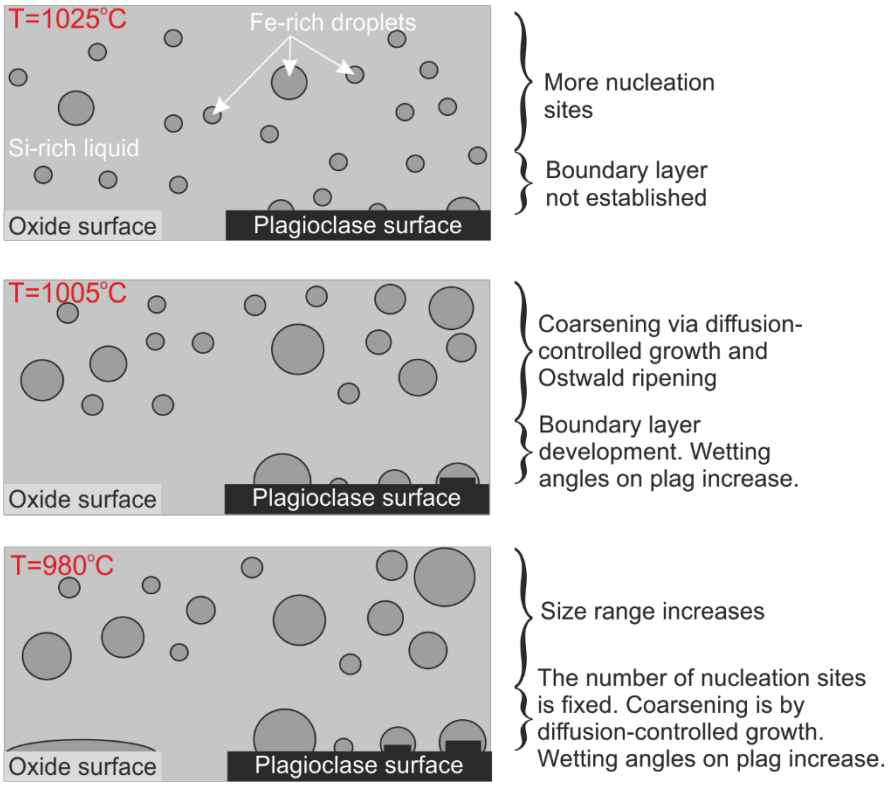

Figure 2.12 Schematic illustration of the evolution of the physical behaviour of the unmixing liquids in these experiments, as temperature decreases.

Note, however, that I do not observe a continuous Fe-rich film surrounding plagioclase grains, as seen in natural samples and some experiments (Morse and Brady, 2017; Hartley 2019 pers. comm.). I suggest the absence of the continuous film of unmixed Fe-rich liquid and the presence, instead, of discrete droplets could be controlled by the growth rate of the plagioclase. The maintenance of continuous films of Fe-rich liquid, which my wetting angle measurements demonstrate are in textural disequilibrium, requires plagioclase growth rates to be significantly faster than that of chemical diffusion in the surrounding liquid. The average plagioclase aspect ratio is 6.0 in the natural samples in which continuous Fe-rich films are observed (e.g. the Kīlauea Iki lava lake) but only 2.1 in my experiments.

Lower plagioclase aspect ratios imply slower growth (Holness, 2014; Sato, 1995), so I suggest that the plagioclase aspect ratios in my experiments are consistent with growth rates that were too low to maintain texturally disequilibrium Fe-rich compositional boundary layers (CBLs).

The CBLs developing around magnetite and pyroxene are enriched in elements such as Si, Al, and Na, consistent with the absence of Fe-rich droplets in the vicinity of these phases (a Si-rich CBL was formed). This is reversed at lower temperatures and, as temperatures decrease, Fe-rich droplets increasingly wet the surface of magnetite and pyroxene. The low wetting angles (23–33° for oxides and 23–32° for pyroxenes; Table 2.4) show that this spatial relationship is more energetically favourable than that of an Fe-rich liquid wetting plagioclase (Holness, 2006): thus this trend towards a concentration of Fe-rich liquid adjacent to mafic phases represents a transition towards textural equilibrium rather than a change in the nucleation kinetics.

2.4.1.3 Homogeneity of the starting liquid

Spatial compositional variations in the starting liquid have a significant effect on the abundance of droplet nucleation sites; Lofgren (1983) showed that experimentally heating a basaltic magma for 1 h, 10°C above the plagioclase saturation limit, removed all plagioclase nuclei and hence inhibited plagioclase crystallisation. Consequently, the experimental charge preparation conditions will affect the number of available nucleation sites both for the exsolving Fe-rich liquid and for crystalline phases. Experiment 1010(6) resulted in anomalously large dendritic crystals with large numbers of very small Fe-rich droplets (<1 μm^2), whereas experiment 1010(8) resulted in a crystal microstructure typical of the experiments comprising smaller, subhedral crystals and a lower number of Fe-rich droplets. Dendritic crystals grow under conditions of diffusion-limited growth, which is commonly caused by a large undercooling (e.g. Mullis, 2003). I suggest that a low nucleation rate in experiment 1010(6) permitted a large undercooling to develop, resulting in the growth of a few, large, (dendritic) crystals. The large, scattered dendritic crystals resulted in the creation of relatively large interstices between crystals, promoting homogeneous droplet nucleation (Holness and Sawyer, 2008; Putnis and Mauthe, 2001).

I attribute these microstructural differences to the experimental charge preparation. Experiment 1010(6) was heated to 1104°C and held for 16 h, while experiment 1010(8) was heated to 1150°C and held for only several minutes: I suggest the longer duration of the isothermal hold led to a greater reduction of crystal nucleation sites in 1010(6). Another potential difference is the Fe content of the Fe-electroplated platinum loop on which the charge was suspended: this could have affected the FeO content of the charge. If experiment 1010(6) had a slightly higher bulk Fe content, combined with the lower energy required to nucleate liquid droplets, then this could have produced the microstructural differences observed.

2.4.2 Microstructural indicators of immiscibility in solidified mafic rocks

Our experimental charges show that microstructural features of the mineral grains develop in conjunction with unmixing of their host liquid. Such features, if recognised, in natural examples of fully solidified rocks in which there is no preserved record of liquid unmixing, could potentially be used as a marker for the occurrence of liquid immiscibility during solidification.

2.4.2.1 Pyroxene and Magnetite feathery fringes

In experimental charges quenched at 1050°C, most grains are equant with smooth planar crystal faces, demonstrating that crystal growth was mainly interface-controlled. Experimental charges quenched below 1030°C (i.e. the onset of unmixing for the liquid compositions used for my experiments) contain Fe-rich droplets that wet the surface of magnetite and pyroxene grains. These Fe-rich droplets are only present on euhedral grain surfaces, indicative of interface-controlled growth. In contrast, the feathery fringes on pyroxene and magnetite, associated with whitlockite, are consistent with diffusion-limited growth and therefore the creation of a CBL surrounding pyroxene and magnetite. Such feathery fringes have the potential to be used as microstructural indicators of unmixing during solidification.

Phosphorus is incompatible in pyroxene, with a clinopyroxene-basaltic liquid partition coefficient ranging between 0.01–0.05 (Anderson and Greenland, 1969; Brunet and Chazot, 2001). If the pyroxene growth rate (typically $1x10^{-7}$ m/s (Dunbar et al., 1995; Kouchi et al., 1983)) exceeds the P chemical diffusion rate in the silicate liquid (~$3.5x10^{-11}$ m^2/s, for a basaltic liquid; Chen and Zhang (2008); Chen and Zhang (2009); Lundstrom et al. (2005)) then P would be enriched in a boundary layer surrounding a growing pyroxene. As crystallisation proceeds, incompatible elements are enriched in the silicate liquid surrounding the growing pyroxene and magnetite. This forms a CBL within which whitlockite nucleates, and where the rate of material transport is likely set by the least mobile component which, in the case of whitlockite, is P. The microstructures I describe suggest that small grains of whitlockite that nucleate and grow in the CBL are either engulfed by the growth of their pyroxene substrate, or that the larger whitlockite grains stunt further pyroxene growth. I suggest that the variation in the width of the pyroxene feathery fringes on different growth faces in my experiments is due to variations in pyroxene growth rates (Kouchi et al., 1983). I could not quantify a consistent preferred crystallographic relationship between whitlockite and augite by EBSD, and suggest that further EBSD work is required to definitively establish the crystallographic relationship between these two phases. P and Ca are incompatible in magnetite, and so the same mechanism outlined for pyroxene could destabilise planar growth faces of magnetite by the development of CBLs.

A remaining question is why a P- and Ca-rich phase forms as a result of CBL development around pyroxene, when pyroxene growth should also cause enrichment in elements such as Al and Na in the CBL. This could, perhaps, be due to the much faster chemical diffusion rates of Al and Na in a silicate liquid that preclude the development of CBLs defined by spatial variations of these elements.

2.4.2.2 Plagioclase pillars

The observed pairing of albitic pillars and Fe-rich droplets (Fig. 2.4d') could result from either the heterogeneous nucleation of the droplet on the surface of a pre-existing pillar, or formation of the pillar by growth from an Fe-rich liquid after heterogeneous nucleation of the droplet on an originally planar plagioclase crystal face. If the former, then I might expect pillars to be a commonly observed feature of rapidly cooled basalts in which diffusion-limited growth occurs, but they are not (Helz and Wright, 1992; Neave et al., 2017). Consequently, following Philpotts (1981b), I suggest that pillar formation post-dates the attachment of the Fe-rich droplets, and that the presence of an Fe-rich droplet destabilises the plagioclase planar growth face, resulting in localised enhanced growth of plagioclase.

This hypothesis is supported by the enrichment of the pillars in elements with a low concentration in the Fe-rich immiscible liquid, such as Na, Al and Si (Veksler et al., 2006). Since the two conjugate liquids become more compositionally distinct with decreasing temperature (Fig. 2.5), early-formed Fe-rich droplets will continue to exsolve elements that would preferentially partition into the Si-rich liquid (e.g. Fig. 1b of Charlier and Grove (2012)) such as those required to grow albitic plagioclase. At a plagioclase growth rate of 1.4×10^{-10} m/s (as calculated for an experimental charge quenched at 1010°C; Table 2.3), a 3 μm pillar protruding from a crystal face would grow in ~6 hours if the Fe-rich droplet were present from 1025°C. This idea is compatible with the suggestion that the viscosity contrasts between the Fe-rich droplets and Si-rich liquid are large and that this affects the chemical diffusion of elements to the growing plagioclase (Philpotts, 1981b; see Appendix Table 2.B). The Fe-rich droplet has a lower viscosity and so rapidly diffuses material to the growing plagioclase face in comparison with diffusion rates through the higher viscosity Si-rich liquid (Philpotts, 1981b).

2.4.3 Wetting angles

2.4.3.1 Are the wetting angles in textural equilibrium?

Wetting angles are a result of the balance of three interfacial energies, and are therefore controlled by the compositions of the crystal substrate, the Fe-rich liquid, and the Si-rich liquid (e.g. Yablonovitch and Gmitter, 1984). For the specific case of the Fe-rich droplets on plagioclase, this force balance is described by the Young equation: $\gamma_{PSi} - \gamma_{PFe} - \gamma_{SiFe} \cos\Theta = 0$; where P denotes plagioclase, Fe denotes the Fe-rich liquid forming the droplet, Si denotes the Si-rich liquid, and Θ denotes the wetting angle (Young, 1805). Although I have little idea of the extent of anisotropy of the γ_{Psi} and γ_{PFe} interfacial energies, I might expect a single value (or narrow range) of the wetting angle if the system were in textural equilibrium, but a wide range of values if it were far from equilibrium. The presence of more than one value of wetting angle in a sample can be ascertained by comparison of the observed cumulative frequency curve for the 2D wetting angle population with that calculated for a system with a single value of 3D angle. If the sample contains a wide range of true 3D angles the observed

cumulative frequency curve will be broader and flatter than the theoretical curve (Elliott et al., 1997; Harker and Parker, 1945; Riegger and Van Vlack, 1960).

The population of apparent wetting angles is generally unimodal (Fig. 2.6), with similarities in distribution for experiments held isothermally for different durations (Fig. 2.6b). The bimodal distribution measured in the experiment quenched at 1030°C may be attributed to the small population of measurements (n = 29; Table 2.4). The cumulative frequency plots show rather narrower distributions than expected for single valued angles intersected in randomly oriented 2D sections (Riegger and Van Vlack, 1960: Fig. 2.13), consistent with the unlikelihood of observing droplets intersected at low angles in experiments containing a limited number of droplets and with a single value of wetting angle in 3D. I conclude therefore that the observed droplet morphology reflects textural equilibrium. This conclusion is supported by the results of Veksler et al. (2008b); (2010), who suggested that Fe-rich droplets with diameters less than 12-14 μm equilibrated with the surrounding liquid on a timescale of several minutes.

2.4.3.2 Wetting angle variations

At the apex of the binodal, the compositional similarity of the two liquids means that the energy of the Fe-rich liquid-plagioclase interface should be equivalent to the Si-rich liquid-plagioclase interface: the wetting angle of the Fe-rich liquid (and that of the Si-rich liquid) on all mineral surfaces at the apex of the binodal should therefore be 90° (as observed, Fig. 2.7a). With decreasing temperature, the divergence of the compositions of the two liquids increases both the energy of the interface between the two liquids and the difference between the two liquid-plagioclase interfacial energies. The 30˚ down-temperature increase of the wetting angle of Fe-rich liquid on plagioclase is controlled by the relative rates at which these interfacial energies change. There is more compositional similarity between the Si-rich liquid and plagioclase (particularly given the increasingly sodic plagioclase compositions at lower temperatures (Appendix Table 2.B)), therefore I expect the energy of this interface to decrease with decreasing temperature, while that of both the Fe-rich liquid-plagioclase interface and the two-liquid interface increases. Since the wetting angle of the Fe-rich liquid increases from 90˚ with decreasing temperature, the dominant control on the wetting angle must be the difference between the two liquid-plagioclase interfacial energies.

The wetting angle of the Fe-rich liquid on magnetite is significantly lower than 90˚ (some 20˚C below the temperature at which unmixing starts), and increases (although only slightly) with decreasing temperature (Fig. 2.7a). Since the Fe-rich liquid and magnetite are compositionally similar, I might expect the energy of this interface to decrease with decreasing temperature, while that of both the Si-rich liquid-magnetite interface and the two-liquid interface increases. The slight increase in wetting angle of the Fe-rich liquid on magnetite with decreasing temperature must therefore be dominated by the increase in the two-liquid interfacial energy.

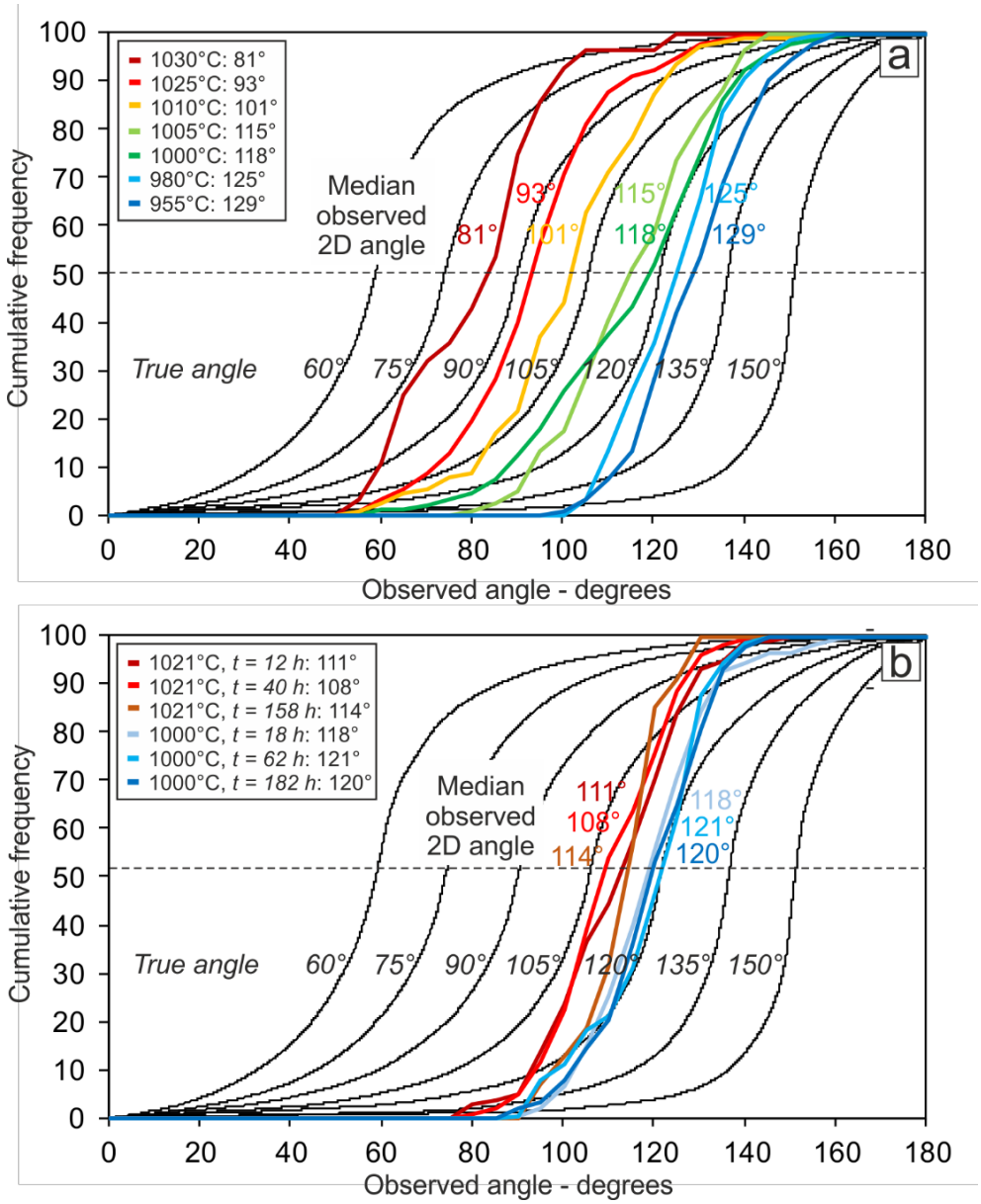

Figure 2.13 Comparison of the calculated distributions of apparent angles in randomly oriented 2D sections through various true (3D) angles (from Riegger and Van Vlack (1960) with the measured cumulative distributions of the observed (2D) angles for experimental charges which have undergone (a) constant cooling and (b) constant cooling and then were held isothermally at 1021°C between t_{12} to t_{158} and at 1000°C between t_{18} to t_{182}.

In experimental charges that underwent constant cooling, the proportion of isolated relative to attached droplet areas increases as wetting angles increase, for angles >90° (Fig. 2.11a). The Mull experiments from Charlier and Grove (2012) have wetting angles <90° and I would therefore expect attached droplets to dominate, yet isolated droplets dominate in the experiments quenched at temperatures >1000°C. I suggest this is due to: i) the composition at which the Mull liquid line of descent intersects the binodal; ii) the shape of the Mull composition binodal (Fig. 2 of Charlier and Grove (2012)); and iii) the extent of Fe-rich liquid accumulation (Fig. 1b of Charlier and Grove (2012)). Furthermore, the relative volume of the two immiscible liquids may affect the effectiveness of the separation of the two

phases (Sato and Sumita, 2007). For the Mull composition, the liquid line of descent crosses the binodal at a central position, closer to the apex than in my Sept Iles composition experiments. Consequently, there is a greater volume of Fe-rich liquid at a given temperature, yet only a fixed crystal surface area on which droplets can sit (Fig. 2.14). At higher temperatures, where crystallinity is lower, this results in more isolated droplets. The Mull binodal is also a different shape to the Sept Iles binodal (Fig. 2 of Charlier and Grove (2012)). Crystallinity increases down-temperature; therefore, the proportion of isolated Fe-rich droplets should simultaneously reduce. In Fig. 1b of Charlier and Grove (2012), it is evident that the experimental charges with a Mull starting composition contain large patches of Fe-rich glass, commensurate with the size of the adjacent crystal grains. These are far larger than the size of the Fe-rich droplets in my Sept Iles composition experimental charges. In my experiments the Fe-rich liquid accumulated in semi-enclosed regions, locally covering entire plagioclase faces, and thereby maintaining the area of Fe-rich glass in direct contact with plagioclase.

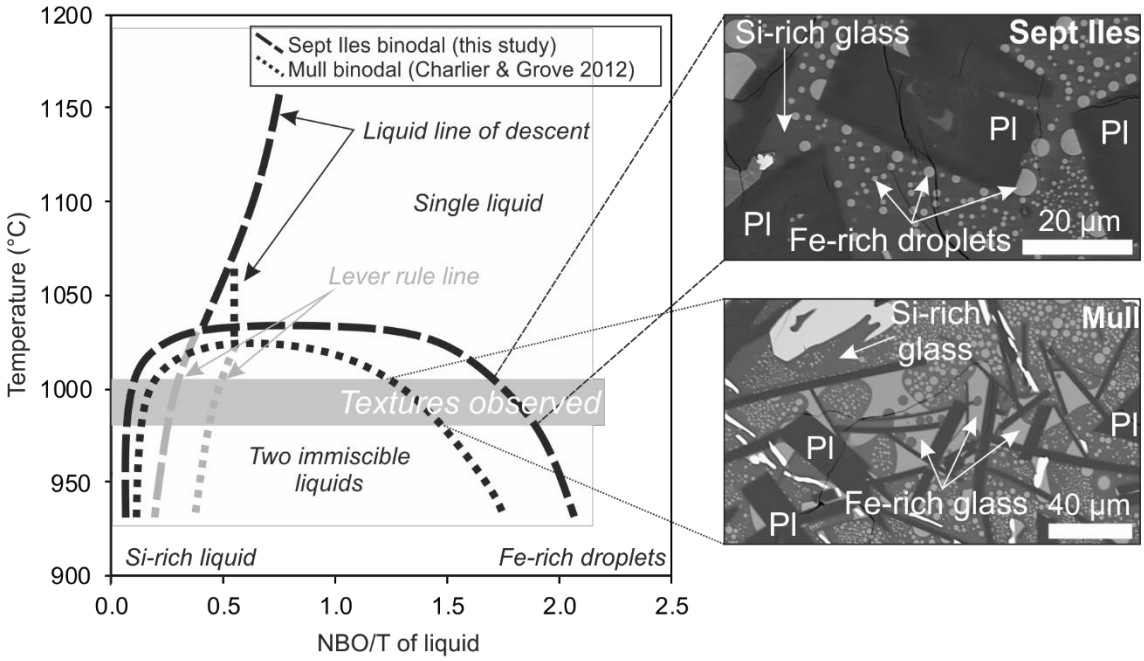

Figure 2.14 Schematic illustration of the evolution of the liquid line of descent through a two-liquid field for a Sept Iles and Mull starting composition. Differing physical behaviour of the immiscible Fe-rich liquid is illustrated for each composition.

2.4.4 Droplet evolution

The evolution (and hence size) of an Fe-rich droplet can be controlled by a range of factors such as coalescence, and growth due either to chemical equilibration driven by the widening of the binodal during cooling, or by Ostwald ripening. Coalescence occurs as droplets collide, and is a function of droplet radius, viscosity, density and the energy of the interface (Yao et al., 2005). Closely adjacent droplets float on their combined interface until the thin layer of liquid between the two droplets drains out (Deka et al., 2019). Ostwald ripening in liquid emulsions is diffusion-controlled and driven by differences in solubility related to differences of surface curvature. Coarsening via Ostwald ripening is

described by either LSW theory (Lifshitz and Slyozov, 1961; Wagner, 1961), which assumes a particle's coarsening rate is independent of its surroundings, or by the "communicating neighbours" (CN) theory (DeHoff, 1991), based on the idea that only particles in close proximity affect each other's evolution (Higgins, 2002).

2.4.4.1 Isothermal evolution

The Fe-rich droplets in my experiments held under isothermal conditions coarsen with time. For charges held isothermally at 1000°C, the DSDs show that the d_{IS} is within bin size error of d_{IS}* (Fig. 2.10d), consistent with some control by Ostwald ripening. Both coalescence and Ostwald ripening (using LSW theory) result in droplet mean diameters increasing with the cube root of time (Crist and Nesarikar, 1995), but these two processes can be distinguished using the distribution of droplet sizes. Farr et al. (2017) calculated that Ostwald ripening leads to a ratio of volume-weighted mean droplet diameter versus the surface-weighted mean droplet diameter ($D_{4,3}/D_{3,2}$) of 1.0239, whereas coalescence is characterised by $D_{4,3}/D_{3,2}$ = 1.0748. Farr et al. (2017) applied this model to an example of Fe-rich immiscible droplets in the experimental charges of Charlier and Grove (2012), finding a broader range of values (between 1.06 and 1.80) than predicted by either coalescence or Ostwald ripening. Similarly, the $D_{4,3}/D_{3,2}$ values for isolated droplets in my isothermal experiments (Table 2.5) lie between 1.09 and 1.54. This again suggests coarsening is controlled neither by Ostwald ripening alone nor by coalescence.

The timescale for coalescence is given by $\frac{\mu R}{\gamma}$, where μ is the dynamic viscosity of the more viscous liquid, R is the average radius of the two droplets, and γ is the interfacial tension between the two unmixed liquids (Paulsen et al., 2014; Rahman et al., 2019; Yao et al., 2005). Using the calculated viscosities in my experiments of 10^6 Pa.s (Appendix Table 2.B), a radius of 0.8–4 μm (Table 2.5), and an estimated interfacial tension of 5–8 mN/m (Veksler et al., 2010), I predict coalescence on timescales of 160–800 seconds, sufficient to expect evidence of partial coalescence to be preserved in the quenched experimental runs. Over 27,000 Fe-rich droplets were analysed in this study, yet only two examples of partially complete coalescence (i.e. two droplets forming a 'figure of eight') were found, and only a few examples of two droplets in close proximity separated by a meniscus (Fig. 2.3). This suggests that coalescence was not a significant process controlling droplet size distribution in these experiments.

Instead, since droplet composition also evolves with dwell time (Appendix Table 2.B), I suggest that coarsening is likely to have been controlled by a combination of kinetic growth and chemical equilibration as the binodal widened during cooling. A further possible cause of the loss of small droplets is the increasing difficulty in nucleation as the pockets of remaining liquid become smaller with increasing crystallinity (e.g. Putnis and Mauthe, 2001).

2.4.4.2 Constant cooling evolution

While the compositional evolution of the isothermal experiments show that these experiments did not reach chemical equilibrium, this is even more the case for the experiments which underwent constant cooling, in which chemical equilibrium is a "constantly moving goalpost". The DSDs in the constantly cooled experimental charges are non-linear. In natural systems, such size distributions have been attributed to changes in cooling rate (Zieg and Marsh, 2002), yet my experimental charges were run with a constant cooling rate of 1°C/h. Such nonlinearity may be due to a combination of diffusion-controlled droplet growth (including Ostwald ripening), and nucleation (e.g. Cashman and Ferry, 1988).

Coarsening during constant cooling increases both d_{IS} and d_{AT}. My data show $D_{4,3}/D_{3,2}$ values for isolated droplets (Table 2.5) lie between 1.09 and 1.21 (with one exception – attributed to differences in experimental starting preparation; Table 2.2). These ratios are broadly consistent with previous analyses of Fe-rich droplet size distributions in the experimental charges of Charlier and Grove (2012) by Farr et al. (2017) and, in common with the isothermal experimental results, suggests a significantly wider size distribution for isolated Fe-rich droplets than predicted if coarsening were exclusively by Ostwald ripening.

The DSDs show that the d_{IS} is within bin size error of the d_{IS}*. Furthermore, the DSDs have a positive slope for $d_{IS}<d_{IS}$* (Fig. 2.9). These observations suggest Ostwald ripening played some role in coarsening (Cashman and Ferry, 1988). The DSDs for isolated droplets rotate towards the horizontal (Fig. 2.9), compatible with the CN theory of Ostwald ripening (DeHoff, 1991; Higgins, 2002). This supports my idea of small-scale compositional heterogeneities influencing unmixing in localised areas within the crystal mush. However, a reduction in the number of small droplets could also result from a lowering of the nucleation rate (due perhaps to a reduction in the driving force for nucleation caused by decreased pore size). The DSDs for attached droplets do not show evidence of coarsening via Ostwald ripening.

2.4.5 Binodal position

The highest-temperature record of the onset of unmixing in semi-isolated pockets of skeletal plagioclase is in the experimental charge quenched at 1030°C. The bulk interstitial liquid records the onset of immiscibility in the experimental charges quenched at 1025°C and below, consistent with previous studies (Charlier and Grove, 2012). For any given quench temperature, I observe a range of compositions of the co-existing Fe-rich and Si-rich liquids (Fig. 2.5). Previously published binodals were determined using the average of these compositions (Charlier 2018 pers. comm.). Here I draw the binodal using the extreme values of the calculated NBO/T values (as discussed below).

There is a small disparity between the compositional ratio of Fe-rich/Si-rich liquids (obtained by applying the Lever Rule to the binodal) and the relative proportions of Fe-rich/Si-rich glass measured in the experimental charges. I attribute this disparity to the analytical limitations imposed by EPMA

spatial resolution, which prevented me from analysing smaller Fe-rich droplets. These analytical limitations also resulted in the observed range in Fe-rich droplet compositions within any one experimental charge, since the larger droplets are not necessarily compositionally comparable to the smaller, sub-micron, droplets. The large Fe-rich droplets are internally unmixed and heterogeneous, sometimes containing abundant nano-scale Si-rich droplets (shown in Fig. 1b of Charlier and Grove (2012)). Consequently, I suggest that the large Fe-rich droplets have a less evolved composition than the smaller Fe-rich droplets. This suggestion is supported by changes in glass compositional analyses from the experimental charges as the isothermal dwell time increases. Since the Fe-rich droplets evolve to more Fe-rich compositions and higher NBO/T compositions (Appendix Table 2.B) with increasing dwell time, I suggest that the Fe-rich end member of the binodal has a higher NBO/T value, for a given temperature, than my compositional analyses suggest. This would widen the binodal (Fig. 2.5), and hence reduce the calculated relative proportion of Fe-rich/Si-rich liquid, resulting in the measured liquid proportions more closely matching the binodal calculated proportions.

Furthermore, I do not know the exact compositional evolution of the bulk liquid line of descent. The bulk liquid NBO/T should first increase prior to magnetite saturation (Fe-enrichment of tholeiitic trends). Then, the NBO/T decreases (Si-enrichment) and this bulk Si-enrichment continues even after the binodal is reached. Consequently, the bulk liquid line of descent gets closer to the Si-rich side of the binodal (Fig. 2.14) while the binodal simultaneously enlarges; it is therefore difficult to predict whether the volume of Fe-rich liquid should decrease or increase with cooling.

Increasing the isothermal dwell time of the experimental charges results in an apparent decrease in the volume of Fe-rich liquid. At first glance, this suggests the unmixed liquid has not attained chemical equilibrium; however, this is at odds with the extensively documented natural examples of emulsions in liquids of similar compositions to those of these experiments (e.g. De, 1974; Luais, 1987; Philpotts, 1979; Philpotts and Philpotts, 2005). I suggest that since these experimental charges continued to crystallise during isothermal equilibration, the continued evolution of the remaining liquid could result in the liquid line of descent exiting the binodal.

2.4.6 Implications for immiscible liquid separation

Our unmixing experiments focus on the evolution of silicate liquid immiscibility microstructures in tholeiitic systems in which the Fe-rich liquid is the minor phase, forming dispersed droplets within a continuous Si-rich phase, with results applicable to a wide array of tholeiitic systems. Previous studies have hypothesised that large-scale phase separation can occur after unmixing of the bulk tholeiitic magma (Charlier et al., 2011; Jakobsen et al., 2011; Namur et al., 2012; VanTongeren and Mathez, 2012). Gravitationally-driven liquid separation in the bulk magma of such systems depends on the Stokes' velocity of the droplets, and would be least efficient close to the binodal, where liquid compositions are similar (Hou et al., 2017; Yuan et al., 2017). The Stokes' velocity of an Fe-rich droplet

is given by: $v = \frac{2g\Delta pR^2}{9\eta}$. Using the known density (ρ), viscosity (η), and average isolated Fe-rich droplet radius (R) (Appendix Table 2.B; Table 2.5), settling velocities range from 10^{-8}–10^{-10} m/year. The maximum migration distance of an average Fe-rich droplet on the solidification timescales of 10 km-scale layered intrusions (e.g. ~100,000 to 1,000,000 years) is 10^{-2}–10^{-3} m. This falls well below the separation length-scale of hundreds of metres suggested by VanTongeren and Mathez (2012) for the Upper Zone of the Bushveld Complex. Large-scale separation of liquid emulsions therefore requires either much larger droplet sizes, or processes such as convection which could facilitate the segregation of the two immiscible liquids if the dense component of the convecting emulsion were retained on the floor of the intrusion and the light component at the roof. While this may be the case for magmas in which the Fe-rich liquid comprises significantly less than 50 vol.%, at higher volume fractions centrifuge experiments show that the Fe-rich droplets may form 'avalanches' that facilitate separation (Veksler et al., 2008b): it is therefore possible that Stokes' law may not apply under such compositional conditions. Additionally, Veksler et al. (2008b) showed that gravitationally-driven separation of a nanoemulsion is possible in both a centrifuge and under static conditions, so treatments of unmixing timescales based on Stokes' law may be unrealistic.

Separation of immiscible liquids within a crystal mush (e.g. Holness et al., 2011; Humphreys, 2009; Humphreys, 2011) is strongly affected by pore diameters, coarsening rates and wetting properties. For example, Chung and Mungall (2009) show that immiscible sulfide droplets with radii 1/10 the average crystal radius travel the furthest through a crystal mush. Plagioclase comprises over 68% of the solid phases in my experiments; the average plagioclase grain is 22.8 μm along the major axis (Table 2.3), so Fe-rich droplets of radius 4.8 μm might be expected to be the most mobile. This is an order of magnitude larger than the average diameter of homogeneously nucleated droplets in my experiments (Table 2.5), so optimal segregation of the two immiscible phases in a crystal mush of equivalent grain size requires significant droplet coarsening (ignoring the effect of pore throat dimension). Consequently, in small-scale, crystal-rich tholeiitic magma bodies cooling on the order of 1°C/h (e.g. dykes and sills of ~10 m width) gravitationally-driven segregation of immiscible homogeneously nucleated Fe-rich droplets is unlikely to be significant. Chung and Mungall (2009) suggest that if the dense immiscible liquid forms a connected net-like texture around crystals (i.e. the dense liquid phase wets the minerals of the mush) then this can promote phase separation. Consequently, coarsening and accumulation of pockets of Fe-rich liquid should better facilitate downwards movement in a mush, relative to dispersed isolated Fe-rich droplets. This is most likely to pertain to mushes, or regions of mushes, rich in phases on which the Fe-rich liquid has a low wetting angle, such as oxides and mafic minerals like olivine and pyroxene (Table 2.4). This effect may be promoted by the presence of water, which enlarges the binodal surface and increases the interfacial tension between the two immiscible liquids (Hou et al., 2018), making coalescence more effective compared to dry tholeiitic systems. The concentration of the elements Ca, Al and Si also has an effect on coarsening rates, with unmixing shown

to be significantly slowed by high concentrations of these elements regardless of temperature (Veksler et al., 2008b). A further factor controlling segregation is that the closer the liquid line of descent is to the centre of the binodal, the greater the volume of Fe-rich liquid at higher temperatures, promoting Fe-rich liquid migration.

2.5 Concluding remarks

The results of this experimental study illustrate how thermal history and crystallisation affect the physical behaviour of an immiscible Fe-rich liquid during cooling of a ferrobasaltic liquid. The key findings are:

1. The onset of unmixing is localised because of heterogeneities in the interstitial liquid produced by compositional boundary layers formed during crystallisation;
2. Accumulations of small grains of whitlockite (similar to apatite in composition) along the margins of pyroxene and magnetite grains, and albitic pillars on plagioclase grains, provide potential microstructural indicators of immiscibility in fully solidified rocks;
3. The wetting angles of Fe-rich immiscible liquids on plagioclase and magnetite increase with decreasing temperature;
4. Heterogeneously nucleated droplets do not coarsen solely via Ostwald ripening during the experiments;
5. Droplet size distributions of homogeneously nucleated droplets are controlled strongly by growth during the process of chemical equilibration driven by cooling, with minimal contribution from coalescence;
6. In small-scale magma bodies (e.g. dykes and sills of ~10 m width), gravitationally-driven segregation of immiscible homogeneously nucleated Fe-rich droplets is unlikely to be significant.

Although the cooling rates of these experiments were analogous to those experienced by a small intrusion, further work at lower cooling rates would provide microstructural evidence applicable to larger bodies.

3 THE EFFECT OF COOLING RATE ON IMMISCIBLE SILICATE LIQUID MICROSTRUCTURE: AN EXAMPLE FROM THE PALAEOGENE DYKES OF NORTHEAST ENGLAND

A version of this chapter is published as:

Honour, V.C., Holness, M.B. and Stock, M.J., in second revision. The effect of cooling rate on immiscible silicate liquid microstructure: an example from the Palaeogene dykes of Northeast England. Mineralogical Magazine, 83(6), 809-820.

Co-authors and reviewers have provided comments on the manuscript.

3.1 Introduction

As mafic silicate melts cool and crystallise, under certain pressure, temperature, compositional, and oxygen fugacity conditions, they can unmix to form an emulsion of two immiscible liquids, one rich in Si and the other dominated by Fe (e.g. Charlier and Grove, 2012). Existing work on the evolution of silicate liquid immiscibility in crystal mush and bulk magmas has typically focused on the chemistry of the unmixed liquids (e.g. Charlier and Grove, 2012; Roedder, 1951; Veksler et al., 2007). However, limited textural observations suggest that cooling rate may have a major effect on the distribution and coarsening of an emulsion (Martin and Kushiro, 1991). As the migration and accumulation of these unmixed liquids are potentially linked to the differentiation of crustal magma bodies (e.g. Veksler et al., 2007) and the formation of some economic mineral deposits (e.g. magnetite-hematite-apatite ores; Frietsch (1978)), further work is essential to establish the controls on their microstructural evolution.

Previous studies investigating the microstructures of systems containing immiscible silicate liquids have typically focussed on centimetre-sized experimental charges (e.g. Charlier and Grove, 2012; Veksler et al., 2006; Veksler et al., 2008b) or kilometre-scale igneous intrusions (Holness et al., 2011), each with very different thermal histories. Experimental investigations are limited to cooling rates of $\gtrsim$1°C/h, as slower cooling rates often result in long-term instability in the run conditions (e.g. Charlier and Grove, 2012; Honour et al., 2019; Veksler et al., 2006; Veksler et al., 2008b). Conversely, although the much slower cooling rates of large igneous intrusions are not as well constrained, they are likely to be on the order of 10^{-7}°C/h (Cawthorn and Walraven, 1998). Published descriptions of unmixed silicate liquid microstructures preserved in natural systems with cooling rates intermediate between these two extremes are rare. Examples include glass quenched during drilling of the partially solidified crust of the Kīlauea Iki lava lake in Hawaii (Helz, 1987), and microstructures in interstitial glass in naturally cooled tholeiitic dykes and sills (e.g. Philpotts, 1982; Philpotts, 1978; Philpotts, 1979).

In this study, I investigate emulsion microstructure preserved in the mesostasis of three basaltic dykes from the northeast of England. Using a conductive thermal model, I calculate the cooling rates across the dykes, and plagioclase aspect ratios and grain sizes are used to constrain the fluid dynamical regime during crystallisation. The cooling rates of the dykes are slower than can be routinely accessed through experimental petrology but are significantly faster than cooling rates in larger igneous intrusions, preserving clear evidence of emulsion microstructures in quenched glass and providing the opportunity to constrain the rates of nucleation and evolution of an unmixing emulsion as a function of cooling rate. Dykes show significant differences in the spatial variation of mineral grain shapes and sizes compared to tabular intrusions of similar thickness but with significantly shallower dips (i.e. sills), as a result of orientation-controlled differences in fluid dynamical regime during solidification (Holness et al., 2017a). Following Holness et al. (2017), I argue that the Paleogene dykes of Northeast England are an exception to this general tendency, with microstructural characteristics indicative of sill-like fluid dynamical behaviour.

3.2 Geological Setting

During the Palaeogene, a mantle plume in the North Atlantic (today located beneath Iceland; Saunders et al. (1997)) caused uplift and thinning of the NW European continental margin, resulting in the ascent of magmas to high crustal levels and emplacement of large igneous bodies in western Scotland (the Skye, Rum-Muck, Arran and Mull central complexes). Emplacement of the Mull Central Complex was associated with the intrusion of a large NW-SE trending dyke swarm across western Scotland, northern England and into the North Sea (Harker and Clough, 1904; Sloan, 1971), extending at least 600 km from its source (Fig. 3.1; Underhill (2009); Wall et al. (2010)). The swarm is dated between 58.04 and 60.56 Ma (Chambers and Pringle, 2001; Mitchell et al., 1989) and is thought to be related to a large caldera collapse event (Macdonald et al., 2010).

Variations in magma propagation rate are thought to have caused the thickness and spacing of the Mull dyke swarms to increase with distance from their source (Jolly and Sanderson, 1995). Modern-day dyke intrusion events in the East African Rift and Iceland show that propagation rates are in the range 0.3–4.7 km/h (e.g. Ágústsdóttir et al., 2016; Ayele et al., 2009; Peltier et al., 2005; Wright et al., 2006). Hence, I infer that the dykes of the Mull swarm took a minimum of 28 days to propagate 200 km from their source to the coast of Northeast England. Following the cessation of flow in the dykes, I assume that the magma crystallised as a closed system (e.g. Holness et al., 2017a).

The basaltic dykes of the Mull swarm are geochemically analogous to the Central Mull tholeiitic magma (Kerr et al., 1999; Macdonald et al., 2010). They were classified based on their petrography and geochemistry by Holmes and Harwood (1929): typical whole-rock compositions of the dykes investigated in this study are presented in Table 3.1. They have varying modal proportions of

plagioclase, olivine and pyroxene, with a glassy matrix preserving evidence of liquid immiscibility (Holmes and Harwood, 1929). I focus on three dykes: (1) the Hartley North Dyke (which Teall (1884) termed the Collywell dyke) is fine-grained with a sinuous strike through a host rock of shale with sandy bands (Jones, 1967; Land, 1974); (2) the Tynemouth Dyke, which cuts the Coal Measures sandstone at the current level of exposure (Land, 1974) and extends SE into the North Sea (Heslop and Smythe, 1910; Holmes and Harwood, 1929; Jones, 1967; Land, 1974; Teall, 1889; Teall, 1884); and (3) the Morpeth Dyke, which is fine-grained, has the highest measured density of the Palaeogene dykes of Northeast England (Heslop and Smythe, 1910; Holmes and Harwood, 1929; Teall, 1884) and is hosted within sandstone interbedded on a 10–20 m scale with fissile mudstone.

Table 3.1 Whole rock geochemistry of the Palaeogene dykes of Northeast England, taken from Holmes and Harwood (1929).

	Talaidh-type dyke (e.g. Hartley North)	Brunton-type dyke (e.g. Tynemouth)	Salen-type dyke (e.g. Morpeth)
SiO_2	51.10	50.81	50.41
Al_2O_3	16.75	15.70	15.14
FeO	8.03	8.54	10.39
MgO	5.89	6.41	6.57
CaO	11.97	12.17	11.30
Na_2O	2.02	1.96	2.29
K_2O	0.66	0.87	0.82
TiO_2	0.96	0.81	1.30
P_2O_5	-	0.10	0.15
MnO	0.37	0.17	0.17
Mg#	57	57	53

3.3 Samples and sample collection

Samples were collected during fieldwork in July 2016, supplemented by additional samples from the Harker Collection of the Sedgwick Museum (University of Cambridge). The Hartley North Dyke was sampled 20 m from the N-S trending Collywell Bay sea wall, on the foreshore at low tide (Table 3.2). Here, the dyke has a strike of 105°, with a variable width (0.83–1.04 m; Fig. 3.2c) and chilled margins. The Tynemouth Dyke is only exposed at low tide and samples were collected along the foreshore, north of the western end of the Tynemouth North pier, at the base of Castle Rock (Fig. 3.2a,b). At this location, it is 3.18 m wide and strikes 103°, with undulating margins on a 0.1–0.2 m scale (Table 3.2). The Morpeth Dyke was sampled on the eastern bank of the Wansbeck, south-east of the North-Eastern Railway viaduct (Table 3.2), where it lies within a 5.25 m wide steep-sided gully perpendicular to the Wansbeck. There is no visible outcrop and samples of olivine-rich basalt were obtained from scattered >0.3 m diameter boulders and <10 cm chips (Fig. 3.2d). Teall's (1884) description of the Morpeth Dyke locality was published 34 years after the viaduct was built when there was significant building work along the bank of the Wansbeck; it is possible that it was quarried out and used for construction, thus creating the well-defined gully.

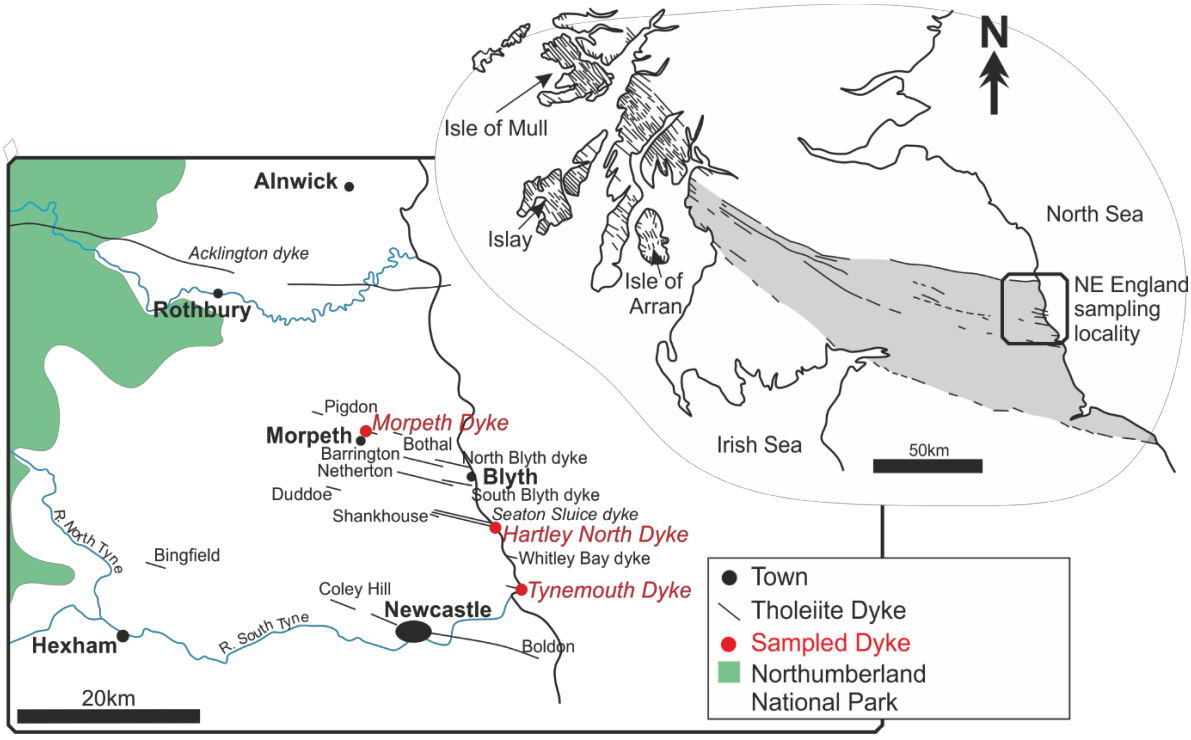

Figure 3.1 Overview of the Mull dyke swarm, together with the location of the dykes examined here. Adapted from Holmes and Harwood (1929).

Table 3.2 Field locations of the Palaeogene dykes of Northeast England analysed in this study. SST = sandstone, MST = mudstone.

Dyke	Latitude (N)	Longitude (W)	Width (m)	Strike (°)	Host Rock	No. of samples
Hartley North	55°04'50.8"	001°28'10.5"	~1.03	105	SST interbedded with MST	8
Tynemouth	55°01'00.9"	001°24'55.5"	~3.18	103	SST	13
Morpeth	55°10'13.6"	001°39'45.1"	<5.25	122	SST interbedded with MST	4 (not *in situ*)

3.3.1 Analytical methods

Samples were analysed in the Department of Earth Sciences, University of Cambridge, using optical microscopy and a Quanta FEG 650 F scanning electron microscope (SEM), set to 10 kV at spot 3, with a 30 µm aperture and a working distance of 10 mm. Back-scatter electron (BSE) images were collected for the polished samples.

Average apparent aspect ratios of plagioclase grains were calculated by measuring the long and short axes of >250 crystals per sample from digital photomicrographs under crossed polars. All discernible plagioclase grains were measured in each photograph. Aspect ratios were calculated using *ImageJ* software, which determines the best-fit ellipse for a pair of orthogonal lines. The 2σ confidence

interval of the average apparent aspect ratio was calculated using the bootstrap method (James et al., 2013) since the shape of the underlying distribution is unknown. Plagioclase grain sizes were also calculated using the average of the long axis length of >250 plagioclase grains. Fe-rich droplet diameters were measured using *CorelDrawX9* from BSE images. All discernible Fe-rich droplet diameters were measured in each photograph.

Preliminary EPMA (electron probe micro-analysis) data on several plagioclase compositions were measured using a CAMECA SX-100 electron microprobe with five WDS spectrometers at the Department of Earth Sciences, University of Cambridge. The instrument uses PeakSight software with ZAF correction. Appropriate natural and synthetic primary standards were used. Plagioclase compositions were analysed at 15 kV, 10 nA with a focused beam; Na and Si were analysed for 10s on peak, Al for 20 s, Ca, Mg, and K for 30 s, and Ti and Fe for 60 s. Relevant mineral and glass secondary standards were run at regular intervals to check for precision and reproducibility.

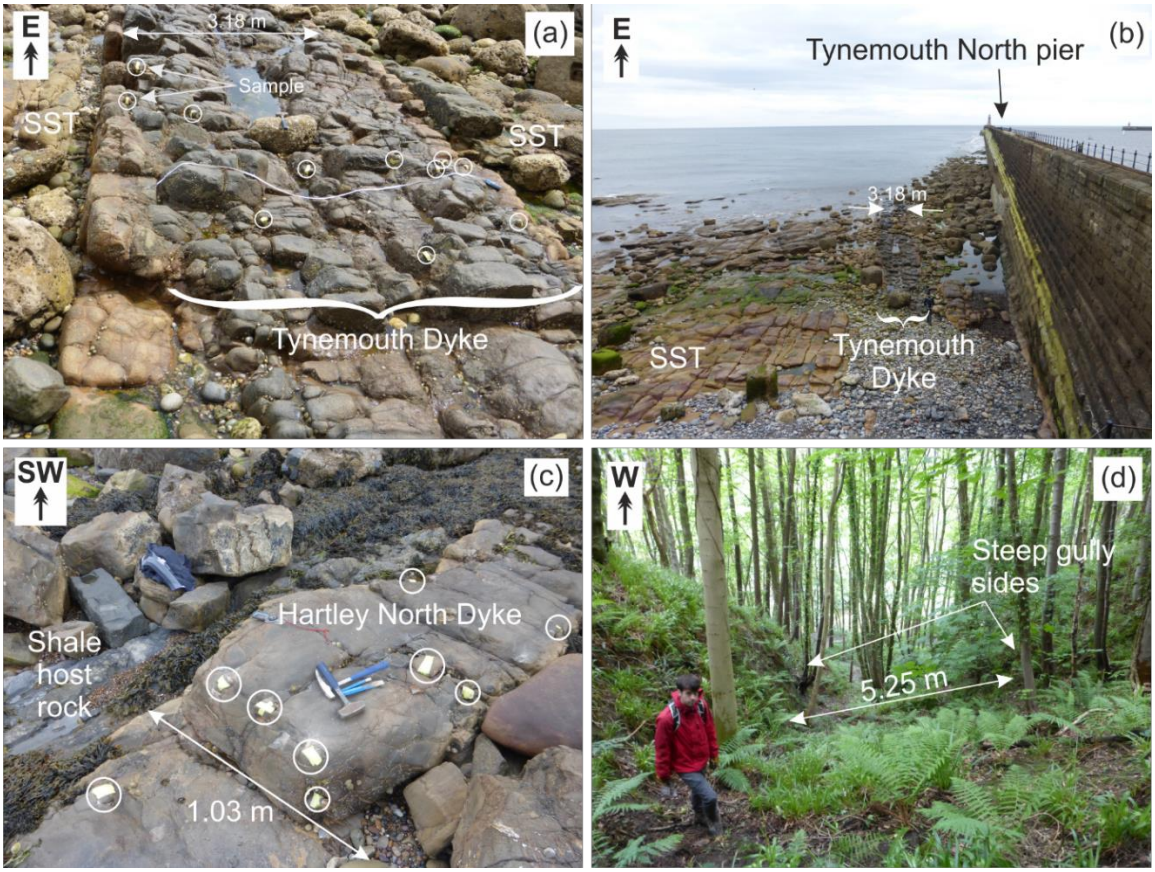

Figure 3.2 Field photographs of the sampling locations in this study. a) Tynemouth Dyke, sampling localities outlined with white circles; b) Tynemouth Dyke exposed north of the Tynemouth North pier; c) Hartley North Dyke sampling localities outlined with white circles; d) the Morpeth Dyke locality.

3.4 Results

3.4.1 Petrography

The Hartley North Dyke is dominated by a matrix of fine-grained plagioclase, clinopyroxene and glass, with variable modal Fe-Ti oxide (Fig. 3.3a). The amount of glass increases from 16 vol.% on the chilled margins to 22 vol.% in the centre of the intrusion. The average matrix plagioclase long axis length (Table 3.3) increases towards the dyke centre, from 189 μm to 231 μm, and the average apparent aspect ratio decreases from 6.0 to 4.6 (Fig. 3.4a; Table 3.3). Rare, large (<2 mm x 0.8 mm) plagioclase phenocrysts with zoned rims are present throughout. Clinopyroxene is fine-grained on the chilled margins (<10 μm), but reaches 100 μm diameter in the dyke centre where the crystals tend to form small clusters. Spherical amygdales filled with calcite and silica are abundant (0.5–1.8 mm in diameter), particularly in the centre of the dyke.

The Tynemouth Dyke is dominated by a fine-grained matrix of elongated plagioclase laths, clinopyroxene, oxides and glass (Fig. 3.3b,c) with rare olivine grains, typically <50 μm in diameter. The glass distribution is patchy, but the average glass mode increases from 18 vol.% on the chilled margin to 26 vol.% in the centre of the intrusion. The glass in the dyke centre is commonly devitrified. The average apparent aspect ratio of the matrix plagioclase (Fig. 3.4b) decreases from 5.4 on the chilled margins to 3.9 in the centre (Table 3.3), as does the relative number of matrix plagioclase grains per unit area. The dyke contains large plagioclase phenocrysts (<9 x 4 mm) with sharply-defined, <0.5 mm wide irregular rim zones and concentrically-arranged melt inclusions that outline internal growth zones. The anorthite number (mol.%) of the large plagioclase phenocrysts decreases from the centre to the rims of the crystals (Appendix Table 3.A). The number of plagioclase phenocrysts increases towards the intrusion centre, where they form polycrystalline clusters enclosed by a shared outer rim zone; the plagioclase rim zone is absent on crystal faces adjacent to pockets of glass (Fig. 3.3c). The grain size range of matrix plagioclase in the Tynemouth Dyke broadens towards the intrusion centre, and the average long axis length increases from 143 μm to 236 μm (Table 3.3). On the chilled margins, clinopyroxene grains are small (<80 μm diameter) and isolated in the matrix, whereas in the centre of the dyke they are larger (<150 μm diameter) and form clusters, or partially enclose plagioclase grains. Grains of Fe-Ti oxides are <50 μm across and are typically found in the mesostasis. Spherical amygdales filled with calcite and silica are irregularly distributed throughout the Tynemouth Dyke, increasing in number and size towards the centre.

The Morpeth Dyke is characterised by a matrix of elongated plagioclase laths, clinopyroxene, olivine, oxides and glass (Fig. 3.3d). The glass mode is analogous to that of the Tynemouth and Hartley North Dykes at ~25 vol.%. Although spatial variations in matrix plagioclase average apparent aspect ratio and grain size could not be quantified due to the lack of outcrop, the long axis length in my samples reaches ~500 μm, while the average plagioclase apparent aspect ratio is 4.8. Large plagioclase phenocrysts (3

x 2 mm) are rare but have strongly zoned rims and melt inclusions in their core. Clinopyroxene is evenly distributed, with grain diameters ranging between 50–200 μm. Rare olivine grains (100–300 μm in diameter) form small monomineralic clusters, typically comprising 3-4 grains. Spherical amygdales filled with calcite and silica are present in all of the samples.

Table 3.3 Petrographic measurements of the Palaeogene dykes of Northeast England. Distances from the dyke margins were measured from the north to south. Plagioclase grain size is reported as average apparent long axis, and shape is reported as the average apparent aspect ratio. HC = samples from the Harker Collection, University of Cambridge. * denotes the position within the dyke transect given in the catalogue of the Harker Collection.

No.	Distance from the north margin (m)	Position	Modal glass %	Plag average apparent long axis (μm)	Plag average apparent aspect ratio	No. plag/ mm^2	Largest Fe-rich Droplet (μm)
Hartley North Dyke; 1.03 m ± 0.05 m wide							
H1	0.05	Margin	18	189	6.0	30	1
H2	0.08	Margin	17	186	6.1	29	<2
H3	0.23	Centre	19	239	5.5	17	3
H4	0.29	Centre	22	228	5.5	16	4
H5	0.32	Centre	20	231	4.6	14	3
H6	0.65	Centre	18	236	4.9	18	3
H7	0.86	Margin	16	223	5.3	18	<2
H8	0.95	Margin	17	256	5.5	15	<2
Tynemouth Dyke; 3.18 m ± 0.20 m wide							
T1	0	Margin	18	143	6.1	41	2
T2	0.2	Margin	20	173	5.7	16	4
T3	0.28	Margin	21	189	6.1	20	7
T4	0.7	Centre	23	245	4.7	9	5
T5	0.86	Centre	24	242	4.5	15	5
T6	1	Centre	26	234	4.6	10	11
T7	1.32	Centre	26	236	4.4	12	12
T8	1.42	Centre	25	230	4.4	14	13
T9	2.13	Centre	26	254	4.7	12	8
T10	2.48	Centre	25	244	4.8	12	6
T11	2.55	Margin	23	178	5.3	16	5
T12	2.76	Margin	22	167	6.1	21	7
T13	2.97	Margin	21	198	6.1	19	1
20287	HC	Centre*	27	210	4.37	20	-
20289	HC	Centre*	26	192	4.38	17	-
20288	HC	Centre*	25	212	4.53	21	-
20290	HC	Margin*	20	168	4.71	36	-
14249	HC	Margin*	21	176	4.73	31	-
4141	HC	Margin*	11	175	5.33	50	-
Morpeth Dyke; <5.25 m wide							
20303	HC	Margin*	25	175	4.91	43	9
20302	HC	Margin*	29	150	4.77	39	8
2362	HC	Margin*	21	-	-	-	-
39782	HC	Margin*	19	-	-	-	-

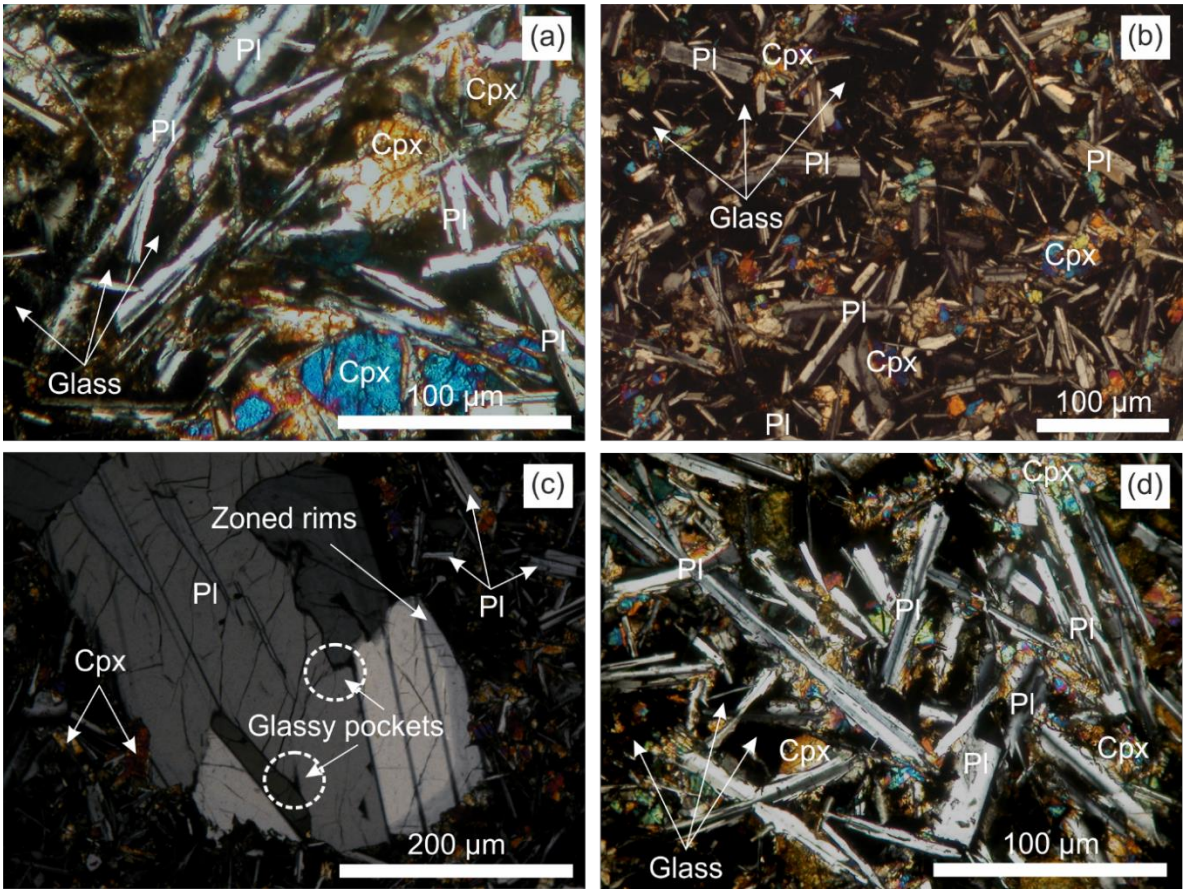

Figure 3.3 Crossed polars (XPL) photomicrographs of the Palaeogene dykes of Northeast England; (a) Centre of the Hartley North Dyke; (b) Centre of the Tynemouth Dyke with abundant plagioclase laths and a glassy mesostasis; (c) A cluster of zoned plagioclase phenocrysts in the centre of the Tynemouth Dyke; (d) Margin of the Morpeth Dyke (spatial information taken from the catalogue of the Harker Collection).

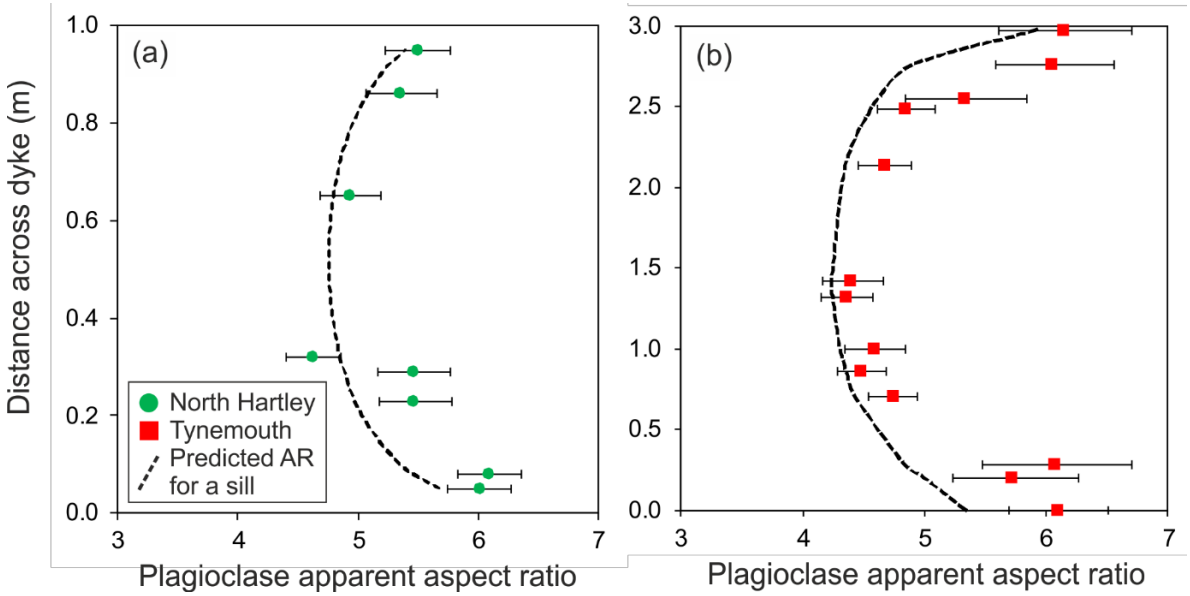

Figure 3.4 Average apparent plagioclase aspect ratios measured across the (a) Hartley North Dyke; (b) Tynemouth Dyke. The dashed line is the predicted average apparent aspect ratio trend following Holness (2014).

3.4.2 Immiscibility microstructures

Evidence of unmixing of the interstitial liquid of the Palaeogene dykes of Northeast England was first reported by Philpotts (1982). The whole rock chemistry means that the Fe-rich immiscible liquid is the minor phase, while the Si-rich conjugate forms the major phase (i.e. Fe-rich droplets are dispersed within a continuous Si-rich liquid). The glass in the dykes is generally altered, with increasing devitrification towards the centres, resulting in poorer microstructural preservation. However, droplets of immiscible Fe-rich material are always present in the mesostasis, regardless of the relative position of samples within the dyke or the dyke width (Fig. 3.5a-f). Where glass is still present, the Fe-rich droplets are spherical to sub-spherical, with a high refractive index and a white-to-brownish colour in plane polarised light. Where the glass is fully or partially devitrified, the droplets are framboidal (Fig. 3.5).

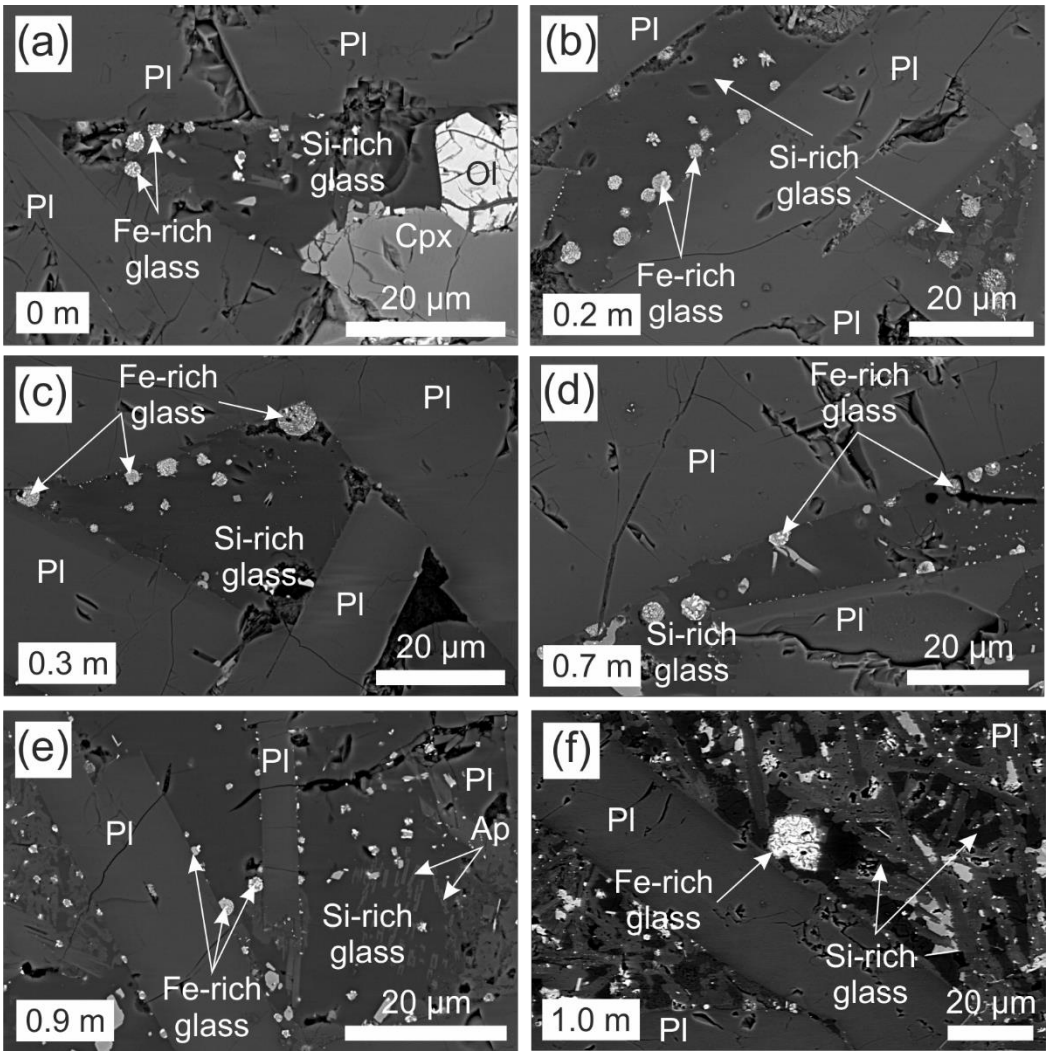

Figure 3.5 BSE images of the Fe-rich emulsion in the Tynemouth Dyke; (a-f) show a progressive transect southwards towards the dyke's centre, with exact distance from the north margin given in the bottom left of each photo. Note the predominance of Fe-rich droplets that are attached to plagioclase, compared to those isolated in the glass, particularly close to the margin.

The Fe-rich droplets are larger (ranging up to 20 µm in diameter) and more abundant in the centre of the dykes than at their margins. On the margins, the Fe-rich droplets are preferentially attached or proximal to plagioclase grains. Towards the dyke centres, the Fe-rich droplets show no preferential association with any crystal phase and there is an increased prevalence of isolated droplets (i.e. droplets that appear unconnected to any crystal phase in 2D section). Where Fe-rich droplets are attached to plagioclase grains, they have apparent wetting angles >90°. They are not found adjacent to mafic phases and I found no evidence of two droplets coalescing (i.e. no Fe-rich droplets with 'figure-of-eight' shapes).

There are variations in the emulsion microstructure between the three dykes. In the Morpeth Dyke, the Fe-rich droplets are larger and have a higher number density than in the Tynemouth and Hartley North Dykes (even in samples from the margin of the dyke; Fig. 3.6). Fe-rich droplets in the Hartley North Dyke are the least abundant and the smallest of those in the three dykes (Fig. 3.6g-i).

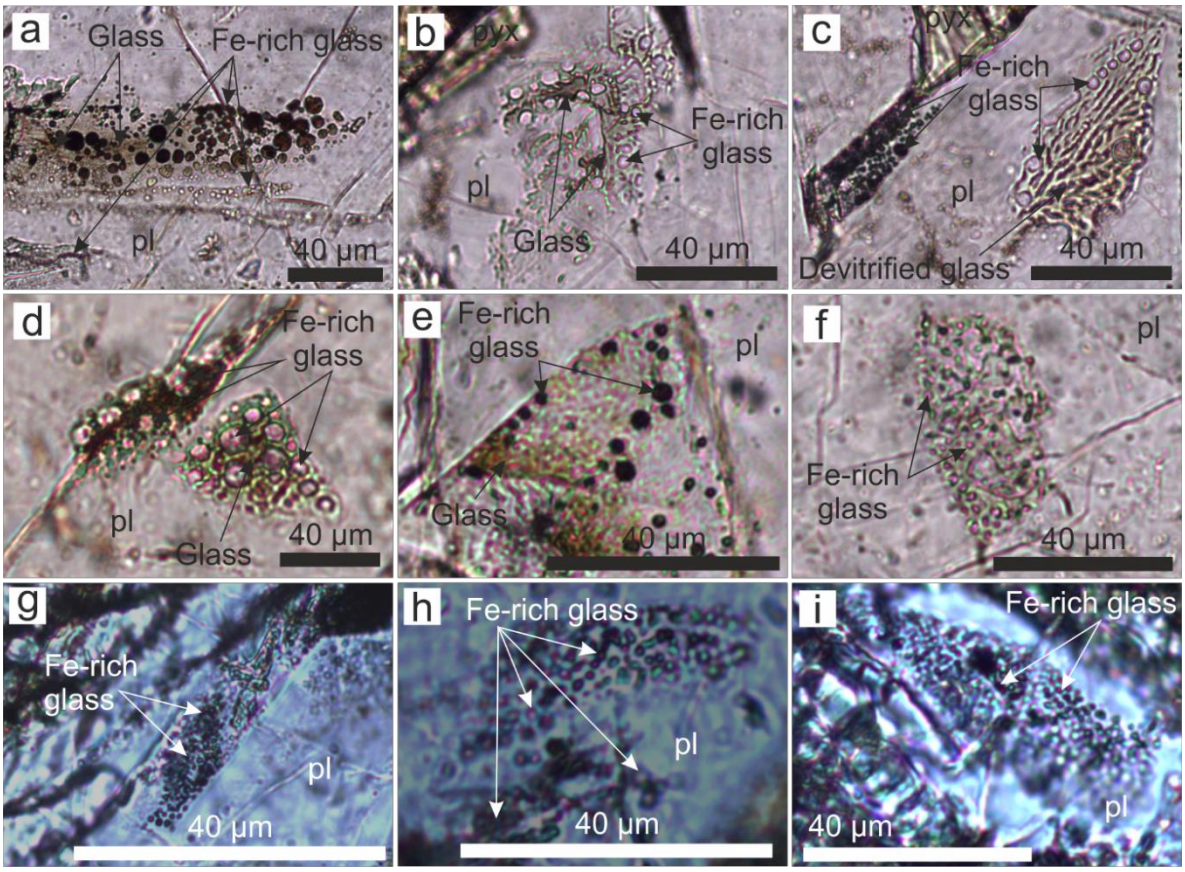

Figure 3.6 Plane polarised light (PPL) images of emulsion microstructures for all three dykes, showing the Fe-rich droplets in the glassy mesostasis. The glass of the mesostasis is commonly brown, with the Fe-rich droplets ranging from white to dark brown. The Fe-rich droplets are typically attached to plagioclase. (a-c) Sample from the margin of the Morpeth Dyke (Table 3.3); (d-e) Sample from the centre of the Tynemouth Dyke; (f) Sample from the margin of the Tynemouth Dyke, (g-i) Sample from the margin of the Hartley North Dyke.

3.5 Discussion

3.5.1 The crystallisation regime

The shape of plagioclase grains grown under interface-controlled conditions is a function of crystallisation time (Holness, 2014). In vigorously convecting magma in a tabular body, plagioclase crystals grow in suspension and the resultant averaging of the thermal history of each grain means that their shape is invariant across the width of the intrusion. In contrast, if the crystallising magma is either static or weakly convecting, solidification is dominated by the nucleation and growth of crystals on inwards-propagating solidification fronts: in such bodies plagioclase average apparent aspect ratio decreases from the intrusion margins towards the centre (Holness et al., 2017a). The average apparent plagioclase aspect ratio at any point across a tabular intrusion that solidified by the inwards-propagation of solidification fronts, assuming diffusive heat loss, is given by:

plagioclase aspect ratio = (log(cooling time in years) - 6.34)/(-1.79) *(equation 3.1)*

Consequently, I can use the spatial variation of plagioclase grain shape to test whether vigorous convection occurred during crystallisation of the investigated dykes.

The highest plagioclase average apparent aspect ratios are observed on the margins of the Hartley North and Tynemouth Dykes, while the lowest ratios are measured in their centres. The plagioclase average apparent aspect ratios across the Hartley North and Tynemouth Dykes match the trends predicted for non-convecting magma bodies using equation 3.1, but are systematically off-set to higher values (Fig. 3.4). It is well-known that aspect ratio decreases as crystallisation proceeds, due to the effects of impingement (Applegarth et al., 2013; Martin et al., 1987; Pupier et al., 2008; Schiavi et al., 2009) but the relationship between plagioclase grain shape and cooling timescales described in equation 3.1 was developed using fully-solidified dolerites (Holness, 2014). I suggest that the relatively high values observed in these samples may be a consequence of the significant volume of uncrystallised material comprising the mesostasis: the average apparent aspect ratio of the plagioclase did not attain the expected low values as crystallisation was incomplete. I also note that there are a number of spherical amygdales in the dykes, which suggest that magma degassed during crystallisation. Devolatilisation could drive plagioclase oversaturation (Hort, 1998; Yoder et al., 1957) and an increase in plagioclase growth rate, which might also result in higher average apparent aspect ratios than predicted by the model of Holness (2014) (Fig. 3.4).

In addition to the differences in the spatial variation of plagioclase grain shape in convecting and non-convecting systems, the average grain size is larger, and the range of grain sizes is narrower, in convecting tabular intrusions, relative to non-convecting intrusions of the same width (i.e. with similar cooling timescales; Holness et al. (2017a)). Fig. 3.7 shows the cumulative frequency of the plagioclase long axis length from the centre and margin of the Hartley North and Tynemouth Dykes, as well as

grain size data from previously identified convecting (a 3.7 m wide basaltic dyke from the Isle of Mull) and non-convecting intrusions (the 3.5 m thick Traigh Bhàn na Sgùrra sill of the Isle of Mull), which have similar widths to the Northeast England intrusions (i.e. within an order of magnitude; Holness et al., 2017a). The cumulative frequency distributions of plagioclase long axis length from the centre and margin of the Tynemouth and Hartley North Dykes are similar to those of the non-convecting Traigh Bhàn na Sgùrra sill, rather than the convecting dyke. Together with the spatial variation of plagioclase grain shape, these data suggest that crystallisation in the Northeast England dykes was dominated by the inwards propagation of solidification fronts, in agreement with Holness et al. (2017) who identified non-convective crystallisation in the Moneyacres dyke in Ayrshire (another member of the Mull dyke swarm). The absence of convection following dyke propagation may have been due to a high crystallite load that resulted in a high magma viscosity (Holness et al., 2017a).

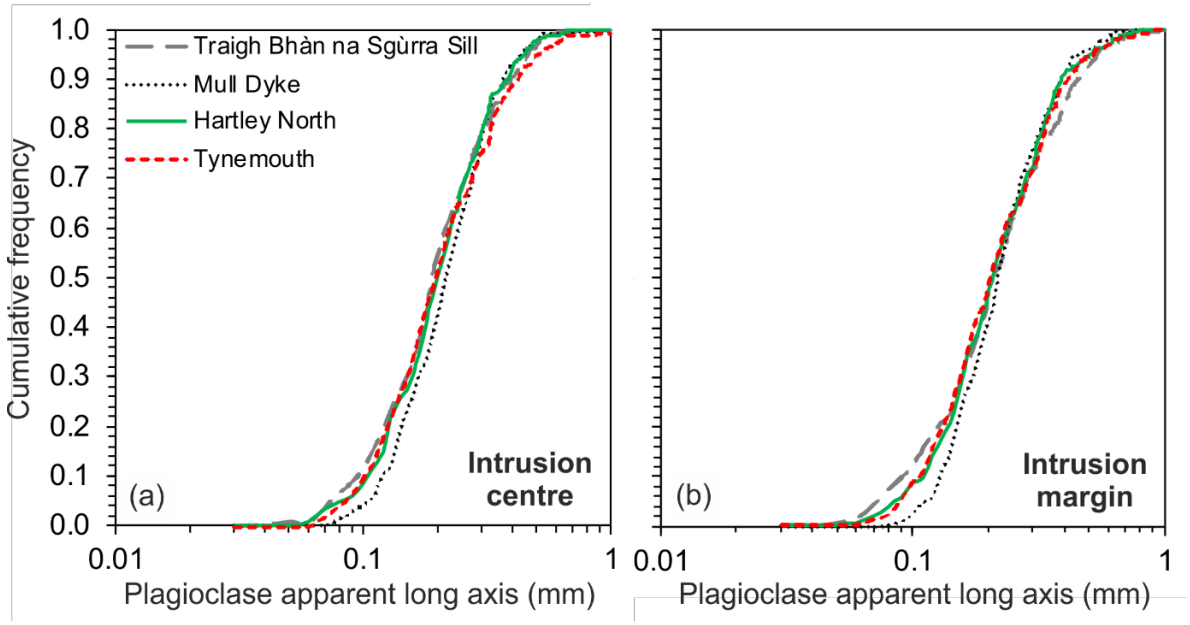

Figure 3.7 The cumulative frequency distributions of grain sizes (measured as the length of the apparent long axis of plagioclase as viewed in thin section) in the centres (a) and margins (b) of the Tynemouth and Hartley North Dykes. A typical convecting dyke (a 3.7 m wide basaltic dyke on the coast of the Isle of Mull) and a non-convecting sill (the 3.5 m wide Traigh Bhan na Sgurra basaltic sill on the Isle of Mull) with similar average grain sizes to the Northeast England Dykes are shown for comparison (data from Holness et al. (2017a)). Static systems have a greater range of grain sizes than convecting systems; the Tynemouth and Hartley North Dykes correspond more closely with the static example).

I consider it unlikely that silicate liquid unmixing occurred during dyke propagation: magma compositions only approach the silicate liquid binodal after significant differentiation (i.e. likely after crystallisation of groundmass plagioclase); I see no evidence of melt inclusions in large plagioclase phenocrysts being trapped from two immiscible liquids (although, they are devitrified; Fischer et al. (2016); Jakobsen et al. (2011)); preliminary geochemical transects across the large plagioclase phenocrysts show no evidence of prior liquid separation (i.e. no evidence of decreasing TiO_2 concentrations towards the rim; Humphreys (2011); Fig. 3.8; Appendix Table 3.A). Unmixing therefore occurred in a static magma, once matrix plagioclase had started crystallising.

3.5.2 Thermal modelling of cooling rate

As the magma in the dykes was static (or only weakly convecting) during solidification, I use a 1D thermal model to calculate the cooling rate at different positions across the intrusions for comparison with the size and abundance of unmixed Fe-rich droplets. The cooling rate of any sample from a tabular basaltic intrusion can be approximated assuming conductive *in situ* heat transfer into the host rock, following the approximation of (Holness et al., 2012):

$$\tau = 0.1\frac{w^2}{K}\left(1+\cos\left(\frac{2\pi z}{w}\right)\right) \qquad \textit{(equation 3.2)}$$

where τ is the time taken to cool from 1200°C to 1000°C (the assumed temperature range of crystallisation, following Cashman (1993); and Holness et al. (2012)), z is the position within the body measured from the centre (in metres), w is the total intrusion thickness (in metres) and κ is thermal diffusivity (m^2/s). I assume a far-field host rock temperature of 0°C and set κ to $4.8.10^{-7}$ m^2/s based on thermal diffusivity measurements of basalt at 1000°C (Hartlieb et al., 2016).

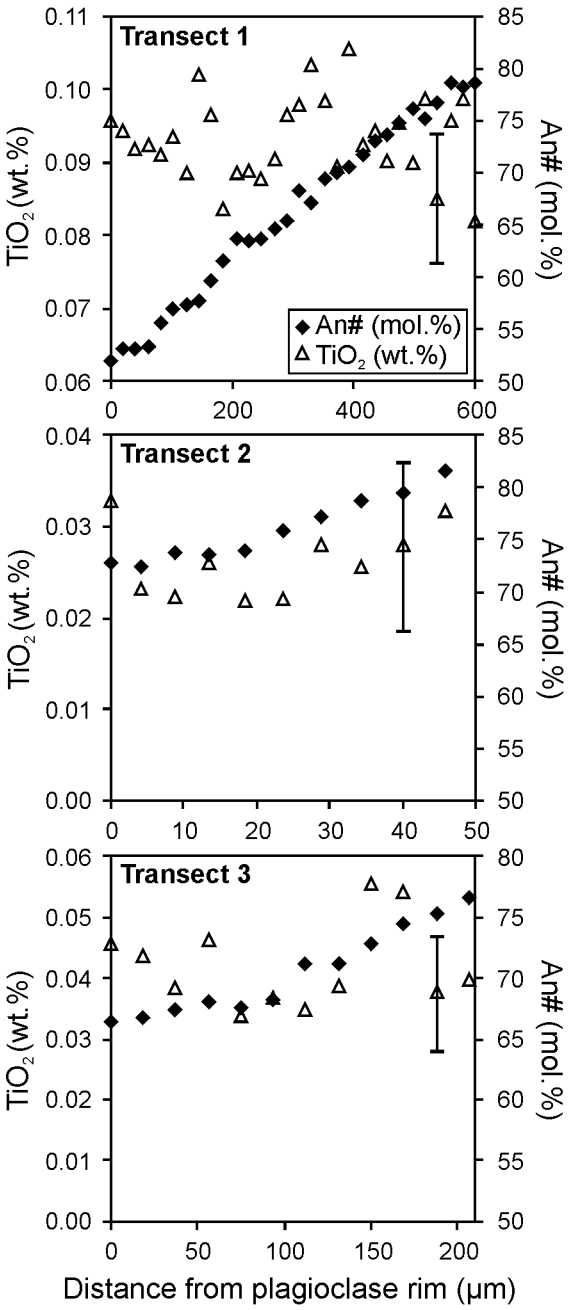

Figure 3.8 EPMA transects showing TiO_2 (wt.%) and anorthite composition (mol.%) from the large plagioclase phenocrysts from a sample taken at 1.32 m from the margin of the Tynemouth dyke (sample T7; Table 3.3). Error bars are representative EPMA standard deviations.

Our 1D cooling model suggests the Hartley North Dyke took 5 days to crystallise in the centre and 0.5 days near the margins (defined in Table 3.3), corresponding to average cooling rates of ~1.7°C/h and ~16.7°C/h, respectively. The Tynemouth Dyke took 43 days to crystallise in the centre and 0.5 days near the margins (defined in Table 3.3), corresponding to average cooling rates of ~0.2°C/h and ~17°C/h, respectively. Assuming the Morpeth Dyke was no wider than the gully in which it was sampled, the centre is predicted to have had a maximum cooling time of 117 days, with an associated average cooling rate of ~0.1°C/h.

3.5.3 The effect of cooling rate on emulsion behaviour

In a static regime, the microstructure of magmatic emulsions is controlled chiefly by temperature and time (e.g. Martin and Kushiro, 1991). Additional factors that can affect microstructural evolution include composition, pressure and fO_2 (e.g. Charlier and Grove, 2012). However, these are second-order variables (Martin and Kushiro, 1991) and are unlikely to vary significantly between compositionally similar mafic dykes (Table 3.1) emplaced at comparable depths.

3.5.3.1 Nucleation

Compositional boundary layers can develop at the interface between crystals and their host liquids; the thickness of these layers depends on the crystal growth rate, the diffusion rate within the liquid, and the relative motion of crystals and their surrounding liquid (Levich, 1962; Zellmer et al., 2016). The development of these compositional boundary layers can promote the localised onset of liquid unmixing, causing Fe-rich droplets to preferentially nucleate on (or near) plagioclase grains (Philpotts, 1981b). Compositional gradients around crystals are best developed during rapid crystal growth; therefore, I would expect Fe-rich droplets to have a greater association with plagioclase crystals at higher cooling rates. This accounts for the greater number of Fe-rich droplets attached to plagioclase crystals in the rapidly cooled margins of the Hartley North and Tynemouth Dykes, relative to their slower cooled centres.

Considering samples from different places within the same dyke, and samples from different dykes, I find that slower cooling rates correlate with increased numbers of Fe-rich droplets in the interstices (i.e. including both heterogeneously nucleated droplets and homogeneously nucleated droplets). This is at odds with the experiments of Martin and Kushiro (1991), which contain more droplets at higher cooling rates, leading them to conclude that slow cooling promotes increased droplet coalescence rather than a decrease in nucleation rate. I suggest that the disparity between my observations and their experimental results can be explained by magma cooling rates at the dyke margins being sufficiently fast that there was insufficient time for droplets to nucleate before the glass transition temperature was reached. Additionally, the smaller grain size and higher aspect ratios of the network-forming plagioclase grains near the intrusion margins (i.e. at high cooling rates) reduced the size of the interstitial liquid pockets, impeding nucleation and resulting in fewer Fe-rich droplets (e.g. Holness and Sawyer, 2008; Putnis and Mauthe, 2001).

The Morpeth Dyke has the most Fe-rich bulk composition of my samples and the Hartley North Dyke is the most Fe-poor (Table 3.1). The bulk FeO content of the dykes positively correlates with the size and abundance of the Fe-rich droplets, and thus the volume fraction of Fe-rich immiscible liquid. This agrees with the experimental results of Charlier and Grove (2012), which demonstrate that differing whole rock compositions affect the shape and size of the silicate liquid immiscibility field and thus the relative volumes of the two immiscible liquids: the abundance of the Fe-rich liquid generally increases

with total FeO of the bulk melt (other elements such as P, alkalis and volatiles also affect the size of the binodal; e.g. Lester et al. (2013)).

Only whole rock compositional data are available for the dykes studied here; these have a Mg# (molar $Mg/(Mg+Fe_{total})$ of ~57 (Table 3.1), which is significantly higher than the Mg# from existing experiments quantifying the silicate liquid immiscibility field (e.g. bulk liquid compositions studied by Charlier and Grove (2012) had Mg# of 29–36). Although the interstitial liquid in the dykes likely has a lower Mg# than their bulk composition (due to olivine and clinopyroxene crystallisation), it is not currently possible to quantitatively constrain the position of these dyke magmas on a binodal using the available geochemical data. This could be achieved with further geochemical work extending the silicate liquid immiscibility experimental database over a greater range of starting compositions.

3.5.3.2 Emulsion coarsening

In my samples, slower cooling rates are associated with larger Fe-rich droplets and a wider droplet size distribution, both across a single intrusion and between intrusions. For example, in the Tynemouth Dyke a three orders of magnitude increase in cooling rate correlates with an order of magnitude increase in droplet size (Fig. 3.9) and a widening of the droplet size distribution. Similarly, droplets are larger and more variable in size in the centre of the slower cooling Tynemouth Dyke than in the centre of the smaller, and therefore faster cooling, Hartley North Dyke. This implies Fe-rich droplet size does not scale linearly with cooling rate, and supports previous experimental work that suggests Fe-rich droplet size and cooling rate are related by an exponential law (Martin and Kushiro, 1991). A regression through their data suggests that variations in Fe-rich droplet size are related to the cooling rate of tholeiitic basalts via:

$$y = 73.159e^{-0.646x} \qquad \textit{(equation 3.3)}$$

where x is the average of the 5 largest diameter (μm) Fe-rich droplets in each sample and y is cooling rate (°C/h).

Using the largest Fe-rich droplets in the centre of the Hartley North Dyke, equation 3.3 predicts a cooling rate of 5.5°C/h, which is faster than the 1.7°C/h calculated using the simple 1D cooling model of Holness et al. (2012). While these estimates are comparable within an order of magnitude, one explanation for the disparity could be that factors other than cooling rate control Fe-rich droplet size. The coarseness of Fe-rich droplets in unmixed silicate melts is a function of diffusion-controlled droplet growth, Ostwald ripening, and/or coalescence. Diffusion-controlled Fe-rich droplet growth is driven by the widening of the silicate liquid immiscibility binodal during cooling or chemical equilibration (Honour et al., 2019). Ostwald ripening is driven by differences in the surface curvature of the Fe-rich droplets as a function of size (McNaught, 1997; Ostwald, 1897). Coalescence occurs as droplets collide and is a function of droplet radius, viscosity, density and the energy of the interface (Yao et al., 2005).

Recent progress in defining the binodal for silicate liquid immiscibility (Charlier and Grove, 2012), and in investigating the microstructure of unmixing magmas with constant cooling rates (Farr et al., 2017; Honour et al., 2019) indicates that liquid composition may also affect droplet size due to an expansion or reduction in the volume of Fe-rich liquid.

The largest Fe-rich droplets in the Tynemouth and Morpeth Dyke are bigger than those measured by Martin and Kushiro (1991). Their model is not calibrated for cooling rates <2°C/h, and thus does not adequately capture the range of cooling rates that my 1D cooling model predicts for the Northeast England dykes. Combining my new data for the Northeast England dykes with the experiments of Martin and Kushiro (1991) extends the range of cooling rates (Fig. 3.9), and I find that the relationship between droplet size and cooling rate (˚C/h) is better expressed by the power law regression:

$$y = 84.681x^{-2.461} \qquad \textit{(equation 3.4)}$$

where x is the average of the 5 largest diameter (µm) Fe-rich droplets in each sample.

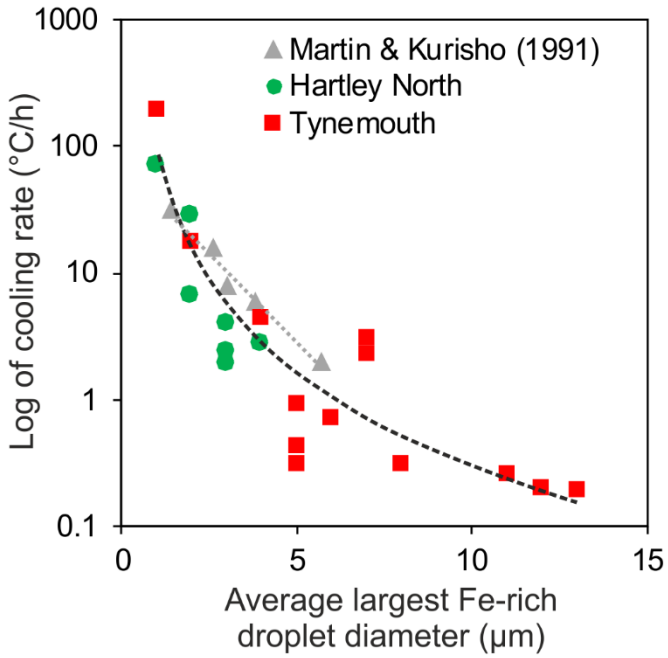

Figure 3.9 The relationship between Fe-rich droplet size (average of 5 largest droplets per sample) and the cooling rate (Table 3.3) for the Hartley North and Tynemouth Dykes. Data from the experiments of Martin and Kushiro (1991) are shown for comparison. The grey dots are for data from Martin and Kushiro (1991) with a trendline showing an exponential regression, while the black dashes are for the whole data set with a trendline showing a power law regression.

At fast cooling rates (>5°C/h) and low proportions of interstitial liquid as would be found on dyke margins (Table 3.3), the time to cool from the moment the remaining liquid intersected the binodal to the moment it cooled to the glass transition could be <60 h, based on the known apex temperature of the silicate liquid immiscibility binodal (1025°C; Charlier and Grove (2012)) and the glass transition

temperature (experimentally determined to be 725°C for a Kīlauea basalt; Ryan and Sammis (1981)). Note that this is likely a maximum estimate as the glass transition temperature increases with faster cooling rates (Giordano et al., 2005) and the Kīlauea Iki lava lake cooling rate was three orders of magnitude slower than that of even the central regions of the dykes studied here (Helz et al., 2014). The results of Honour et al. (2019) show that 60 h is insufficient time for Ostwald ripening of the Fe-rich droplets.

In the dyke centres, where cooling rates were slower and there was a higher proportion of interstitial liquid, the coarser droplet size may be a consequence of diffusive processes (either Ostwald ripening or droplet growth driven by chemical equilibration as the binodal widened down-temperature) and/or coalescence. Such diffusive processes may be accelerated by a decrease in viscosity of the Si-rich immiscible liquid caused by the presence of volatiles, prior to degassing (Kohn, 2000). I do not see rapid increases in the Fe-rich droplet size across the dyke width (Table 3.3), as would be expected if droplet coarsening were driven by coalescence, and hence I suggest that diffusion-controlled growth is the most probable coarsening mechanism, in agreement with the experimental results of Honour et al. (2019), who show that droplet coalescence is negligible in rapidly quenched ferrobasaltic experiments.

3.5.3.3 Microstructures

In many natural examples of rapidly-cooled basaltic rocks containing evidence of immiscibility, the faces of plagioclase grains parallel with the long axis of the grain (e.g. (100), (010)) and in contact with glass are not planar but are decorated with micron-scale pillar-like structures that are invariably enclosed by Fe-rich droplets of a slightly larger diameter (Philpotts, 1981b). No plagioclase pillars are observed in the dykes studied here, which is surprising given that Fe-rich droplets are attached to plagioclase grains in all three intrusions. Philpotts (1981b) suggests that pillar formation post-dates the attachment of the Fe-rich droplets, and that the presence of an Fe-rich droplet destabilises the plagioclase planar growth face, resulting in localised enhanced growth of plagioclase. The Fe-rich droplet has a lower viscosity than the surrounding Si-rich liquid and so rapidly diffuses material to the growing plagioclase face in comparison with diffusion rates through the higher viscosity Si-rich liquid (Philpotts, 1981b). From detailed study of these microstructures in experiments and natural examples (Honour et al., 2019), this hypothesis is supported by the enrichment of the pillars in elements with a low concentration in the Fe-rich immiscible liquid, such as Na, Al and Si (Veksler et al., 2006). On the dyke margins, the cooling rate was >10°C/h. This is faster than in the experimental studies and other natural samples (i.e. lava flows and lava lake crust; Charlier and Grove (2012)) and the absence of observable pillars in the marginal samples may be because the plagioclase growth rate (likely ~$5x10^{-12}$ m/s; Kirkpatrick (1977)) was too slow to permit pillar development before the system cooled through the glass transition. However, this cannot explain the absence of pillars in the centre of the dykes where cooling rates were slower. An alternative explanation may be that the nucleation of the Fe-rich droplets on the plagioclase growth faces occurred too late in the growth history for significant pillar formation.

3.6 Conclusions

1. Plagioclase aspect ratios and grain sizes are consistent with the magma in the Tynemouth and Hartley North Dykes being static, or only weakly convecting, during crystallisation.
2. 1D thermal modelling assuming conductive heat transfer suggests that the Hartley North (1.03 m wide), Tynemouth (3.18 m wide) and Morpeth (<5.25 m wide) Dykes took 5, 43, and <117 days to crystallise, respectively. This equates to cooling rates in the dyke centres of 0.1–1.7°C/h.
3. The emulsion microstructure varies as a function of cooling rate, both between intrusions and within individual intrusions. Slower cooling rates and increasing size of pockets of interstitial melt correlate with increasing Fe-rich droplet number density.
4. Both the largest Fe-rich droplet size and the range of droplet sizes increase at slower cooling rates. The size of the largest droplets and cooling rate are related by the expression $y = 84.681x^{-2.461}$. This study demonstrates that Fe-rich droplet size correlates with the cooling rate of igneous intrusions of similar compositions.

4 COMPOSITIONAL BOUNDARY LAYERS TRIGGER LIQUID UNMIXING IN A BASALTIC CRYSTAL MUSH

A version of this chapter is published as:

Honour, V.C., Holness, M.B., Charlier, B., Piazolo, S.C., Namur, O., Prosa, T.J., Martin, I., Helz, R.T., Maclennan, J. and Jean, M.M., 2019. Compositional boundary layers trigger liquid unmixing in a basaltic crystal mush. Nature Communications 10, 4821.

The Atom Probe Tomography data presented in this chapter was collected and initially processed by Prosa, T.J. and Martin, I. from CAMECA, who are co-authors on the manuscript. Interpretation of the results and subsequent processing was my own work. Co-authors and reviewers have provided comments on the manuscript.

4.1 Introduction

The unmixing of mafic magmas into immiscible pairs of Fe-rich and Si-rich conjugates was first identified in lunar samples (Roedder and Weiblen, 1970c) and subsequently in terrestrial volcanic and plutonic rocks (Charlier et al., 2013; De, 1974; Dixon and Rutherford, 1979; Jakobsen et al., 2005; Namur et al., 2012; Philpotts, 1979). Given the preferential partitioning of elements of economic interest into the Fe-rich conjugate (Veksler et al., 2006), a detailed understanding of the mechanisms by which significant differences in viscosity, density and wetting properties of the two liquids control the physical behaviour of the unmixed liquids in a crystal mush is essential to better understand the origin of ore deposits hosted in mafic bodies (Kolker, 1982; Nielsen et al., 2015; Ripley et al., 1998). Such an understanding is also vital to decode the processes responsible for the production of silicic melts by the differentiation of basalts.

Since solidified rocks do not generally preserve a record of parental melts, our ability to track the onset and evolution of magma unmixing has relied on experiments (Bogaerts and Schmidt, 2006; Charlier and Grove, 2012; Hou et al., 2018) and thermodynamic modelling (Ghiorso and Carmichael, 1980). In this study, I use microscale high-resolution imaging, electron probe microanalysis (EPMA), and nanoscale atom probe tomography (APT) to study a suite of samples from the 1959 Kīlauea Iki lava lake. The samples were drilled from the upper crust of the solidifying lava lake in 1976, 1979, 1981 and 1988 with each core reaching a different depth (Table 4.1; Fig. 4.1). These samples provide a unique opportunity to study the systematic evolution of unmixing during crystallisation in a natural system. The Kīlauea Iki sample suite (Fig. 4.2, 4.3) is complemented by additional examples of glassy tholeiitic basalts from the Laki eruption, Iceland (Neave et al., 2017; Passmore et al., 2012) and basalt flows from

the Snake River Plain (SRP), USA (Embree et al., 1976; Jean et al., 2018), which preserve similar microstructural evidence of immiscibility (respectively, Fig. 4.4, 4.5).

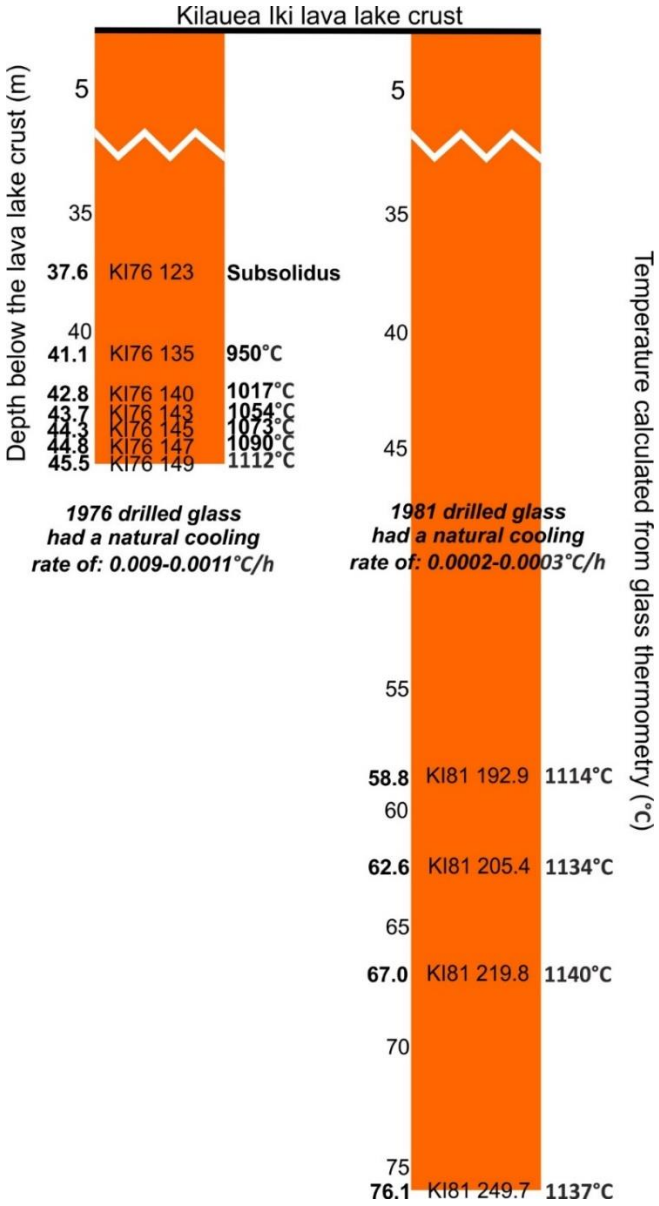

Figure 4.1 Depth and corresponding temperature immediately prior to drilling of the Kīlauea Iki lava lake sample suite from the 1976 and 1981 drill cores. As the Kīlauea Iki lava lake cooled, the isotherms in the lava lake crust moved downwards at a progressively slower rate (Barth et al., 1994; Helz et al., 2014). Consequently, the samples in the two drill cores each experienced a different cooling rate.

4.1.1 Principles of unmixing

The miscibility gap is defined by the binodal curve, which outlines a region on a phase diagram below which it is energetically favourable for a single-phase liquid to unmix (Fig. 1.1). Below the binodal, the spinodal defines the temperature-composition space in which there are no thermodynamic barriers to unmixing and infinitesimally small fluctuations in composition and density grow spontaneously by uphill diffusion (Cahn, 1961), leading to phase separation (Fig. 1.5). The interface between the two

phases is characterised by low amplitude concentration differences that sharpen with time (James, 1975). The two main mechanisms of unmixing of cooling liquids are therefore nucleation (either homogeneous or heterogeneous) below the binodal of droplets of the volumetrically minor phase or, if the liquid experiences a large, (near-) instantaneous undercooling, by spontaneous spinodal decomposition (Cahn, 1961). Crystal growth also occurs during cooling, with the possibility of the formation of compositional boundary layers in the immediately surrounding liquid, although the effect of this on unmixing has not previously been considered.

4.2 Samples analysed

4.2.1 Kīlauea Iki Lava Lake, Hawaii, USA

The Kīlauea Iki lava lake formed following the 14 November 1959 summit eruption (Helz, 1980). The lava ponded in a crater, forming a closed magma system of $40x10^6$ m^3. The lava lake was successively sampled through its 35 year crystallisation history. Much of the drilling was done through partially molten rock, meaning cooling water was pumped down alongside the drill bit to quench the samples. The samples studied are from the 1976-1, 1979-1, 1981, and 1988-2 drill cores (Table 4.1), which are 0.06m diameter and obtained using diamond bits. Coring resulted in 99% recovery (Table 4.2). The Kīlauea Iki lava lake samples chosen to characterise the Fe-rich compositional boundary layer (Fe-rich CBL) are cut from (or very close to) the base of each drill section, where the glass content was highest (Fig. 4.2, 4.3).

Table 4.1 Polished sections studied from the Kīlauea Iki lava lake (Y = sample was analysed with this technique).

Sample	Sample depth (m)	SEM	EPMA	APT
KI76 123	37.6	Y		
KI76 135	41.1	Y		
KI76 140	42.8	Y	Y	
KI76 143	43.7	Y	Y	
KI76 145	44.3	Y	Y	
KI76 147	44.8	Y	Y	Y
KI76 149	45.5	Y	Y	
KI79 197.3	60.1	Y		
KI79 202.0	61.6	Y		
KI81 192.9	58.8	Y	Y	
KI81 205.4	62.6	Y	Y	
KI81 219.8	67.0	Y	Y	
KI81 249.7	76.1	Y	Y	
KI88 266.6	81.3	Y		
KI88 300.0	91.4	Y		
KI88 336.3	102.5	Y		
KI88 354.9	108.2	Y		

Table 4.2 1976-1 drill core drilling schedule over the length of core studied (Helz 2018 pers. comm.).

Depth (m)	Core recovered (m)	Comments
32.0 – 35.1	3.0	-
35.1 – 38.1	3.0	-
38.1 – 41.1	3.0	-
41.1 – 42.8	1.6	KI 140 sample is from the bottom of this core.
42.8 – 44.3	1.5	KI 145 sample is from the bottom of this core.
44.3 – 45.5	1.2	KI 149 sample is from the bottom of this core.
45.5 – 46.0	-	Fragmental glass below 45.5 m.

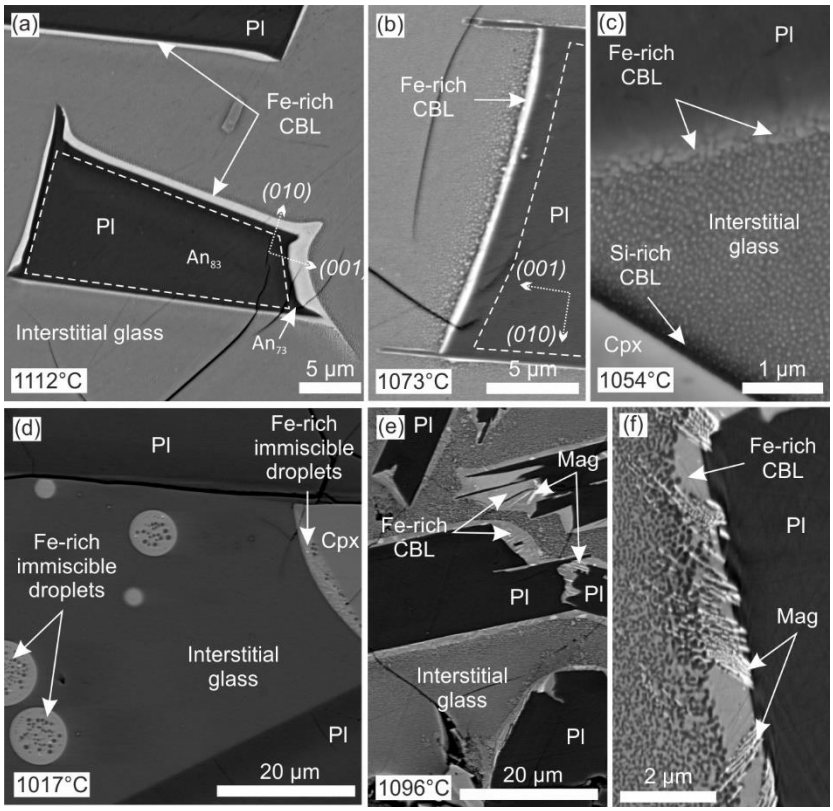

Figure 4.2 Compositional boundary layer morphology in BSE images, from samples of the 1976 Kīlauea Iki lava lake (a-d) The changing morphology of immiscible liquids in the 1976 drill core from the Kīlauea Iki lava lake, viewed in BSE images. (a) Plagioclase (Pl) lath surrounded by an Fe-rich compositional boundary layer sampled at 45.4m depth in the crust (quench temperature of 1112°C). (b) A thinner compositional boundary layer surrounding plagioclase (quench temperature of 1073°C) and the nanoemulsion is coarser. (c) At 43.7m depth (quench temperature of 1054˚C), the compositional boundary layer surrounding plagioclase is discontinuous and sub-micrometre thick. Note the presence of darker (more Si-rich) glass immediately surrounding pyroxene (Cpx) grains. The bulk of the glass comprises a nanoemulsion (not visible here). (d) Isolated and attached Fe-rich droplets in interstitial glass at 42.8m depth (quench temperature 1017°C). Note the Fe-rich liquid wets the pyroxene with a low wetting angle. (e) and (f) Compositional boundary layers surrounding plagioclase from Snake River Plain tholeiites. The calculated natural quench temperature of this sample is 1096°C. Note the oxide dendrites within the compositional boundary layer and partially embedded in the plagioclase.

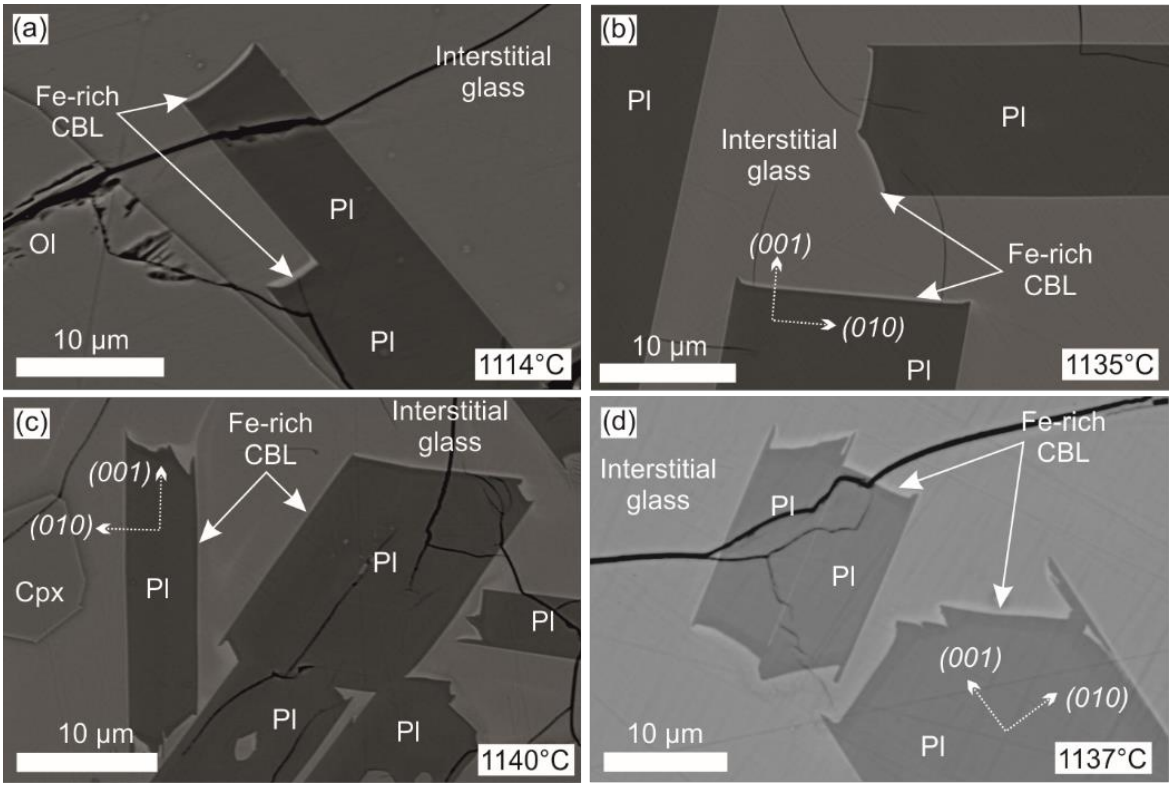

Figure 4.3 The physical behaviour of immiscible liquids from the 1981 drill core from the Kīlauea Iki lava lake. (a) BSE image of plagioclase (Pl), and olivine (Ol), surrounded by interstitial glass with an Fe-rich compositional boundary layer around the plagioclase grain, quenched from 1114°C during drilling. (b) Well-formed plagioclase grains, surrounded by an Fe-rich compositional boundary layer (CBL). The Fe-rich CBL is thicker in the fastest growth direction of the plagioclase on the (001) face. Note the homogeneity of the interstitial glass, quenched from 1135°C during drilling. (c) Plagioclase laths surrounded by an Fe-rich compositional boundary layer and clinopyroxene (Cpx) surrounded by a Si-rich compositional boundary layer, quenched from 1140°C during drilling. (d) Plagioclase grains with swallow-tail terminations extending from the (001) face. The plagioclase grains are surrounded by an Fe-rich compositional boundary layer, within the interstitial glass quenched from 1137°C during drilling.

4.2.2 Laki Lava Flow, Iceland

The Laki polished section (LAK04; Fig. 4.4) is from episodes VI–X of the 1783–1784 CE basaltic Laki eruption in Iceland, for which the lava flow discharged from fissure VII. It was collected at c. 15 km from the source vent, and underwent sufficiently fast cooling rate to form a glassy rind. Further details can be found in Neave et al. (2013); Passmore et al. (2012).

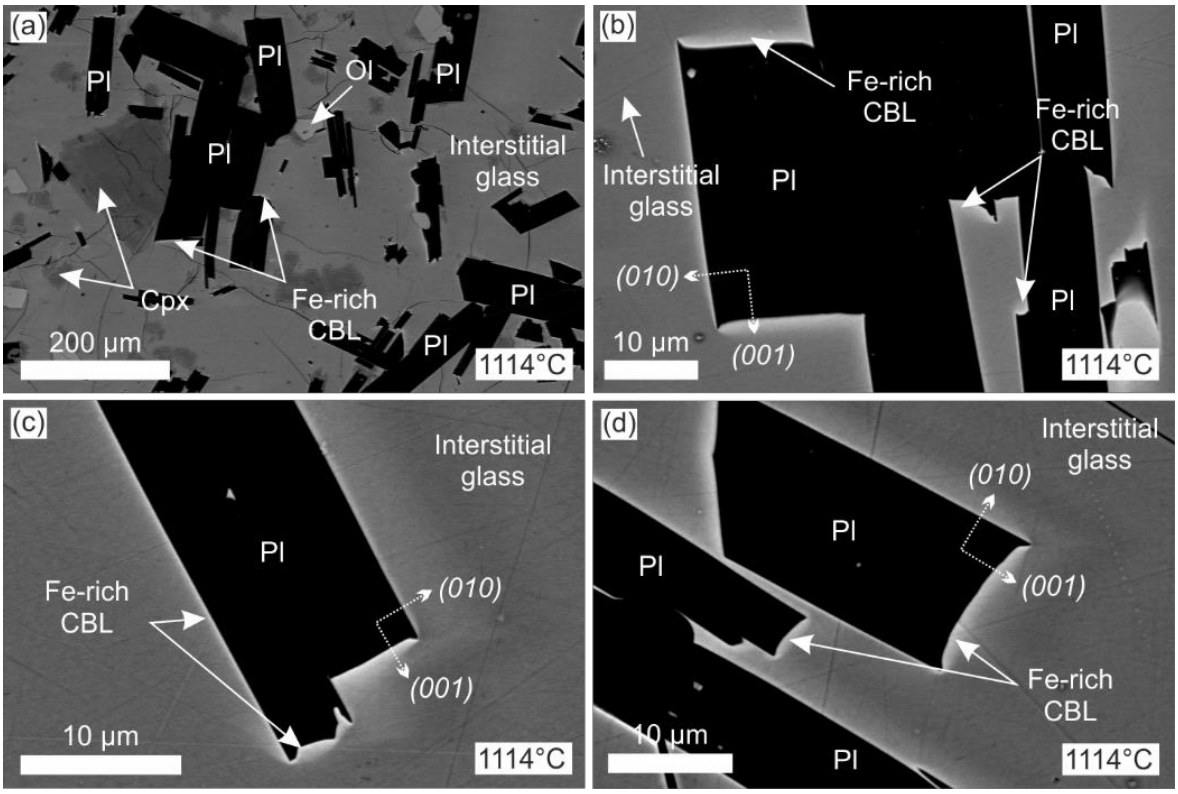

Figure 4.4 The physical behaviour of immiscible liquids from the Laki eruption, Iceland, preserved by natural quench. (a) An overview of the sample, showing plagioclase (Pl), clinopyroxene (Cpx) and olivine (Ol), representative of the residual liquid at 1114°C. (b), (c), (d) Plagioclase laths surrounded by a diffuse Fe-rich compositional boundary layer (CBL) representative of the residual liquid at 1114°C; the Fe-rich CBL is thicker in the fastest growth direction of the plagioclase on the (001) face.

4.2.3 Snake River Plain Basalt (SRP), USA

The samples studied are from the Snake River volcanic province in southern Idaho, USA, from the Sugar city drill core through the basalt flows (Fig. 4.5; Table 4.3). These flows contain many glassy horizons. Further information is available in Embree et al. (1978); Jean et al. (2018).

Table 4.3 Polished sections studied from the Snake River Plain tholeiites (Y = sample was analysed with this technique).

Sample depth from core top (m)	SEM	EPMA
90.8	Y	
91.3	Y	
91.5	Y	Y
91.7	Y	Y
95.9	Y	

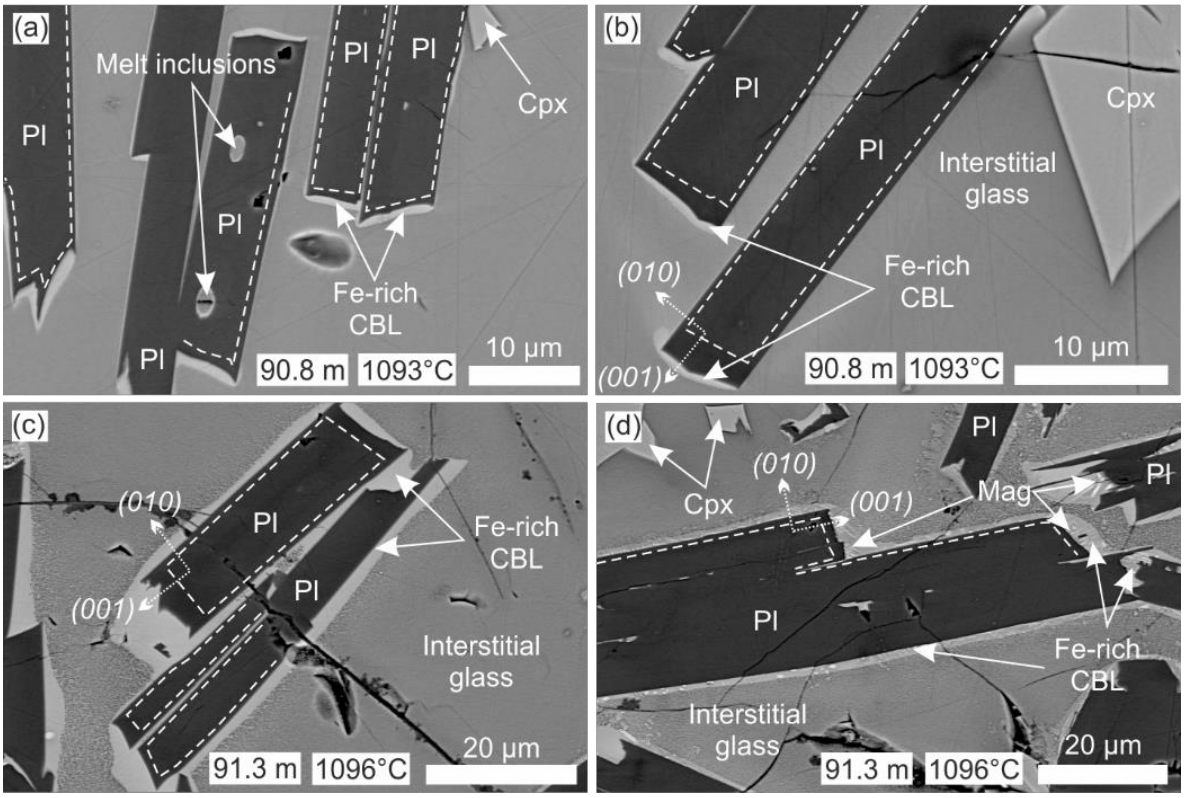

Figure 4.5 The physical behaviour of immiscible liquids from the naturally quenched Snake River Plain basaltic flow, USA, sampled from the Sugar City Exploration Well, Idaho. (a) Plagioclase (Pl) laths surrounded by an Fe-rich compositional boundary layer (CBL). Note the melt inclusions hosting a nanoemulsion of immiscible liquids. Temperature is determined by glass thermometry (see Methods). The Fe-rich CBL is thicker in the fastest growth direction of the plagioclase on the (001) face. (b) Plagioclase laths surrounded by an Fe-rich CBL representative of the residual liquid at 1093°C. Note the darker (i.e. more silicic) glass surrounding the pyroxene (Cpx). (c) Plagioclase laths surrounded by an Fe-rich CBL, representative of the residual liquid at 1096°C. (d) Plagioclase laths surrounded by an Fe-rich CBL, representative of the residual liquid at 1096°C. Note the magnetite crystals nucleated on the plagioclase surface and growing through the Fe-rich CBL.

4.3 Methods

4.3.1 Scanning electron microscopy (SEM)

Samples were characterised using microscopy and a Quanta FEG 650 F SEM for semi-quantitative mineral compositions, element EDS X-ray maps and backscatter electron (BSE) imagery, set to 10 kV at spot 3, with a working distance of 10 mm at the Department of Earth Sciences, University of Cambridge. The BSE imaging of the interstitial liquid (to identify whether it is comprised of a nanoemulsion), is at the spatial resolution limits of the SEM. Plagioclase aspect ratio, outer growth rim thickness and Fe-rich compositional boundary layer thickness were measured using BSE images.

4.3.2 Electron probe micro-analysis (EPMA)

Glass and plagioclase mineral compositions were measured by EPMA using a CAMECA SXFiveFE with five WDS spectrometers at the Department of Geology, Mineralogy and Geophysics, Ruhr-Universität Bochum and a CAMECA SX-100 with five WDS spectrometers at the Department of Earth

Sciences, University of Cambridge, both using PeakSight software with ZAF correction. The glass analytical routine was run at 15 kV and 8 nA with a 2 µm beam; the plagioclase analytical routine was run at 15 kV and 15 nA with a 2 µm beam. Appropriate glass and silicate mineral secondary standards were analysed. Analyses of Fe-rich immiscible droplets and Fe-rich compositional boundary layers were challenging due to the small area presented (<25 µm²) and the unknown 3D shape creating uncertainty about the electron beam interaction volume (this was modelled using *Casino v2.48* software (Drouin et al., 2007); Fig. 4.6). This means that the Fe-rich conjugate analyses may have a component of mixing with the Si-rich conjugate due to the minimum volume with which the probe beam interacts. In the Kīlauea Iki lava lake sample from the 1976 drill core at 45.5 m depth below the lake surface, three continuous EPMA line profiles were taken across the glass, extending 50 µm from the Fe-rich CBL surrounding the plagioclase (Appendix Table 4.C). Likewise, in a sample from 44.8 m depth below the Kīlauea Iki lava lake surface, five continuous EPMA profiles were collected outwards from the Fe-rich CBL for comparison with atom probe tomography analyses (see section 4.3.5).

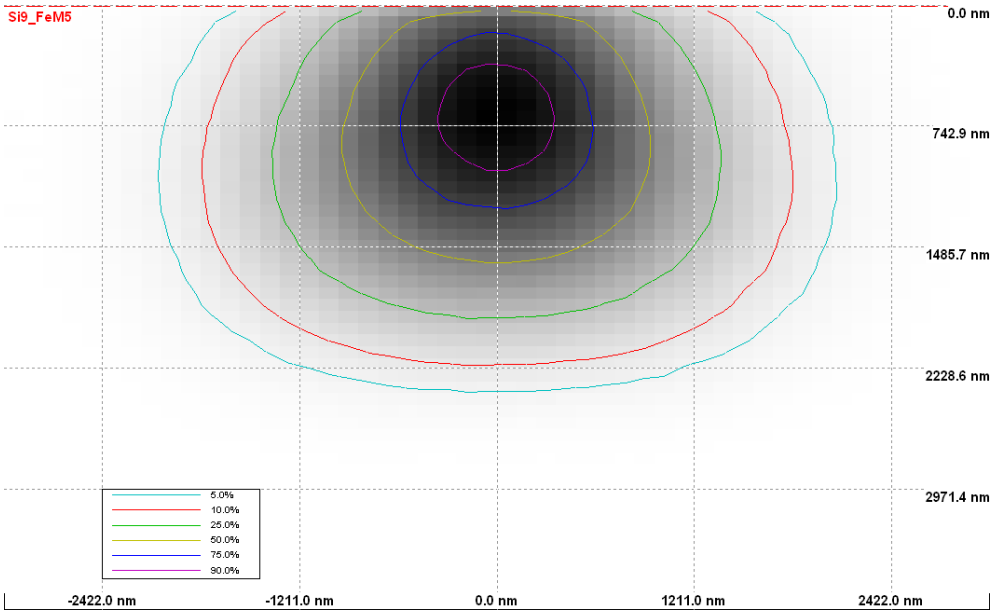

Figure 4.6 The modelled interaction volume of a 2 µm, 15 kV focused electron beam interacting with an Fe-rich homogeneous glass, calculated using *Casino v2.48 software*.

4.3.2.1 Glass Thermometry

For consistency, liquid temperature estimates for the samples from Laki, Snake River Plain and Kīlauea Iki were recalculated using MgO glass compositions from EPMA and the relationship T (°C) = $26.3MgO^{liq}$ + 994.4°C (Putirka, 2008) and where possible, checked against published values (Guilbaud et al., 2007; Helz and Thornber, 1987). This equation was developed from previous geothermometry work based on samples drilled from the Kīlauea Iki lava lake. All temperatures referred to are the pre-quench temperature of the liquid.

4.3.3 Plagioclase growth rates

The rate of plagioclase growth in directions parallel to (010) is calculated from the slope of plots of the largest long axis plagioclase crystal in each sample versus time (following Kirkpatrick, 1977). Time is determined by assuming a constant cooling rate for samples from the KI76 drill core (of 0.001°C/h; Helz et al. (2014)) from the onset of plagioclase nucleation at 1163°C (Helz, 1987) to the calculated temperature of the sample. The growth rate is an estimate as I assume that there is a constant cooling rate, when in reality the movement of the lava lake isotherms progressively changed the slope of the geotherm (Barth et al., 1994; Helz et al., 2014), resulting in a non-linear cooling rate. The growth rate of plagioclase is anisotropic; the crystals in the lava lake are euhedral, growing in a melt-rich environment, so rapid growth in directions parallel to (010) resulted in limited impingement on adjacent grains (Fig. 4.7). To account for the crystal growth in two directions, the growth rate is halved (Kirkpatrick, 1977). There are many sources of error including those associated with measuring the plagioclase long axis, determining the largest crystal and converting temperature differences to time scales.

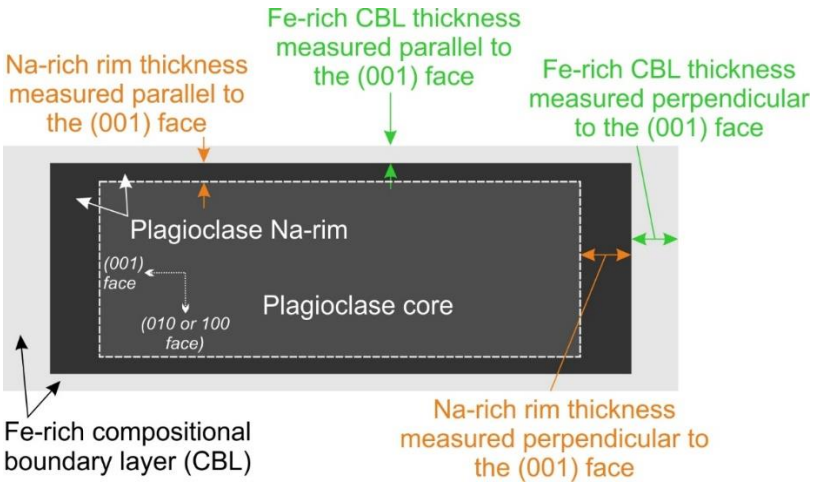

Figure 4.7 A schematic diagram showing a plagioclase grain surrounded by an Fe-rich compositional boundary layer.

4.3.4 Sample preparation for Atom Probe Tomography (APT)

A dual-beam focused-ion-beam (FIB) scanning electron microscope (FEI Helios 660 with EasyLift™ micromanipulator) was used to fabricate APT specimens. Standard lift-out methodology was used to transfer material wedges from the sample to a micro-tip-array carrier-coupon (Miller et al., 2007). Specimens were sharpened using standard annular milling methods (Larson et al., 1999) with an additional low energy milling step (Thompson et al., 2006).

4.3.5 APT measurements and analysis

Twenty APT tips were analysed at CAMECA Instruments Inc., Madison, Wisconsin, USA, from specimens prepared from a sample taken at 44.8 m depth in the 1976 drill core from the Kīlauea Iki lava lake (1090°C; Helz and Thornber (1987)). Fourteen APT specimens examined the interstitial glass

on a 14 μm long traverse away from a plagioclase grain. Additionally, six APT specimens were analysed of plagioclase and the Fe-rich CBL.

The measurements were performed on a LEAP® 5000 XR in laser-pulse mode. Typical analysis conditions used by CAMECA were: specimen base temperature of 30 K, constant detection rates between 5–10 ions per 1000 pulses, a laser pulse energy of 200 pJ, a pulse frequency set to achieve 2000 Dalton, and a time-of-flight range typically 125-250 kHz. Standard IVAS^{TM} shank reconstruction was used for all reported data (Larson et al., 2013). For one of the analyses completed before specimen failure, the SEM-measured analysis depth was used to calibrate the APT tip reconstruction. These reconstruction parameters were subsequently used for all reconstructions.

It is important to note that APT is most suitable for *relative* compositional data rather than absolute compositional data due to issues with mass ranging and efficiency of recovery during analysis (Exertier et al., 2018).

IVAS^{TM} 3.8 was used to extract linear 1D concentration profiles from within sub-volumes of the three-dimensional datasets. Profiles were taken across the Fe- and Si-rich immiscible conjugate boundaries of the nanoemulsion parallel with the analysis direction (z-axis) of the glass tip to ensure maximum spatial resolution and prevent artificial features. To delineate these immiscibility boundaries, a 6 at. % Fe atomic concentration isosurface was constructed to define the Fe-rich phase of the nanoemulsion i.e. the shape/morphology of the Fe-rich immiscible conjugate of the nanoemulsion. The data for these linear 1D compositional profiles stem from an elongate bar with a square profile of 10 nm by 10 nm. This enabled me to choose 1D profiles that were perpendicular to the interface of the Fe- and Si-rich immiscible conjugate boundaries and minimise any "smearing" artefacts in the compositional profiles.

4.4 Results

4.4.1 Occurrence of crystal compositional boundary layers

All samples studied contain macrocrysts (>0.5 mm) of clinopyroxene and olivine in a groundmass of plagioclase 100–300 μm microcrysts (Helz, 1980; Neave et al., 2017; Passmore et al., 2012) and glass (compositions are presented in Appendix Table 4.A). The modal percentage of glass increases linearly with increasing depth in the upper crust of the Kīlauea Iki lava lake; in the 1976 drill core the modal glass percentage increases from 14.3% at 42.8 m depth to 44.4% at 45.5 m (Barth et al., 1994). In samples from the three localities, optimising the contrast-brightness in BSE images at high magnification reveals that plagioclase grains are surrounded by a continuous compositional boundary layer (CBL; Zellmer et al. (2016)), which is enriched relative to the bulk melt with elements incompatible in plagioclase, chiefly Fe, with Mg, P, Mn and Ti. The Fe-rich CBLs are compositionally similar to the Fe-rich immiscible liquid analysed in experimental and natural sample studies (Fig. 4.8)

(Fig. 4.8; Charlier and Grove, 2012; Honour et al., 2019; Krasov and Clocchiatti, 1979; Philpotts, 1981a; Philpotts, 1982; Ryabov, 1989; Veksler et al., 2007).

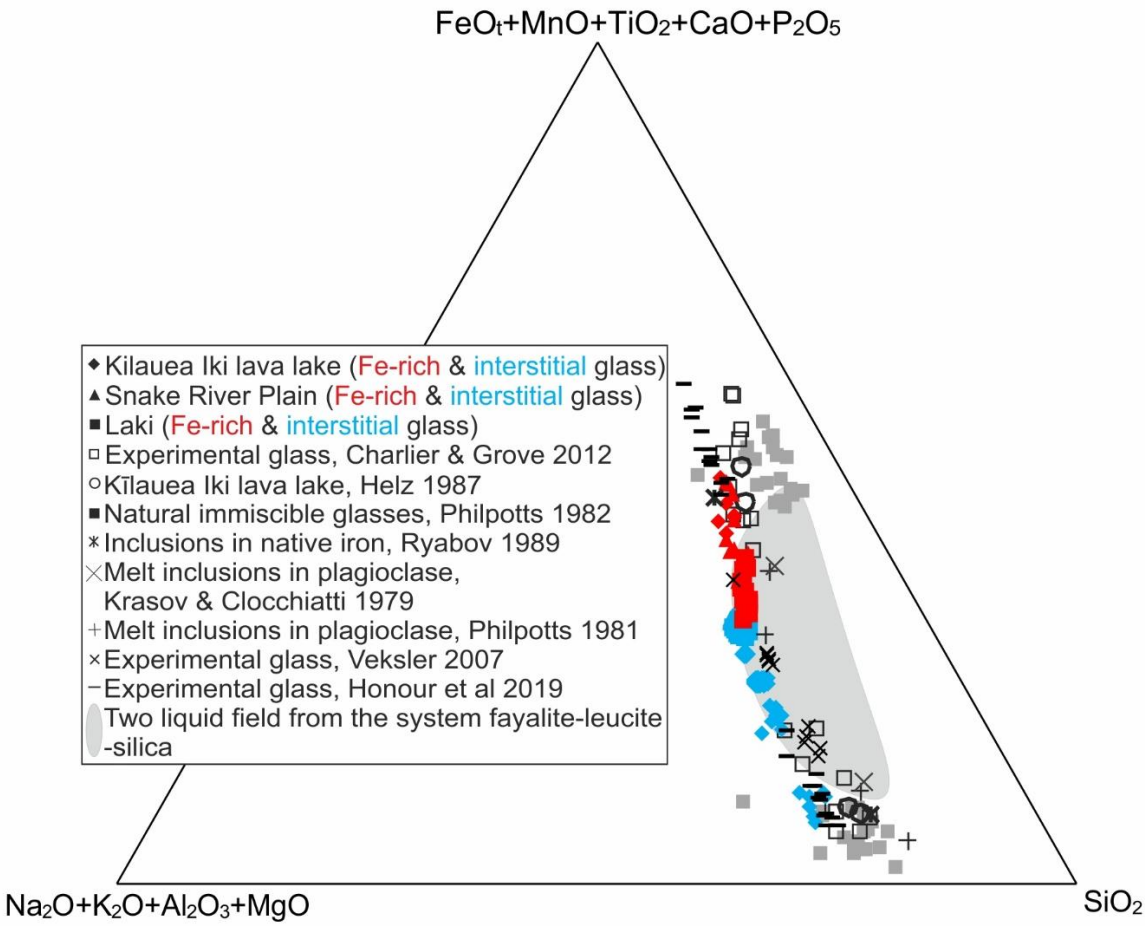

Figure 4.8 Plot of the composition of Fe-rich and Si-rich immiscible liquids preserved as glassy droplets in a range of tholeiitic volcanic rocks, melt inclusions, and experiments. The light grey area is the two-liquid field from the fayalite-leucite-silica system. EPMA compositions determined for this study are overlaid; the Fe-rich compositions are plotted in red, while the surrounding interstitial glass is plotted in blue.

I examined samples from the 1976 Kīlauea Iki drill core at progressively shallower depths (between 45.5 m–37.6 m) to trace the temporal evolution of the Fe-rich CBLs. Pre-quench temperatures range from 1112˚C to sub-solidus, based on glass thermometry, with absolute calibration uncertainties of ± 8°C (Helz and Thornber, 1987; Putirka, 2008; Appendix Table 4.A). Plagioclase crystallisation commenced at 1163°C (Helz, 1987; Helz et al., 2014). As the Kīlauea Iki lava lake cooled, the isotherms moved downwards in the lava lake crust (Barth et al., 1994; Helz et al., 2014) and cooling rates decreased with time. Hence, the cooling rates experienced by specific core samples strongly depend on where (and when) they were collected. Samples studied from the 1976 Kīlauea Iki drill core cooled at 0.009–0.011°C/h, whereas samples from the 1981 and 1979 drill cores cooled at a slower rate (0.0002–0.0003°C/h; Fig. 4.1; Helz et al., 2014).

The Kīlauea Iki plagioclase is typically well-facetted (Fig. 4.2, 4.3), indicating interface-controlled growth (Kirkpatrick, 1975). It is normally zoned (with a maximum compositional difference of ~10

mol. % An (Helz, 1987)), generally exhibiting a core and a well-defined relatively Na-rich rim (identifiable in EDS and BSE images). The thickness of the Fe-rich CBL varies from 0.5–2.5 µm and is thickest on the fastest growing faces of the grain, which are those perpendicular to (010) (Fig. 4.2a, b; Fig. 4.7). The aspect ratio of the Fe-rich CBL (defined as the ratio of the thickness of the CBL on the faces perpendicular to (010) and the thickness of the CBL on the (010) faces) positively correlates with the aspect ratio of the plagioclase Na-rich rim (defined as the ratio of the rim thickness on the faces perpendicular to (010) and the rim thickness on the (010) faces; Fig. 4.9). Both these aspect ratios decrease upwards towards the lava lake surface.

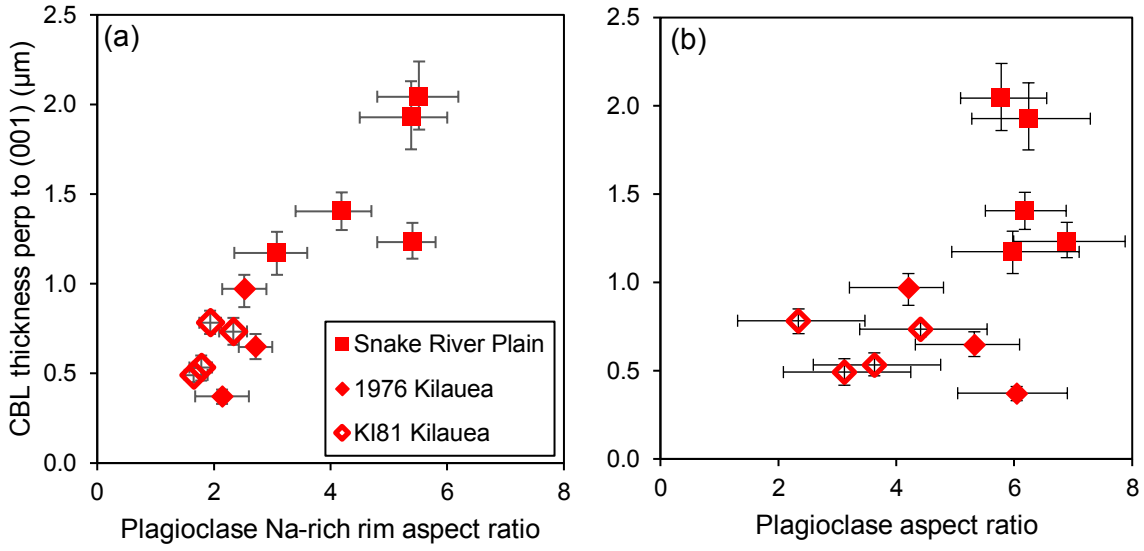

Figure 4.9 (a) The average aspect ratio of the Na-rich rims on the plagioclase compared with the thickness of the Fe-rich compositional boundary layer (CBL) perpendicular to (001) crystal face for samples from Snake River Plain (SRP), and the 1976 and 1981 Kīlauea Iki lava lake drill cores. (b) Average overall aspect ratio of plagioclase grains against Fe-rich compositional boundary layer (CBL) perpendicular to (001) crystal face. Uncertainties were determined by the bootstrap method. This data is plotted from Appendix Table 4.B.

The Fe-rich CBL is most noticeable, being both continuous and homogeneous, in samples collected deeper than 44 m (>20% glass) in the Kīlauea 1976 drill core. At 43.7 m (1054°C), the Fe-rich CBL is discontinuous, comprising sub-micron Fe-rich droplets surrounded by a continuous Si-rich phase (Fig. 4.2c). By 42.8 m (1017°C), Fe-rich CBLs are absent and evidence of immiscibility is confined to apparently isolated pockets of glass (generally 1–3 mm² in 2D) in which 5–10 µm diameter Fe-rich droplets are attached to plagioclase with a high apparent wetting angle (>100°; Fig. 4.2d), together with isolated Fe-rich droplets of comparable diameter dispersed within the Si-rich continuous phase. Locally, at 42.8 m (1017°C), Fe-rich droplets adhere to pyroxene grains with a low apparent wetting angle (<40°; Fig. 4.2d).

In samples with thick, >1 µm, Fe-rich CBLs (i.e., the deeper 1976 drill core samples; Fig. 4.10a) the contact between the Fe-rich CBL and the interstitial glass appears gradational over 3–6 µm in BSE

images, with the margin of the Fe-rich CBL comprising an emulsion of Fe-rich immiscible droplets dispersed in a Si-rich continuous phase: the Fe-rich droplets fine away from the Fe-rich CBL. Shallower drill core samples with thinner Fe-rich CBLs, exhibit a sharp contact between the Fe-rich CBL and the surrounding interstitial glass (Fig. 4.2b). Plagioclase grains in the deepest sample studied (45.5 m) have prominent spines, <25 μm long, extending in the direction of fastest growth (Fig. 4.2a,b), and these indicate a period of diffusion-limited growth (Cahn, 1967). The spines are rarer and shorter (<1 μm long) in shallower samples with thinner Fe-rich CBLs. Pyroxene is surrounded by a 1–2 μm wide Si-rich compositional boundary layer (Si-rich CBL) which, although less well developed than the Fe-rich CBL around plagioclase, mirrors the attributes of the latter.

While each sample experienced the same rate of quenching, the character of the Fe-rich CBL systematically evolves through the 1976 and 1981 Kīlauea Iki drill cores. Hence, the formation of the CBL cannot be related to drilling-induced quenching. This interpretation is supported by the observations that: (i) plagioclase grains are surrounded by an Fe-rich CBL regardless of their position relative to the drill core edge (and therefore the rate of quenching); (ii) the Na-rich plagioclase rim width correlates with Fe-rich CBL thickness (Fig. 4.9a); (iii) the Na-rich rim aspect ratio is consistent with slower growth than that expected during a quench (Holness, 2014); and (iv) locally, the Fe-rich CBL contains dendritic crystals of oxide partially embedded in the plagioclase substrate, consistent with simultaneous oxide and plagioclase growth (Fig. 4.2e, f).

Similar Fe-rich CBL microstructural features are observed in the glass of the SRP tholeiites from the Sugar City drill core, and in the Laki samples preserved by a natural "quench" as the lava flows cooled rapidly through the glass transition temperature (Fig. 4.4, 4.5). This occurred at temperatures between 1093°C to 1096°C for the SRP basalts and at 1114°C for the Laki sample (based on glass thermometry; Putirka (2008)) comparable to the drill-related quenching of the 1981 Kīlauea Iki drill core samples at 1114 – 1140°C (Helz and Thornber, 1987). In the 1981 Kīlauea Iki drill core, the Fe-rich CBL is thin yet well-defined, thinning with decreasing drill core depth over 8.2 m, from an average of 0.8 to 0.5 μm for the Fe-rich rim perpendicular to the (001) plagioclase face (Fig. 4.10c). The SRP Fe-rich CBL is well-defined, thinning with decreasing drill core depth over 5 m, from 2.0 to 1.5 μm for the Fe-rich rim perpendicular to the (001) plagioclase face (Fig. 4.5; 4.10b), while the Laki sample has more diffuse, thinner Fe-rich CBLs (~0.7 μm; Fig. 4.4).

4.4.2 Kīlauea Iki glass compositions

With decreasing depth in the 1976 drill core relative to the lake surface, SiO_2 concentrations of the apparently homogeneous bulk liquid increase from 50 to 65 wt.%, while FeO_{total} concentrations decrease from 12 to 5 wt.% (Fig. 4.11). Correspondingly, the FeO concentration of the Fe-rich droplets increases with decreasing depth: at 45.5 m (1112°C) the average FeO concentration is 21 wt.%, increasing to 27 wt.% at 42.8 m depth (1017°C), consistent with published compositions for immiscible liquids (Fig.

4.8; Charlier and Grove, 2012). There is no change in the crystal assemblage associated with these variations in glass composition. Furthermore, because the Kīlauea Iki lava lake system was open with respect to H_2O and had a confining pressure typically less than 6 bars (Helz et al., 2014), the observed compositional variations cannot have resulted from variations in either H_2O content or pressure.

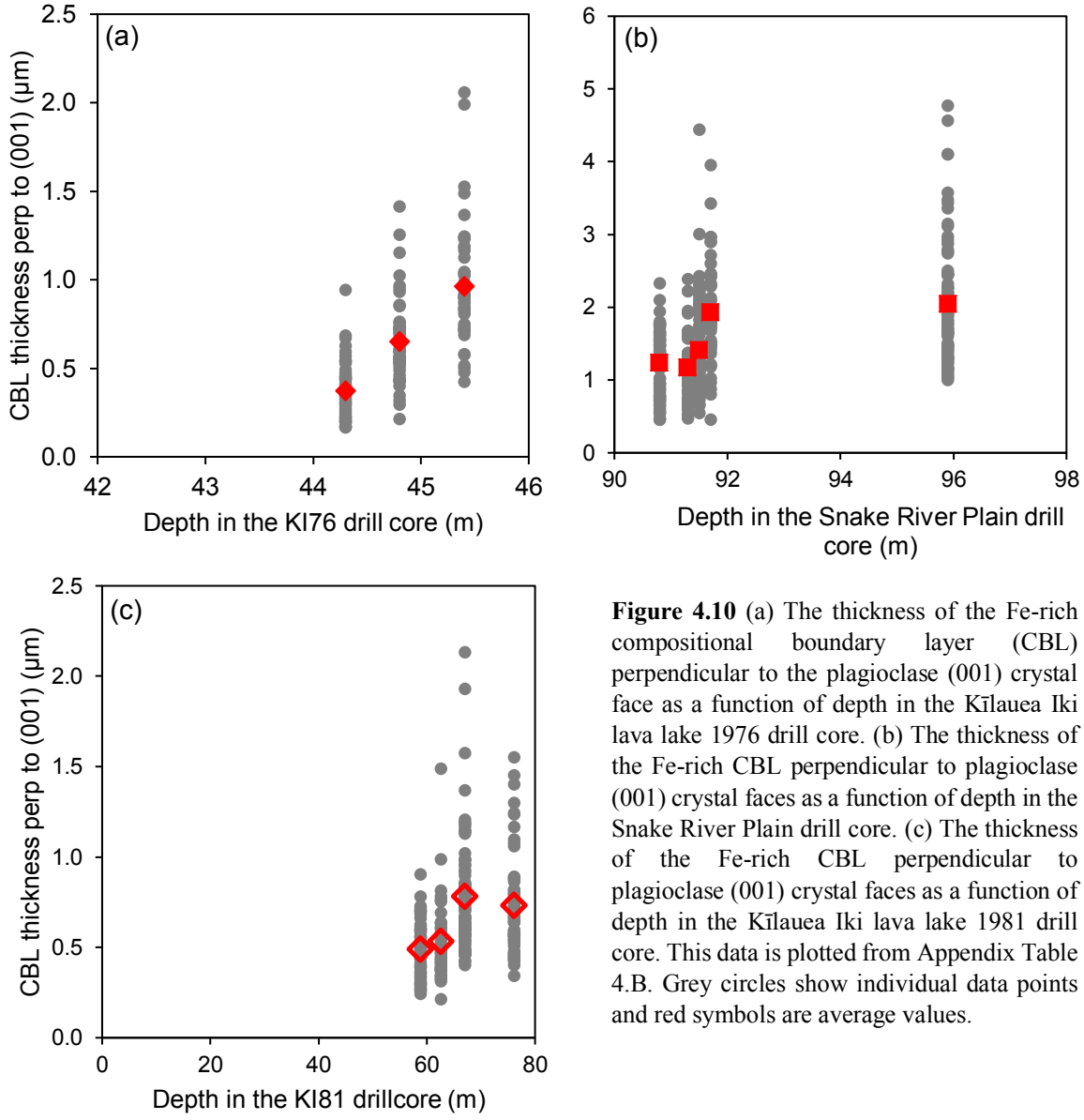

Figure 4.10 (a) The thickness of the Fe-rich compositional boundary layer (CBL) perpendicular to the plagioclase (001) crystal face as a function of depth in the Kīlauea Iki lava lake 1976 drill core. (b) The thickness of the Fe-rich CBL perpendicular to plagioclase (001) crystal faces as a function of depth in the Snake River Plain drill core. (c) The thickness of the Fe-rich CBL perpendicular to plagioclase (001) crystal faces as a function of depth in the Kīlauea Iki lava lake 1981 drill core. This data is plotted from Appendix Table 4.B. Grey circles show individual data points and red symbols are average values.

EPMA profiles extending 50 µm outwards from the Fe-rich CBL (at 45.5 m) show constant SiO_2 concentrations, whereas oxides such as FeO, TiO_2 and MgO are depleted in a 10 µm wide zone adjacent to the Fe-rich CBL (Fig. 4.12); these are oxides that preferentially partition into an Fe-rich immiscible liquid (Schmidt et al., 2006). In the same 10 µm wide zone there is a small increase in elements such as Al_2O_3 and Na_2O; these are oxides that preferentially partition into a Si-rich immiscible liquid. This chemical concentration pattern is expected for the formation of a two-phase mixture by nucleation and growth (Fig. 1.5; Findik, 2012).

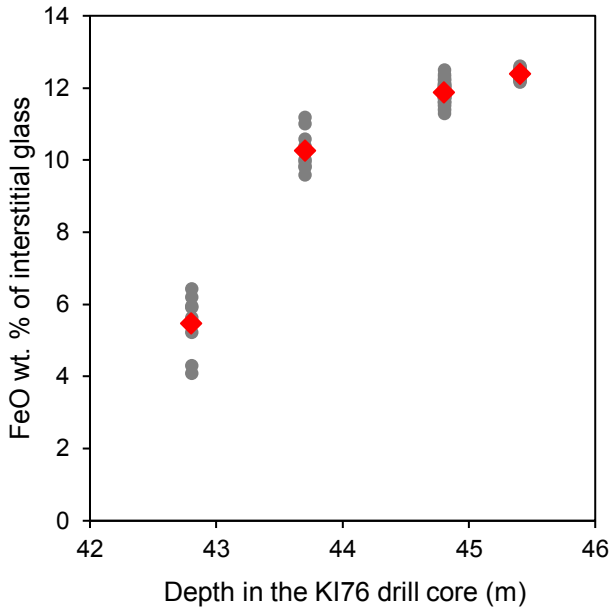

Figure 4.11 The FeO_{total} concentration (wt.%) of interstitial glass as a function of depth in the Kīlauea Iki lava lake 1976 drill core (the data is plotted from Appendix Table 4.A). Grey circles are individual data points and red diamonds are average values.

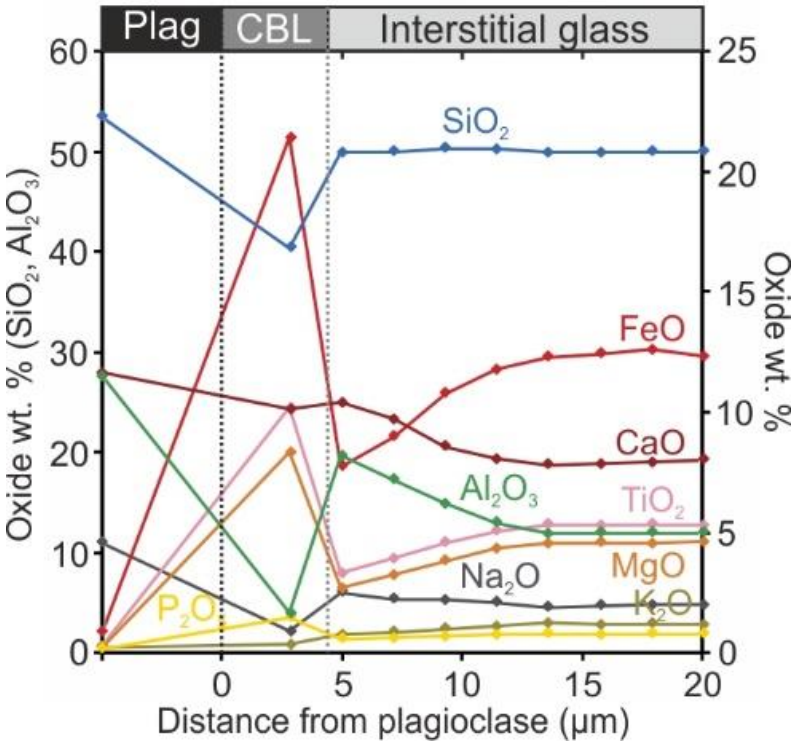

Figure 4.12 A micron-scale compositional transect obtained using EMPA through Si-rich glass adjacent to an Fe-rich CBL. Sample from the crust of the Kīlauea Iki lava lake, sampled from the 1976 drill core at 45.5 m (quench temperature of 1112°C). Note the two different scales depending on element.

4.4.2.1 Atomic scale chemical and spatial characteristics

Three-dimensional APT reconstructions of compositional data (Fig. 4.13) of the Kīlauea Iki lava lake 1976 drill core sample from 44.8 m (1090°C; Helz and Thornber (1987)) show that the Fe-rich CBL surrounding plagioclase grains is internally homogeneous (Fig. 4.14), with a sharp contact against

plagioclase (Fig. 4.15) and a diffuse contact over 10 nm with the adjacent liquid (Fig. 4.16; Appendix Table 4.D). There is no marginal Fe-enrichment of the plagioclase, even at the nanoscale (Fig. 4.15). The Fe-rich CBL is rich in those elements expected to preferentially partition into an Fe-rich immiscible liquid (Bogaerts and Schmidt, 2006). The APT compositional data shows distinct jumps between the different components with no indication of diffusion-related elemental profiles (Fig. 4.16), therefore I discount significant post-solidification diffusion of elements between the two glasses.

EPMA traverses across the interstitial liquid surrounding the Fe-rich CBLs (from the same sample at 44.8 m) show a homogeneous composition (Appendix Table 4.C). At the greater spatial resolution provided by the APT it is evident that the interstitial liquid (up to 14 μm away from the Fe-rich CBL; Fig. 4.13) is actually a nanoemulsion in which the Fe-rich immiscible liquid forms branch-like interconnected structures and isolated clusters within the continuous interstitial liquid. The Fe-rich immiscible liquid is separated from the interstitial liquid by sharp boundaries (glass tip 179377, shown in Fig. 4.16), with no quantifiable spatial variations in morphology, composition, size or spacing. Concentrations of Si increase within 2–4 nm of the nanoemulsion phase boundary on the Si-rich side; likewise, Fe concentrations increase on the Fe-rich side (Fig. 4.16). Importantly, these compositional features are present regardless of the size of the individual regions; they are consistent with spinodal decomposition (Findik, 2012).

The Fe-rich CBL and the Fe-rich immiscible liquid of the nanoemulsion are largely similar in composition, but the Fe-rich CBL is depleted in Al and Na relative to the Fe-rich immiscible liquid of the nanoemulsion: the Al and Na concentration of the Fe-rich immiscible liquid of the nanoemulsion lies on a mixing line between plagioclase and the Fe-rich CBL (Fig. 4.17; Appendix Table 4.A and 4.D).

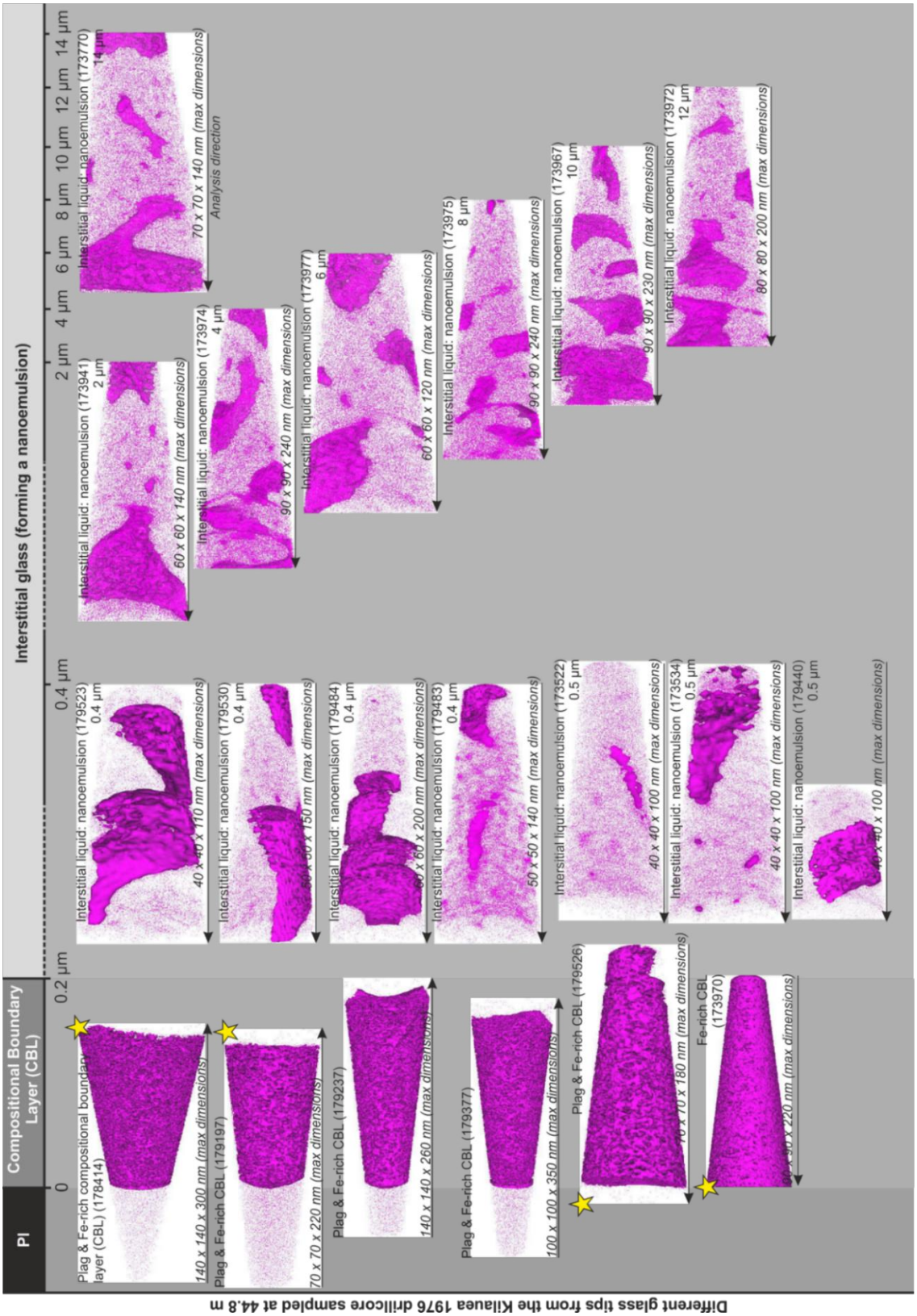

Figure 4.13 Three-dimensional reconstruction of APT data from twenty glass tips analysed across a plagioclase grain, its adjacent Fe-rich CBL and the surrounding interstitial liquid (comprised of a nanoemulsion) in a sample from Kīlauea Iki lava lake 1976 drill core, quenched from ~1090°C during drilling at a depth of 44.8 m. Each dot represents a single atom, but not all atoms are shown. The yellow star denotes samples shown in Fig. 4.14 and 4.15.

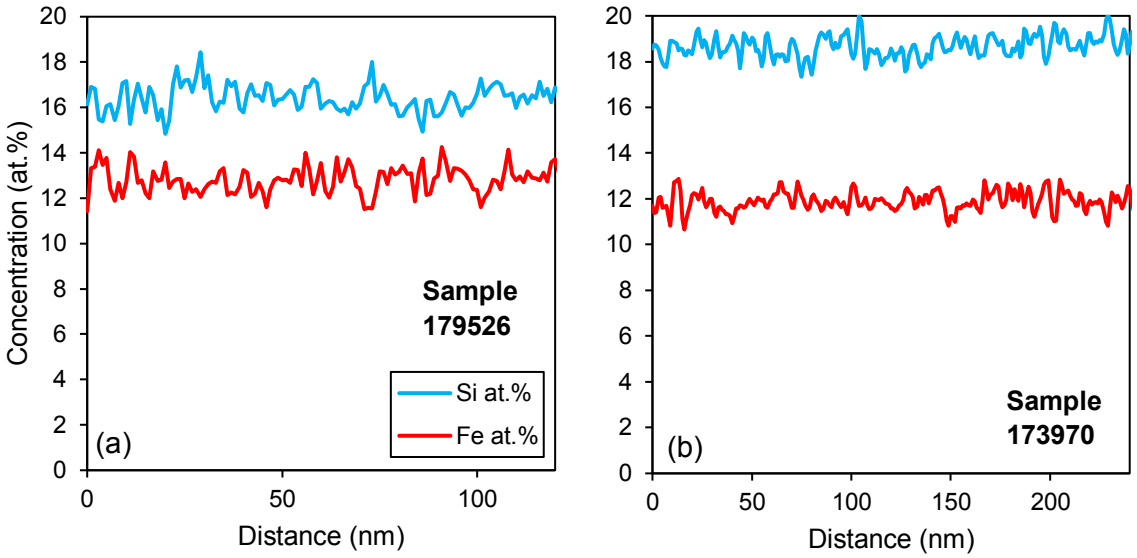

Figure 4.14 APT relative compositional data for sample (a) 179526, (b) 173970, for Si at.% and Fe at.% across the Fe-rich compositional boundary layer sampled by those glass tips in Fig. 4.13 that are marked with a yellow star. The two samples are taken from the Kīlauea Iki lava lake 1976 drill core, quenched from ~1090°C during drilling at a depth of 44.8 m. The standard deviations across the Fe-rich CBL for each are 0.6 and 0.6, respectively. Data points are plotted at 1 nm distances; however, for clarity the data markers have been removed.

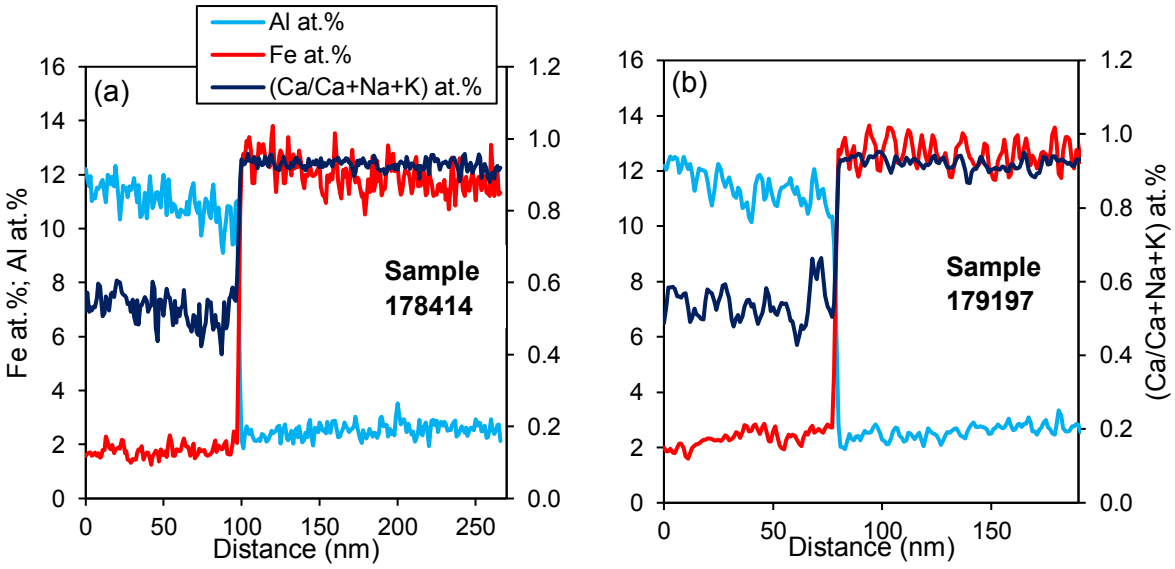

Figure 4.15 APT relative compositional data for sample (a) 178414, (b) 179197, for Al at.%, Fe at.%, and (Ca/Ca+Na+K) at.% across the margin of a plagioclase grain surrounded by an Fe-rich CBL – see glass tips in Fig. 4.13 that are marked with a yellow star. Sample is taken from the Kīlauea Iki lava lake 1976 drill core, quenched from ~1090°C during drilling at a depth of 44.8 m. The standard deviations across plagioclase for each are 0.6, 0.3, and 0.05, respectively. The respective standard deviations across the Fe-rich CBL for each are 0.4, 0.6, and 0.05. Data points are plotted at 1 nm distances; however, for clarity the data markers have been removed.

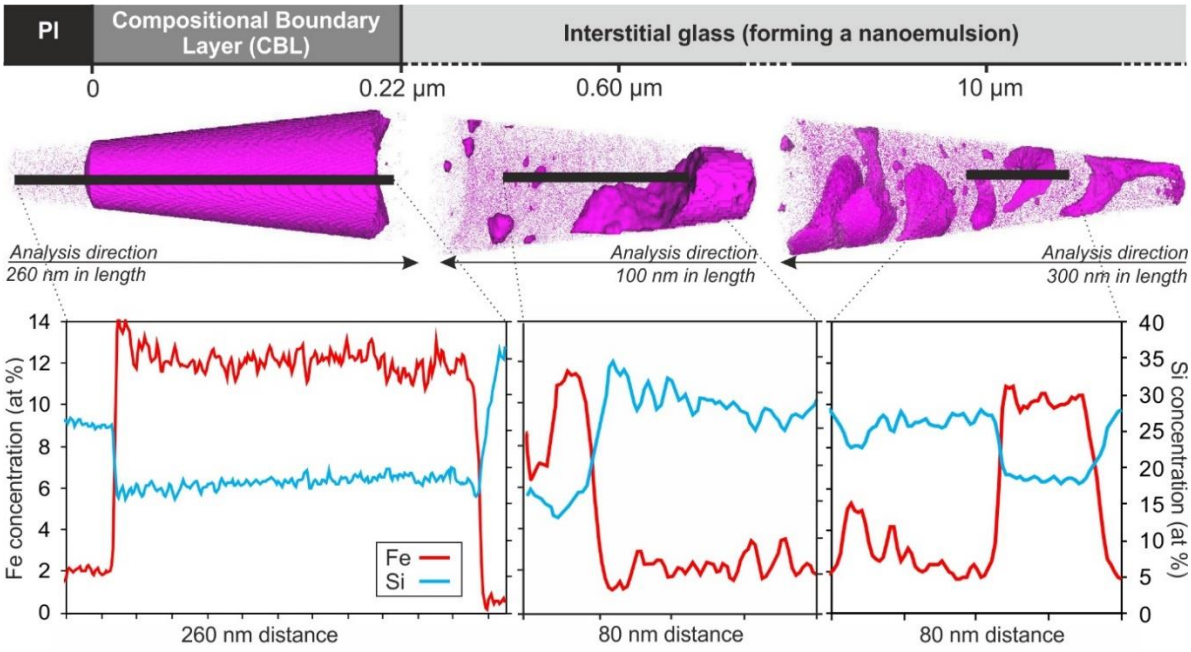

Figure 4.16 Three-dimensional reconstruction of atom probe tomography data from compositional boundary layers around plagioclase from three representative APT tips, including 1D element profiles across the compositional boundaries; Kīlauea Iki lava lake sample from 44.8 m depth (quench temperature of 1090°C). Each dot represents a single atom, but not all the atoms are shown. One-dimensional compositions from sub-volumes represented by black bars are plotted for Fe and Si concentrations (at. %) for each APT tip.

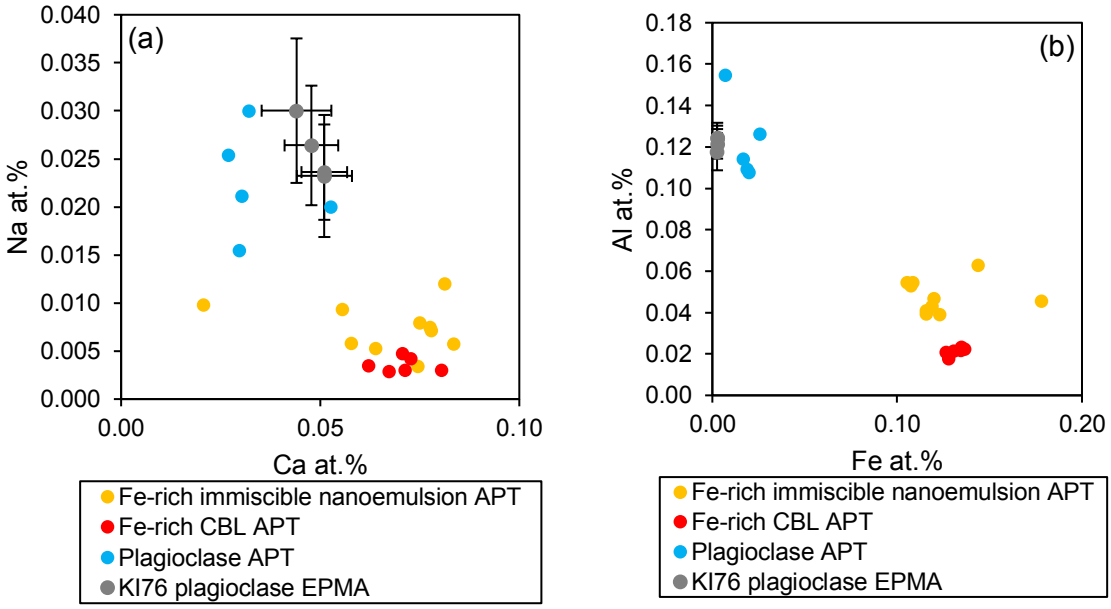

Figure 4.17 (a) Relative APT compositions of plagioclase, its Fe-rich compositional boundary layer (CBL), and the Fe-rich immiscible liquid of the surrounding nanoemulsion. (b) Relative APT compositions of plagioclase, its Fe-rich CBL, and the Fe-rich immiscible liquid of the surrounding nanoemulsion. The data are plotted from Appendix Table 4.A and 4.D. The sample is from the Kīlauea Iki lava lake 1976 drill core, quenched from ~1090°C during drilling at 44.8 m. EPMA analyses of plagioclase are shown with two standard deviation errors.

4.5 Discussion

4.5.1 Nucleation and evolution of unmixing: triggers and relationships

The non-zero wetting angle (Holness, 2006) of Fe-rich liquid on a non-mafic mineral, and the spatial correlation between Fe-rich CBL thickness and the growth rates of different plagioclase faces (Fig. 4.9) both demonstrate that the Fe-rich CBL surrounding plagioclase, and the weakly developed Si-rich CBL surrounding pyroxene, are disequilibrium features created during crystal growth. That the Fe-rich CBLs are continuous, with no evidence of separation into individual droplets required for textural equilibrium, must therefore be due to continuing plagioclase growth sustaining the Fe-rich CBL and preventing it from reaching textural equilibrium.

The creation and maintenance of a CBL around a growing crystal requires plagioclase growth rates to be commensurate with, or surpass, the diffusion rates of elements in the surrounding liquid. Different elements have different diffusion rates in different viscosity melts (Zhang et al., 2010); however, diffusion coefficients for the Makaopuhi and Alae lava lakes (Kirkpatrick, 1977) range from $5x10^{-15}$ m^2/s to $5x10^{-14}$ m^2/s – these are lava lakes of similar composition to the Kīlauea Iki lava lake, but smaller in size. The Makaopuhi and Alae lava lakes have plagioclase growth rates of ~5 x 10^{-11} to 10^{-12} m/s (Kirkpatrick, 1977); I calculate slightly slower plagioclase growth rates of c. 10^{-12} m/s for Kīlauea Iki lava lake samples, which is unsurprising given that the samples are from a bigger lava lake and are sampled from deeper in the lake (Appendix Table 4.B). Over a distance of 20 μm, the plagioclase growth rate is comparable to that of the diffusion rate.

Previous studies suggest that cryptic crystal chemical zonation in plagioclase on the 1 μm scale may result from CBL development (Zellmer et al., 2016). My data showing the Na-rich rims on the same scale as the surrounding Fe-rich CBLs (Fig. 4.9), and the relatively Na- and Al-poor composition of the Fe-rich CBL compared with the nanoemulsion Fe-rich liquids (Fig. 4.17), are consistent with the plagioclase Na-rich rim forming at the same time as the Fe-rich CBL. This may lead to a cyclic process of formation and destruction (Zellmer et al., 2016), whereby the development of Fe-rich CBLs in a continuously evolving system facilitates the growth of Ca-poor plagioclase, which then reverts to relatively Ca-rich growth if the CBL is destroyed by magma flow. The morphology of the plagioclase grains from the Kīlauea Iki lava lake (Fig. 4.2, 4.3; along with the SRP data set, Fig. 4.5) suggests that once the Fe-rich CBL has formed, crystal growth switches from interface-controlled to diffusion-limited, resulting in the growth of extended spines on the grain corners where the Fe-rich CBLs are less depleted in crystal-forming elements (Hammer and Rutherford, 2002; Zellmer et al., 2016).

The Fe-rich CBL surrounding plagioclase becomes thinner as solidification proceeds (Fig. 4.10), and the Fe-rich CBL evolves during solidification into a series of attached Fe-rich immiscible droplets (at 42.8 m, 1017˚C, Fig. 4.2d) indicative of an approach to textural equilibrium. This suggests the rate of

plagioclase growth, and hence the extent to which textural equilibration is prevented, decreases with progressive crystallisation and liquid evolution, perhaps due to a change in cooling rate. Isolated Fe-rich droplets in the shallowest (and most solidified) Kīlauea Iki lava lake sample provide further evidence of a temporal evolution in the unmixing process (the idealised evolution is illustrated in Fig. 4.18). This is consistent with unmixing later in the crystallisation history occurring by homogeneous nucleation in the bulk liquid, rather than being triggered by crystal growth, plausibly because only later in the crystallisation history is the undercooling sufficient to drive homogeneous nucleation.

The 1976 Kīlauea Iki lava lake transect covered by this sample suite cooled at 0.009°C/h – 0.0011°C/h (Helz et al., 2014). If I assume a constant cooling rate, the temporal difference between the deepest (45.5 m) and shallowest (42.8 m) samples containing immiscible microstructures is of the order of 11–14 months, suggesting that the differences I observe in the distribution and morphology of the unmixed Fe-rich liquids developed over a year. As the isotherms moved downwards with time and the slope of the thermal gradient of the lava lake became shallower (Helz et al., 2014), this estimate is likely a maximum.

Although compositional heterogeneities in liquids surrounding growing crystals are typically associated with diffusion-limited crystal growth (Cahn, 1967), my observations show that they may also result from growth under interface-controlled conditions (shown by the equant plagioclase morphology; Fig. 4.18; t1a and t1b). Furthermore, the creation of an Fe-rich CBL enriched in components rejected by plagioclase promotes full unmixing in liquids close to the binodal, without the need to nucleate and grow droplets. The same is true for the Si-rich CBL developed around pyroxene (Fig. 4.2c). My observations thus demonstrate that kinetic effects related to crystal growth strongly affect the location and nucleation of unmixing, particularly at temperatures above 1020°C.

4.5.2 Nanoemulsion formation

The observed nanoemulsion in the Kīlauea Iki lava lake drill cores (Fig. 4.13) may have formed as the water used during drilling encountered each sample, undercooling sufficiently that the spinode was attained before homogeneous nucleation occurred. Alternatively, it could be a preserved feature of unmixing during the solidification of the Kīlauea Iki magma at natural rates, which has been hitherto missed as these nanoemulsions are only visible with the spatial resolution of APT. The natural cooling rates of the SRP and Laki samples may have been sufficient to promote spinodal unmixing, and future work will need to focus on such fine-scale unmixing in both natural and experimental samples, complementing work on nanoemulsions formed by quenching from high temperatures during meteorite impacts (Hamann et al., 2013).

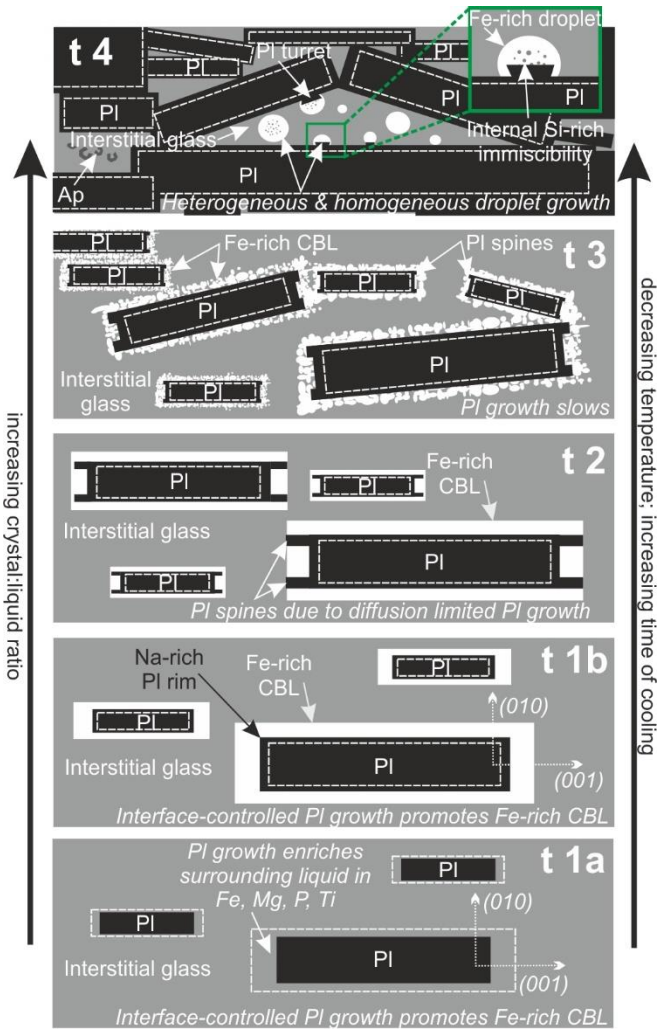

Figure 4.18 Schematic diagram depicting the evolution of unmixing features with progressive cooling at natural rates based on my data. Interface-controlled plagioclase growth promotes the formation of an Fe-rich compositional boundary layer, due to enrichment of the surrounding liquid in metalliferous elements. The Fe-rich CBL evolves temporally, coeval with the increasing crystal:liquid ratio, as a function of time and temperature, from panel t1 to t4, where t4 represents the lowest temperature and longest time of cooling. Overall, the creation of an Fe-rich CBL enriched in components rejected by plagioclase promotes full unmixing in liquids close to the binodal, without the need to nucleate and grow droplets. As plagioclase growth slows, an Fe-rich CBL can no longer be maintained and Fe-rich droplets nucleate both homogeneously and heterogeneously. Note that the processes illustrated in the cartoon are italicised.

4.5.3 Effect of crystal growth on the position of the binodal

An outstanding question is why Fe-rich CBLs, which are such a prominent feature of the samples from Laki, SRP, and Kīlauea Iki (Fig. 4.2-4.5), have not been commonly observed in experimental studies of immiscibility in basaltic glass (with one exception; Wang et al. (in prep)). Depending on the contrast-brightness optimisation for BSE imaging, such Fe-rich CBLs can easily be overlooked. Additionally, I suggest that the generally high nucleation density in experimental charges, results in a high crystal surface:liquid ratio, which prevents the development of steep compositional gradients in the surrounding liquid. I propose that at slow cooling rates typical of natural basaltic magmas, a lower nucleation rate, larger crystals, and thus a low crystal surface:liquid ratio, mean that kinetic effects

associated with crystal growth lead to earlier (higher temperature) unmixing of an Fe-rich immiscible liquid (in the form of an Fe-rich CBL), compared to experimental analogues. The spread in my compositional data for the Fe-rich CBL and Fe-rich immiscible droplets (Fig. 4.19) is attributed to limits on the spatial resolution of the EPMA (see section 4.3.2).

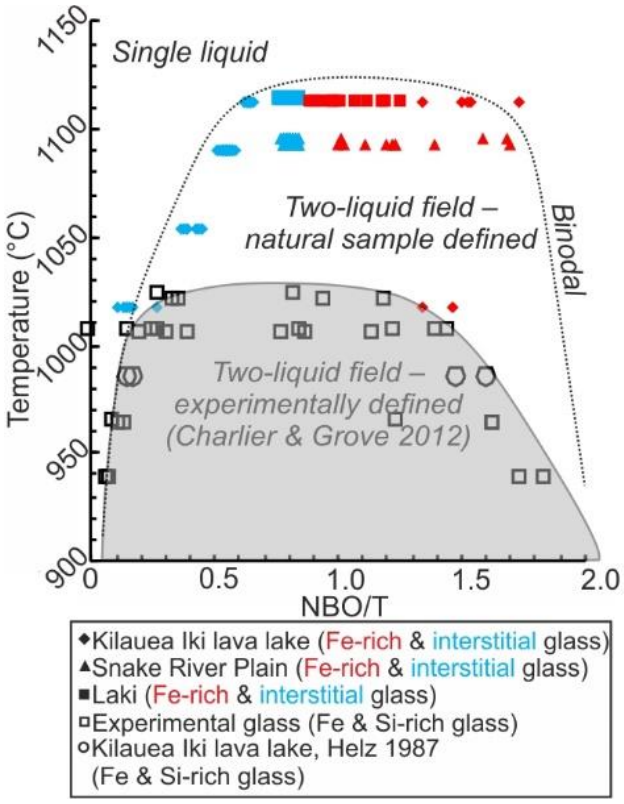

Figure 4.19 The silicate liquid immiscibility field. Temperature as a function of the degree of polymerisation (NBO/T: NBO = non-bridging oxygens and T = Si + Al + P + Ti); calculated from EPMA data on the glasses from Appendix Table 4.A. The shaded grey region represents the experimentally defined two-liquid field (Charlier and Grove, 2012), the dotted line represents the maximum compositional space where the natural examples show evidence of unmixing by a compositional boundary layer.

My calculated liquid temperature estimates were used to constrain the position of the binodal, plotted with respect to the parameter NBO/T (Fig. 4.19; where NBO is the number of non-bridging oxygens and T is the concentration of the tetrahedrally-coordinated network-forming cations Si, Al, P and Ti (Mysen, 1983)). The highest temperatures at which Fe-rich CBLs are present in samples from Laki, SRP and Kīlauea Iki are 1114°C, 1096°C and 1112°C, respectively; this is significantly hotter than previous suggestions for the top of the binodal at 1020°C (Charlier and Grove, 2012; Honour et al., 2019), although closer to the temperature of ~1060˚C suggested for the onset of immiscibility in the Upper Zone of the Bushveld Complex in South Africa (Fischer et al., 2016). The calculated temperature at which homogeneously nucleated Fe-rich immiscible droplets appear (around 1020°C; Fig. 4.19) broadly correlates with the temperatures experimentally derived for the onset of immiscibility (Charlier and Grove, 2012), supporting the hypothesis that the discrepancy between my observations and those

of experimental studies is indeed caused by crystal growth in natural samples promoting Fe-rich CBL formation, and hence unmixing, at temperatures higher than required for homogeneous nucleation of droplets.

The timing and extent of Fe-rich CBL development in natural samples depends on magma composition and the kinetics of diffusion and crystal growth. My work suggests that, if pre-existing phenocrysts act as nuclei, interface-controlled growth at high temperatures could result in immiscibility occurring at a higher temperature than previously recognised.

4.5.4 High temperature unmixing: its importance for phase separation and chemical evolution

This study provides direct evidence from natural samples of the morphological evolution of an unmixing basaltic liquid with progressive cooling (Fig. 4.18). The data demonstrate the importance of crystal growth induced spatial heterogeneities in liquid composition in triggering unmixing. The application of APT on natural glass gives a unique insight into the 3D nanoscale morphology of two unmixed liquids at a high spatial resolution (Fig. 4.16). In the slowly cooled natural samples, the development of an Fe-rich CBL illustrates unmixing at a considerably higher temperature (and lower corresponding under-cooling) than observed in experimental charges (Fig. 4.2-4.5), with a progressive attainment of the expected equilibrium morphology of the emulsion. It is clearly not safe to assume that the onset of unmixing is controlled by thermodynamics alone: kinetic factors play an important role.

The calculated density difference between the Fe-rich immiscible liquid (both Fe-rich CBL and Fe-rich immiscible droplets) and Si-rich conjugates examined here (following Bottinga and Weill, 1970) is small (<0.3 g/m^3), as they are in close proximity to the apex of the miscibility gap (Hou et al., 2017; Fig 4.19). This similarity means separation of the two conjugates is likely to be inefficient. However, as an immiscible Fe-rich end-member evolves down-temperature from the apex of the binodal, the density difference will increase. My study provides direct evidence of a continuous film (in textural disequilibrium) of Fe-rich liquid coating plagioclase grains (Fig. 4.2-4.5). Conceivably, when the density of the Fe-rich liquid reaches a critical density threshold, the continuity of this film could facilitate the downwards movement of the dense, inviscid liquid. Consequently, the onset of unmixing at higher temperatures than previously thought increases the potential for the relative movement of the two immiscible liquids in a gabbroic crystal mush, as at higher temperatures there are lower crystal fractions, and hence mush permeability is higher.

Finally, I note that Iceland and the SRP are tholeiitic provinces with a dearth of intermediate compositions (Charlier et al., 2013). It is thought-provoking to consider whether the identification of a mechanism for higher temperature unmixing at lower crystallinities has relevance to the formation of the Daly gap.

5 LATE-STAGE SEGREGATION EVOLUTION IN THE SKAERGAARD INTRUSION

The whole rock data presented in this chapter were analysed by Nic Odling at the Grant Institute, University of Edinburgh. Data processing and interpretation of the results was my own work.

Layered intrusions provide an insight into the geochemical evolution of magmas, increasing our understanding of processes operating in solidifying mushes in the shallow crust (O'Driscoll and VanTongeren, 2017). The well-exposed Skaergaard Intrusion of East Greenland is viewed as an unparalleled example of closed-system behaviour and uninterrupted fractionation of basaltic magma, enabling study of paradigms and controversies in igneous petrology. If we understand active magma chambers as mushy and crystal-rich (e.g. Huang et al., 2015), then the study of migrating interstitial liquids in layered intrusions can be used to test and refine models of sub-volcanic systems, such as trans-crustal mush zones (e.g. Cashman et al., 2017).

The Skaergaard Intrusion was discovered by Lawrence Wager in 1930. Between 1935–36 he led the first scientific expedition to the intrusion and his influential account of its geology was published three years later (Wager and Deer, 1939). Much of the early work on Skaergaard focused on mapping, petrological and mineralogical studies, with later research expanding into geochemistry. Study of the Skaergaard Intrusion has helped shape ideas about the processes of magma differentiation, crystal fractionation and cumulate theory, applicable to the layered intrusion and volcanology communities (e.g. Wager and Brown, 1968).

Excellent exposure, combined with extensive petrological and geological context, makes the Skaergaard Intrusion an ideal natural laboratory to answer questions about the behaviour of crystal mush and the effects of silicate liquid immiscibility in large-scale systems with very slow cooling rates. In this chapter, the key questions I address are:

a) *How did the late-stage interstitial liquids evolve during solidification of the intrusion?*

b) *When did the late-stage accumulated liquids reach silicate liquid immiscibility?*

c) *How does mush rheology affect the migration of late-stage liquids?*

5.1 Previous work on the Skaergaard Intrusion

5.1.1 The Regional Geology

The Skaergaard Intrusion forms an irregular oval outcrop, covering an 8 x 11 km area and it is ~4 km thick (Nielsen, 2004). It intrudes the surrounding Precambrian basement gneiss (to the north and west; Kays et al. (1989)), a thin succession of Cretaceous to Early Palaeocene sediments (on the island of Mellemø and to the north-west; Andersen and Brooks (2003)), and is overlain by >6.5 km of Eocene basaltic plateau lavas (to the east and south; Higgins and Soper (1981); Fig. 5.1). Subsequent tectonic rotation has caused the intrusion to tilt by 10–20° to the south, exposing a near-complete stratigraphic transect; in the north the lower parts of the intrusion are exposed, while in the south the contact with the roof zone has locally been preserved (Wager and Deer, 1939).

Skaergaard is thought to have solidified over ~100,000 years (Wotzlaw et al., 2012). Zircons from the last stages of crystallisation have been dated at 55.960 ± 0.018 Ma using the U–Pb system (Wotzlaw et al., 2012), superseding the previous fission track age of 54.6 ± 1.7 Ma (Brooks and Gleadow, 1977). Given the zircon crystallisation ages (sampled from an intercumulus gabbroic pegmatite in the lower portion of the intrusion), Wotzlaw et al. (2012) estimate the emplacement age of the intrusion to be ~56.02 Ma.

5.1.1.1 Regional faulting

The shape of the intrusion is thought to have been controlled by pre- and syn-magmatic NNW–SSE and NE–SW extensional faulting (Irvine, 1992; Nielsen, 2004), particularly on the western margin (Nielsen, 2004). Humphreys and Holness (2010) postulated that such faulting may have affected cumulate formation during intrusion solidification. Post-solidification faults, running sub-parallel to the coast-parallel flexure (Nielsen and Brooks, 1981), have been mapped across the intrusion by Bird et al. (1986); and McBirney (1989), and are shown in geological cross-sections of the intrusion developed by Nielsen (2004).

5.1.2 Cumulate nomenclature

A key challenge for studying layered intrusions is that the solidified remnants are only indirect records of the evolution of the parental magma. As such, the nomenclature of igneous cumulates is extensive and names can be descriptive or genetic. Originally Wager (1960) described cumulus crystals as: “discrete crystals successively separated from the magma as a result of their greater density”. However, it is now known that Skaergaard cumulate plagioclase was less dense than the bulk magma, so should have floated (e.g. Bottinga and Weill, 1970; McBirney and Noyes, 1979), rendering the specific definition of Wager (1960) redundant. As Irvine (1982) stresses, “because of their connotations, the words were ‘foes of reality’”.

Irvine (1982) defines 'cumulate' so that crystal settling is a *possible but not essential* process in the origin of the rock. Following this nomenclature, I use *cumulate* as characterised by a cumulus framework of touching grains, where the *cumulus grains* are the fractionated primocrysts. Generally, these are cemented together by *postcumulus material* that crystallised from the interstitial liquid in the interstices. Specifically, in orthocumulates, postcumulus material should be abundant and the cumulus grains should largely be in their original primocryst shapes. In adcumulates, postcumulus material occurs as minor, discrete occurrences and if there was extensive post-accumulation growth, the cumulus grains should have mutual interference boundaries developed through overgrowths (Irvine, 1982).

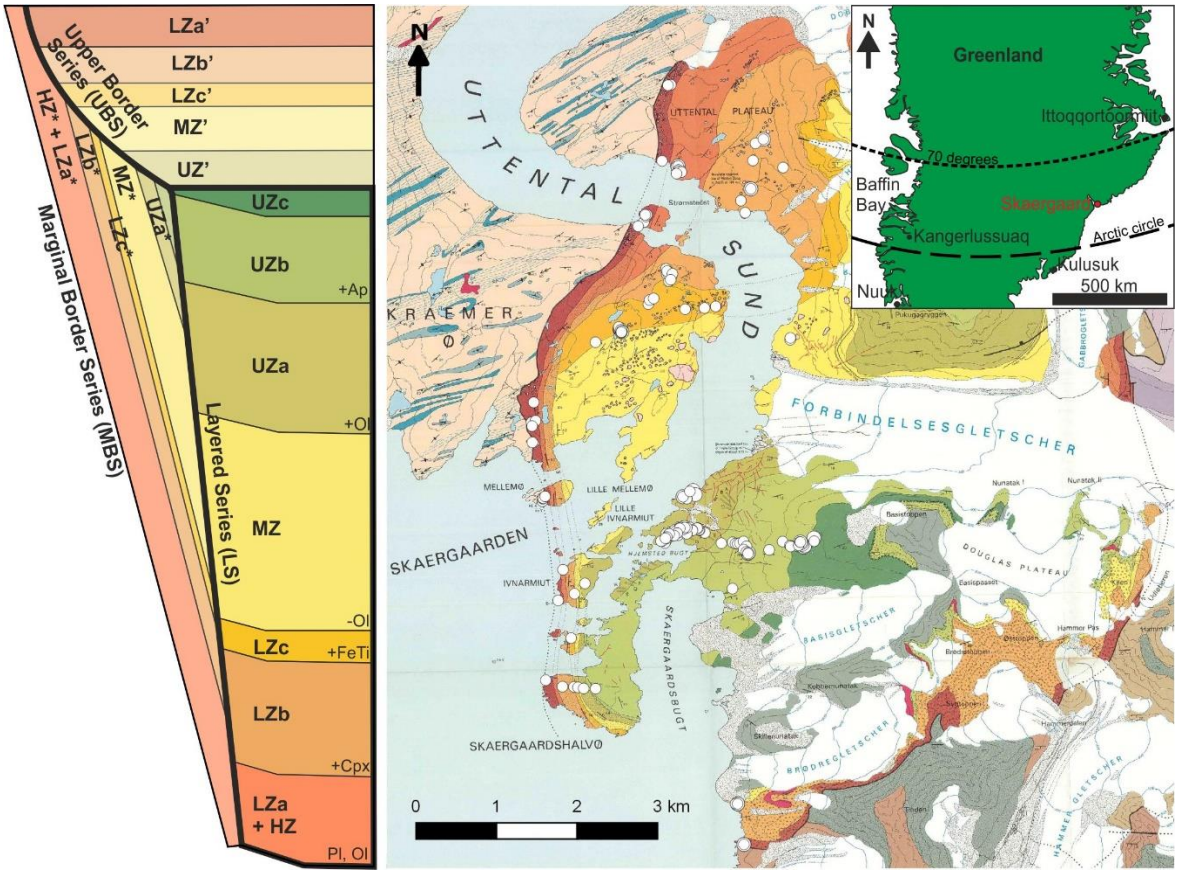

Figure 5.1 Geological map of the Skaergaard Intrusion, by McBirney (1989), with the white circles showing the location of samples investigated in this study (Appendix Table 5.A). Map in the upper right corner shows the location of the geological map area in Greenland. Schematic cross-section of the Skaergaard intrusion on the left-hand side shows the relationships between the LS, UBS and MBS. LZ = Lower Zone; MZ = Middle Zone; UZ = Upper Zone; MBS = Marginal Border Series; UBS = Upper Border Series. Subdivisions of each series and the sequence of crystallization in the LS are shown on the schematic cross-section.

The cumulate paradigm has been subject to repeated discussions, both past and present (e.g. Campbell, 1978; Holness et al., 2017b; Irvine, 1982; McBirney and Hunter, 1995; O'Driscoll and VanTongeren, 2017), with discussion focussing on the question of whether *layered intrusions are modified post-crystallisation?* The conventional view, and the one on which the ideas in this thesis are based, is that layered intrusions are largely a record of the progressive crystallisation of one or more magmas. In this model the bulk rock is a mixture of the minerals crystallised along the cotectic, plus the crystallised

interstitial liquid. Debate continues about whether the crystal pile accumulated by *in situ* nucleation and growth (e.g. Campbell, 1978) or by gravitational deposition (Holness et al., 2017a). The unconventional view of cumulate rocks is that they have undergone extensive modification and recrystallisation in melt-poor conditions during and after solidification (e.g. Boudreau, 2017; Boudreau and McBirney, 1997; McBirney and Hunter, 1995) and consequently, as stated by Allen Glazner "using the rocks as they now appear to infer magmatic processes is about as difficult as trying to decipher sedimentary process from a metamorphic rock" (Boudreau, 2017).

Modification by postcumulus metasomatism chiefly results in *recrystallised rocks* or *replacement rocks* (Irvine, 1982). The former typically has the same modal assemblage as the primary igneous rock but a different texture; the latter has a different modal assemblage, generally with fewer phases. Commonly postcumulus metasomatism transgresses layering and so recrystallisation and replacement can occur on a volume-for-volume basis. Therefore, the key to establishing if cumulates underwent postcumulus metasomatism is the microstructure (Holness et al., 2017b).

5.1.3 Lithological Divisions

The Skaergaard Intrusion crystallised in concentric zones from the margins inwards, forming three major divisions: (i) the Upper Border Series crystallised from the roof of the intrusion downwards (UBS, ~50 km^3) and is ~600 m thick (Nielsen, 2004), (ii) the Marginal Border Series crystallised along the walls of the intrusion inwards (MBS, ~50 km^3), and (iii) the Layered Series crystallised and accumulated from the floor upwards (LS, ~200 km^3) and is ~3000 m thick (Nielsen, 2004; Fig. 5.1). The last unit to crystallise was the Sandwich Horizon, located between the UBS and the LS, 700 m below the intrusion roof (Wager and Deer, 1939). At the interface between the solidified cumulate pile and the bulk magma, a slurry of crystals and liquid comprised a porous layer, referred to herein as mush. The stratigraphic thicknesses used here are taken from Nielsen (2004) and Morse (2008b), Table 5.1.

Subdivisions in the intrusion are defined by cumulus mineral assemblages. The further from the margins of the intrusion, the greater the evolution in mineral composition; olivine evolves from Fo_{70} to Fo_1, and plagioclase from An_{70} to An_{25} (e.g. Maaløes, 1976; McBirney, 1996; Namur et al., 2014; Tegner and Cawthorn, 2010; Wager and Brown, 1968).

The deepest gabbros in the LS are not exposed and are referred to as the Hidden Zone (HZ). The exposed rocks of the LS are divided into: Lower Zone (LZ), Middle Zone (MZ), and Upper Zone (UZ), defined by the presence, disappearance and reappearance, respectively, of cumulus olivine. The LZ and UZ are subdivided into three further subzones on the basis of their cumulus mineral assemblages (Wager and Deer, 1939): LZa comprises cumulus olivine and plagioclase with poikilitic clinopyroxene and interstitial ilmenite and titanomagnetite; LZb comprises cumulus olivine, plagioclase, and clinopyroxene, with interstitial oxide; and LZc is defined by the appearance of cumulus titanomagnetite

and ilmenite (Holness et al., 2007), alongside cumulus olivine, plagioclase, and clinopyroxene. In the UZ, UZa comprises cumulus plagioclase, clinopyroxene and marks the reappearance of cumulus olivine; UZb has cumulus apatite as well as the cumulus phases of UZa; and UZc has the same cumulus phases as UZb, but clinopyroxene becomes ferro-bustamite (an Fe-rich pyroxenoid), which subsequently inverted to ferro-hedenbergite (Lindsley et al., 1969). From a textural perspective, the deepest gabbros in the LS are coarse-grained orthocumulates, but the proportion of interstitial material decreases with increasing stratigraphic height, leading to adcumulates higher in the sequence (Wager and Deer, 1939).

Table 5.1 Skaergaard subzone thicknesses after Nielsen (2004) and Morse (2008b)

Zone	Volume (km^3)	Thickness to 2350 m	Cumulative metres
UZc	4.7	81	2550
UZb	16.8	289	2469
UZa	20.8	358	2180
MZ	28.3	487	1822
LZc	15.5	267	1334
LZb	50.4	868	1068
LZa + HZ	74.7	LZa = 200; HZ = 500	200
MBS	49.5		
UBS	41.5		

The MBS is divided into the 'Tranquil Division' and the 'Banded Division' based on outcrop-scale features (Wager and Brown, 1968). The 'Tranquil Division' was argued to be analogous to the HZ and lies closest to the contact with the country rock. It hosts two distinctive rock types: the Wavy Pyroxene Rock (Humphreys and Holness, 2010) and the Perpendicular Feldspar Rock (Wager and Deer, 1939). The Wavy Pyroxene Rock is characterised by mafic clots, and mafic-bottomed–felsic-topped clots of 0.2–0.4 m diameter, heterogeneously distributed through the gabbro. The Perpendicular Feldspar Rock is characterised by elongated parallel plagioclase grains, oriented perpendicular to the intrusion contact (Hoover, 1989). The 'Banded Division' is subdivided into units corresponding to the LS in mineralogy and composition: LZa*, LZb*, LZc*, MZ*, UZa* and UZb*. UZc* is generally absent from the MBS. The 'Banded Division' hosts distinctive vertical centimetre-thick colloform bands dominated by fine-grained mafic minerals: these bands are thought to have formed during reactive porous flow as the bulk liquid was sucked into the contracting wall mush during solidification (Namur et al., 2013).

The UBS is divided into LZ', MZ' and UZ' following the liquidus mineral assemblages of the LZ, MZ and UZ respectively (Salmonsen and Tegner, 2013). The first appearance of each cumulus mineral in the UBS occurs at plagioclase anorthite contents comparable to those in the LS.

Following previously used nomenclature, all Skaergaard cumulates are referred to as gabbros despite plagioclase having $<An_{50}$ in rocks more evolved than MZ (e.g. Hoover, 1989; Salmonsen and Tegner, 2013; Wager and Brown, 1968), making these rocks, strictly, ferrodiorites.

5.1.4 Cumulus minerals

The primocryst compositions systematically evolve up-stratigraphy in the LS. Plagioclase core compositions vary from ~An_{70} in the HZ to An_{25} at the Sandwich Horizon (Maaløes, 1976; McBirney, 1996; Namur et al., 2014; Tegner and Cawthorn, 2010; Wager and Brown, 1968). Olivine core compositions evolve from Fo_{68} at the base of the intrusion to almost pure fayalite (Fo_2) in the Sandwich Horizon (Wager and Brown, 1968). While absent from the MZ, olivine is hypothesised to have been close to the liquidus (McBirney, 1996). Inverted pigeonite (Ca-poor) and clinopyroxene (Ca-rich) vary from Mg# 52.7 to Mg# 68.8 respectively (where Mg# = Mg/(Mg + Fe_{total})), evolving to almost end-member hedenbergite (an Fe-rich pyroxene end-member) close to the Sandwich Horizon (McBirney, 1996).

5.1.5 Mineralisation

In the Skaergaard Intrusion, a potentially economic stratigraphic zone is the Triple Group in the MZ of the LS (e.g. Andersen et al., 1998; Bird et al., 1991; Nielsen and Brooks, 1995; Nielsen and Gannicot, 1993; Nielsen et al., 2015). The Triple Group is rich in Au and platinum group elements (PGEs). It is composed of three macro-layers, concordant with layering, in the top 100 m of the MZ. The horizon contains >30 million ounces of PGEs, chiefly Pd, and >10 million ounces of Au (Nielsen et al., 2005). This horizon is significant for its precious element concentrations in economic quantities, but it is not the focus of this thesis.

Prospective Fe-Ti-V economic mineralisation is located in two intervals in the Skaergaard Intrusion (Sørensen et al., 2016): one transcends the upper reaches of the LZ and the base of the MZ (Fe-Ti-V), and the other is associated with the PGE-Au reefs (Ti-V) near the top of the MZ. The former has modal layering defined by magnetite and ilmenite. Five 0.5–2 m thick, laterally continuous oxide-rich intervals form a 50 m thick sequence within the upper part of the LZc gabbro. These intervals are numbered 1 to 5 up stratigraphy (Andersen and Weatherley 2017 pers. comm.). These layers are semi-continuous along strike from the centre of the intrusion to the margin; however, they vary from wispy and laterally discontinuous layers close to the margin, to strongly defined and laterally continuous layers further inwards. Currently, there are no estimates for the extent or tonnage of each interval. The intervals concentrate significant volumes of Fe-rich minerals; this has implications for the liquid line of descent of the bulk magma, and potentially for our understanding of the accumulation of Fe-rich liquids. The Fe-Ti-V mineralisation located in LZc is discussed in this thesis.

5.1.6 The liquid line of descent

The Skaergaard cumulates represent the solidified products of continuous fractional crystallisation, so the intrusion is typically considered as a closed system (e.g. Wager and Deer, 1939; Wager and Brown, 1968). Fluctuations in primocryst mineral chemistry, along with the textural maturity of the cumulus

microstructure, in the HZ suggest that the intrusion was inflated to its final size very early in its formation by several pulses of magma saturated in plagioclase and olivine (Holness et al., 2007). Namur and Humphreys (2018) suggest that fractional crystallisation dominated until UZa, after which they suggest fractional crystallisation became less effective.

The liquid line of descent for basaltic magmas has long been debated, with discussion centred around the classical works of Bowen (1928) and Fenner (1929). Bowen argued that basaltic magma composition evolves towards silica enrichment, while Fenner argued for iron enrichment with a constant or small silica depletion. There is disagreement surrounding the trend of the Skaergaard liquid line of descent. Modelling and the compositional evolution of the LS cumulates supports the Fenner trend (e.g. Brooks and Nielsen, 1978; Jang et al., 2001; McBirney and Naslund, 1990; Morse, 1990; Tegner, 1997; Thy et al., 2008; Veksler, 2009; Wager and Brown, 1968), while mass-balance considerations and experimental petrology of the intrusion supports the Bowen trend (e.g. Ariskin, 2003; Hunter and Sparks, 1987; Hunter and Sparks, 1990; Toplis and Carroll, 1996). Advocates of the Bowen trend suggest that the absence of evolved silica-rich rocks indicates erosion of the intrusion or eruption (Hunter and Sparks, 1987). A reconstruction by mass balance produced a liquid line of descent intermediate to the Bowen and Fenner trends (Nielsen, 2004). However, Veksler and colleagues argue that the differing liquid evolution trends could be explained by silicate liquid immiscibility (e.g. Veksler, 2009; Veksler et al., 2007; Veksler et al., 2008a).

5.1.6.1 Oxygen fugacity

The Skaergaard Intrusion crystallised as a closed system with a constant oxygen content and variable fO_2, controlled by crystallisation (e.g. Osborn, 1959). During the formation of LZa and LZb gabbros, fO_2 is estimated to have been near the fayalite-magnetite-quartz (FMQ) oxygen buffer (Buddington and Lindsley, 1964; Kersting et al., 1989). Calculated and experimental fO_2 trends for the Skaergaard Intrusion show a change to more reducing conditions in the upper part of the MZ, dropping to −2 ΔFMQ in UZc (Frost et al., 1988; Lindsley and Frost, 1992; McBirney and Naslund, 1990; Morse et al., 1980; Williams, 1971). Fractionation of large amounts of magnetite (the main phase that contains high contents of ferric iron) is a requirement for fO_2 to become more reducing in the UZ (Juster et al., 1989; Presnall, 1966; Roeder and Osborn, 1966; Snyder et al., 1993; Toplis and Carroll, 1996). Similarly, Jang et al. (2001) suggest that the onset of magnetite fractionation would have removed Fe_2O_3 from the magma or the fO_2 trend above MZ may reflect a new fO_2 buffer in the system. The model of Thy et al. (2008) established that the calculated and experimental fO_2 trends could only occur after significant magnetite fractionation, larger than the content of magnetite in the LS gabbros. They suggest that, in a closed system, UZ formation would not have led to a strong reduction in fO_2.

5.1.7 The onset of silicate liquid immiscibility in the Skaergaard Intrusion

That the bulk magma in the Skaergaard Intrusion split into two immiscible conjugates was first hypothesised by Holgate (1954). He based his argument on a comparison between the calculated liquid lines of descent of Skaergaard and the experimental studies of Greig (1927); he argued that the Skaergaard liquid line of descent entered the liquid immiscibility field. However, due to the absence of direct evidence for magnetite-apatite saturated liquids in the intrusion, others concluded that the liquid line of descent did not encounter the silicate liquid immiscibility binodal (Bowen, 1928; Hunter and Sparks, 1987; Philpotts, 1967).

McBirney (1975) pursued the idea of silicate liquid immiscibility in Skaergaard, collating evidence of: 1) the presence of unmixed liquids in experimentally melted samples of UZ cumulates; 2) abundant granophyres in the roof zone, which McBirney and Nakamura (1974) suggested were the immiscible counterparts of UZc cumulates; and 3) the presence of metre-scale segregations of ferrogabbros in the 'average gabbro' of the LS. Hanghøj et al. (1995) also suggested the presence of an Fe-rich immiscible liquid in the intrusion. They studied crystallised melt inclusions in plagioclase and, alongside mass balance calculations, inferred the MZ silica composition was equivalent to, or possibly even lower than, the initial Skaergaard melt silica composition, and relatively enriched in iron.

The first direct evidence of unmixed liquids in the bulk magma of Skaergaard was provided by the identification of two populations of primary melt inclusions in apatite from UZb ferrogabbros, one light in colour with ~65.6 wt.% SiO_2 and the other dark with ~40.7 wt.% SiO_2 (Jakobsen et al., 2005). Subsequent experimental evidence suggested that unmixing of the bulk magma occurred earlier in the intrusion's crystallisation, in LZc (Veksler et al., 2007; Veksler et al., 2008a). However, this hypothesis is not supported by field evidence (McBirney, 2008; Morse, 2008a; Philpotts, 2008). In addition, the experiments were criticised for not taking into account applicable petrological phase equilibria (Morse, 2008a; Philpotts, 2008). More recently, it has been suggested that liquid unmixing occurred at a bulk magma composition equivalent to near the base of UZb, when there was less than 10% of melt remaining (Nielsen et al., in review); this is consistent with the conclusions from the mineralisation model of Nielsen et al. (2015). However, modelling by Thy et al. (2008) suggests that liquid immiscibility is not a requirement for strong iron enrichment occurring concurrently with limited silica enrichment in the intrusion.

Evidence of immiscibility in the *interstitial* liquid of the crystal mush is provided by: replacive symplectites grown during reaction between an Fe-rich liquid and adjacent primocrysts, driven by the differential loss of the buoyant Si-rich conjugate (Holness et al., 2011); differences in TiO_2 content of plagioclase adjacent to pockets of crystallised late-stage liquids (Humphreys, 2011); and the presence of Fe-rich melt inclusions in LZc, MZ and UZ (Jakobsen et al., 2011).

Throughout this discussion of liquid unmixing, it is important to remember that it is only possible to directly study what these liquids have left for us to observe, i.e. what they crystallised: "it is like the red wine stain on the carpet in the living room. The red wine was there - now we only see the stain" (Nielsen 2019 pers. comm.). Consequently, there remains no consensus on when the onset of silicate liquid immiscibility in the bulk magma occurred, despite its importance in changing the physical properties and the chemical evolution of the bulk magma. In particular, the efficiency of unmixing and separation of the two liquids in the crystal mush has implications for ore deposit formation from the Fe-rich liquid e.g. Nielsen et al. (in review); Nielsen et al. (2015).

5.1.8 Macro-scale layering structures

The floor cumulates of the Skaergaard Intrusion are typically layered: this layering is principally defined by changes in colour (and hence modal mineralogy), but can also be defined by differences in grain size. The layering is generally concordant, planar, and parallel with the intrusion floor, with sedimentary-like features on a variety of scales and localised complex geometry (Irvine et al., 1998; McBirney and Noyes, 1979). Different types of layering formed by a range of dynamic and non-dynamic processes (Irvine et al., 1998). The former resulted from grain movement in a non-static magma, while the latter resulted from processes occurring within the crystal mush, such as reactive porous flow (Namur et al., 2013) or self-organisation of mobile interstitial liquid that enhances existing layering (Namur et al., 2015a; Vukmanovic et al., 2018).

Examples of dynamic layer-forming processes in the Skaergaard Intrusion include: progressive fractionation that results in cryptic layering, as defined by changes in mineral compositions (McBirney and Noyes, 1979; Wager and Brown, 1968); crystal settling resulting in density sorting and the formation of modally-graded layers (McBirney and Noyes, 1979; Wager and Brown, 1968); hydrodynamic sorting during deposition from localised crystal-rich currents derived from the intrusion wall, resulting in the formation of modally-graded trough layering (Fig. 5.2; Irvine and Stoeser, 1978; Irvine et al., 1998; Vukmanovic et al., 2018; Wager and Brown, 1968); and intermittent convection that results in cyclic modal layering (Naslund et al., 1991). These dynamic layer-forming processes operate on the metre to tens-of-metres scale. On the intrusion-wide scale, dynamic large-scale slumping from the intrusion sidewalls

Figure 5.2 Trough layering in UZa: Trough H showing stacked, crescentic, modally graded layers surrounded by average gabbro. Looking east.

contributed to the development of the floor mush that formed the LS (e.g. Baker and McBirney, 1985; Holness et al., 2017c).

An ongoing debate surrounding layered intrusions is whether layering is unmodified from primary deposition, or modified post-accumulation, and to what degree the information extracted from layering can be used to infer the primary magmatic and accumulation processes (Namur et al., 2015a; O'Driscoll and VanTongeren, 2017). A suggested example of non-dynamic processes forming layering is dissolution-precipitation, whereby material at high stress crystal contacts is dissolved and re-precipitated in low stress areas (Boudreau and McBirney, 1997). This process, essentially that proposed for layer formation in high-grade gneisses, has been suggested to have resulted in the wholesale modification of primary igneous microstructures, modal mineral proportions and mineral compositions (e.g. Boudreau and McBirney, 1997; McBirney, 1996; McBirney, 2009; McBirney and Hunter, 1995; McBirney and Noyes, 1979). The validity of this idea has been challenged by detailed microstructural work on the modal layering, demonstrating its primary igneous origin (e.g Holness et al., 2009).

5.1.9 Gravitational collapse of unstable crystal mush

Mechanical instabilities are known to occur along solidification fronts within magma chambers (e.g. Marsh, 1996; Marsh, 2006; Žák and Paterson, 2010). These boundary layer instabilities can take different forms depending on the rheology and density of the mush and bulk magma (e.g. Bergantz, 2000; Jaupart and Tait, 1995). For example, along the horizontal roof of a chamber, magma convection can produce chemical and physical instabilities that cause crystal-rich batches to descend, or 'drip' from the roof (e.g. Bergantz and Ni, 1999), while at a sloping margin, convection can generate a sidewall current (Jaupart and Tait, 1995; Paterson et al., 2016; Paterson et al., 2019). Marsh (1996; 2006; 2015) examined the growth of solidification fronts in chambers where the cooling rate is faster at the roof than at deeper levels along walls. He suggested that these fronts may detach from the roof, generating a crystal-rich magma avalanche. Overall, slumping of mushes in magma bodies (chambers, plutons, intrusions) can occur by any process creating instability, including: tectonic, fluid-assisted, stoping, or gravity-driven processes.

It has been suggested that the trough layering in the Skaergaard Intrusion is of a magmatic-sedimentary origin, formed by crystal-rich magmatic currents which descended from the nearby walls of the intrusion and which flowed across the chamber floor, depositing cumulus grains with a lineated fabric (Irvine, 1983; Irvine and Stoeser, 1978; Vukmanovic et al., 2018; Wager and Deer, 1939; Wager and Brown, 1968).

In the MBS there are lens-shaped coarse-grained gabbroic segregations on the centimetre- to metre-scale (Humphreys and Holness, 2010), distributed across the average gabbro of the wall cumulates. Humphreys and Holness (2010) proposed that these distinctive segregations were formed by the

slumping of the vertical mush as a result of gravitational collapse or syn-magmatic faulting. The slumping caused tears in the mush as they formed on a faster timescale than the interstitial liquid could flow into them. The tears formed lower pressure zones, which sucked in the interstitial liquid. This is analogous to the 'hot tearing' of metal alloys at low porosities ($\varphi = < 0.25$), which is known to initiate in the interstitial liquid of metal alloys (Eskin and Katgerman, 2004). The mineral chemistry and texture of these lens-shaped segregations in the MBS of Skaergaard suggest that the tearing of the mush occurred relatively early in the crystallisation history of the intrusion (Humphreys and Holness, 2010).

While there is no field evidence in the LS of crystal-rich batches descending from the roof of the Skaergaard Intrusion, the LS does host large fallen blocks (or autoliths) with compositions ranging from troctolite, to gabbroic anorthosite to oxide-rich gabbro (Irvine et al., 1998). The autoliths range in size from metre-scale to tens of metres in diameter. In the LS, although the fallen blocks are not *sensu stricto* magma slumping, in of themselves, they caused localised distortion and slumping of the LS cumulates (Irvine et al., 1998).

5.1.10 Mush thickness

The physical relationship between the fallen blocks documented across the intrusion and the cumulate layering provides key evidence of an interface layer (i.e. a mush layer) between the top of the cumulate pile and the bulk magma in the intrusion (Irvine et al., 1998). The mush porosity is likely to have been in the range $\varphi = 0.4–0.6$, as controlled by the packing efficiency of the cumulus primocrysts. A crystal mush has the potential to behave like a hydrogranular medium (see section 5.1.11). The base of the mushy layer has been defined in various ways, generally based on mush permeability (Boudreau and Meurer, 1999) or rheology (Brown et al., 1987).

A range of mush thicknesses have been suggested for the Skaergaard Intrusion during solidification. Nielsen et al. (2005) postulated that the mush thickness at the Triple Group horizon (in the MZ) was 60 m at most. Tegner et al. (2009) proposed a mush thickness of tens of metres for the LS using comparisons between the calculated trapped liquid fraction and rock density. McKenzie (2011) developed a simplified compaction model, using P_2O_5 whole rock data from the LS, to calculate a mush thickness of 300 m. Holness et al. (2017c) used the stratigraphic distance between the arrival of a new cumulus phase and the associated textural maturity of the microstructure, as measured by a step-change in dihedral angle, to argue that the mushy zone in the LZ was ~100 m thick (Holness et al., 2017c). This thinned to only a few metres by the base of UZa (Holness et al., 2017c). Given the horizon-specific mush thickness measurements, references herein to mush thickness will be based on Holness et al. (2017c).

With increasing stratigraphic height in the intrusion there is a decrease in the proportion of interstitial material, which has been attributed to an increasing efficiency of compaction (Tegner et al., 2009).

However, the thickness of the mush does not correlate with the efficiency of liquid expulsion from the cumulate (Holness et al., 2017c), and there is no correlation between the intensity of syn-magmatic deformation and the amount of retained interstitial liquid (Holness et al., 2017c). Thus, compaction is unlikely to have been a significant factor in creating adcumulates in the Skaergaard Intrusion. Alternative methods for adcumulate formation include compositional convection within the mush (Tait and Jaupart, 1992; Toplis et al., 2008) and diffusion of unwanted elements (i.e. elements incompatible in crystallising material) out of the trapped residual liquid in a thin mush (Wager and Deer, 1939).

5.1.11 The mush as a hydrogranular medium

The prior work and discussions surrounding the Skaergaard Intrusion inadvertently illustrate the important point that the cumulus model for layered intrusions is an oversimplified end-member; the reality of the processes lies somewhere between the classical model of cumulus assemblage and *in situ* crystallisation, dependent on a variety of dynamic factors such as rheology and density relationships. Recent work describing mush as a hydrogranular media helps elucidate its behaviour.

A liquid-rich crystal mush is an example of a hydrogranular medium whereby grains are loosely connected with only a few contact points, and the dynamics are controlled both by fluid and grain-grain interactions (Bergantz et al., 2017). An example of grains linked together in a continuous three-dimensional network of chains is highlighted in a basaltic lava flow; Philpotts and Dickson (2000) show that feldspars form chains in the upper solidification front and were transported down through the lava flow in plumes of dense crystal mush.

Discrete-element numerical modelling using crystal force chains reveals the time-transgressive rheological behaviour of hydrogranular media (Bergantz et al., 2017; Schleicher and Bergantz, 2017). Crystal force chains are ephemeral, typically comprising about ten grains before bifurcating; therefore, a crystal mush can behave simultaneously in a viscous, plastic, and brittle manner at low interstitial liquid fractions (Bergantz et al., 2017; Holness et al., 2017c). This means that when a hydrogranular medium is rapidly loaded (e.g. by rapid accumulation of overlying crystals), it causes hardening of the surrounding crystal mush, to the degree that the mush locally behaves like a solid. The everyday analogy to this is that you can run across corn starch, whereas if you walked slowly you would sink (e.g. McKnight, 2016). The transient nature of hydrogranular media inherently removes evidence of all, or some, of the mush behaviour from the solidified cumulates, and as such it is often difficult to identify examples in the field of fully solidified rocks that originally behaved as hydrogranular media (Paterson et al., 2019).

5.1.12 Late-stage liquid segregations

The distribution of late-stage liquid segregations in fully solidified cumulates can help provide an understanding of the rheology of crystal mush during solidification. This is because the physical

properties of the mush affect the mechanisms of liquid segregation, liquid accumulation and the response of the crystal mush to stress. While a variety of meso-scale structures in granitoids have been holistically studied to unravel their hypersolidus histories (Paterson et al., 2019), and thus differentiate between magmatic and solid-state structures, the same has not been done for basaltic bodies. Such an understanding of mush rheology from late-stage segregations hinges on the late-stage segregations preserving the primary igneous fabric and assemblage; whereas some authors have postulated replacement, metasomatism and water ingress models for the formation of these various structures (e.g. Larsen et al., 1992; McBirney and Sonnenthal, 1990). Conflicting ideas about the genesis of late-stage segregations are discussed in turn for each structure.

The Skaergaard Intrusion preserves a variety of structures on a range of scales, attributed in some form to late-stage liquid movement. These include gabbroic pegmatites, bodies of melanogranophyres, granophyric segregations, clot-like granophyres, replacement anorthosites, dendritic anorthosites, and Wavy Pyroxene rock (e.g. Humphreys and Holness, 2010; Kays et al., 1981; Larsen and Brooks, 1994; McBirney and Sonnenthal, 1990; Sonnenthal, 1992; Wager and Deer, 1939; Wager and Brown, 1968). Here, I present a review of the literature on the late-stage liquid segregations, distinguishing between structures on the basis of the extent of liquid evolution.

5.1.12.1 Evolved late-stage segregations

The Skaergaard Intrusion is cut by a number of felsic bodies with a range of highly evolved compositions: i) acid granophyre (the Tinden Sill); ii) transitional granophyre (Sydtoppen); iii) transgressive granophyres; iv) clot-like granophyres; v) melanogranophyres; vi) segregation granophyres; and vii) anorthosites. The first three (i – iii) were identified by Wager and Brown (1968) and are associated with felsic material derived from the Precambrian country rocks; therefore, they will not be discussed further. The others rock types are each discussed in turn.

Clot-like granophyres (iv) occur exclusively in the MBS, and their origin has been much debated. Wager and Deer (1939) described them as xenoliths of felsic gneiss, ranging from centimetres in diameter to tens of centimetres. Thirty years later, Wager and Brown (1968) suggested they were products of fractional crystallisation. The subsequent textural, major element and trace element study by Kays et al. (1981) concluded that they were assimilated portions of gneissic country rock. However, Stewart and DePaolo (1990) reported no strong isotopic compositional similarities between the clot-like granophyres and the gneissic country rock. This issue remains unresolved.

Melanogranophyres (v) are characterised by abundant granophyre hosting elongate skeletal grains of Fe-rich clinopyroxene (Naslund, 1984). The melanogranophyres are in UZc of the LS and UZ' of the UBS, with the volume of melanogranophyre increasing towards the Sandwich Horizon (Wager and Brown, 1968). The morphology of the melanogranophyres range from discrete pods to lenses to sills,

1–2 m diameter (Wager and Brown, 1968). Tegner (1997) estimated the ratios of liquid that formed the LS:UBS:melanogranophyre as 74:24:2, 69:23:8, and 64:21:15 for UZa, UZb, and UZc, respectively. The melanogranophyre liquid is suggested to have separated from the bulk magma as an immiscible liquid during late-stage crystallisation (McBirney, 1975; McBirney and Nakamura, 1974).

Segregation granophyres (vi) are interstitial pockets of a fine-grained intergrowth between quartz and alkali feldspar, often at a eutectic point where the composition approximates to the orthoclase-albite-quartz ternary minimum (Bowen, 1928). They are interpreted as crystallised pockets (on the micron to millimetre scale) of interstitial liquid in the interstices created by the cumulate framework, which originated from liquids unmixing in the bulk magma (Holness et al., 2011; Larsen and Tegner, 2006), i.e. they represent the Si-rich end-member of an immiscible liquid conjugate. The segregation granophyres are associated with ilmenite intergrowths in the LZ and MZ (Holness et al., 2011); the titanomagnetite–ilmenite intergrowths represent the Fe-rich end-member of immiscible liquid conjugates. Granophyre segregations are associated with plagioclase-rich cumulate regions whereas the titanomagnetite–ilmenite intergrowth pockets are associated with olivine- and clinopyroxene-rich cumulate regions (Holness et al., 2011). Combined, the granophyre-rich and mafic-rich pockets represent up to 4·4 % (by area) of the LS (Stripp, 2009).

Late-stage anorthosites (vii) are discussed in the literature as a) dendritic anorthosites (McBirney and Sonnenthal, 1990; Sonnenthal, 1992) and b) 'replacement anorthosites' (Larsen et al., 1992; McBirney and Sonnenthal, 1990). The 'replacement anorthosites' are metre-scale structures comprised of almost monomineralic anorthosites, sometimes associated with mafic segregations. They form pods and lenses in the trough layering of UZa. The dendritic anorthosites occur on the surface of the magmatic layering plane and are composed of almost monomineralic anorthosites (Sonnenthal, 1992). Both types of late-stage anorthosite are suggested to be examples of local scale metasomatism caused by an aqueous fluid with a high HCl/HF fugacity ratio that reacted with the primary cumulus assemblage (McBirney, 1996; McBirney and Hunter, 1995; McBirney and Naslund, 1990; McBirney and Sonnenthal, 1990; Sonnenthal, 1992). Sonnenthal (1992) concluded that deformation of the crystal mush was important in the formation of the dendritic anorthosites. It has also been proposed that the 'replacement anorthosite' lenses crystallised from the felsic conjugate of an unmixed silicate liquid (Larsen and Brooks, 1994).

5.1.12.2 Less-evolved late-stage segregations

The less-evolved late-stage segregations in the Skaergaard cumulates comprise: i) gabbroic pegmatites; ii) mafic segregations; iii) Wavy Pyroxene rock; and iv) replacement pyroxenites. Gabbroic pegmatites have been described as coarse-grained micro-magma chambers, which crystallised from the margins inwards (Larsen and Brooks, 1994), and have been documented by numerous authors in LZ, MZ, and UZa (e.g. Larsen and Brooks, 1994; McBirney and Noyes, 1979; McBirney and Sonnenthal, 1990; Wager and Deer, 1939; Wager and Brown, 1968). The gabbroic pegmatites range from tens of

centimetres to metres in diameter, and generally form podiform pipes/chimneys in LZ with the major axis *perpendicular* to magmatic layering. Conversely in UZa, they form sills with the major axis *parallel* to magmatic layering (Larsen and Brooks, 1994; McBirney and Sonnenthal, 1990). Larsen and Brooks (1994) described three structural elements to the gabbroic pegmatites: a granophyric zone (found at the stratigraphically highest point in the podiform pegmatite), a gabbroic zone and the margin of the gabbroic zone. The gabbroic pegmatite morphology is more spherical in the MBS compared to the LS, and is on the metre-scale: the colloform banding wraps around the gabbroic pegmatites (Namur et al., 2013). Late-stage methane-rich and saline aqueous solutions are hypothesised to have been involved in the formation of the gabbroic pegmatites, from H_2O-NaCl-CH_4 fluid inclusions analysed in quartz, apatite and feldspar from gabbroic pegmatites in the upper part of MZ and UZ (Larsen et al., 1992).

Mafic segregations (ii) are found throughout the LS and MBS, and are typically paired with a felsic segregation (described as a 'replacement anorthosite'). The mafic segregations are on the tens of centimetre-scale and contain variable proportions of olivine, pyroxene, and magnetite. Like their felsic counterparts, the mafic segregations are suggested to result from localised metasomatism (McBirney, 1996; McBirney and Hunter, 1995; McBirney and Naslund, 1990; McBirney and Sonnenthal, 1990; Sonnenthal, 1992). It has been proposed that the mafic (ii) and felsic (anorthosite) segregations were two unmixed silicate liquids (Larsen and Brooks, 1994). McBirney and Sonnenthal (1990) did not identify an association between the gabbroic pegmatites and the mafic segregation, nor the felsic segregation.

There are many mineralogical similarities between the Wavy Pyroxene rock ((iii) see section 5.1.3), and the gabbroic pegmatites of the LS and MBS (Humphreys and Holness, 2010). Wager and Brown (1968) hypothesised that the Wavy Pyroxene rock melt-rich segregations were a nucleation effect parallel to the intrusion's thermal gradient. However, Humphreys and Holness (2010) argued that they formed by the tearing of poorly consolidated MBS crystal mush and were infilled with locally-derived interstitial liquid (see section 5.1.9).

'Replacement pyroxenites' (iv) are pyroxene-rich segregations of olivine and Ca-rich pyroxene with amoeboidal morphologies. Occurring on the metre to tens of metres-scale, they were named and documented by McBirney and Sonnenthal (1990) in the MBS, on Kraemer Island and Ivnarmiut Island and their formation has been compared to the processes forming skarns (McBirney and Sonnenthal, 1990). The 'replacement pyroxenites' boundaries cross-cut the model magmatic layering (McBirney and Sonnenthal, 1990).

5.1.12.3 Examples of late-stage liquid segregations in other layered intrusions

In the large, mafic-ultramafic layered intrusion of the Bushveld Complex in South Africa, discordant Fe-rich pegmatoidal pipes are suggested to form from the downwards drainage of dense, immiscible Fe-rich silicate magma through the cumulus sequence (Scoon and Mitchell, 1994). Many of these discordant, pipe- or tube-like bodies, particularly the large ones, are structurally controlled and occur in areas where the gabbroic cumulates have been disturbed (Viljoen and Scoon, 1985). Field relations suggest emplacement occurred while the layered cumulates were hot and incapable of brittle failure (Cawthorn et al., 2000). Two subgroups of mafic pegmatoidal pipes are distinguishable: an olivine-clinopyroxene pegmatite and an Fe-Ti oxide pegmatite (Scoon and Mitchell, 1994; Viljoen and Scoon, 1985). Zoned pegmatitic bodies, with a core of Fe-Ti oxide pegmatite, are stratigraphically transitional phase between the two subgroups (Scoon and Mitchell, 1994). With increased stratigraphic height in the Complex, the pegmatites become richer in Fe-Ti oxides (Viljoen and Scoon, 1985). The whole rock composition of the Fe-Ti oxide pegmatites is comparable to that of an Fe-rich immiscible liquid (Reid and Basson, 2002; Scoon and Mitchell, 1994), with a typical mineral assemblage of ferro-augite, olivine, magnetite, ilmenite, alongside local abundances of sulfides, Fe-amphibole and apatite (Cawthorn et al., 2000; Reid and Basson, 2002; Scoon and Mitchell, 1994; Viljoen and Scoon, 1985). For a given stratigraphic height in the Complex, the pegmatites are always more compositionally evolved, as measured in the major and trace element mineral chemistry. This is also seen in the Sr and Nd isotope data, the Mg# of the ferromagnesium silicates and the presence of magnetite on the liquidus (Reid and Basson, 2002). The pegmatitic bodies formed by magmatic replacement of the host cumulates by Fe-rich liquids draining down through the cumulates and accumulating (e.g. Bateman, 1951; Scoon and Mitchell, 1994). The Fe-rich liquids derived from within the crystallising cumulate pile (Viljoen and Scoon, 1985). Cawthorn et al. (2000) suggest that the dissolution of the host gabbro, rather than pure mechanical dilation, created the space for the emplacement of the bodies. The pegmatitic bodies may have resulted from the metasomatic replacement of pre-existing cumulates or they may have crystallised directly from the pegmatitic fluids derived from within the crystallising cumulate pile (Scoon and Mitchell, 1994). It is hypothesised that the Si-rich conjugate was reincorporated into the bulk magma, and so there is an absence of feldspar in the Fe-rich pegmatitic bodies (Scoon and Mitchell, 1994). Post-solidification, the bodies may have acted as vertical channels for low-temperature hydrothermal fluids to migrate through the intrusion (Cawthorn et al., 2000).

Other examples of late-stage segregations in layered intrusions include the dunitic and pyroxenitic bodies, which cross-cut the layered Stillwater Complex in Montana, USA. These coarse-grained, metre-scale bodies have been hypothesised to form from an aqueous rich fluid metasomatically altering harzburgites and pyroxenites to dunites, at temperatures near the solidus (Raedeke and McCallum, 1984). In the Kiglapait Intrusion (north Labrador), anomalously Fe-rich cumulates in the layered

sequence of the cumulates are interpreted to result from ponding of Fe-rich magmas on the chamber floor (Morse, 1996).

Comparisons have been made between the discordant, mafic, pegmatitic bodies of the Bushveld Complex, Stillwater, and Skaergaard Intrusions (McBirney and Sonnenthal, 1990; Raedeke and McCallum, 1984; Scoon and Mitchell, 1994). Scoon and Mitchell (1994) argue that these ultramafic rocks are all related to channelled infiltration, attributed to dense Fe-rich liquids, rather than more buoyant Si-rich liquids.

5.1.13 Temperature of the Skaergaard magma during crystallisation

The temperature of the magma determines the liquidus phases and the size of the silicate liquid immiscibility field (Charlier and Grove, 2012). Various methods have been used to constrain the temperature of crystallisation for the Skaergaard Intrusion. These include a consideration of the pressure of the ferrohedenbergite-ferrobustamite inversion (Lindsley et al., 1969); a model based on the solidus of adcumulates (Morse et al., 1980); a thermometer based on cumulus plagioclase composition (Kudo and Weill, 1970); the results of gabbro melting experiments at one-atmosphere pressure (McBirney and Naslund, 1990); and finally, the relationship between crystallisation temperature and plagioclase compositions described by the empirical linear relationship of T (°C) = 899 + 3.6 An; 1σ = 20 °C (Thy et al., 2009). The results of studies constraining magma temperatures down the liquid line of descent are summarised in Table 5.2.

Published studies aimed at determining crystallisation temperatures for the late-stage Skaergaard liquids have used geothermometers such as the augite-ilmenite thermometer (Bishop, 1980), the two-feldspar thermometer (Price, 1985), and the plagioclase–hornblende thermometer (Larsen and Tegner, 2006). The temperatures calculated for the late-stage liquids by Larsen and Brooks (1994); and Larsen and Tegner (2006) are significantly lower (>100°C) than those of other studies (Table 5.2). It is difficult to constrain the temperature at which the replacive symplectites formed (Holness et al., 2011; Stripp, 2009), but Holness et al. (2011) suggest that the microstructures grew while residual melt remained. The compositions of coexisting two-pyroxene and olivine–clinopyroxene vermicule pairs from symplectitic intergrowths suggest temperatures of 824°C and 873°C respectively at the Triple Group Level in the MZ (QUILF; Andersen et al. (1993)). This is lower than the UZc bulk magma temperature but higher than the granitic eutectic minimum (680-660°C; Larsen and Tegner (2006)). The temperatures in Table 5.2 are generally consistent with experimentally determined temperatures at which tholeiitic magmas reach the silicate liquid immiscibility binodal (Charlier and Grove, 2012).

Table 5.2 Published temperature (°C) estimates for the crystallisation of the Skaergaard Layered Series and the late-stage liquids.

Layer	Layered Series temperature (°C)					Late-stage liquids temperature (°C)	
	Lindsley et al. (1969)	*Morse et al. (1980)*	*McBirney and Naslund (1990)*	*Morse (2008b)*	*Thy et al. (2009)*	***Margin of gab peg*** *Larsen and Brooks (1994)*	***Pegmatitic granophyre*** *Larsen and Tegner (2006)*
UZc	980-950		1007		1000		
UZb			1062	1059			
UZa			1089	1083	1063		
MZ		1100	1105	1112		1014	
LZc			1124	1121			824
LZb		-	1145	1173	1127	1006 (859 for central gab peg)	829
LZa		1230	1161			1002	780
HZ				1191	1160		

5.1.14 Post-magmatic evolution of the Skaergaard Intrusion

During the last stages of solidification, a hydrothermal system formed in the cumulate rocks and surrounding host rocks; hydrothermal fluids continued to circulate for a minimum of 300,000 years (Norton and Taylor Jr, 1979). The hydrothermal circulation is postulated to have commenced between 700°C and 800°C (Norton et al., 1984). The degree of alteration can be traced using oxygen isotopes (Norton and Taylor Jr, 1979; Taylor Jr and Forester, 1979), and is most intense around fractures and dykes (Bird et al., 1986; Taylor Jr and Forester, 1979). The alteration is most prominent in the south and east of the intrusion, where the cumulate rocks are in contact with the overlying, highly fractured basalt lavas that form the roof of the intrusion and the upper part of the eastern wall (Norton and Taylor Jr, 1979). The hydrothermal alteration led to a significant re-setting of oxygen and hydrogen isotope ratios in the uppermost parts of the intrusion (Taylor Jr and Forester, 1979). Hydrothermal alteration of the cumulate rocks in contact with the gneiss (i.e. around the western and northern edge of the intrusion) is more limited. The degree of oxygen isotope ratio variation is a function of the temperature of the hydrothermal system and the amount of water that moved through the fractures.

5.2 Chapter structure: Late-stage segregation evolution in the Skaergaard Intrusion

Previous studies of late-stage segregations in the Skaergaard Intrusion have been focused on particular localities in the intrusion, with minimal consideration of the role of silicate liquid immiscibility in controlling the migration rates and pathways of late-stage segregations in the crystal mush. Here, I present a synthesis of the behaviour of late-stage segregations in the Skaergaard mush, inferred from field observations, petrology, whole rock geochemistry and mineral chemistry. I documented a variety of late-stage structures in the LS and the MBS of the Skaergaard Intrusion between 07/08/2017 and 07/09/2017; localities sampled are shown in Fig. 5.1 and detailed in Appendix Table 5.A. I establish field relationships between the different types of segregation and link their morphological and whole rock compositional variation to the physical properties of the crystal mush and the progressive compositional evolution of the bulk magma. I also examine changes in element concentrations in plagioclase grains from the late-stage segregations.

There have been a number of different names given to the Skaergaard late-stage liquid structures (see section 5.1.12), yet little attempt has been made to develop a holistic approach to understanding them. The various rock names in the literature range from process-based to observation-based. I will use observation-based names in my fieldwork observations. The observations below detail how the morphology of the gabbroic pegmatites evolve up-stratigraphy as a function of mush thickness in the LS. I then detail the relationship between the gabbroic pegmatites and the paired mafic and felsic segregations, before describing how the modal mineralogy of the paired mafic and felsic segregations evolve up-stratigraphy, with each conjugate liquid tending towards silicate liquid immiscibility end-members (Fe-rich and Si-rich end-member). New geochemical and petrological data for the late-stage segregations are correlated with the new field relationships to provide an integrated model for the formation of the late-stage segregations.

5.3 Fieldwork observations

5.3.1 Layered Series

LZa hosts rare podiform pegmatites, whose major axis cuts the magmatic layering at a high angle (Larsen and Brooks, 1994). The LZa pegmatites reach up to 1.5 m in diameter with sharp boundaries. Near the coastline of Uttental Plateau (N 68°12.291' W 31°43.369'), four distinct modal assemblages were observed in LZa pegmatites: (A) olivine pyroxenite comprising medium-grained olivine and pyroxene (0.3–0.8 cm) with interstitial oxide; (B) coarse-grained gabbro comprising pyroxene with plagioclase (1–2 cm); (C) coarse-grained rock comprising plagioclase (0.5–2 cm) and large euhedral

amphibole grains <8 cm long; (D) medium-grained plagioclase-rich rock containing pyroxene and oxide oikocrysts. The contacts separating each assemblage are sharp. Where visible, the olivine-pyroxenite preferentially occurs at the stratigraphic base of the pegmatite. LZa is the only location where all four components were found (Fig. 5.3). There is no distortion of the surrounding host gabbro fabric.

The pegmatites of **LZb** are also podiform but are more common and larger than those in LZa, reaching 5 m by 2 m (e.g. N 68°12.133' W 31°42.036'). The LZb pegmatites are dominated by a gabbroic assemblage of coarse-grained pyroxene, plagioclase and dendritic magnetite (B). Zones rich in coarse-grained plagioclase (C) are often associated with interstitial quartz and miarolitic cavities, which preferentially occur at the stratigraphic top of the pegmatite. Despite the notable abundance of the podiform gabbroic pegmatites in LZb, they do not disrupt the host gabbro foliation. Tendrils of gabbroic pegmatite (0.2 m wide) branch out from some podiform pegmatites, running parallel with the magmatic layering (Fig. 5.4). The pegmatites also show evidence of upwards migration by a combination of brittle and ductile behaviour: a 2.2 m by 0.6 m podiform pegmatite crystallised parallel to magmatic layering yet is associated with oval-shaped pods (~0.4 m diameter) cutting the modal layers up-dip by 3 m vertical height (N 68°12.322' W 31°41.988'; Fig. 5.5).

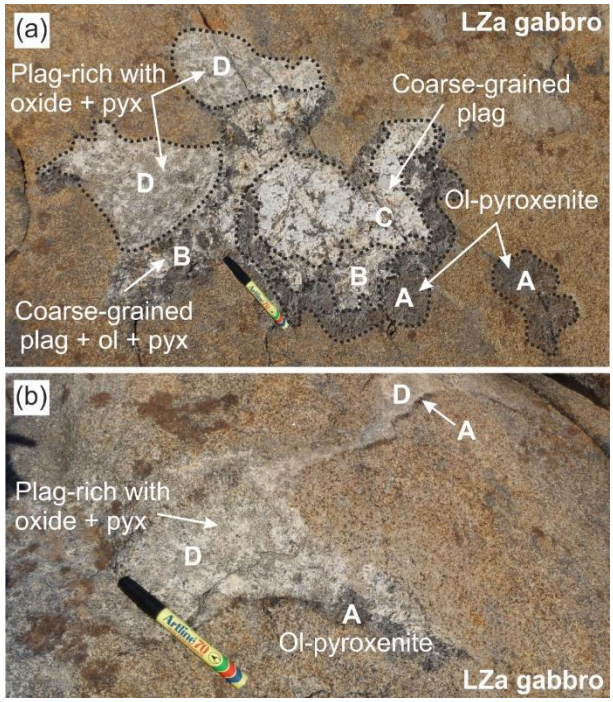

Figure 5.3 Gabbroic pegmatites in LZa (a) metre-scale late-stage segregation with four discrete assemblages and sharp contacts with the surrounding gabbro. (b) Sub-metre late-stage segregation, with two distinct compositions. Note the olivine pyroxenite is at the lowest stratigraphic level in both (a) and (b). Annotated letters correspond to: A = olivine pyroxenite comprising medium-grained olivine and pyroxene with interstitial oxide; B = coarse-grained gabbro comprising pyroxene with plagioclase; C = coarse-grained rock comprising plagioclase and large euhedral amphiboles; D = medium-grained plagioclase-rich rock containing pyroxene and oxide oikocrysts.

The pegmatite mineral assemblage in **LZc** is comprised of pyroxene and oxides (associated with the pegmatite margins), together with plagioclase and quartz. The pegmatites in LZc are podiform with sharp boundaries against the host gabbro. An interesting exception is provided by a small vertical diapir-shaped gabbroic pegmatite, about 0.1 by 0.3 m (Fig. 5.6) found at the LZb–LZc boundary on Kramer Island (N 68°11.538' W 31°43.512'). Large plagioclase grains (1–2 cm long) cut the boundary between pegmatite and host gabbro; the alignment of the pegmatitic plagioclase is continuous with the host gabbro foliation. The modal mineralogy of the gabbroic pegmatite matches that of the LZc gabbro.

Wispy lenses of stratified mafic-rich and near monomineralic felsic-rich segregations are found stratigraphically above the gabbroic pegmatites in the LZ. In **LZa**, composite wispy lenses of mafic- and felsic-rich segregations occur <2 m above the gabbroic pegmatites, and often cut the magmatic layering. In **LZb**, the wispy lenses are locally found up to 5.5 m from the stratigraphic top of the gabbroic pegmatites (locality N 68°11.575' W 31°43.520'; Fig. 5.7). Similarly in LZb, a large anorthosite diapir (Figure 4b in Larsen and Brooks, 1994) lies 5 m above a 3 m by 4 m podiform gabbroic pegmatite body (Fig. 5.4).

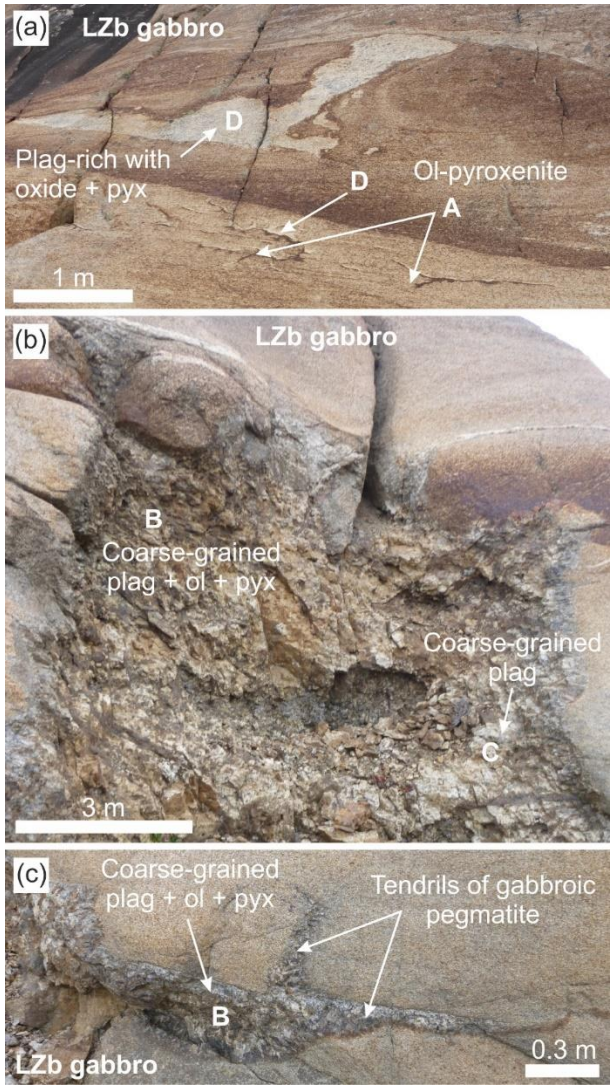

Figure 5.4 Late-stage segregation structures in LZb. (a) Felsic-rich diapir deforming the magmatic layering, with conjugate mafic-rich and felsic-rich segregations below the diapir. Note the mafic-rich segregations are stratigraphically lower than the felsic-rich segregations. (b) Coarse-grained gabbroic pegmatite with sharp boundaries against the LZb gabbro. The magmatic layering is not deformed. (c) Coarse-grained gabbroic pegmatite tendrils propagating through LZb gabbro. Annotated letters as defined for Fig. 5.3.

The wispy lenses range in size from 0.2–0.6 m along the major axis, with aspect ratios generally >1:6. The modal mineralogy of the stratified wispy lenses is suggestive of crystallisation from two liquids. The base of the stratified wispy lenses is always the mafic-rich segregation: an olivine-pyroxenite with interstitial magnetite and plagioclase. The top is always the felsic-rich rock: an anorthosite with oikocrysts of pyroxene and oxide (Fig. 5.8; N 68°12.245' W 31°43.367'). The plagioclase grains of the wispy lenses have a lower aspect ratio compared to the plagioclase of the host gabbro. The interstitial oxide content of the wispy lenses increases up stratigraphy, as does the size of the plagioclase laths (potentially reflecting the plagioclase size difference between the LZa and LZb gabbros). In **LZc**, the mineralogy of the wispy lenses notably tends towards more extreme end-members: the mafic-rich rock is oxide-dominated, while the felsic-rich rock is an anorthosite with magnetite dendrites but no pyroxene oikocrysts.

The majority of the wispy lenses in LZa are composite, containing both a basal mafic-rich rock and an overlying felsic-rich rock, whereas in LZb the lenses can be separated on the centimetre-scale (Fig. 5.9).

This separation develops up stratigraphy, and in LZc it is typical for the two components to be separated by more than 0.5 m.

The morphology of a single component wispy lens is a function of its modal assemblage. The felsic-rich lenses extend outwards and upwards along stratigraphic horizons, cutting magmatic layering (for up to 20 m), and covering a large area (in a 2D plane; Fig. 5.8); the 3D expression is generally confined to an along strike trend. The mafic-rich lenses extend down-stratigraphy, with limited side-ways expression (Fig. 5.10). The wispy lenses are associated with ductile deformation of the surrounding host LZ gabbro. Examples from LZb include: felsic-rich wispy lenses surrounded by strongly aligned plagioclase in the host gabbro (Fig. 5.11); a felsic-rich diapir disrupting magmatic layering (Fig. 5.4a); mafic-rich and felsic-rich segregations forming branching structures that deform the surrounding mush over a vertical stratigraphic distance of >4 m (N 68°11.577' W 31°43.477'; Fig. 5.12).

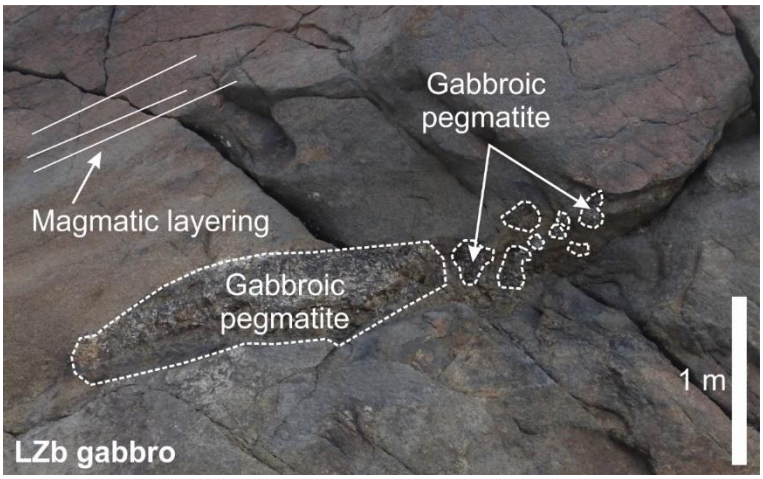

Figure 5.5 Podiform gabbroic pegmatite with smaller blobs of gabbroic pegmatite 1 m up-section in LZb.

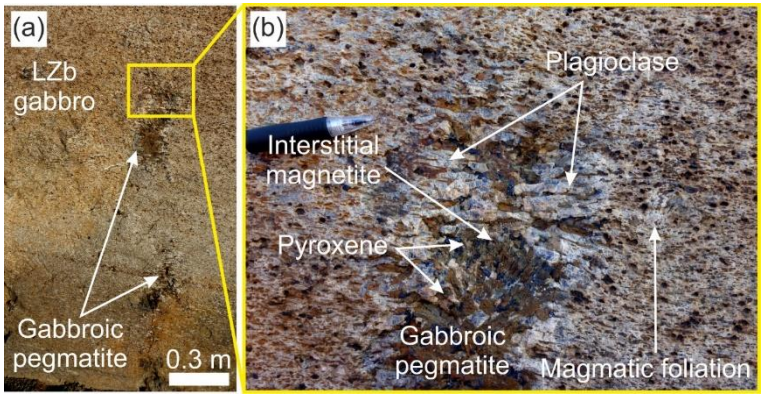

Figure 5.6 (a) Gabbroic pegmatite in LZb gabbro. (b) Coarse-grained plagioclase cross-cut the boundary of the gabbroic pegmatite and follow the fabric of the LZb gabbro.

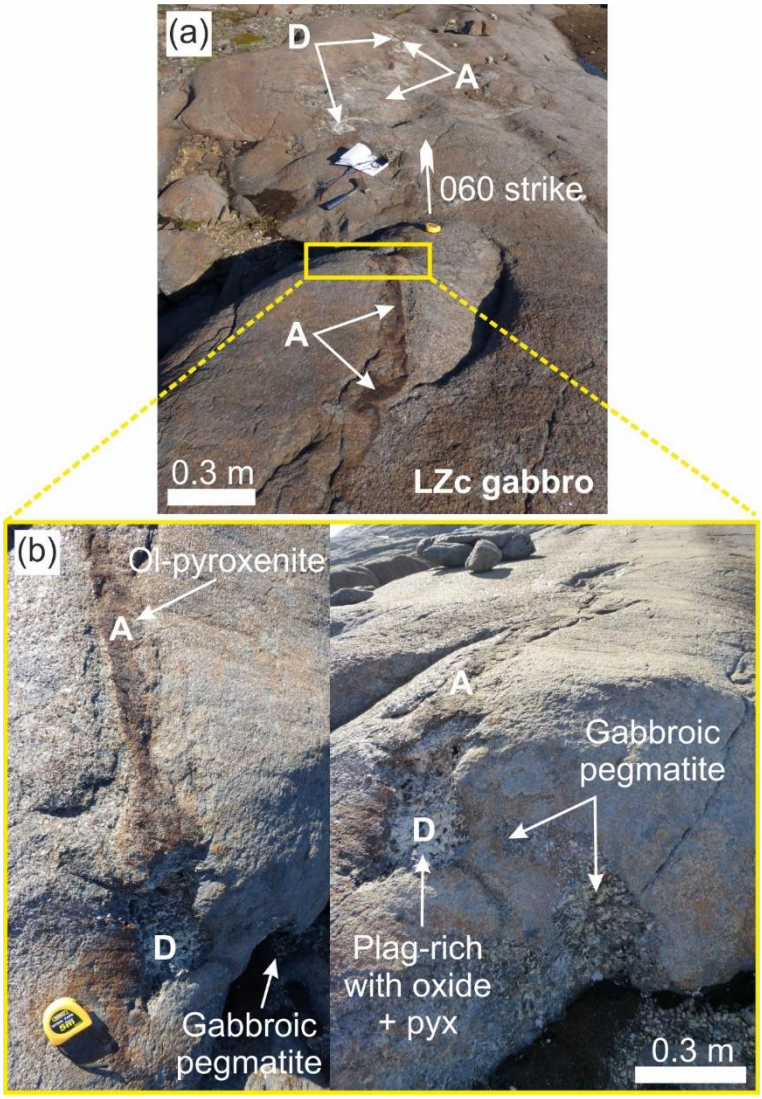

Figure 5.7 (a) Along strike expression of felsic-rich and mafic-rich segregations cutting the LZc gabbro; (b) the mafic-rich and felsic-rich segregations are located up-stratigraphy of the (c) podiform gabbroic pegmatite. The mineralogy of the annotated letters is detailed in Fig. 5.3: A is referred to as the mafic-rich segregation; D is referred to as the felsic-rich segregation.

Mafic-rich and felsic-rich wispy lenses are associated with fallen roof blocks in the LZ (e.g. N 68°12.271' W 31°41.448'; Fig. 5.13). The mafic-rich material is at the base, while the felsic-rich material lies above.

No gabbroic pegmatites were observed in **MZ**. I found examples of wispy lenses of stratified mafic-rich and felsic-rich rock, which run parallel with the magmatic layering at N 68°11.133' W 31°41.383'; however, these are uncommon. As documented in LZb and LZc, the two components form both composite wisps and separated wisps (Fig. 5.14).

UZa hosts gabbroic pegmatites that are morphologically distinct from those in LZ. The gabbroic pegmatites form dykes (5–15 cm wide), connected to localised 30 x 10 m gabbroic pegmatite sills (~20

cm thick) extending parallel to planar magmatic layering, and spaced every ~10 m of stratigraphy (Larsen and Brooks, 1994). These structures are abundant near the 'North House foundations' at N 68°10.075' W 31°43.303' (Fig. 5.15). There is a notable absence of wispy lenses in the lower part of UZa.

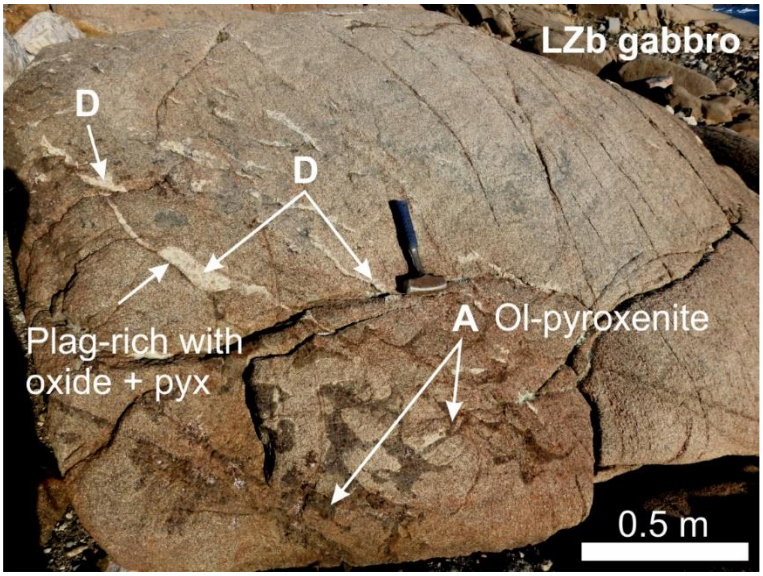

Figure 5.8 Felsic-rich and mafic-rich segregations in LZb gabbro. The felsic-rich wisps migrate laterally and are located stratigraphically up-section relative to the mafic-rich segregations. The mineralogy of the annotated letters is detailed in Fig. 5.3: A is referred to as the mafic-rich segregation; D is referred to as the felsic-rich segregation.

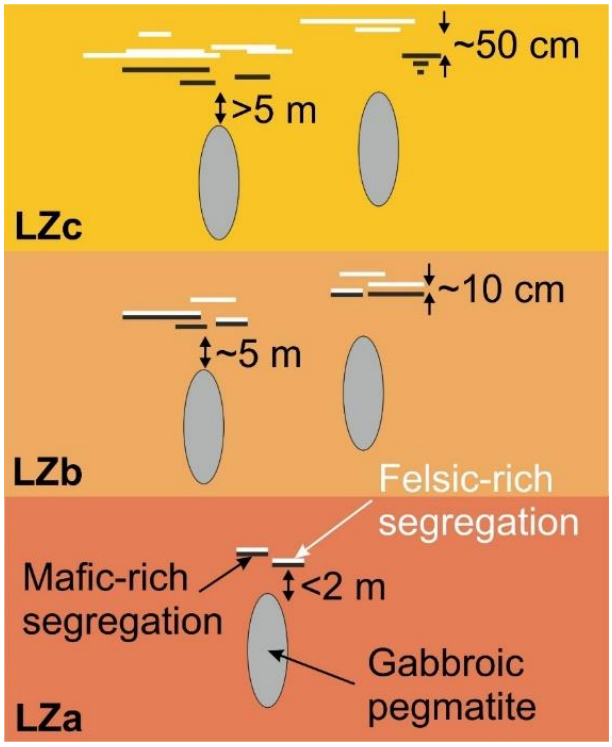

Figure 5.9 A schematic cartoon summarising the key field observations of the segregated mafic-rich and felsic-rich wispy lenses, and their association with the gabbroic pegmatites in the LZ.

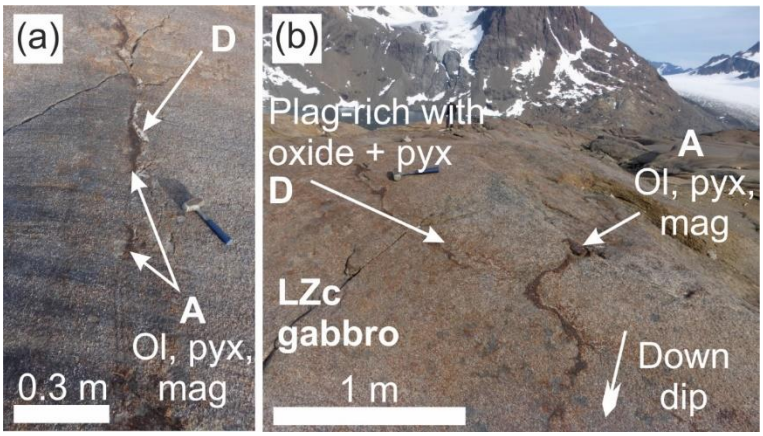

Figure 5.10 (a) Conjugate mafic-rich and felsic-rich segregations in LZc gabbro. (b) The mafic-rich lenses extend down-stratigraphy, with limited side-ways expression. The mineralogy of the annotated letters is detailed in Fig. 5.3: A is referred to as the mafic-rich segregation; D is referred to as the felsic-rich segregation.

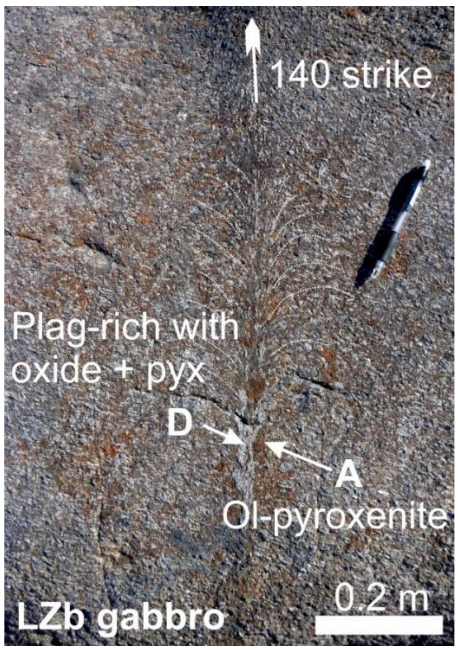

Figure 5.11 The felsic-rich and mafic-rich segregations distort the surrounding LZb gabbro. The mineralogy of the annotated letters is detailed in Fig. 5.3: A is referred to as the mafic-rich segregation; D is referred to as the felsic-rich segregation.

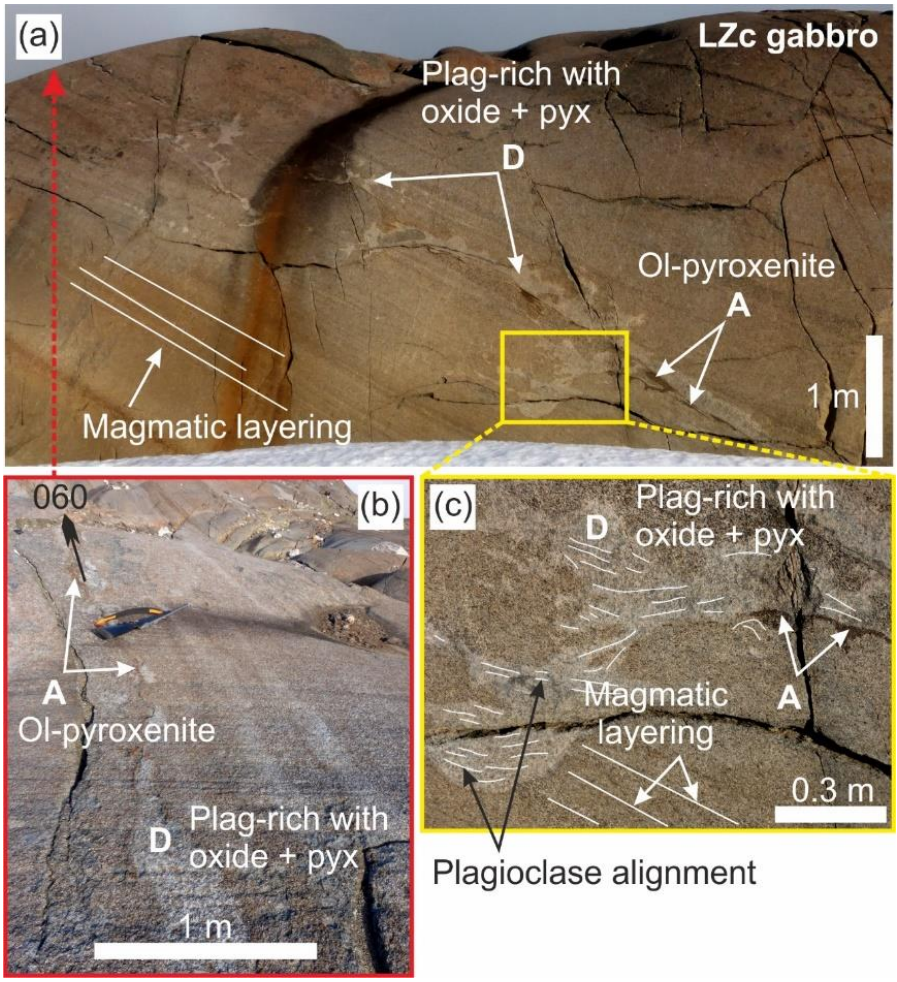

Figure 5.12 (a) Felsic-rich segregations extend along magmatic layering and cross-cut the magmatic layering of the LZc gabbro. (b) The along strike propagation of the felsic-rich and mafic-rich segregations. (c) Alignment of the plagioclase laths in the felsic-segregation is distinct from the magmatic layering of the LZc gabbro. The mineralogy of the annotated letters is detailed in Fig. 5.3: A is referred to as the mafic-rich segregation; D is referred to as the felsic-rich segregation.

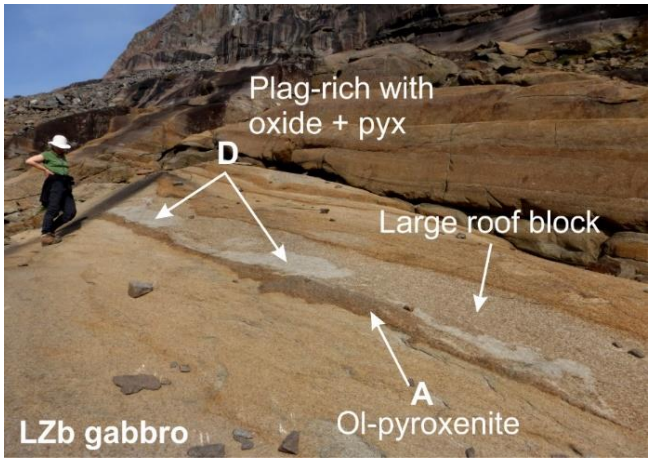

Figure 5.13 Roof block in LZb gabbro. The roof block has been intruded by felsic-rich segregations, with mafic-rich segregations along the base. The mineralogy of the annotated letters is detailed in Fig. 5.3: A is referred to as the mafic-rich segregation; D is referred to as the felsic-rich segregation.

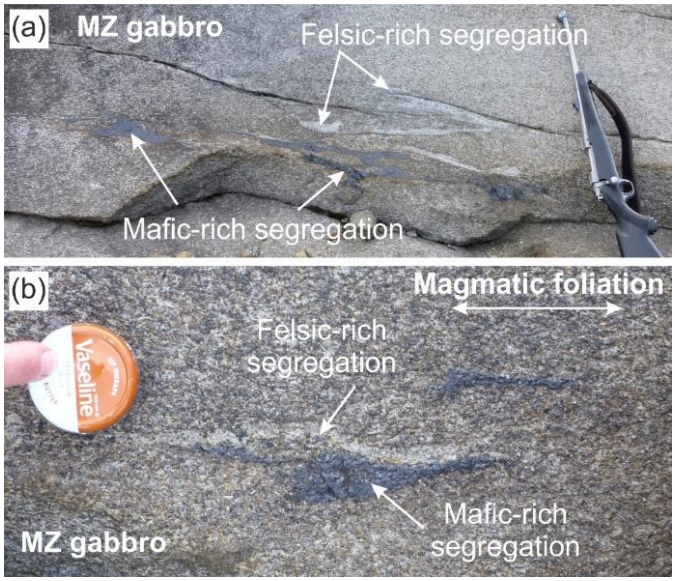

Figure 5.14 (a) Felsic-rich and mafic-rich segregations in the MZ, with the felsic-rich segregations stratigraphically up-section. (b) Conjugate segregations with magnetite dominated mafic-rich segregations.

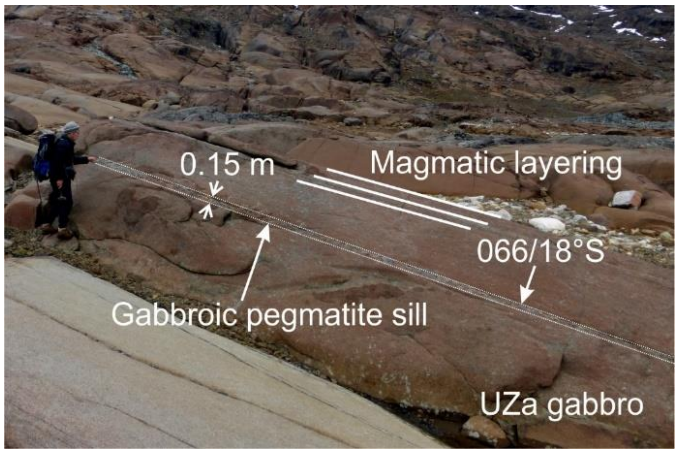

Figure 5.15 Gabbroic pegmatite sill running parallel with the magmatic layering of the UZa gabbro. There are no mafic-rich or felsic-rich segregations associated with the gabbroic pegmatite sill.

The upper part of UZa hosts the iconic trough layering of the Skaergaard Intrusion (Irvine and Stoeser, 1978; Irvine et al., 1998; Vukmanovic et al., 2018; Wager and Brown, 1968). The onset of trough layering in the UZa stratigraphy occurs just above the abrupt appearance of elongate, needle-like plagioclase, 1–2 cm in length, in the UZa gabbro at a clearly-defined stratigraphic horizon (Holness 2017 pers. comm.). Above this horizon, the clearly identifiable abundant elongate plagioclase grains are homogeneously distributed throughout the UZa gabbro.

The sill-like gabbroic pegmatites and feeder dykes do not penetrate the trough layering in the upper part of UZa. Instead, the gabbroic pegmatites in the upper part of UZa revert to the metre-scale podiform

morphology typical of pegmatites in LZa and LZb. The gabbroic pegmatites are abundant on the margins of the troughs, forming a 'pegmatite field' extending 15 m outwards from the trough margin, but are absent within the troughs themselves (Fig. 5.16). The pegmatite fields associated with each set of trough layers are separated along strike by zones of undisturbed UZa gabbro.

The gabbroic pegmatites in the UZa trough layering horizon are predominantly comprised of lithology (B) and (C) (as defined for gabbroic pegmatites in LZa – see section start). Some gabbroic pegmatites have associated copper staining. The gabbroic pegmatites associated with the trough layers are larger than those in LZ, ranging from 0.2–15 m along the major axis. They are largest in the centre of each pegmatite field (Fig. 5.16). The pegmatite fields become smaller, and the number of pegmatites they contain decreases, as the margin of the intrusion is approached.

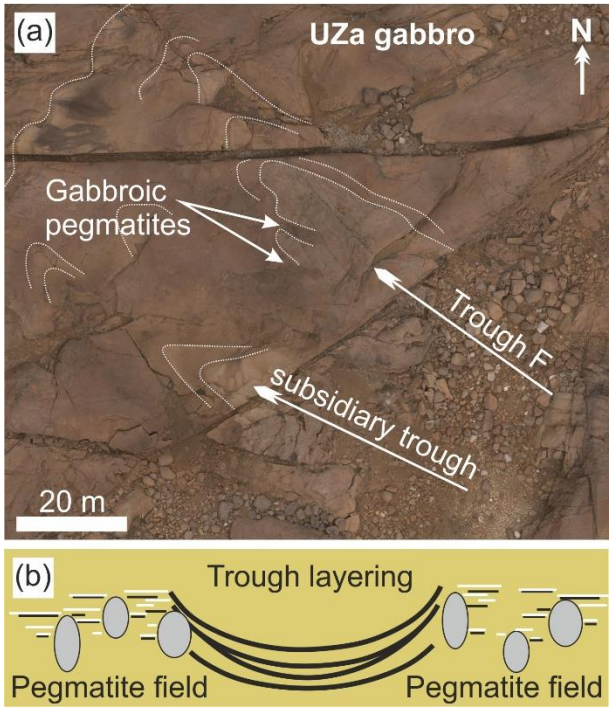

Figure 5.16 (a) Drone photograph (courtesy of Jens Andersen) of the UZa trough layering, focused on Trough F. The gabbroic pegmatites are located along the trough margins. (b) Cartoon schematic of the gabbroic pegmatite fields either side of the UZa trough layering.

Wispy lenses are associated with the gabbroic pegmatites in the trough layering horizon. The wispy lenses are located directly above and alongside the gabbroic pegmatites. This contrasts with the relationship observed in LZ, in which the wispy lenses were 5-10 m stratigraphically above the gabbroic pegmatites. Nevertheless, the fabric of the gabbro surrounding the wispy lenses is deformed. The mafic-rich segregations of the wispy lenses have a higher oxide proportion than the mafic-rich segregations of LZc; the felsic-rich segregations of the wispy lenses remain anorthositic.

Dendritic anorthosites, as described by McBirney and Sonnenthal (1990); and Sonnenthal (1992), occur in the pegmatite fields on either side of the trough layering in UZa. These thin (~5 mm) dendritic structures are concordant with the magmatic layering of the trough layers, extending for 0.5–16 m along their major axis. The dendritic structures are composed of plagioclase and interstitial magnetite, with an associated mafic-rich component comprising magnetite with olivine and pyroxene (analogous to the felsic-rich and mafic-rich wispy lenses). Ten separate dendritic structures were studied from twelve pegmatite fields. They are invariably connected to the stratigraphic top of nearby gabbroic pegmatites (Fig. 5.17), in clear contradiction to McBirney and Sonnenthal (1990) who claimed "no direct connection between these pegmatites and dendrites". However, there is no quantifiable relationship between the apparent 2D exposed size of the gabbroic pegmatite and the abundance and size of the associated dendritic structures.

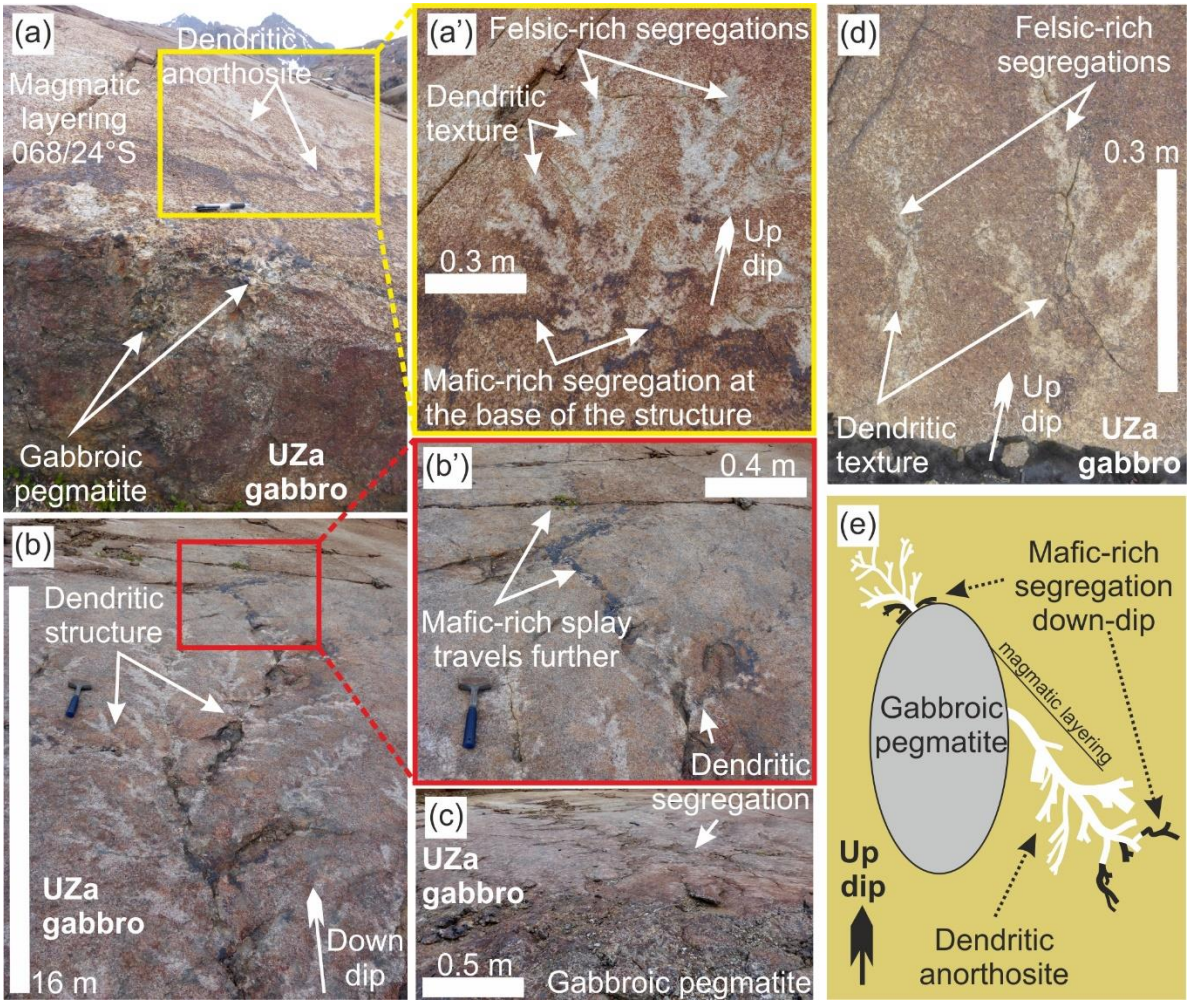

Figure 5.17 (a) The felsic-rich and mafic-rich segregations are up-dip of the gabbroic pegmatites, (a') the segregations form dendritic structures along the magmatic layering. Note the mafic-segregation is always located down-dip. (b) the dendritic structures can extend for up to 16 m and (b') the mafic-rich segregations are located down-dip. (c) the dendritic structures occur where the gabbroic pegmatite intersects a well-defined magmatic layer. (d) felsic-rich segregation up-dip with minimal mafic-rich component. (e) cartoon schematic showing the relationship between the gabbroic pegmatite, the strong magmatic layering of UZa trough layering and the felsic- and mafic-rich segregations, with the mafic-rich segregation always down-dip.

The planes of the magmatic layering containing the dendritic structures have dips ranging between 14–24°S. Sonnenthal (1992) reported that the branches of the anorthosite dendrites point up-dip; however, new fieldwork evidence documents a variety of orientations (Table 5.3). Crucially, the mafic-rich component of the dendrites is always oriented down-dip of the felsic-rich component (Fig. 5.17).

UZb does not host gabbroic pegmatites, but does contain rare wispy lenses of felsic-rich and mafic-rich segregations (on the centimetre- to metre-scale). The felsic-rich segregations are coarser-grained than those in UZa, and are comprised of plagioclase, magnetite, pyroxene and amphibole, often surrounded by a rusty coloured halo. Numerous felsic-rich segregations are exposed on an eroded surface in the lower part of UZb (N 68°09.727' W 31°42.302'). The segregations comprise ~3% of the 2D area.

At higher levels in the stratigraphy, UZb has packets of slumped and deformed gabbro (0.5–2 m thick), which can be traced laterally for tens of metres (e.g. N 68° 9.705' W 31° 42.220'; N 68° 9.700' W 31° 42.224'). Felsic-rich and mafic-rich segregations are preferentially found in these disrupted horizons, with mafic-rich segregations typically showing evidence for downwards migration over 1–2 m through the deformed stratigraphy (Fig. 5.18).

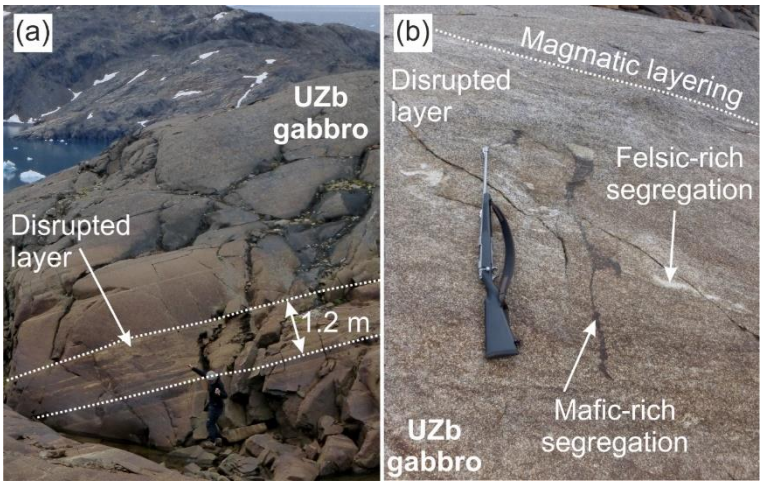

Figure 5.18 (a) In UZb gabbro there are metre-scale laterally continuous disrupted and deformed layers. (b) Within the disrupted layers there are felsic-rich and mafic-rich segregations; the mafic-rich segregation migrates stratigraphically downwards.

Stratigraphically above the deformed horizons of UZb there is strong primary modal layering, which is laterally continuous for tens to hundreds of metres. The mafic component of the modal layering forms a continuous basal layer, tens of centimetres thick; it is overlain by the felsic component. Intriguingly, and of relevance to this work, the felsic component forms tendrils rising off the top of the basal mafic layer, analogous in morphology to sedimentary flame structures in a compacting mudstone. This illustrates the differential properties (density, viscosity) of two contrasting compositional assemblages.

Within **UZc** are the melanogranophyres of Wager and Brown (1968) – see section 5.1.12. The assemblages of these late-stage segregations are comparable to that of the LZ gabbroic pegmatites and

associated wispy lenses. The melanogranophyres form pegmatitic, layer-conformable, 300 m wide by 0.2 m thick sills dominated by plagioclase, with some pyroxene, oxide and amphibole (e.g. locality N 68°09.750' W 31°41.307'). The sills thin towards their margins with no associated change in grain size (Fig. 5.19). Other pegmatitic melanogranophyre bodies in the same horizon of UZc have a podiform morphology (typically 1 m by 3 m), with the major axis cutting the magmatic layering. The stratigraphically highest part of the podiform pegmatite is a segregated, medium-grained plagioclase assemblage with interstitial pyroxene. This suggests the pegmatitic bodies of UZc, referred to in the literature as melanogranophyres, are analogous to the gabbroic pegmatites from stratigraphically lower in the LS, and henceforth will be discussed as part of the same family of features.

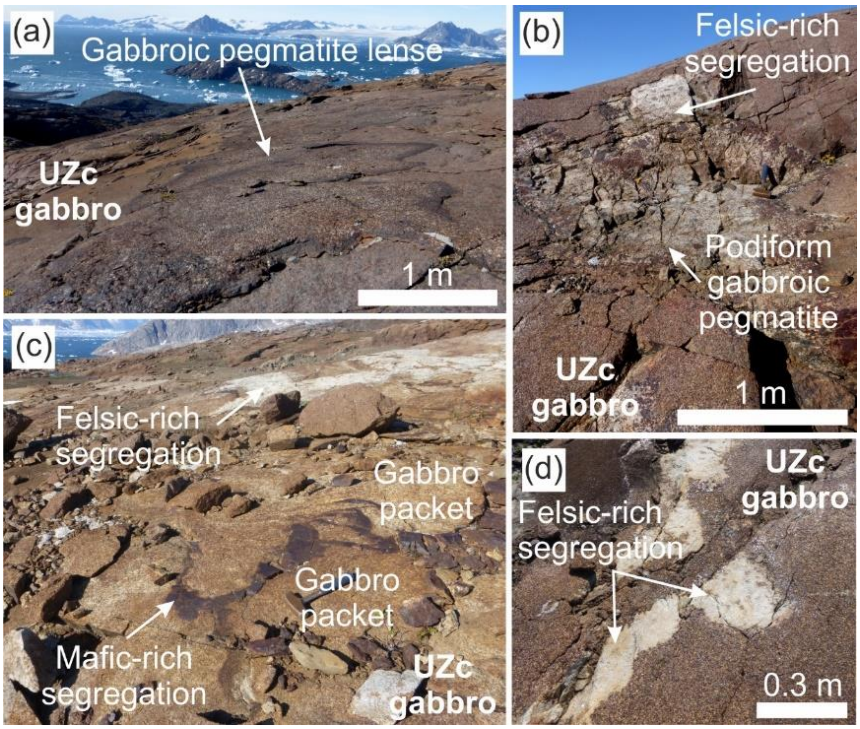

Figure 5.19 (a) The gabbroic pegmatite lense follows the magmatic layering of the UZc gabbro. (b) Podiform gabbroic pegmatites cross-cut the magmatic layering of UZc gabbro. (c) Mafic-rich and felsic-rich segregations surrounding UZc gabbro packets. (d) Felsic-rich segregations with sharp contacts against the UZc gabbro.

As in UZb, mafic-rich segregations are associated with deformation of the UZc gabbro. At locality N 68°09.794' W 31°41.036' there is a 20 by 30 m area of mafic-rich and felsic-rich segregations within a slumped layer of UZc gabbro in which the mafic-rich segregations extend 3 m downwards. The pathways created by the mafic-rich segregations show evidence of having caused brittle deformation to the surrounding gabbro, which appears to now be formed of disrupted blocks of otherwise foliated cumulates (Fig. 5.19c). In contrast, the felsic-rich segregations are laterally extensive along the magmatic layering, with minimal evidence of disruption to the UZc gabbro. Locally, a felsic-rich rock forms a thin layer (<10 mm thick) below the pegmatitic melanogranophyre lenses, e.g. at locality N 68°09.745' W 31°41.262'.

Table 5.3 Field data collected on dendritic anorthosite structures that lie concordantly along magmatic layering, and which are associated with gabbroic pegmatites.

Longitude (decimal deg)	Latitude (decimal deg)	Strike of plane	Dip of plane	Dendrite propagation trend	Dendrite growth direction relative to slope
31.72511667	68.16433333	080	20	315	Up slope
31.7231	68.16456667	068	24	21	Up slope
31.72301667	68.16456667	068	24	30	Up slope
31.72298333	68.16451667	078	20	354	Up slope
31.72311667	68.16461667	074	18	80	Along plane
31.72291667	68.16468333	064	20	150	Down slope
31.72213333	68.16468333	094	18	24	Up slope
31.7219	68.16468333	070	22	162	Down slope
31.72221667	68.16473333	095	15	140	Along plane
31.72735	68.164	055	14	240	Along plane

5.3.2 Upper Border Series and roof zone

My observations of the UBS were confined to fallen boulders and a single locality. **LZa'** gabbro is cut by gabbroic pegmatites and granophyre: the two are not observed in the same locality. A boulder of LZa' at N 68°11.120' W 31°41.386' contains a linear, 20 cm wide gabbroic pegmatite cutting the host gabbro (Fig. 5.20). The gabbroic pegmatite has a modal mineralogy consistent with that of LZb gabbro, but in this pegmatite, pyroxene did not nucleate on its margins, as is typical in the LS.

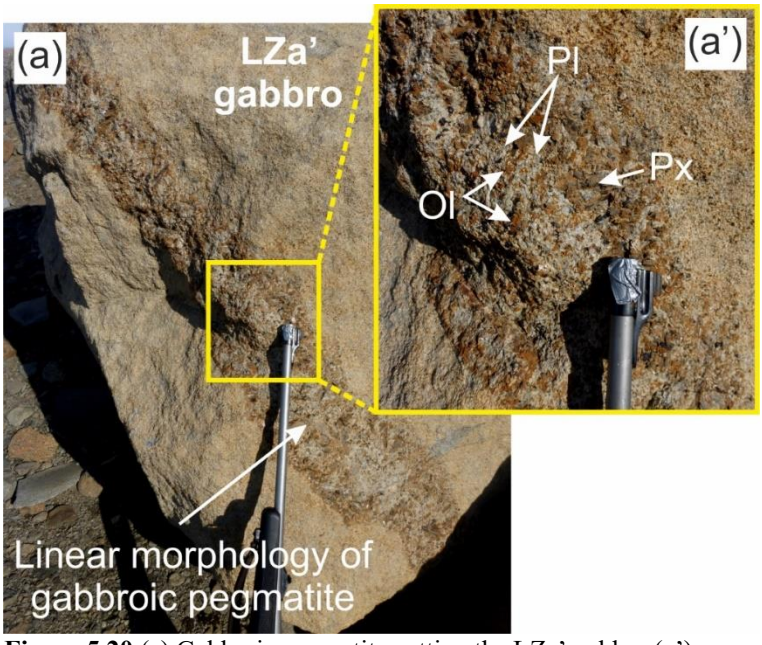

Figure 5.20 (a) Gabbroic pegmatite cutting the LZa' gabbro (a').

Close to the Brødregletscher glacier (locality N 68°08.031' W 31°42.505'), boulders of LZa' are cut by a number of late-stage features with a range of compositions including 2–10 cm wide dykes of fine-grained granophyre with large (<5 cm) green-blue euhedral amphiboles, and discontinuous felsic-rich

pods and lenses. The LZa' host gabbro locally displays evidence of brittle failure as exemplified by the sharp fracture pattern of the granophyre dykes.

At the roof zone contact of the intrusion with the Palaeocene basalt, close to the Brødregletscher glacier (locality N 68°07.759' W 31°42.407'), there is a network of sharply-defined granophyre-filled fractures, 1–2 cm wide. Some of the fractures are traceable to rounded granophyre diapirs, with well-defined boundaries (Fig. 5.21). In the larger fractures (5 cm wide), plagioclase and amphibole preferentially nucleate on the margins, with granophyre in the centre.

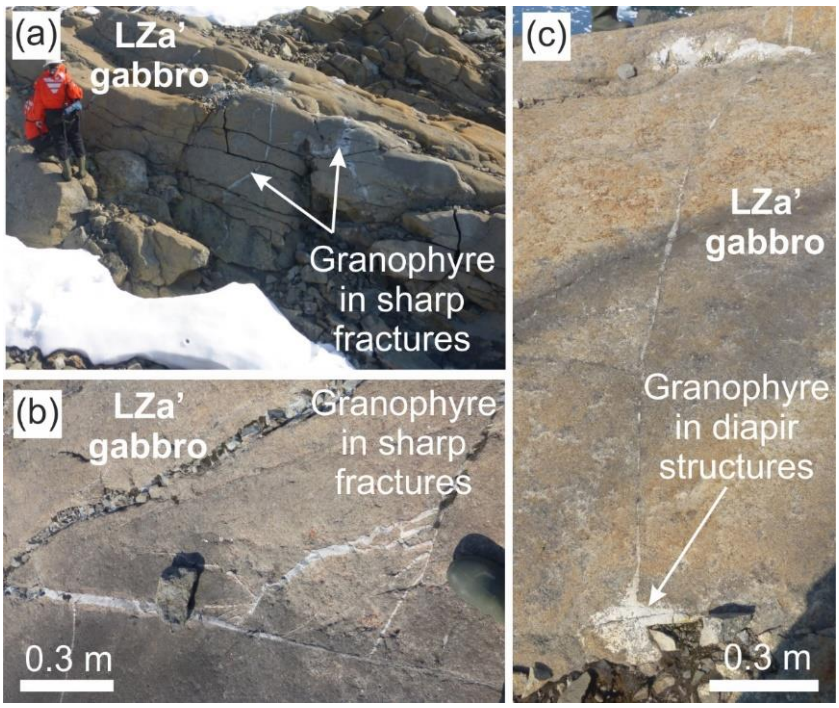

Figure 5.21 Roof zone of the intrusion with (a) granophyre in centimetre-wide fractures. (b) Sharp granophyre fractures. (c) Granophyre in diapir structures connected by thin granophyre-filled fractures.

5.3.3 Syn-magmatic faulting: field evidence from late-stage structures

5.3.3.1 Fe-Ti-V marker horizon

The five distinct layers of the Fe-Ti-V mineralisation horizon transgress the LZc–MZ boundary (see section 5.1.5). In a localised area (30 by 20 m in dimension) and trending N-S, Layers 1, 3 and 4 are characterised by 'oxide-rich seeps' (around N 68°11.202' W 31°44.429'), originating from the overlying oxide layers and cutting the underlying gabbro. In Layer 1 the oxide-rich seeps extend down-stratigraphy for 12–18 m, while the oxide-rich seeps below Layer 3 extend downwards by 16–24 m. Layer 4 is associated with fewer oxide-rich seeps, and these extend downwards <0.5 m (Fig. 5.22). Close to the base of the oxide layers, the oxide-rich seeps have deformed the gabbro in a ductile fashion. At greater depths below the oxide layers, the seeps have fractured the gabbro resulting in misaligned gabbro packets (0.3–0.5 m along the packet's major axis), surrounded by mafic seeps. In each gabbro

packet the plagioclase foliation is rotated relative to the surrounding magmatic layering (e.g. N 68°11.210' W 31°44.428'; Fig. 5.23).

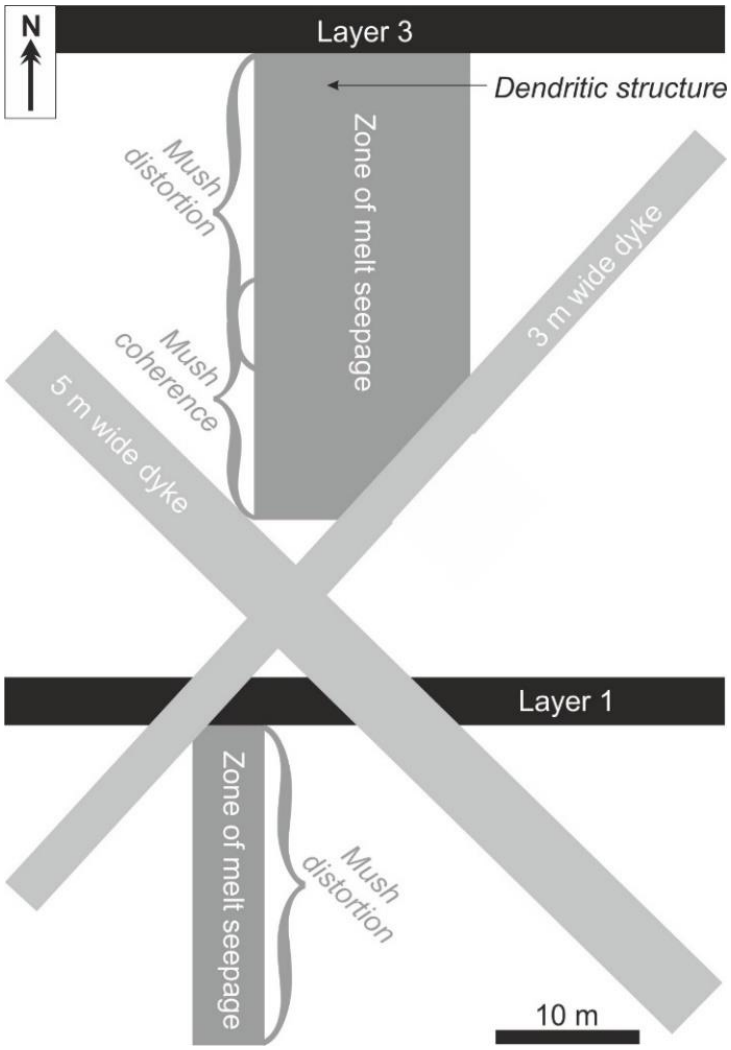

Figure 5.22 Cartoon showing a plan view of the Fe-Ti-V horizons, cross-cutting dykes, and the different characteristic behaviour of the gabbroic mush of the LZc gabbro i.e. mush distortion where the magmatic fabric of the LZc gabbro is distorted/slumped vs mush coherence where the magmatic fabric of the LZc gabbro shows brittle fracture characteristics. Layer 2 of the Fe-Ti-V horizons does not extend through the localised area shown in this figure.

Rare felsic-rich segregations are present, but the volume of material is insignificant in comparison to the oxide-rich seeps and the felsic-rich segregations do not follow any particular trend. In places, the felsic-rich segregations locally deform the LZc gabbro on a scale of tens of centimetres (Fig. 5.24; N 68°11.202' W 31°44.429'). The felsic-rich segregations are plagioclase-dominated, and of a similar grain size to the surrounding gabbro. In the same localised area, a dendritic anorthosite structure extends 1.2 m concordantly along a defined magmatic layering plane. The magmatic layering plane strikes 032 and dips 34° eastward, while the dendritic anorthosite structure has a N-S trend (comparable to the oxide-rich seeps). The dendritic anorthosite structure is identical to those associated with the gabbroic

pegmatites in the vicinity of the UZa trough layering. While there is a large (0.8 m wide) podiform gabbroic pegmatite in the stratigraphic interval between Layer 3 and 4 (N 68°11.195' W 31°44.408'), there is no obvious connection between it and the dendritic anorthosite structure on the magmatic layering plane.

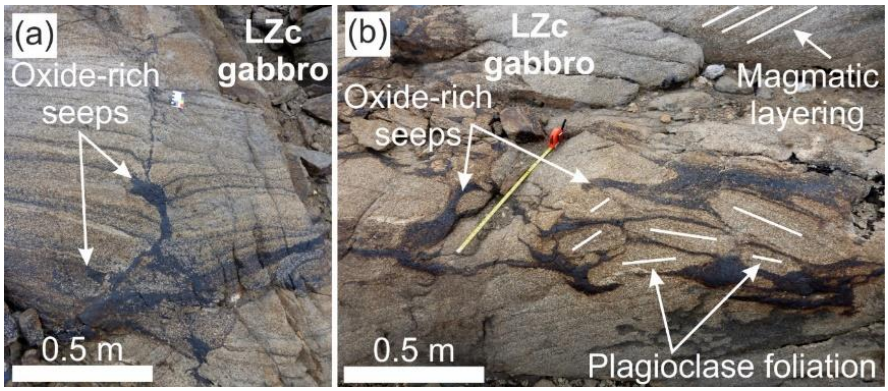

Figure 5.23 (a) Oxide-rich seeps cross-cutting the magmatic layering of the LZc gabbro. (b) Oxide-rich seeps surrounding packets of misoriented LZc gabbro.

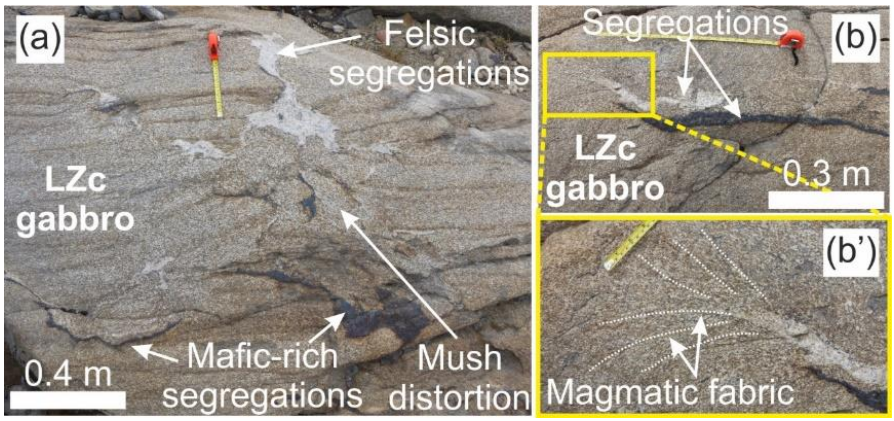

Figure 5.24 (a) Felsic-rich and mafic-rich segregations distorting the magmatic layering of the LZc gabbro. (b) Some felsic-rich and mafic-rich segregations run parallel with the magmatic layering, causing distortion of the LZc gabbro fabric (b').

5.3.3.2 Felsic-rich segregations

Close to Homestead bay on Kraemer Island, magmatic modal layering of LZc is cross-cut by syn-magmatic faulting on the sub-metre scale, and the magmatic layering is offset by 0.2–0.5 m. The faulting structures are defined by oriented plagioclase grains and dip to the north (Fig. 5.25). There are some *en echelon* pockets of gabbroic pegmatite (Fig. 5.25b), opening with a trend of 110˚, at an oblique angle to the faulting. The *en echelon* coarse-grained gabbroic pockets are rich in plagioclase and pyroxene, with some magnetite and granophyric patches. These pockets are <0.6 m along their major axis and are analogous in morphology to the Wavy Pyroxene rock structures described by Humphreys and Holness (2010).

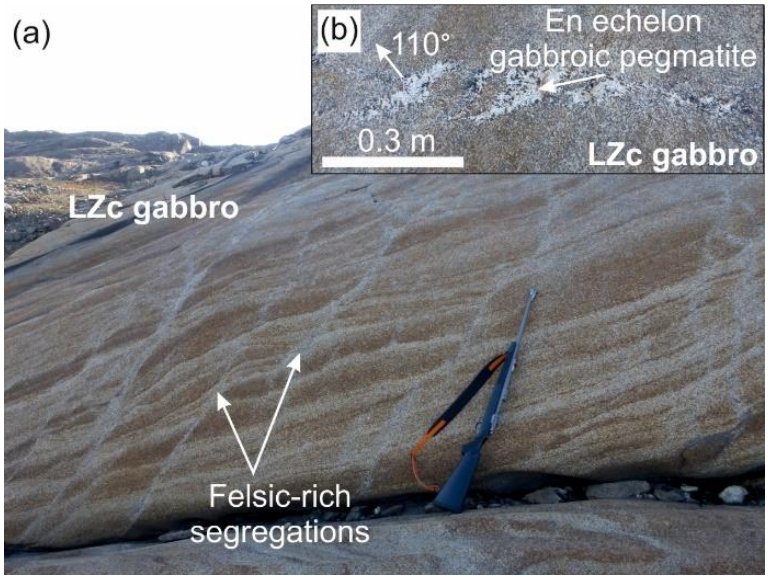

Figure 5.25 (a) Deformation of the LZc gabbro with cross-cutting felsic-rich segregations. (b) En echelon gabbroic pegmatites are found associated with the deformed LZc gabbro shown in (a).

5.4 Analytical methods

5.4.1 Samples collected

I collected sixty-nine samples across the Skaergaard Intrusion between 07/08/2017 and 07/09/2017. These samples cover the full suite of lithologies, with the exception of the HZ, the Sandwich Horizon, MZ' and UZ' (Fig. 5.1). The samples collected represent a comprehensive range of late-stage structures (Appendix Table 5.A).

The position of each surface sample was recorded by global positioning system (GPS; Appendix Table 5.A). The true stratigraphic distances between samples were established by correcting for the local dip of layering (as determined by McBirney (1989)) and correlating with the reference stratigraphy of the LS by Tegner et al. (2009). Following Tegner et al. (2009), I use 2177 m as the total stratigraphic thickness of the LS, with the baseline for the stratigraphic height located at the MBS–LZa boundary on Uttental Plateau.

It is worth noting that significant differences exist in the relative thicknesses of some zones and subzones of Tegner et al. (2009) compared with those given by Wager and Brown (1968). For example, the locations of the LZ–MZ and MZ–UZ boundaries are stratigraphically higher and lower, respectively, reducing the MZ thickness relative to that of the Wager and Brown (1968) stratigraphy. In contrast, the thicknesses of LZc and UZa are greater than those reported by Wager and Brown (1968).

5.4.2 Sample preparation for whole rock analysis

Prior to crushing, the weathered material was removed by rock-saw to reduce the risk of contamination and each sample was dried to remove surface moisture. Whole rock preparation was carried out at the Grant Institute, University of Edinburgh. A tungsten carbide jaw crusher was used, followed by a tungsten carbide milling vessel in a vibratory ring mill. This ensured any contamination from the equipment would be consistent. Tungsten carbide milling materials may contaminate a sample with Co, W, Nb, and Ta; however, accurate measurements of these element concentrations was not critical for this present study (Hickson and Juras, 1986; Iwansson and Landström, 2000). Cross-contamination was minimised by thorough cleaning of the equipment between samples with methylated spirit and compressed air. The mass of each sample was reduced at each sample preparation stage, with care taken to ensure differential settling of particles did not affect the sample reduction.

5.4.3 X-ray fluorescence (XRF)

Major and trace element whole rock analyses were obtained by fused bead and pressed powder pellet, XRF analyses at the Grant Institute, University of Edinburgh. The analyses were conducted using a PANalytical Axios sequential fully automatic wavelength-dispersive X-ray fluorescence spectrometer. Loss on ignition ranged from -3.7–2.6%, with final totals within the 99–100% range. XRF does not differentiate between FeO and Fe_2O_3, therefore the oxidation resulted in a "gain on ignition" in the Fe-rich samples.

Calibration of the wavelength dispersive XRF was validated using reference materials and certified reference materials (CRMs). Following UKAS accredited procedures two in-house QC materials were analysed within each batch of fusion and within the sample run to assure the quality of the fusion and analysis. The flux used for fusion was checked to ensure it was sufficiently pure. Three of the samples were triplicates; these suggest the analyses are representative of the total bulk rock (even for the pegmatitic samples), with the standard deviation of the unknowns (variance of the triplicates compared to their mean) below 0.3 for the felsic and gabbroic material, and below 0.9 for Fe-rich material – with the exception of Fe_2O_3, which had a standard deviation of 2.1. The published values of the CRMs by Govindaraju (1994) were recovered within 1% for the major element analyses and within 5% for the trace element analyses. All values reported for the major and trace elements were above detection limit.

5.4.4 Optical and SEM microscopy

Samples were characterised at the Department of Earth Sciences, University of Cambridge using transmitted and reflective light microscopy. The polished thin sections were analysed by the FEI Quanta FEG 650 F scanning electron microscope (SEM) at the Department of Earth Sciences, University of Cambridge, using a 10 kV beam at spot 3, with a 30 µm aperture and a working distance of 10 mm.

This provided semi-quantitative mineral compositions, element energy dispersive X-ray spectroscopy (EDS) maps and back-scatter electron (BSE) imagery.

5.4.5 Mineral compositions

Minerals compositions were measured using a CAMECA SX-100 electron microprobe with five WDS spectrometers at the Department of Earth Sciences, University of Cambridge. The instrument uses PeakSight software with ZAF correction. Appropriate natural and synthetic primary standards were used. Plagioclase compositions were analysed at 15 kV and a 2 μm beam, with major elements run at 10 nA and generally analysed for 20 s on peak. Relevant mineral secondary standards were run at regular intervals to check for precision and reproducibility. The secondary standard mineral compositions had standard deviations below 0.5 for the majors. Plagioclase cores and rims were analysed. Given the size of the analysed plagioclase grains, the beam interaction volume remained within the plagioclase, as determined by Monte Carlo simulations using *Casino v2.48* software (Drouin et al., 2007).

5.5 Results

5.5.1 Late-stage microstructures of the late-stage segregations

5.5.1.1 Layered Series

The LZ is characterised by podiform pegmatites, comprised of all, or a number of components (A) – (D), as described by field observations. (A) The olivine pyroxenite consists of primocrysts of clinopyroxene (< 1.5 cm diameter) with subhedral olivine (1–2 mm diameter), subhedral plagioclase (< 4 mm diameter), and euhedral apatite along grain boundaries < 500 μm long. Anhedral, globular oxides cut across grains of olivine, clinopyroxene and plagioclase, often with interstitial biotite rooted on the surface; however, there are no disequilibrium microstructures (Fig. 5.26a). Despite the volumetric abundance of (B) – the coarse-grained gabbro – it was not possible to select samples appropriate for thin section analyses of (B). (C) Coarse-grained plagioclase (0.5–2 cm) is associated with large amphiboles and clinopyroxene on the centimetre-scale. The clinopyroxene and amphibole typically have undulating grain boundaries. Interstitial granophyric pockets, 1–10 mm across, have planar-sided boundaries defined by adjacent primocrysts (usually plagioclase or amphibole) with an impingement-controlled pocket shape (Fig. 5.26b). The granophyric pockets comprise intergrowths of quartz with plagioclase and/or alkali feldspar. Some granophyric pockets host large euhedral apatite grains, < 1 mm in diameter. In close proximity to the granophyric pockets (typically separated by a primocryst) are interstitial intergrowths dominated by large, dendritic ilmenite crystals, intergrown with either plagioclase or clinopyroxene. The oxide intergrowths are spatially associated with euhedral grains of magnetite. The size of the intergrowths varies from 0.5–5 mm. (D) Medium-grained, subhedral

plagioclase laths with a zoned rim are surrounded by large interstitial clinopyroxene grains (> 1 cm diameter) with varying amounts of small (< 500 μm diameter) grains of amphibole, biotite (generally rooted on an oxide), apatite, rare anhedral olivine, and granophyric patches (Fig. 5.26c). Intergrowths of ilmenite cut across the grains and are spatially associated with magnetite. Within the LZ gabbroic pegmatites (A)–(D), the late-stage microstructures are limited to paired intergrowths i.e. the non-replacive symplectites of Holness et al. (2011).

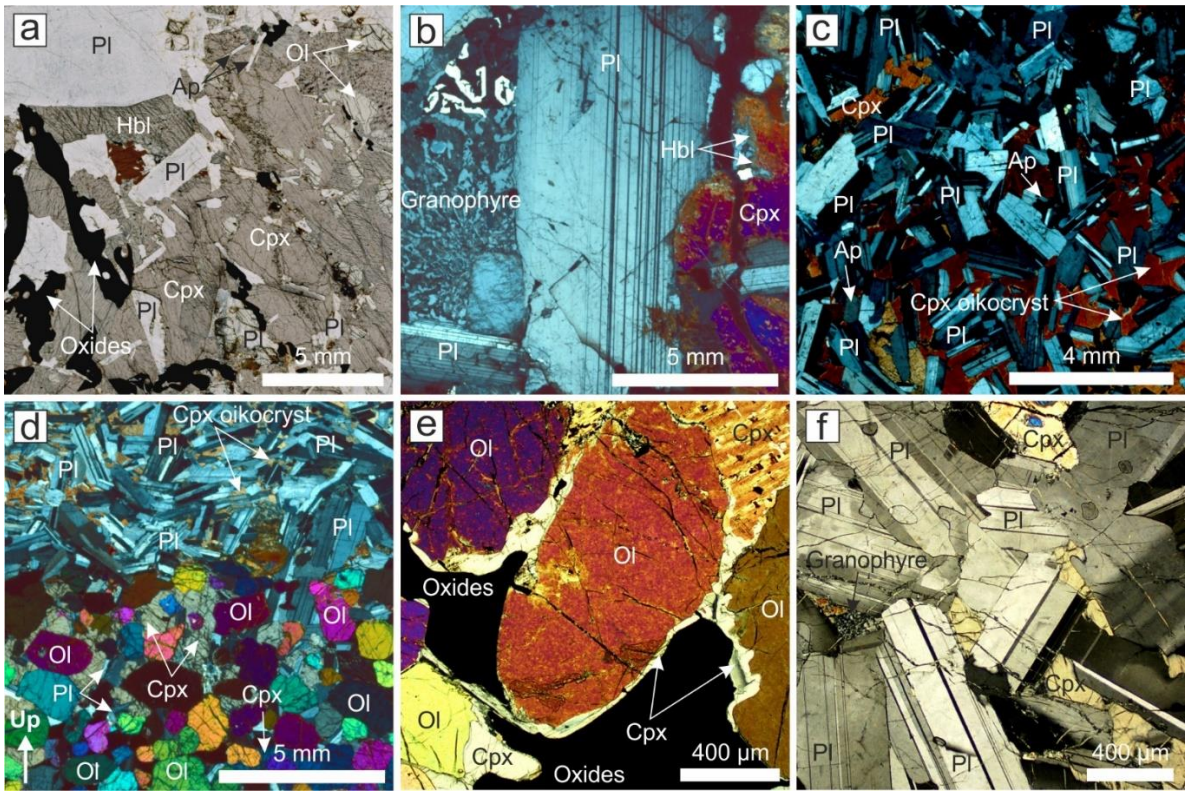

Figure 5.26 Microstructures of the LZ late-stage segregations (a) PPL photomicrograph of the olivine pyroxenite consisting of primocrysts of clinopyroxene (Cpx), olivine (Ol), plagioclase (Pl), hornblende (Hbl) and apatite (Ap; along grain boundaries). Globular oxides cut across primocryst grains. (b) XPL photomicrograph of coarse-grained plagioclase associated with amphiboles and clinopyroxene. Interstitial granophyric pockets have planar-sided boundaries defined by adjacent primocrysts. (c) XPL photomicrograph of medium-grained plagioclase laths with a zoned rim are surrounded by large interstitial clinopyroxene grains with varying amounts of small apatite grains. (d) XPL photomicrograph of a composite lense of mafic- and felsic-rich segregations, with the felsic-rich segregation overlying the basal mafic-rich segregation. (e) XPL photomicrograph of the mafic segregation comprising rounded olivine grains with oikocrysts of clinopyroxene, interstitial plagioclase and globular ilmenite and magnetite. (f) XPL photomicrograph of a plagioclase dominated felsic-rich segregation, with granophyric pockets

Stratigraphically above the podiform gabbroic pegmatites are composite lenses of mafic- and felsic-rich segregations (Fig. 5.26d). The mafic-rich segregation comprises rounded olivine grains (typically 2-6 mm diameter), with oikocrysts of clinopyroxene, interstitial plagioclase and globular ilmenite and magnetite (Fig. 5.26e). The volume of oxides increases stratigraphically upwards to the MZ. Along the contacts between the average gabbro and the mafic-rich segregation there are clinopyroxene-plagioclase stepped grain boundaries and replacive symplectites. The felsic-rich segregations are plagioclase

dominated, with the plagioclase laths (0.5–2 mm along their long axis) aligned parallel with the boundary between the paired mafic- and felsic-rich segregations (Fig. 5.26f). Oikocrysts of clinopyroxene, magnetite and ilmenite dominate the plagioclase interstices, with occasional Ti-rich biotite. The plagioclase of the felsic-rich segregations typically have a thin outer rim (< 100 μm thick). Overall the mafic- and felsic-rich segregations have late-stage microstructures consistent with a reactive Fe-rich liquid, and indicate a weak separation of immiscible liquids (as characterised by Holness et al. (2011) for the LS).

The petrology of the gabbroic pegmatites evolves upwards through the LS, with olivine primocrysts becoming more fayalitic, the clinopyroxene tending towards ferro-augite, and the plagioclase becoming more albitic. Within UZa, there are different late-stage microstructures when comparing the podiform pegmatites in the trough layering and the gabbroic pegmatite sills and feeder dykes in the lower part of UZa. The gabbroic pegmatitic sills and dykes are characterised by extensive ilmenite intergrowths, varying from 1–5 mm in size and typically associated with clinopyroxene and magnetite (Fig. 5.27a). There are polycrystalline olivine rims between oxides and pyroxene, and replacive symplectites between oxides and plagioclase (Fig. 5.27b). In close proximity to the upper boundary of the sills there are granophyric pockets (Fig. 5.27c) adjacent to ilmenite intergrowths suggesting two conjugate immiscible liquids with poor separation. The plagioclase of the gabbroic pegmatites have an outer rim (50–100 μm wide) at the top of the gabbroic pegmatite sills, but are not typically zoned in the lower parts. Euhedral apatite grains up to 400 μm in diameter lie along grain boundaries, with no particular association with either mafic or felsic phases.

The gabbroic pegmatites of the UZa trough layering have associated mafic- and felsic-rich segregations up-stratigraphy. At the contact between the mafic-rich segregation and the UZa average gabbro there are replacive symplectites between the oxides and the average gabbro plagioclase (Fig. 5.27d,e). The felsic-rich segregations are plagioclase dominated, with some interstitial mafic pockets i.e. magnetite, ilmenite, biotite, and interstitial granophyric pockets (Fig. 5.27f). Plagioclase outer rims are common but thin, typically <100 μm.

The mafic-rich segregations of UZb are characterised by olivine, clinopyroxene, oxides and an abundance of euhedral apatite, with occasional grains of plagioclase (Fig. 5.28a). The apatite grains lie along silicate and oxide grain boundaries and range from 50–1000 μm in length, smaller (<200 μm diameter) apatite grains are found as inclusions in primocryst phases, as well as within the ilmenite intergrowths (Fig. 5.28b). There are occasional polycrystalline olivine rims between oxides and pyroxenes, close to the mafic-rich segregation contact with the UZb gabbro. The felsic-rich segregations of UZb are dominated by euhedral plagioclase (Fig. 5.28c). The plagioclase grains have 100 μm rims surrounding the tabular core. Interstitial pockets 500–1000 μm in diameter within the felsic-rich

segregations are granophyric or are dominated by ilmenite intergrowths, with several large (>100 µm long) apatite grains. The shape of the pockets are controlled by the surrounding plagioclase grains.

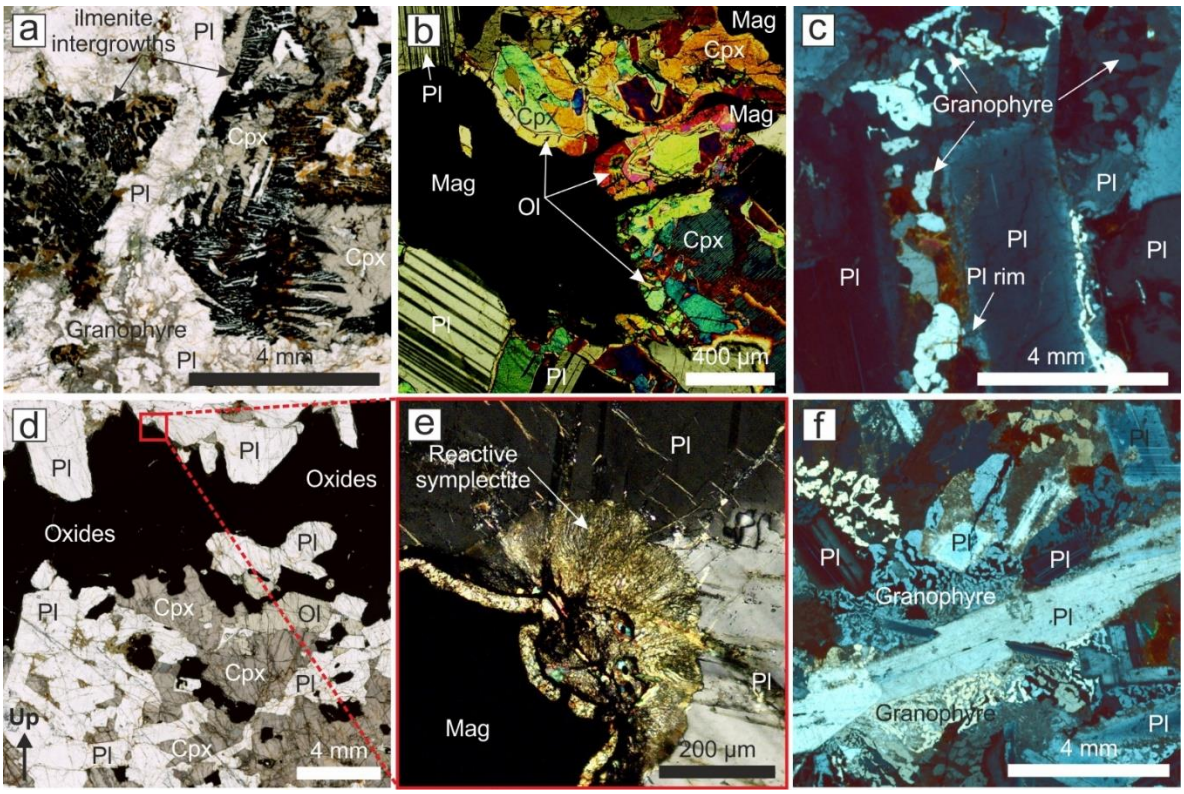

Figure 5.27 Comparisons between the microstructures of the late-stage segregations from the lower parts of UZa, with those from the trough layering of UZa (a) PPL photomicrograph of the gabbroic pegmatitic sills and dykes are characterised by extensive ilmenite intergrowths, typically associated with clinopyroxene and magnetite (Mag). (b) XPL photomicrograph of polycrystalline olivine rims between oxides and pyroxene. (c) XPL photomicrograph of plagioclase grains in close proximity to the upper boundary of the sills, where there are granophyric pockets. Note the outer rim on the plagioclase grains. (d) PPL photomicrograph of the contact between the mafic-rich segregation and the UZa average gabbro, where there are (e) replacive symplectites between the oxides and the average gabbro plagioclase (XPL photomicrograph). (f) XPL photomicrograph of the plagioclase dominated felsic-rich segregations, with some interstitial granophyric pockets.

UZc is comprised of coarse-grained pegmatitic segregations, with overlying mafic- and felsic-rich segregations. In the upper parts of the pegmatitic segregations there are adjacent millimetre-scale pockets of paired intergrowths of ilmenite and granophyre. Likewise, within the plagioclase-dominated felsic-rich segregation there are mafic-rich and granophyric pockets 1–3 mm in diameter. The mafic pockets consist of olivine, altered Fe-rich pyroxene, and apatite grains up to 300 µm long (Fig. 5.28d,e). The plagioclase from the felsic-rich segregations have 50 µm albitic rims where in contact with a granophyric interstitial pocket (Fig. 5.28f). The mafic-rich segregations from UZc are characterised by large (~4 mm dimeter) oikocrysts of Fe-rich olivine, with heavily altered, rounded, Fe-rich pyroxene grains (typically 1–2 mm in diameter). Subhedral plagioclase laths are distributed throughout and are of comparable dimensions to the pyroxenes. Interstitial oxides with coarse exsolution lamellae (on the 10–20 µm scale) of magnetite and ilmenite host sulfide bleb inclusions ranging from 20–100 µm in diameter. Some oxides form 200 µm diameter inclusions in the olivine oikocrysts. There are abundant

euhedral apatite grains, < 1000 µm in length, which lie along grain boundaries. Apatite inclusions within the altered pyroxene, plagioclase and oxides are generally smaller.

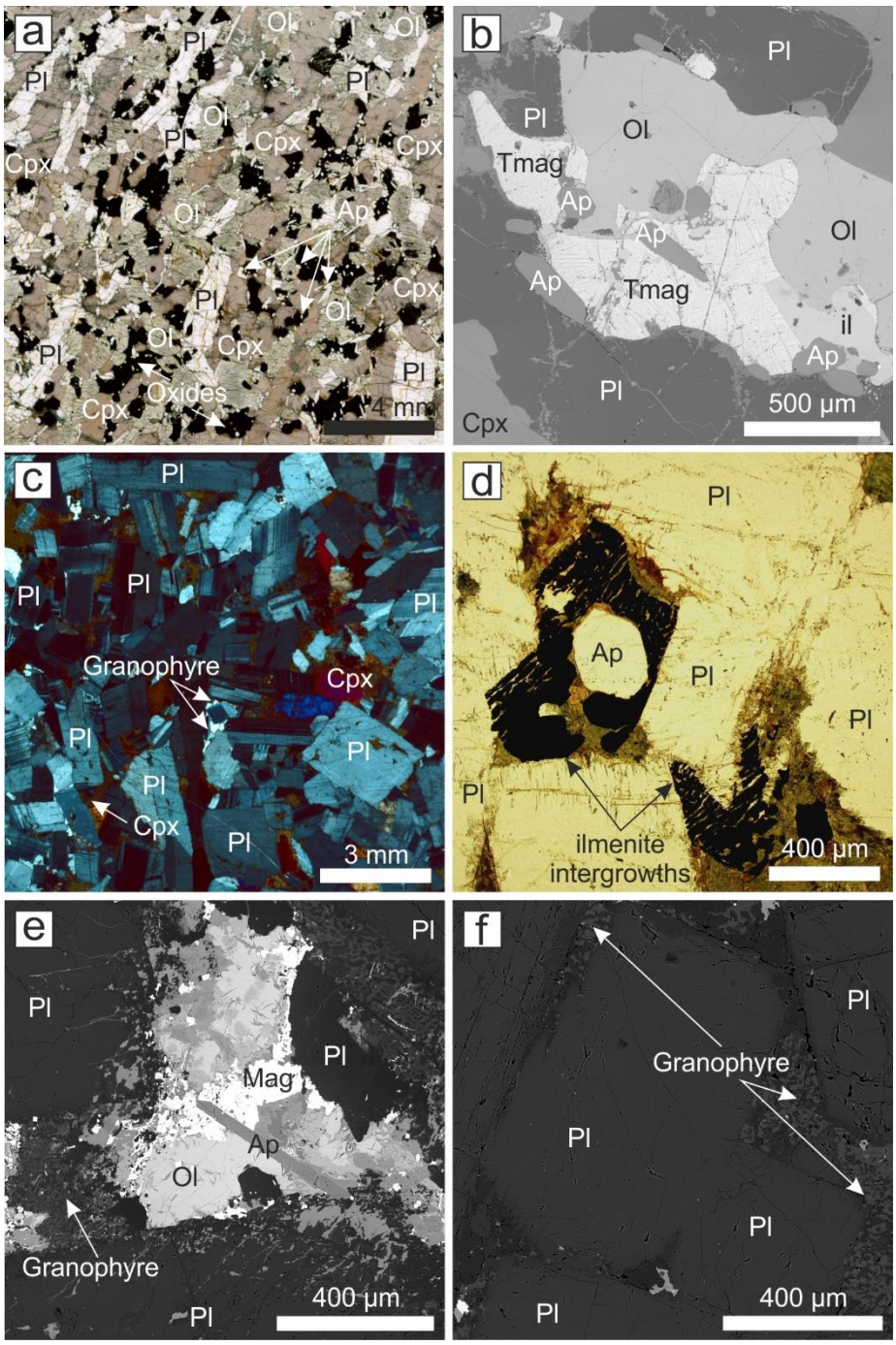

Figure 5.28 Microstructures of the UZb and UZc late-stage segregations (a) PPL photomicrograph of the mafic-rich segregations of UZb are characterised by olivine, clinopyroxene, oxides and an abundance of euhedral apatite, with grains of plagioclase. (b) BSE image of apatite grains and titanomagnetite (Tmag) associated with olivine in the mafic-rich segregation of UZb. (c) XPL photomicrograph of the felsic-rich segregations of UZb, dominated by euhedral plagioclase with granophyric pockets. (d) PPL photomicrograph of the felsic-rich segregations of UZc, with an interstitial mafic pocket consisting of olivine, altered Fe-rich pyroxene, and apatite grains up to 300 µm long. (e) BSE image of the felsic-rich segregations of UZc, highlighting the range of mafic minerals in mafic rich pockets between plagioclase grains. (f) BSE image of the felsic-rich segregations of UZc, highlighting the granophyric pockets.

5.5.1.2 Upper Border Series and roof zone

LZa' is cut by a number of centimetre-scale fractures, filled with fine-grained granophyre. Within the fractures are euhedral apatite grains, <1 mm in diameter, and large (<5 cm) green-blue euhedral amphiboles. At the roof zone contact of the intrusion, centimetre-scale fractures are filled with a fine-grained granophyre.

5.5.1.3 Syn-magmatic faulting and the Fe-V-Ti marker horizon

The oxide-rich seeps within LZc are dominated by primocryst magnetite and ilmenite, with interstitial ilmenite extending along magnetite grain boundaries (Fig. 5.29a,b). The contact between the oxide-rich seep and the surrounding LZc average gabbro is characterised by a range of late-stage microstructures. Stepped grain boundaries on clinopyroxene-plagioclase grain boundaries, polycrystalline olivine between oxides and pyroxene (Fig. 5.29c), and replacive symplectites (Fig. 5.29d) all indicate a localised reaction between the host gabbro and the late-stage oxide-rich seep (Holness et al., 2011; Holness et al., 2007; Stripp, 2009).

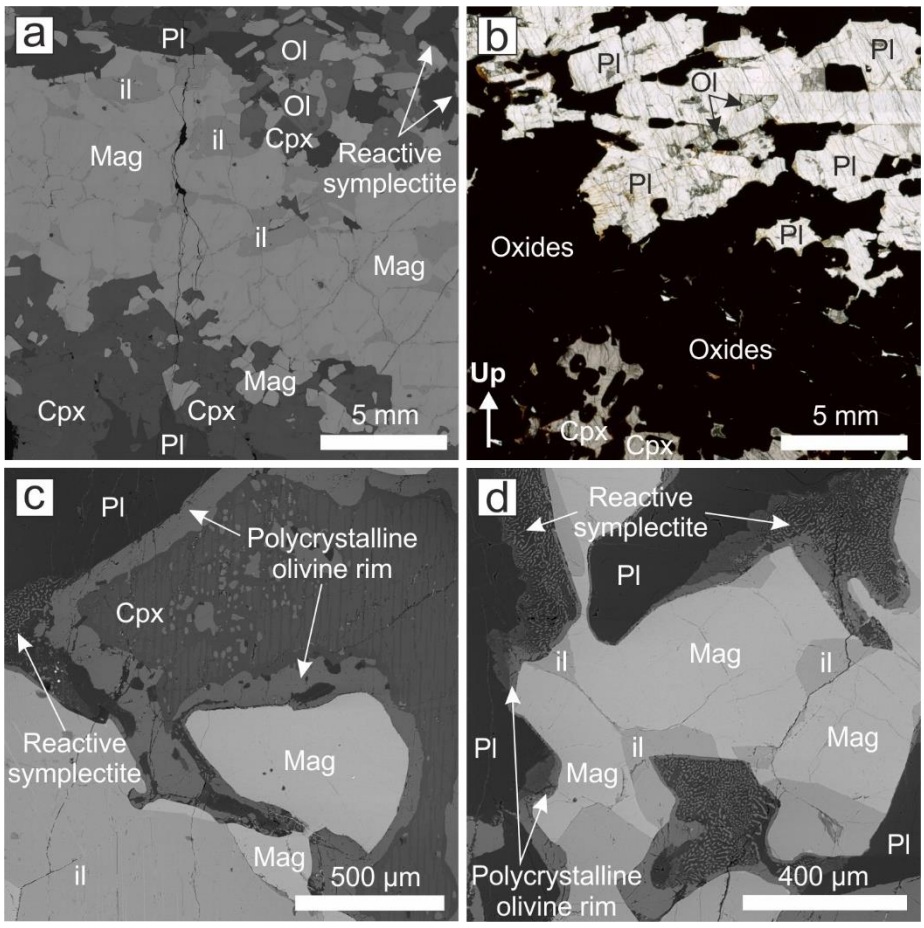

Figure 5.29 Microstructures of the Fe-V-Ti marker horizon (a) BSE image of the oxide-rich seeps within LZc, dominated by magnetite and ilmenite, with interstitial ilmenite extending along magnetite grain boundaries. (b) PPL photomicrograph of the oxide-rich seeps within LZc. (c) BSE image of the polycrystalline olivine between oxides and pyroxene, and (d) replacive symplectites.

5.5.2 Whole rock geochemistry of the late-stage segregations

Following the nomenclature used in my fieldwork observations, whole rock major and trace element data is presented for the gabbroic pegmatites and the mafic- and felsic-rich segregations (Appendix Table 5.B and 5.C). The term gabbroic pegmatite relates specifically to component (B) of the podiform pegmatitic structures. The SiO_2 concentration in the felsic-rich segregations range from 52.9 to 76.7 wt.%, while the SiO_2 concentration in the mafic-rich segregations ranges from 6.3 to 44.9 wt.%. The SiO_2 concentrations of the gabbroic pegmatites are intermediate between the mafic- and felsic-rich segregations. There is a negative correlation between the concentrations of SiO_2 against $Fe_2O_{3\ total}$ and TiO_2 for all three major lithologies (Fig. 5.30), with the mafic-rich segregations having the highest concentrations of $Fe_2O_{3\ total}$ and TiO_2, reaching a maximum of 62.5 wt.% and 24.5 wt.% respectively.

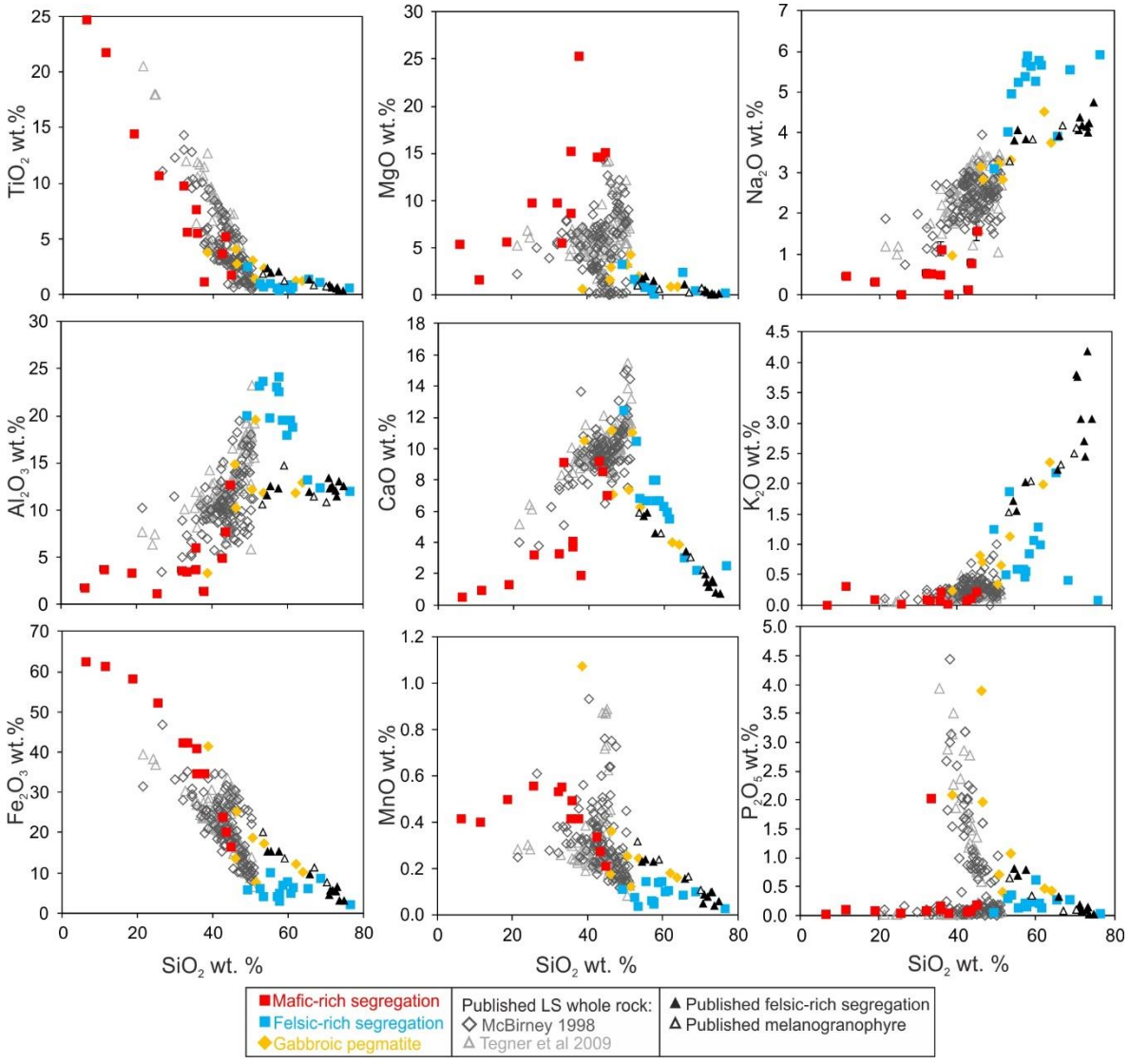

Figure 5.30 Harker plots for major elements (wt.%), presented by mafic- and felsic-rich segregation, gabbroic segregation, and overlain with published whole rock data for the gabbros of the layered series (McBirney, 1998; Tegner et al., 2009); published whole rock values for the melanogranophyre of UZc (McBirney, 1989) and published whole rock values for the felsic-rich segregations (Larsen and Brooks, 1994; McBirney, 1989). Representative 1σ error bars are smaller than the size of the data point.

The $Fe_2O_{3\ total}$ and TiO_2 concentrations are lowest in the felsic-rich segregations, respectively at ~2 wt.% and <0.5 wt.%. Magnesium numbers (Mg# ($X_{Mg}/[X_{Mg} + X_{Fetotal}]$)) range from 44 for the mafic-rich segregations to <1 for the felsic-rich segregations.

Gabbroic pegmatites stratigraphically higher in the LS have a lower Mg#. This Mg# trend is also seen for the Fe-rich ultramafic pegmatoidal bodies distributed within the Bushveld Complex (Viljoen and Scoon, 1985). MnO concentrations have a strongly negative correlation with SiO_2 concentrations greater than 20 wt.% and a positive correlation with concentrations below 20 wt.% SiO_2; this is true for the gabbroic pegmatites, mafic- and felsic-rich segregations. The felsic-rich segregations have the widest spread of K_2O, CaO and Al_2O_3 concentrations at 0.1–2.2 wt.%, 2.5–10.4 wt.%, and 11.9–24.1 wt.%, respectively. Total alkali contents ($Na_2O + K_2O$) range from 4.5–7.0 wt.% for the felsic-rich segregations and 0.1–1.8 wt.% for the mafic-rich segregations. The mafic-rich segregations lie in the ultrabasic field on a total alkali-silica plot, the felsic-rich segregations are classified from intermediate to acid, while the gabbroic pegmatites are classified from intermediate to basic. P_2O_5 concentrations are generally <0.5 wt. % for the felsic-rich segregations, the mafic-rich segregations reach 2.0 wt.% P_2O_5, while in the gabbroic pegmatites P_2O_5 concentrations range between 0.4–3.9 wt.%.

The whole rock data for the felsic-rich segregations and gabbroic pegmatites are largely consistent with the published whole rock data for the various late-stage segregations for different heights within the intrusion (Fig. 5.31) (Larsen and Brooks, 1994; McBirney, 1989; Wager and Brown, 1968). The exceptions are the concentrations of K_2O, Na_2O, and Al_2O_3, for which the felsic-rich segregations have K_2O concentrations 1.5 wt.% lower than the published concentrations for similar rock types, but Na_2O concentrations 1.5 wt.% higher and Al_2O_3 concentrations 10 wt.% higher.

The whole rock major element concentrations for the mafic- and felsic-rich paired segregations are mostly consistent with concentrations from conjugate immiscible liquid pairs analysed from immiscible melt inclusions, unmixing experiments and immiscible groundmass mesostasis (Fig. 5.32) (e.g. Helz, 1987; Honour et al., 2019; Jakobsen et al., 2005; Jakobsen et al., 2011; Longhi, 1990; McBirney and Nakamura, 1974; Philpotts, 1982; Veksler et al., 2007) – see section 5.65 for a discussion of the expected partition coefficients between the two liquids, also Fig. 1.8. There are some exceptions, including CaO and P_2O_5 concentrations. CaO concentrations are higher in the felsic-rich segregations relative to the mafic-rich segregations and P_2O_5 concentrations in the mafic-rich segregation are relatively low (Fig. 5.31) in comparison to expected concentrations from experiments (e.g. Chapter 2). At higher levels in the LS, the compositional gap between the mafic- and felsic-rich segregations is greater and the concentration of $Na_2O+Al_2O_3+K_2O+MgO$ is reduced in both segregations.

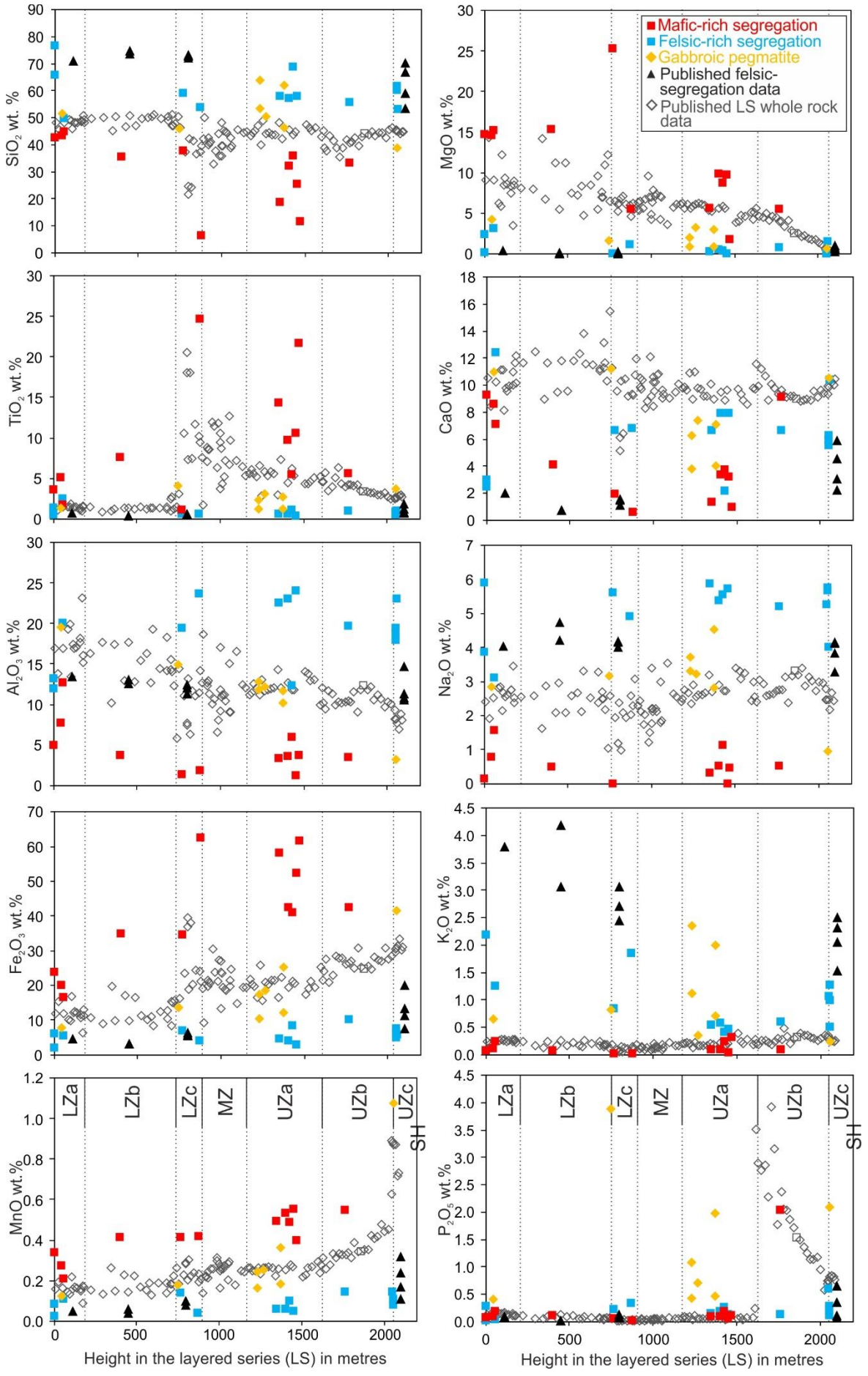
Mafic-rich segregation
Felsic-rich segregation
Gabbroic pegmatite
Published felsic-segregation data
Published LS whole rock data
SiO2 wt. %
MgO wt.%
TiO2 wt.%
CaO wt.%
Al2O3 wt.%
Na2O wt.%
Fe2O3 wt.%
K2O wt.%
MnO wt.%
P2O5 wt.%
LZa
LZb
LZc
MZ
UZa
UZb
UZc
SH
Height in the layered series (LS) in metres

Figure 5.31 (previous page) Whole rock major element variations with stratigraphic height (wt.%), presented by mafic- and felsic-rich segregation, gabbroic segregation, and overlain with published whole rock data for the gabbros of the layered series (Tegner et al., 2009), and published whole rock values for the melanogranophyre of UZc (McBirney, 1989) and the granophyre tops of the gabbroic pegmatites (Larsen and Brooks, 1994). Representative 1σ error bars are smaller than the size of the data point.

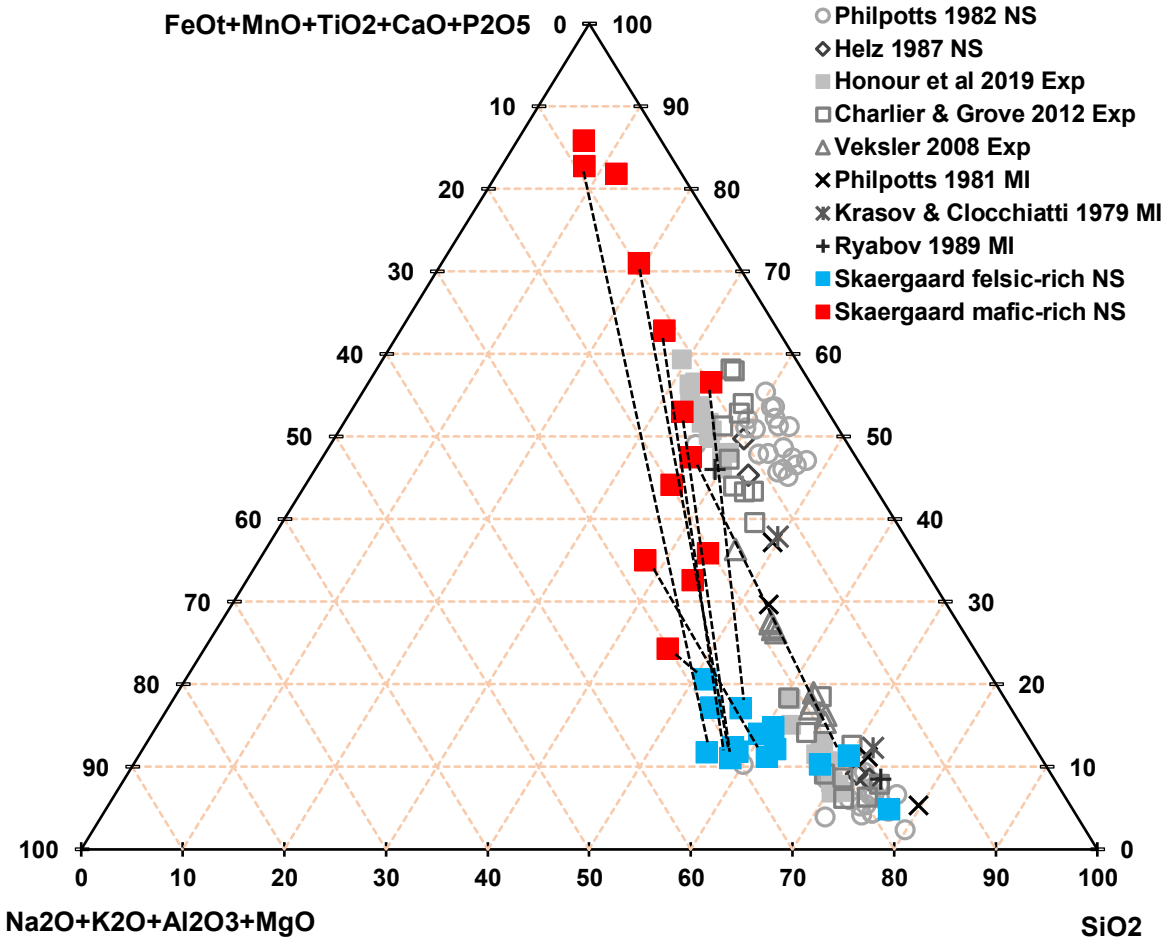

Figure 5.32 Plot of the composition of immiscible Fe-rich and Si-rich immiscible liquids preserved as glassy droplets in a range of tholeiitic volcanic rocks and tholeiitic experiments (in grey), with the Skaergaard mafic- (Fe-) rich and felsic- (Si-) rich segregations overlain (filled red and blue squares). Tie lines link samples where two adjacent conjugate pairs were accessible for sampling in the field. NS = data from natural samples; EXP = experimental data; MI = melt inclusion data.

The concentrations of the gabbroic cumulates from the LS are plotted for comparative purposes with the concentrations of the late-stage segregations (Fig. 5.31). The major element concentrations of the gabbroic pegmatites are typically comparable to the surrounding cumulate LS gabbro for a given height (McBirney, 1998; Tegner et al., 2009); with the main exceptions being the higher K_2O concentrations of the gabbroic pegmatites compared to the surrounding LS gabbro and the lower MgO concentrations.

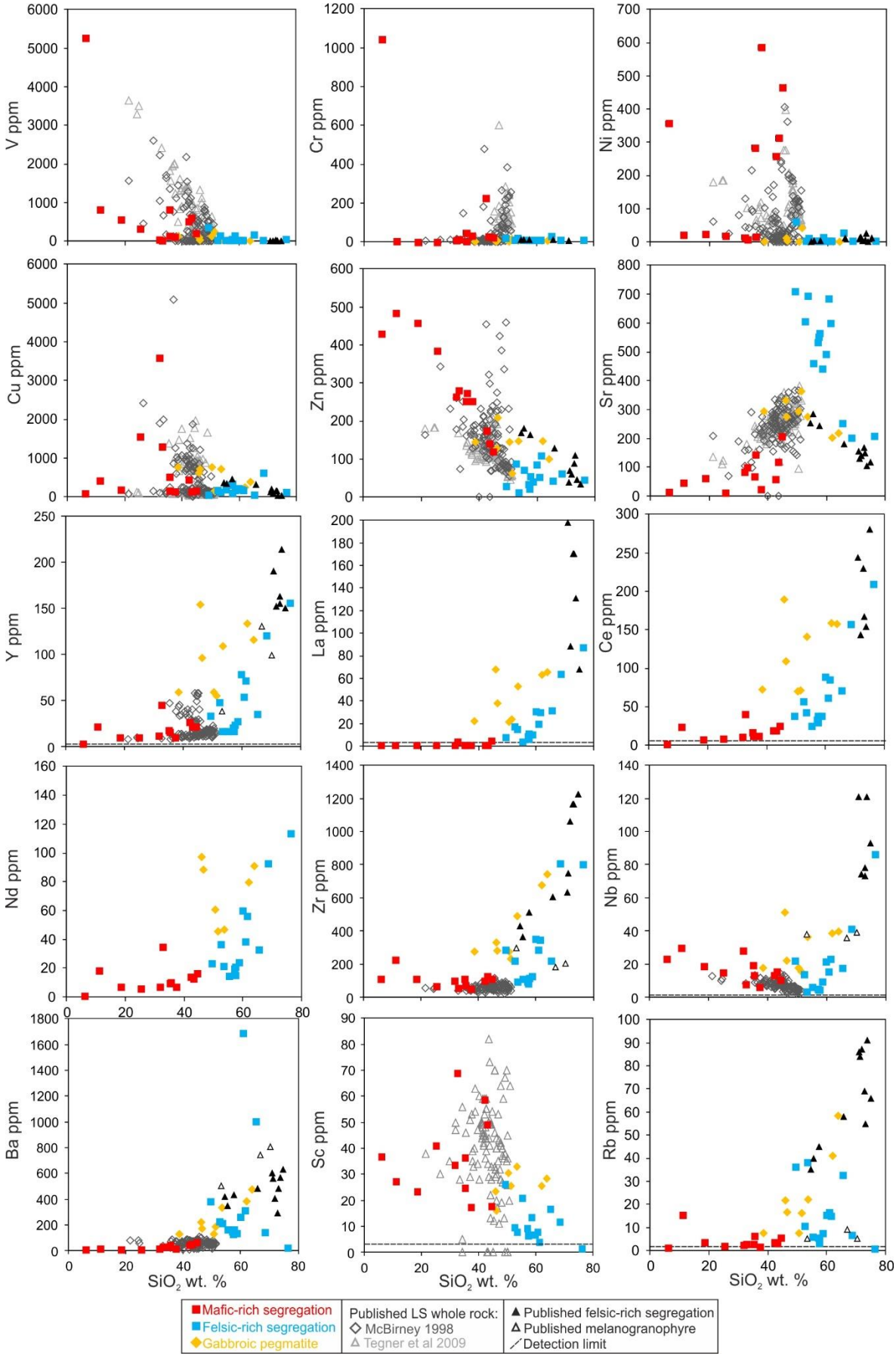
V ppm
Cr ppm
Ni ppm
Cu ppm
Zn ppm
Sr ppm
Y ppm
La ppm
Ce ppm
Nd ppm
Zr ppm
Nb ppm
Ba ppm
Sc ppm
Rb ppm
SiO2 wt. %
Mafic-rich segregation
Felsic-rich segregation
Gabbroic pegmatite
Published LS whole rock:
McBirney 1998
Tegner et al 2009
Published felsic-rich segregation
Published melanogranophyre
Detection limit

Figure 5.33 (Previous page) Harker plots for trace elements (ppm), presented by mafic- and felsic-rich segregation, gabbroic segregation, and overlain with published whole rock data for the gabbros of the layered series (McBirney, 1998; Tegner et al., 2009); published whole rock values for the melanogranophyre of UZc (McBirney, 1989) and the felsic-rich segregations (Larsen and Brooks, 1994; McBirney, 1989). Representative 1σ error bars are smaller than the size of the data point.

The trace element concentrations of the gabbroic pegmatites are typically unrelated to the concentrations in the LS gabbro (McBirney, 1998; Tegner et al., 2009), with the exception of Sr, Zn and Cu (Fig. 5.33; Fig. 5.34). The gabbroic pegmatites are geochemically characterised by elevated concentrations of REEs, Nb, Ba, Zr with low concentrations of V, Cr and Ni compared to the surrounding LS gabbro concentrations. It is possible that the high Nb concentrations are a consequence of contamination from the whole rock sample preparation (see section 5.4.2). However, the same high Nb concentrations, relative to the LS gabbro concentrations, are shown for the published felsic-rich segregation data too (Fig. 5.34). UZa is notable for the consistently high (or highest) gabbroic pegmatite concentrations of Cu, Zn, REEs, Zr, and Rb, reaching maximum values of 720 ppm, 207 ppm, 160 ppm (for Ce), 720 ppm and 60 ppm respectively (Fig. 5.34).

The mafic-rich segregations have high concentrations of elements such as V, Cu, Ni, Zn and Sc associated with low concentrations of SiO_2 (less than 40 wt. %), conversely there is a positive correlation between SiO_2 concentrations and the concentrations of REEs, Rb, Ba, Zr and Sr in the felsic-rich segregations (Fig. 5.33; Fig. 5.34). There is typically good correlation between the new whole rock concentrations of the felsic-rich segregation and the previously published data on similar rock types by Larsen and Brooks (1994). There is no correlation between the concentrations of Ni and Cu, nor the concentrations of Cr and V in the mafic-rich segregations.

5.5.3 Plagioclase mineral chemistry of the late-stage segregations

I analysed the major element geochemistry of plagioclase primocryst cores and rims from the late-stage segregations of the LS; analyses are presented from the gabbroic pegmatites, as well as the mafic- and felsic-rich segregations (Fig. 5.35; Appendix Table 5.D and 5.E). These data are compared to analyses of the LS gabbro primocryst plagioclase, and previous plagioclase analyses of the late-stage segregations (Humphreys, 2011; Larsen and Brooks, 1994; Namur and Humphreys, 2018).

Chemical diffusion rates for different elements will vary between minerals, as well as with temperature. For slow cooling rates relevant to the Skaergaard Intrusion, only the slowest diffusing elements will retain the compositional variability caused by continuous differentiation of the crystallising liquid (Humphreys, 2009). Suitable elements can be used to assess the processes that occurred in the late-stage segregations during solidification. In this study I look at plagioclase mineral chemistry as it is a phase present in the gabbroic pegmatite, mafic- and felsic-rich segregations.

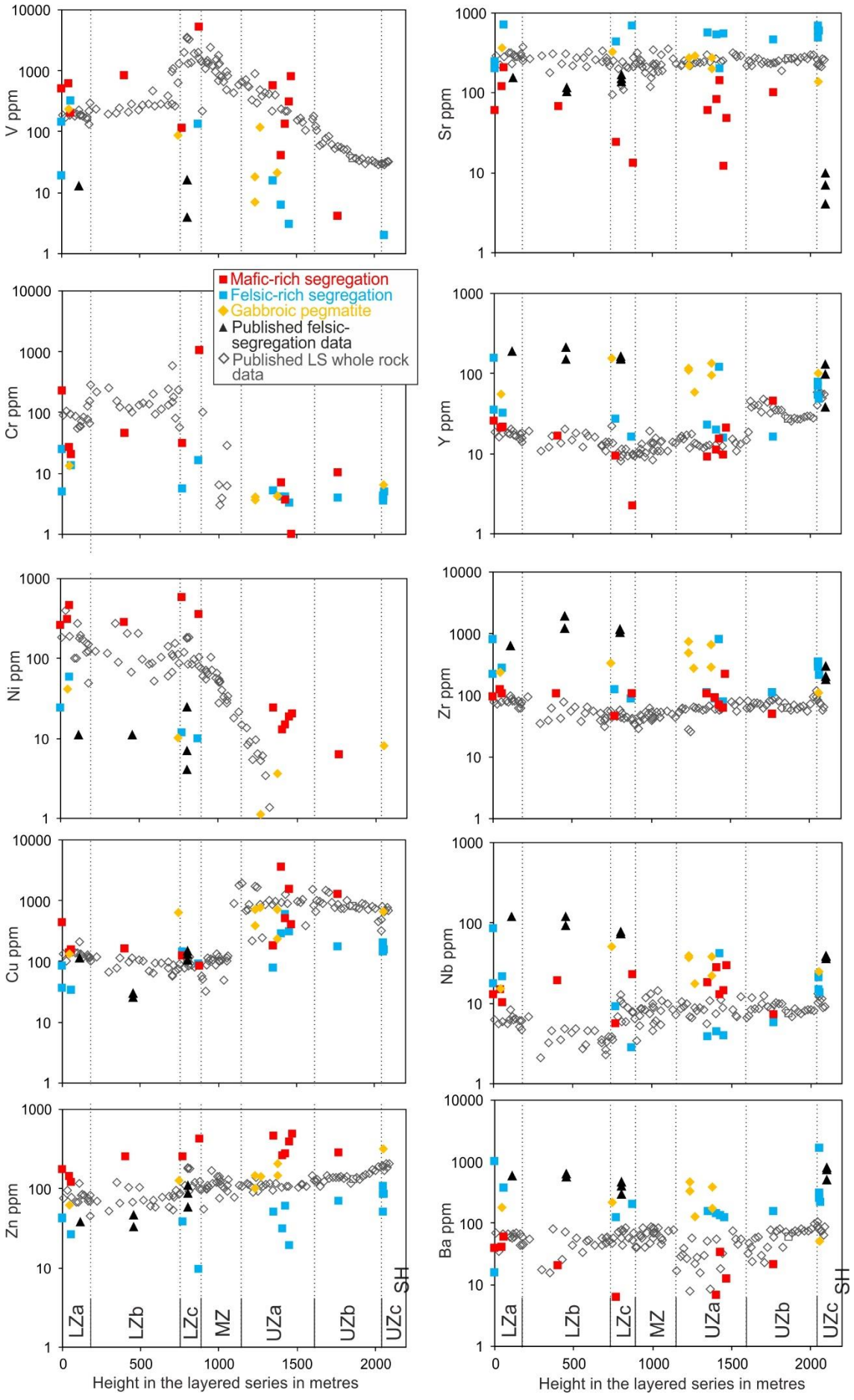
Mafic-rich segregation
Felsic-rich segregation
Gabbroic pegmatite
Published felsic-segregation data
Published LS whole rock data
V ppm
Sr ppm
Cr ppm
Y ppm
Ni ppm
Zr ppm
Cu ppm
Nb ppm
Zn ppm
Ba ppm
LZa
LZb
LZc
MZ
UZa
UZb
UZc
SH
Height in the layered series in metres

Figure 5.34 (Previous page) Whole rock trace element variations with stratigraphic height (ppm), presented by mafic- and felsic-rich segregation, gabbroic segregation, and overlain with published whole rock data for the gabbros of the layered series (Tegner et al., 2009), and published whole rock values for the granophyre tops of the gabbroic pegmatites (Larsen and Brooks, 1994). Representative 1σ error bars are smaller than the size of the data point.

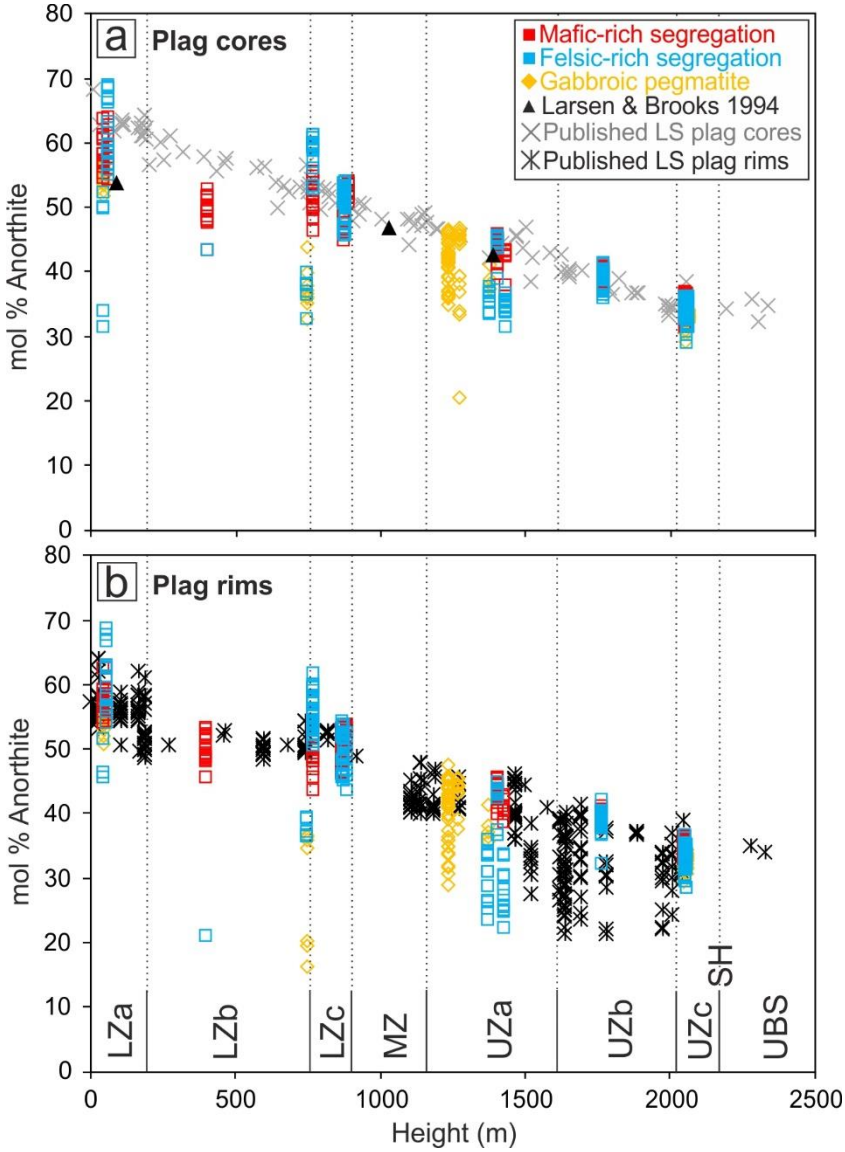

Figure 5.35 Plagioclase anorthite variations with stratigraphic height (mol.%) for plagioclase cores (a) and plagioclase rims (b), analysed from the mafic- and felsic-rich segregations, gabbroic segregations, and overlain with published plagioclase anorthite data for the gabbroic pegmatites (Larsen and Brooks, 1994) and the gabbros of the layered series (Jang et al., 2001; Namur and Humphreys, 2018; Toplis et al., 2008).

Major element chemical diffusion in plagioclase is too slow for equilibrium to be maintained between crystal and liquid, so a decreasing plagioclase anorthite composition is a reliable indicator of variations in the composition of the late-stage segregation liquid (as used by Humphreys (2009); Humphreys (2011)).

5.5.3.1 Comparisons to the cumulates of the Layered Series

The plagioclase from the late-stage segregations is more albitic with increasing stratigraphic height through the LS (Fig. 5.35). Plagioclase core anorthite compositions (An# calculated as mol.% Ca/(Ca+Na+K)) from the late-stage segregations are typically equivalent to plagioclase rim anorthite compositions from the adjacent LS gabbro i.e. they are more albitic, especially in LZa-c. This is consistent with the observations of Larsen and Brooks (1994). Furthermore, the typical compositional difference between the average plagioclase late-stage segregation core and rim is <5 mol % anorthite (similar to that identified by Larsen and Brooks (1994)).

5.5.3.2 Plagioclase chemistry from different components of the late-stage segregations

I firstly compare plagioclase *core* compositions between the different components of the late-stage segregations: the pegmatitic gabbro, mafic- and felsic-rich segregations. The plagioclase anorthite compositions of the mafic-rich segregations have a restricted range within each layer of the intrusion, from ~An_{64-52} in LZa, through ~An_{53-43} in LZc, to ~An_{36-30} in UZc; the felsic-rich segregations typically host plagioclase with a wider range of anorthite compositions from ~An_{69-45} in LZa, through ~An_{60-43} in LZc, to ~An_{36-29} in UZc, with plagioclase cores from the gabbroic pegmatites (where analysed) typically having An# compositions in-between (Fig. 5.35). The plagioclase *rims* of the late-stage segregations follow the same trends as outlined above (Fig. 5.35).

5.6 Discussion

5.6.1 Formation of the late-stage segregations

The formation of the late-stage segregations could occur by a number of processes, either operating alone or together:

- Intrusion of pristine magma
- Accumulation of residual magma from the interstices of the surrounding cumulates
- Metasomatic alteration from fluid interaction (with the fluid possibly derived from the evolving magma)

Field relations of nascent gabbroic pegmatites in LZb with plagioclase laths cross-cutting the boundary between the LS gabbro and the late-stage segregations suggest the gabbroic pegmatites formed prior to the cumulate mush solidifying, with the liquid originating from the cumulate mush pile. The whole rock major element concentrations of the gabbroic pegmatites follow the elemental trends and concentrations of the LS gabbro for any given stratigraphic height. The anorthite composition of the plagioclase cores in the late stage segregations are analogous to the LS gabbro plagioclase rim compositions, suggesting that the late-stage segregations formed from the cumulate interstitial liquid passively accumulating within the crystal mush. This fits with the conclusions of Larsen and Brooks (1994) who documented

similarities in mineral chemistry between the late-stage segregations and the LS primocrysts between LZa to UZa; they concluded that the gabbroic pegmatites represented the crystallised batches of accumulated intercumulus liquid. The crystals within the gabbroic pegmatites are euhedral with well-formed terminations, which would have required growth in a liquid with no impedance. Consequently, metre-scale pockets of liquid must have accumulated within the mush. Henceforth the late-stage segregations are considered to have crystallised from late-stage liquids. The changing morphology of these late-stage liquids is summarised in Fig. 5.36. Liquid accumulations in crystal mush on a variety of scales are not unusual, with examples of segregation veins on the metre-scale documented from the Kīlauea Iki lava lake (Helz, 1980) and examples from the centimetre-scale observed from the Brandur, Fontur and Saxi nodules from Icelandic eruptions (Boyes, 2018).

5.6.1.1 The pegmatitic texture

"Gabbroic pegmatite" is an observational term in reference to the astounding size of the crystals within these segregations, and is the term that has been previously used in the literature (e.g. Larsen and Brooks, 1994; McBirney and Noyes, 1979; McBirney and Sonnenthal, 1990; Wager and Deer, 1939; Wager and Brown, 1968). However, the literature offers few insights into the origin of such pegmatitic textures (Irvine, 1987; Larsen and Brooks, 1994; Larsen et al., 1992; McBirney and Sonnenthal, 1990), so here I briefly speculate on how they could have arisen. My field observations and those of Larsen and Brooks (1994) recognised that (where possible) the minerals crystallised off the margins of the gabbroic pegmatite. This suggests that there was heterogeneous nucleation into a static environment. There is no clearly defined feeder visible from field observations. These are typical characteristics of granitic pegmatites in hydrous silica-saturated magmas, associated with an exsolved vapour phase (Cameron et al., 1949; Philpotts and Ague, 2009).

The size of the crystals in a solidifying magmatic system is determined by the concentration of elements in the surrounding environment and the proximity to other nuclei (Vernon, 2004). Jahns and Burnham (1969) suggested that growth of pegmatitic-sized crystals is promoted by slow cooling rate, coupled with high diffusion rates through a vapour phase. London (2005) disputed this, concluding that pegmatitic textures, rather than regular 'plutonic' textures, reflect a change in the state of the system such that the probability of forming nuclei of certain phases is decreased. London (2008) suggests the reason that granitic compositions commonly produce pegmatites whereas mafic magmas do not, stems from the differences in the viscosities of the liquids, and therefore the ionic diffusivity. Mafic liquids have lower viscosities resulting in more rapid ionic diffusion (Zhang et al., 2010) that fosters crystal nucleation closer to the liquidus. Felsic liquids have higher viscosities, which impede the ionic diffusion necessary to initiate nucleation, and hence felsic liquids cool further below their liquidus temperature before crystallisation commences. Pegmatitic textures are the result of this undercooling. London (2005) concludes that the magnitude of liquidus undercooling at the onset of crystallisation determines the texture.

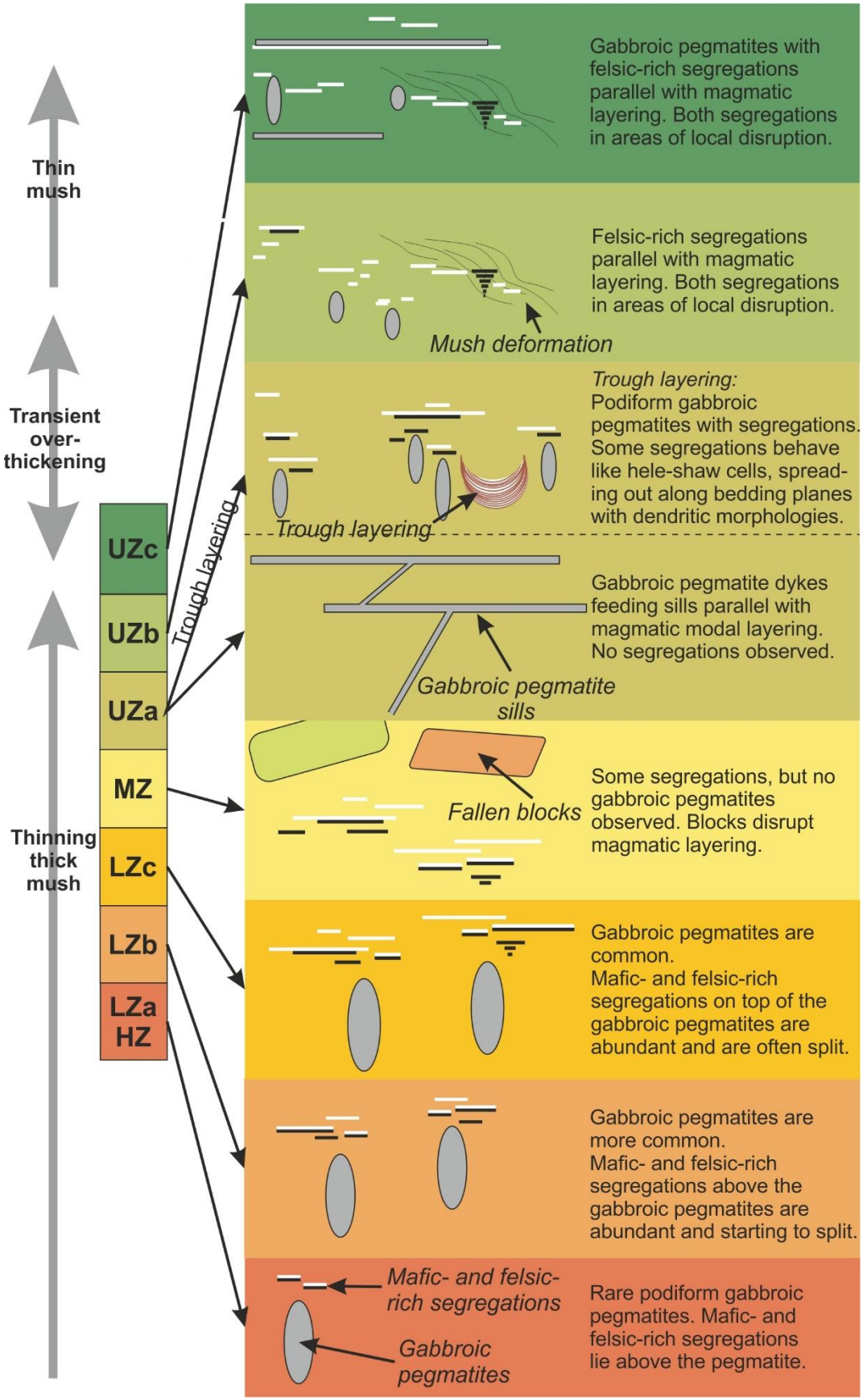

Figure 5.36 A schematic cartoon summarising the key field observations of the segregated mafic-rich and felsic-rich segregations, and their association with the gabbroic pegmatites throughout the LS. The cartoon also shows the relationship between the gabbroic pegmatite morphology and the mush thickness as the intrusion was solidifying.

London (2019 pers. comm.) suggests that for gabbroic pegmatites to form, mafic liquids must cool much more rapidly than felsic liquids to achieve the degree of undercooling necessary to form a pegmatitic textures.

The gabbroic pegmatites documented in this study were not silica saturated but they were relative evolved (with bulk rock Mg# decreasing through the LS; Appendix Table 5.B). All the mineral phases are pegmatitic (and at least an order of magnitude greater than the surrounding LS gabbro grain size), so there must have been a change in the total nucleation density of the accumulated liquid compared to the surrounding LS gabbro. Miarolitic cavities at the stratigraphic top of gabbroic pegmatites (from LZb upwards) suggest that vapour saturation occurred during crystallisation. This supports the idea of a H_2O-NaCl-CH_4 solution coexisting with the liquid from which the gabbroic pegmatites crystallised, as shown by primary fluid inclusions in plagioclase with 22.8 wt.% dissolved NaCl (Larsen et al., 1992). Prior to exsolution, the volatiles in the liquid would have lowered the viscosity, increasing the diffusion rate of the elements to the crystal (Dingwell et al., 1996; Hort, 1998). London and Morgan (2012) suggests this should have increased nucleation, yet I observe a pegmatitic texture. Furthermore, the average size of crystals in the gabbroic pegmatite do not noticeably vary between LZ and UZ, nor spatially within the LS. This is of note as granitic pegmatites are often found associated with the margins of plutonic bodies, in the domain of most rapid cooling (London, 2008) i.e. rapid cooling of viscous liquids will promote large undercoolings before nuclei form. Consequently, I would have expected larger crystals in the gabbroic pegmatites on the margins of the LS in close proximity to the MBS and UBS where cooling rates would have been faster. It is also pertinent to note that the late-stage mafic- and felsic-rich segregations, which are spatially associated with the gabbroic pegmatites, have a comparable grain size to each other, and the surrounding LS gabbro. This implies that nucleation was not inhibited in these late-stage liquids, and so poses the question of what the relationship is between the liquid forming the gabbroic pegmatite and the liquid forming the mafic- and felsic-rich segregations. Further work exploring this interesting quandary would be valuable and the Skaergaard Intrusion would be a fantastic natural laboratory to explore various hypotheses on the formation of mafic pegmatites (discussed further in section 6.1.2).

5.6.2 Crystal mush and late-stage liquid migration

There is a relationship between the morphology of the gabbroic pegmatites and the independently determined thickness of the mush (Holness et al., 2017c). The morphology of the late-stage liquid accumulations changes from podiform in the LZ to sill-like morphologies running parallel with the modal layering in the lower part of UZa. This occurs in the context of the mush thickness decreasing with increasing stratigraphic height, from tens of metres thick in the LZ to metres or thinner in the upper parts of the intrusion (Holness et al., 2017c). Significantly, in the upper part of UZa, where the trough layering occurs, the gabbroic pegmatites revert to a podiform morphology (Fig. 5.36). This gabbroic pegmatite morphology is analogous to that of the gabbroic pegmatites in LZ and implies that the late-

stage liquid accumulated in a thick mush. Recent fieldwork observations (Holness 2017 pers. comm.) coupled with EBSD analyses independently show that the trough layering represents a sudden transient overthickening of the mush as a result of mush collapsing from the intrusion walls and acting in a sedimentary manner (Vukmanovic et al., 2018). Overall, the gabbroic pegmatite morphology is podiform in thick mush but planar in thin mush, as a result of the surrounding LS mush rheology and thickness (Fig. 5.36).

The strength of the surrounding LS mush is a property of the networks formed by the crystals in the mush, i.e. it is a function of crystal force chains (Bergantz et al., 2017). In the LZ, not only is there field evidence of the diapiric rise of liquid blobs on the sub-metre scale (Fig. 5.5), but also branching tendrils from the podiform pegmatites indicating brittle fracturing (Fig. 5.4). One explanation for such contradictory observations of ductile and brittle behaviour is granular force chains causing loading of the crystal mush. This results in transient mush hardening that can lead to the preservation of brittle fracturing features (Bergantz et al., 2017; Schleicher and Bergantz, 2017). Creation of such an ephemeral environment depends on the mush porosity, crystal shapes within the mush, and the force of the incoming liquid – high porosity results in the mineral-mineral contacts disconnecting, which would prevent transient mush hardening and result in ductile behaviour. In zones of thin mush, the gabbroic pegmatites form planar sill-like morphologies that rarely cut or deform the magmatic layering. This could be due to insufficient hydrostatic overpressure to exceed the strength of the mush if the cumulus crystals were locked.

In the LZ Fe-Ti-V layers there is evidence of a change from ductile to brittle deformation with stratigraphic depth within the crystal mush (Fig. 5.22). Oxide-rich seeps originating from the Fe-Ti-V layers (further geochemical investigation is needed to verify this relationship, which is inferred from field observations) caused ductile deformation of the surrounding mush as it migrated down stratigraphy. At the maximum depth below the Fe-Ti-V layers (24 m below), the seeps have fractured the LZc gabbro, resulting in misaligned gabbro packets (Fig. 5.23). This indicates the mush was more cohesive at greater depths, suggesting a mush thickness of 20 m.

Late-stage segregations in UZc are associated with deformed crystal mush, i.e. in slumped layers of UZc gabbro (Fig. 5.19). The solidified remnants of mafic-rich liquid extend 3 m down stratigraphy, deforming the mush in a ductile manner. Below 3 m, the pathways created by the mafic-rich seep caused brittle deformation to the surrounding mush, implying the mush had integral strength. The felsic-rich liquids are laterally extensive along magmatic modal layering and have not been lost from the interstitial liquid in the floor cumulates, as documented between LZc-UZa by Holness et al. (2011). This supports the idea of a thin, strong mush layer, in which the passive buoyancy-driven migration of the late-stage liquids is limited.

5.6.3 Was there silicate liquid immiscibility in the late-stage segregations?

The composition (Fig. 5.32) and morphology (Fig. 5.8) of the wispy lenses of mafic- and felsic-rich segregations suggests that they are the solidified remnants of two immiscible conjugates. The mafic- and felsic-rich segregations evolve towards more immiscible end-member compositions upwards through the LS stratigraphy. Below LZc the mafic-rich segregation is an olivine pyroxenite, but in LZc and above it is dominated by oxides. This is consistent with the evolution of a mafic- and felsic-rich liquid down the silicate liquid immiscibility binodal (Fig. 2.5). Given the shape of the binodal in temperature-composition space, this implies that the temperature at which the late-stage liquids were crystallising decreased upwards through the intrusion.

The remnants of the two immiscible liquids show contrasting physical behaviour due to their different properties. Following Charlier and Grove (2012), I plot the whole rock data as a function of NBO/T (where NBO is the number of non-bridging oxygens, T is the tetrahedrally coordinated network forming cations: Si + Al + P + Ti). This is a measure of the degree of polymerisation in silicate melts (Mysen, 1983). The NBO/T for mafic-rich segregations increases with increasing height in the LZ, conversely the NBO/T for the felsic-rich segregations decreases (Fig. 5.37). In the UZ there is a range of NBO/T values for the mafic-rich segregations, while the NBO/T values for the felsic-rich segregations are relatively constant. The calculated density (using Bottinga and Weill, 1970) of the mafic-rich segregations varies from 2.81–3.84 g/cm^3, while for the felsic-rich segregations density varies from 2.35–2.57 g/cm^3 – such a calculation is based on the assumption that the sampled late-stage segregation is the fully crystallised liquid, with no liquid loss. The density difference between the segregation pairs is smallest in LZa, at 0.19 g/cm^3, and largest in UZa, at 1.00 g/cm^3. Viscosities calculated from the whole rock geochemistry suggests that the liquid from which the gabbroic pegmatite crystallised had a viscosity on the order of 10^2 Pa.s (this assumes a closed system); while the liquid from which the mafic- and felsic-rich segregations crystallised had viscosities on the order of 10^{-1} Pa.s and 10^4 Pa.s, respectively. Consequently, the mafic-rich liquid could migrate down through the mush, whereas the felsic-rich liquid is closer to the density of the average gabbro and so closer to neutral buoyancy, meaning the liquid extends outwards along the magmatic layering.

The mafic- and felsic-rich segregations are consistently found stratigraphically above podiform pegmatites, suggesting a relationship between the two. Previously, field and compositional relationships between the mafic- and felsic-rich segregations were attributed to high temperature metasomatism (McBirney and Sonnenthal, 1990). They argued that the LS was largely solidified at the time of late-stage segregation formation and that they saw "no relations between the replacement features and slumping or compaction". Any structure to the segregations was attributed to the movement of metasomatic fluids. However, the consistent morphological relationship of the upper felsic-rich segregations and the lower mafic-rich segregations within the same LS average gabbro (e.g. Fig. 5.8) is inconsistent with metasomatic alteration from a single fluid. Furthermore, the morphology of the two

segregations is each very different, despite metre-scale proximity to the other (Fig. 5.8; 5.10). This suggest two distinct starting compositions for the liquids.

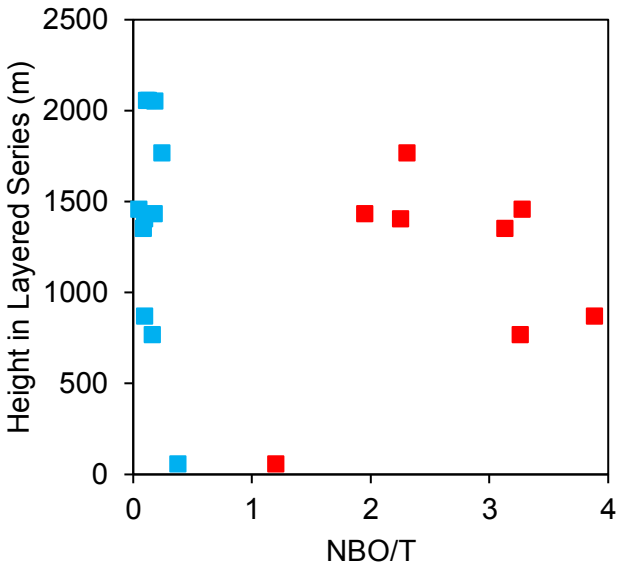

Figure 5.37 Plot of NBO/T against height in the layered series of the Skaergaard intrusion. Conjugate mafic- (Fe-) rich and felsic- (Si-) rich segregations are represented by filled red and blue squares.

The gabbroic pegmatites originated from the interstitial liquid of the LS (based on the plagioclase mineral chemistry). Unmixing has been documented within the bulk and the interstitial liquid of the LS (e.g. Holness et al., 2011; Humphreys, 2011; Jakobsen et al., 2005; Veksler et al., 2007; Veksler et al., 2008a), with the contentious debate in the Skaergaard literature being centred on *when* unmixing occurred. Previously published estimates for the onset of unmixing in the interstitial liquid from reactive microstructures suggest LZc (Holness et al., 2011; Stripp, 2009), while Humphreys (2011) used Ti concentrations in plagioclase to conclude that the interstitial liquid unmixes even in the most primitive cumulates. Therefore, it is reasonable to assume that the accumulated interstitial liquid (of which the gabbroic pegmatites are the crystallised remnants) unmixed. Based on the major element whole rock data and petrological observations, I suggest that silicate liquid immiscibility occurred in the late-stage segregations from LZa.

Unmixing of the gabbroic pegmatite liquid in LZa-c was tenuously proposed by Larsen and Brooks (1994), based on the whole rock geochemistry of granophyric patches and field observations of sharp contacts with the adjacent gabbro. I augment this with detailed petrologic and fieldwork evidence (along with further whole rock analyses). The gabbroic pegmatites of LZa host ilmenite-rich and granophyre paired intergrowths. The presence of both liquids demonstrates that segregation of the two liquids was weak and that liquid migration in the gabbroic pegmatite was incomplete. Otherwise all the mafic-rich liquid would have consistently accumulated at the base of the pegmatitic structure. The olivine pyroxenite (A – a mafic-rich liquid) is not, however, observed at the base of any gabbroic pegmatitic

structures, except in LZa. I observe stepped clinopyroxene-plagioclase grain boundaries, Type 1 symplectites and polycrystalline olivine rims in LZb mafic-rich segregations, where in contact with the surrounding LZb gabbro. These microstructures provide evidence of unmixing as the mafic-rich segregation is out of equilibrium with the LS gabbro, causing it to react with surrounding crystals (Holness et al., 2011). This supports the idea of silicate liquid immiscibility occurring in the late-stage segregations from LZa.

Such mafic- and felsic-rich structures have also been identified as unmixed liquids by Coint and Keiding (2019) in the 1.8 Ga monzonitic Raftsund intrusion in the Vesterålen-Lofoten Archipelago in Northern Norway. Using similar methods to this study, they combine field observations, microstructures, whole rock geochemistry and trace elements in clinopyroxene (Coint et al., 2017) to arrive at this conclusion. Likewise, Scoon and Mitchell (1994) interpreted the occurrence of Fe-rich pegmatites in parts of the Bushveld Complex as originating from immiscible Fe-Ti-rich silicate melts.

5.6.4 Unmixing and segregation

Having established that the mafic- and felsic-rich segregations are indeed the crystallised residue of conjugate immiscible liquids, the question then arises of *where* the unmixing and then segregation occurred. One scenario is that the gabbroic pegmatites are considered "micro-magma chambers", as envisioned by Larsen and Brooks (1994), in which continual crystallisation evolved the remaining liquid fraction towards the silicate liquid immiscibility binodal. In this scenario, the remaining liquid fraction unmixed within the gabbroic pegmatite, forming an emulsion. During unmixing the composition of the minor and major immiscible phases would be determined by the intersection of the liquid line of descent with the binodal. Assuming the whole rock composition of the solidified gabbroic pegmatites approximates to the composition of the original accumulated interstitial liquid, then the NBO/T of the sample, paired with crystallisation temperature estimates (Larsen and Brooks, 1994), and assuming a binodal similar to that of the Sept Iles (Fig. 2.5), suggests that in LZa, the Fe-rich liquid would be the minor phase. The Lever Rule suggests the Fe-rich liquid would comprise around 20% of the emulsion, rising to 30% in LZb. In UZa, the gabbroic pegmatites have a range of compositions, which suggest the minor Fe-rich phase would comprise between 20-50% of the emulsion; while in UZc, the Fe-rich liquid is suggested to have dominated (the NBO/T of the whole rock composition for the pegmatite exceeds the compositional extent of the Sept Iles binodal). Furthermore, the miarolitic cavities at the stratigraphic top of the gabbroic pegmatites are evidence of a vapour phase, and the addition of H_2O changes the shape and size of the binodal (Fig. 1.4). Hence, these estimates should be treated with caution, but they provide an interesting point of discussion.

Experimental work on ferrobasalts proposes that in magma bodies <~10 m in size, gravitationally-driven segregation of immiscible micron-scale Fe-rich droplets is unlikely to be significant (Chapter 2). However, given that Fe-rich droplet size scales with cooling rate (Chapter 3), segregation could occur

given the slow cooling rate of the Skaergaard Intrusion and the differing starting composition of the gabbroic pegmatites in comparison to the experimental starting compositions (of Chapter 2). I test the idea of whether segregation after unmixing occurred by studying the microstructural and field observational evidence. Plagioclase grains separate granophyric and ilmenite intergrowth pockets in the LZ gabbroic pegmatites suggesting segregation of the two immiscible conjugate liquids. Furthermore, field evidence suggests that segregation of the unmixed liquids did occur within the LZa gabbroic pegmatites, over a localised distance (i.e. on the centimetre-scale), as shown by olivine pyroxenite preferentially found at the base of the late-stage segregation structures.

As the pegmatitic crystals grew in the gabbroic pegmatites, the interstitial unmixed liquid fractions would have evolved. The interstitial liquid in the crystallising gabbroic pegmatite would be more buoyant than the original accumulated late-stage liquid, and so would have percolated upwards through the surrounding thick mush. It is interesting to consider the effect of volatiles here. Miarolitic cavities at the top of the gabbroic pegmatites suggest exsolution of a volatile phase. This could have occurred by second boiling in the gabbroic pegmatite, i.e. continued crystallisation of the gabbroic pegmatites until volatiles saturated. Alternatively, the buoyant expulsion of an emulsion of unmixed interstitial liquid from the top of the gabbroic pegmatite may have sufficiently reduced the pressure within the gabbroic pegmatite to cause bubble nucleation. Bubbles coexisting with the mafic- and felsic-rich segregation may have provided additional nucleation sites in the mafic- and felsic-rich segregations (Davis and Ihinger, 1998), resulting in the immiscible segregations having a grain size consistent with the surrounding Skaergaard average gabbro.

As the emulsion buoyantly rose above the gabbroic pegmatite and cooling continued, unmixing to more extreme end-member compositions occurred. Due to the differing physical behaviour of the two conjugates, buoyant rising of the emulsion induced segregation; the density difference between the mafic- and felsic-rich segregations and the gabbroic pegmatite is typically -0.5 and +0.2 g/cm^3 respectively. The greater density difference characterising the mafic-rich liquid resulted in downwards migration, while the felsic-rich liquid reached a level of neutral buoyancy and spread out along the magmatic layering of the LS gabbro.

The mafic-rich liquid would be out of equilibrium with the surrounding cumulus minerals. As such, reactive symplectite structures would be predicted. These are apparent in samples cutting the boundary between the solidified remnants of the mafic-rich liquid and the surrounding LS gabbro, from LZ and UZ.

A clear example of the mafic- and felsic-rich segregations originating from the gabbroic pegmatites are the dendritic anorthosites of the UZa trough layers, where the mafic-rich segregation is always found stratigraphically down-dip and is the volumetrically minor phase (Fig. 5.17). While the podiform gabbroic pegmatites cut the strong magmatic layering, the mafic- and felsic-rich segregations squirted

along the well-defined planes of the layering. The dendritic morphology is analogous to the complex, highly branched structures resulting from Hele-Shaw flow (Pihler-Puzović et al., 2013; Saffman and Taylor, 1958). This forms when Stokes flow (i.e. flow involving a liquid with a high viscosity, slow velocity, and a Reynolds number <<1) occurs between two parallel flat plates separated by an infinitesimally small gap (Hele-Shaw, 1898). It has been experimentally shown that when the two parallel flat plates are rigid-walled cells, the resultant morphology is narrow highly branched fingers of the intruding liquid, whereas when bounded by an elastic-walled cell, the resultant morphology is short, stubby fingers (Pihler-Puzović et al., 2013). Consequently, formation of the dendritic anorthosites can be best approximated to Hele-Shaw flows in a rigid-walled cell. This implies that the magmatic layering had sufficient integral rigidity that it did not deform when these liquids rose off the gabbroic pegmatites and spread outward along the magmatic layering. The dendrites have no consistent orientation with respect to the dip of the magmatic layering, suggesting that gravity alone did not control the initial intrusion and spread of the immiscible liquids. Hence, Hele-Shaw flow provides a feasible model for the observed features. Post-intrusion between the magmatic layers, gravity acted to effectively separate the unmixed liquids; I observe that the mafic-rich liquid of the dendrite always travelled the furthest in the down-dip direction. Overall, the immiscible liquids were largely extruded from the top of the gabbroic pegmatite as an emulsion, which separated within the surrounding crystal mush, as controlled by the physical characteristics of each immiscible liquid and gravity. It is interesting to note that the scale over which complete separation of the mafic- and felsic-rich liquids occurred in the dendrites is on the same scale as the total width of the studied NE England dykes (of Chapter 3) within which the immiscible liquids remained an emulsion. Furthermore, the experimental data (of Chapter 2) suggested that Fe-rich droplets on the micron-scale would not effectively separate. However, in Skaergaard, where there were very slow cooling rates, I observe clear separation of two immiscible liquids. This emphasises that cooling rates are highly significant in the coarsening and separation of an emulsion.

These ideas contrast with that of McBirney and Sonnenthal (1990), who attribute the branching dendritic anorthosites to the transport of components by a reactive fluid infiltrating the magmatic layering, with the length over which the fluid infiltrates qualitatively linked to the rate of diffusion. Their model cannot explain the close relationship between the mafic- and felsic-rich segregations, the down-dip segregation of the mafic-rich segregation, nor the differential morphologies of the two segregations despite the surrounding LS gabbro being devoid of heterogeneities.

5.6.5 Are the late-stage segregations ‘micro-magma chambers’?

If the gabbroic pegmatites are indeed the origin of the mafic- and felsic-rich segregations then the gabbroic pegmatites are an open system. The gabbroic pegmatite liquids are representative of the intercumulus liquid, as shown by the whole rock geochemistry and plagioclase anorthite composition (Fig. 5.31; 5.35). If the minerals crystallising in the gabbroic pegmatite liquid are in equilibrium with

the accumulated liquid, then the gabbroic pegmatite should follow the whole rock differentiation trends of Skaergaard.

My fieldwork and the major element concentrations of the late-stage segregations (Fig. 5.32) are suggestive of the mafic- and felsic-rich segregations being the remnants of an emulsion that has separated. Trace elements have preferential partition coefficients between two immiscible liquids, as shown by experimentally determined coefficients (Fig. 1.8; Schmidt et al., 2006; Veksler et al., 2006). However, many of the calculated trace element partition coefficients from the mafic- and felsic-rich segregations are inconsistent with the known experimentally determined partition coefficients (Fig. 5.38). In particular, the trace element partition coefficients calculated for Ba, Sr, LREEs and Zr show the opposite of the experimentally expected partition coefficients, with the biggest disparities between the experimental and the calculated segregation partition coefficients observed in the UZa trough layering horizon. Such a calculation of the trace element partition coefficients assumes crystallisation in a closed system.

The trace elements showing unexpected partitioning behaviour are high field strength elements (HFSE) and large lithophile elements (LILE). HFSE are commonly regarded as immobile in geological systems (Gill, 2010; Pearce and Cann, 1973), so subsequent leaching from the mafic-rich segregation, remobilisation, and deposition of the LREE and Zr in the felsic-rich segregation would be surprising. Recent observations and experimental work show that HFSEs and REEs can be mobilised in alkali, Cl-rich and F-rich systems (Sheard et al., 2012; Wilke et al., 2012; Williams-Jones et al., 2012; Yang et al., 2014). The gabbroic pegmatite fluid inclusions (Larsen et al., 1992) suggest an exsolved H_2O-NaCl-CH_4 fluid, so it is possible that these elements were lost from the magmatic liquid to an aqueous fluid. Interestingly, CaO concentrations (Fig. 5.38) in the mafic- and felsic-rich segregations also show the reverse partitioning trend to that expected between two immiscible liquids. Overall, the depletion trends are not consistent across all the HFSEs and LILEs. One explanation could be that part of the mafic-rich immiscible fraction remained trapped within the gabbroic pegmatite and so the mafic-rich segregation located above the gabbroic pegmatite would have been out of equilibrium with its conjugate felsic-rich segregation.

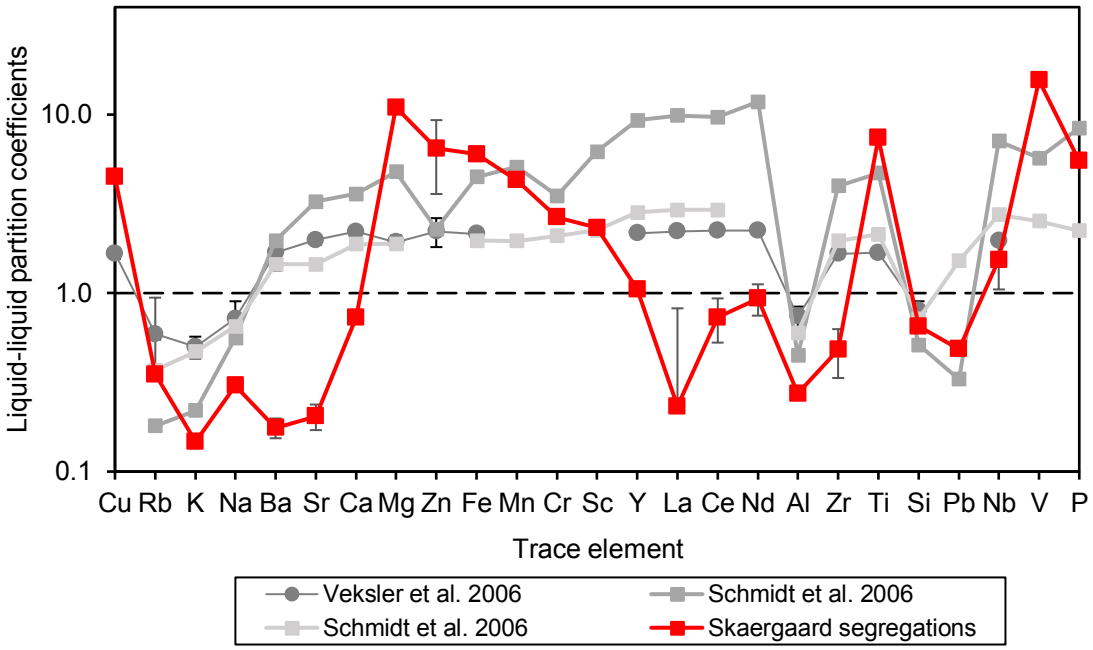

Figure 5.38 Liquid-liquid partition coefficients for (Cfe/Csi) for a range of trace elements; these values (in grey) are experimentally determined (and shown in Figure 1.8). Overlain in red are the liquid-liquid partition coefficients as calculated for conjugate pairs of mafic- (Fe-) rich and felsic- (Si-) rich segregations from the Skaergaard Intrusion.

5.7 Summary

The gabbroic pegmatites represent the passive late-stage accumulations of the interstitial liquid from the cumulus pile. When the crystal mush is thick, the gabbroic pegmatites have a podiform morphology, whereas when the crystal mush is thin, the gabbroic pegmatites have a planar sill-like morphology.

Field evidence reveals a relationship between the mafic- and felsic-rich segregations and the gabbroic pegmatites. The mafic- and felsic-rich segregations appear to originate from the gabbroic pegmatite where unmixing started. A buoyant emulsion rose into the overlying crystal mush and the contrasting physical properties of the two liquids caused gravitational driven segregation to occur. Miarolitic cavities within the gabbroic pegmatite indicate the presence of a segregated vapour phase within the late-stage segregations, which affected the viscosity of the liquid prior to exsolution of the volatile phase. The changes in viscosity impacted the microstructures produced.

The mafic- and felsic-rich segregations are immiscible liquids, which show different physical behaviour within the surrounding crystal mush after separation. Timescales of cooling are shown to be a key factor in the coarsening and complete segregation of the two immiscible liquids.

6 CONCLUDING REMARKS

This thesis sought to investigate the physical behaviour of immiscible silicate liquids evolving within a crystal mush at different cooling rates. The focus has been on ferrobasaltic systems, where the Fe-rich conjugate forms the minor phase, and the Si-rich conjugate the major phase. The wider implications of studying silicate liquid immiscibility can be distilled to the potential of the process to form ore deposits and the effect of the process on the liquid line of descent of differentiating magmas. For the process of unmixing to be of broad significance to the geological community, near or complete segregation of the two immiscible liquids is required. In the published literature, a range of methods have been used to show large- and small-scale segregation of unmixed liquids preserved in the geological record, including mineral geochemistry, melt inclusions and field evidence (e.g. Fischer et al., 2016; Holness et al., 2011; Humphreys, 2011; Jakobsen et al., 2005; Namur et al., 2012; VanTongeren and Mathez, 2012). This thesis contributes to our understanding of the physical constraints on such unmixing segregation, combining experiments, image analysis, geochemistry, petrology and field evidence, to build up a holistic understanding of factors affecting the coarsening of unmixed liquids. As is typical of scientific work, the studies herein contain assumptions and limitations, the most significant of which is the focus on ferrobasaltic systems, and it is important to acknowledge that this constrains the wider applicability of my conclusions to other natural analogous.

The thesis began (Chapter 2) with an experimental approach to quantify how Fe-rich droplets nucleate and coarsen with decreasing temperature, a growing crystal fraction, and a constant cooling rate of 1°C/h. These experiments expanded on the detailed geochemical experimental study of Charlier and Grove (2012), which provided important context for the study of the physical behaviour of an emulsion. The experimental cooling rate used is typical of cooling across a magma body on the tens of metre-scale or less. The major conclusion is that in small-scale magma bodies on the ~10 m scale, gravitationally-driven segregation of immiscible homogeneously nucleated Fe-rich droplets is unlikely to be significant; it is not valid to assume that an Fe-rich immiscible liquid will always tend to migrate downwards into structural traps. The experimental set up only varied temperature and the duration for which each experiment was held isothermally; it did not address the effect of cooling rate, which is crucial for kinetic studies and will affect the application of the experiments to different natural systems. The cooling rate used in the experiments was approaching the limit that can be stably maintained experimentally.

To tackle the problem of assessing slower cooling rates, in Chapter 3 I used natural samples taken from transects across basaltic dykes. By using crystal microstructures to determine the cooling rate at different points across the dyke width, I showed that at slower cooling rates there is a higher Fe-rich droplet number density and an increase in Fe-rich droplet size. This was an interesting result for investigating the potential for segregation of unmixed liquids as Fe-rich droplet coarsening is more

likely to lead to Fe-rich liquid accumulation: coarser droplets are more likely to migrate and segregate than a micron-scale emulsion. Although there are other factors that will affect coarsening, such as composition, pressure and fO_2 (e.g. Charlier and Grove, 2012), my results suggest that the conclusions from experimental studies may be not applicable for systems with very slow cooling rates.

In Chapter 4 I studied the role of crystal growth in triggering unmixing at crystal-melt interfaces and I highlighted the effect of compositional boundary layers in the localised formation of immiscible liquids. This work shows that compositional boundary layers facilitate the development of liquid immiscibility at temperatures above those that experiments illustrate unmixing can be produced by nucleation. Crucially, at higher temperatures the crystal fraction in melts is lower and so there is greater potential for the migration and segregation of two immiscible liquids.

Chapter 5 investigates late-stage segregations in the Skaergaard Intrusion and shows that, given sufficient time, unmixed liquids will undergo near-complete segregation on a metre-scale but the migration distance is hindered by the thickness and permeability of the crystal mush. As such, in temperature-composition space, the onset of unmixing in relation to the liquidus is crucial. At low crystal fractions there is a greater possibility of immiscible liquid segregation, unimpeded by a high crystal fraction; however, this requires high temperature unmixing. Such evidence is suggested in Chapter 4, whereby Fe-rich immiscible liquid surrounds growing plagioclase grains at temperatures >1100°C.

There are several major outstanding debates in igneous petrology to which this thesis is relevant: first that magmatic rocks at the surface of the Earth are mainly basalts or rhyolites but intermediate compositions are poorly represented (i.e. the Daly gap (e.g. Charlier et al., 2013; Charlier et al., 2011)); second that volcanoes are underlain by extensive crustal-scale mush zones (Cashman et al., 2017); and third that our understanding of the formation of enigmatic varieties of Fe-rich ore deposits is incomplete. In the first instance, my work on compositional boundary layers around crystals suggests that, if crystals act as nuclei and kinetic effects are recognised, immiscibility may occur in natural samples at higher temperatures than previously thought (>1100°C; complementing work by Hou and Veksler (2015)). At a larger-scale, such high temperature unmixing and movement could have important implications for the formation of the Daly gap through the dearth of intermediate magma compositions (e.g. Charlier et al., 2013; Charlier et al., 2011). In the second instance, if active magma systems are dominated by crystal-rich mush, then the migration of interstitial liquids in exhumed layered intrusions may have direct relevance to volcanological processes. My study of the Skaergaard late-stage segregations (Chapter 5) show that the physical properties of the mush (rheology and thickness) control the morphology of the accumulating late-stage liquids and that these form metre-scale heterogeneities in the mush. In the third instance, early onset of unmixing can play a role in ore genesis by potentially enabling the relative movement of the two immiscible liquids in a gabbroic crystal mush (Chapter 4).

Furthermore, the experimental work on the coarsening of Fe-rich droplets at different temperatures also has relevance to studies on the migration of sulfide droplets in magma (e.g. Chung and Mungall, 2009; Mungall and Su, 2005).

As analytical techniques become capable of ever greater resolutions, with ever smaller detection limits, an awareness of processes that can cause heterogeneities in glasses and zoning in crystals will be important for reliable geochemical interpretations of igneous processes. For example, silicate liquid immiscibility can cause small-scale spatial heterogeneities in glass compositions, as shown in Chapters 2, 3 and 4. My work on Fe-rich droplet nucleation and coarsening, nanoemulsions, and the formation of compositional boundary layers around growing crystals highlights the importance of petrologic study of samples, prior to geochemical work to identify where analyses measure emulsions rather than a single glass phase.

6.1 Future directions of study

This thesis has raised a number of different areas of future study, which I feel would be valuable to the field of igneous petrology and the study of silicate liquid immiscibility.

6.1.1 Microstructures of immiscible liquids

6.1.1.1 Experiments

There is a clear need to expand the microstructural study of Chapter 2 to experiments of differing starting compositions. Ideally experiments with a more Fe-rich starting composition, where the Si-rich conjugate is the minor phase forming droplets distributed within a continuous Fe-rich liquid. The same analyses detailed in Chapter 2 could be replicated for such a set of atmospheric pressure, drop-quench experiments quantifying the evolution of Si-rich droplets at a constant cooling rate of 1°C/h. This would expand the applicability of the microstructural study to a wider range of natural systems. It could also be combined with geochemical analyses to further investigate the shape of the binodal for more Fe-rich samples (work started by Charlier and Grove (2012)). Further investigation into the effects of isothermal dwell times on the experimental microstructure of the immiscible droplets would provide a valuable indication of the stability of the immiscible liquids. The experiments of Chapter 2 are cooled at a constant rate and the effect of fluctuating temperatures, potentially simulating a new magma injection into a body of melt, was not considered. Temperature cycling is common in magmatic systems and needs to be accounted for when analysing chemical zoning of igneous crystals and rock textures. Oscillating temperature dramatically speeds up recrystallisation of magma analogues (e.g. Mills et al., 2011), so fluctuating temperatures are likely to promote emulsion coarsening, which could have implications for the efficiency of segregation of two immiscible silicate liquids. Chapter 2 highlights the kinetic barriers to Fe-rich droplet coarsening in the timeframe of solidification in natural systems;

optimal migration of Fe-rich liquids could occur if the dense liquid accumulates and exceeds the pore throat pressure between grains (e.g. Chung and Mungall, 2009; Mungall and Su, 2005).

6.1.1.2 Natural samples

It would be interesting to use natural samples for the equivalent, quantified microstructural study as completed in Chapter 2; this would require a series of well-characterised samples with a glassy mesostasis and a known cooling rate(s) – similar to those collected from the NE England dykes (Chapter 3). However, it is difficult to find natural samples where the glass is not devitrified, as devitrification inhibits automated image analysis. Sadly, devitrification of the glass in the NE England dykes prevented such quantitative image analysis for my study of the emulsion microstructure. Further investigation of the Cohassett Flow samples, where Philpotts and Philpotts (2005) identified unmixing, could be promising.

6.1.1.3 Novel image analysis techniques

Experimentation with different imaging techniques would greatly benefit microstructural studies of immiscible liquids. First, techniques reaching a greater resolution will enable better understanding of the controls on emulsion nucleation and coarsening of droplets. Currently, image analyses of SEM BSE images (as in Chapter 2 and 3) are constrained by the SEM magnification limit, photograph pixel resolution and the number of images that can be analysed. The magnification limit reaches a maximum with a half field width of ~5 μm because effective imaging of the Fe-rich liquid requires an SEM operating voltage >15 kV. Different options for larger area analyses of droplets forming an emulsion include small-angle X-ray scattering (SAXS) and in-situ Raman spectroscopy. From these it is theoretically possible to get *in situ* information on the size distribution of nano- to micron-scale droplets (e.g. Toplis and Reynard, 2000). Second, gaining an understanding of the 3D morphology of the emulsion is highly desirable. The power of 3D imaging was elucidated by atom probe tomography (APT) analyses (as shown in Chapter 4), which revealed the nano-scale morphology and boundaries between unmixing liquids and showed that APT has the potential for microstructural application to basaltic glasses (e.g. Saxey et al., 2018). Combining nano-scale morphological analyses with geochemistry would be highly insightful: currently, APT provides relative compositional information, so there is a requirement for APT calibrated primary standards and data processing techniques, standardised across APT labs. 3D information would also be incredibly useful for quantifying the wetting angles of unmixing liquids on different crystal phases and different crystal faces. Building up such a database was begun in Chapter 2 using 2D images and a large number of measurements, but further work using X-ray tomography to measure the angles in 3D, potentially at nano-metre resolution would be ideal. Third, in a new paper by Pleše et al. (2018), the authors showed the 4D evolution of bubbles on the surface of crystals. A similar study would be valuable to see the heterogeneous nucleation of immiscible liquids on crystals and any potential changes in wetting angles. This would provide a fascinating insight into the evolution of unmixing liquids, which is currently limited to the

snapshots preserved during quenching. Collecting microstructural measurements in real time is an exciting avenue of future research on the growth kinetics of crystal-rich systems. Projects running crystal growth experiments in a synchrotron (Hartley 2019 pers. comm.) could be combined with additional studies on unmixing, as such projects have noted the development of compositional boundary layers around plagioclase (similar to those described in Chapter 4).

6.1.2 Skaergaard

Focusing on the future direction of work in Skaergaard, the extensive, high resolution drone footage of the LS (imaged by Jens Andersen during our 2017 field campaign) could be used to calculate the volume of magmatic interstitial liquid accumulated in late-stage segregations, visible in the aerial images. This would build on the estimates of Tegner et al. (2009), who concluded that the volume of melanogranophyre in the UZ increases towards the roof of the intrusion.

On a tangent to immiscible liquids, the Skaergaard Intrusion would be a fantastic natural laboratory to explore hypotheses on the formation of mafic pegmatites. One such example being that as plagioclase growth on the (001) face dominates at fast cooling rates, in Skaergaard the growth rate on the (010) face tends towards the growth rate of the (001) face due to the very slow cooling rate of the intrusion (Holness, 2015). EBSD of pegmatitic plagioclase crystals from the gabbroic pegmatites could provide us with more information on the dominate growth direction providing some indication of the relative cooling rate.

7 REFERENCES

Abraham, F., 2012. The Nature of the Nucleation Process, Homogeneous nucleation theory: the pretransition theory of vapor condensation. Elsevier, pp. 1-8.

Ágústsdóttir, T., Woods, J., Greenfield, T., Green, R.G., White, R.S., Winder, T., Brandsdóttir, B., Steinthórsson, S. and Soosalu, H., 2016. Strike-slip faulting during the 2014 Bárðarbunga-Holuhraun dike intrusion, central Iceland. Geophysical Research Letters, 43(4): 1495-1503.

Andersen, D.J., Lindsley, D.H. and Davidson, P.M., 1993. QUILF: A pascal program to assess equilibria among Fe Mg Mn Ti oxides, pyroxenes, olivine, and quartz. Computers & Geosciences, 19(9): 1333-1350.

Andersen, J.C., Rasmussen, H., Nielsen, T.F. and Ronsbo, J.G., 1998. The Triple Group and the Platinova gold and palladium reefs in the Skaergaard Intrusion; stratigraphic and petrographic relations. Economic Geology, 93(4): 488-509.

Andersen, J.C.Ø. and Brooks, C.K., 2003. The (virtual) Skaergaard Intrusion. http://www.skaergaard.org.

Anderson, A. and Greenland, L., 1969. Phosphorus fractionation diagram as a quantitative indicator of crystallization differentiation of basaltic liquids. Geochimica et Cosmochimica Acta, 33(4): 493-505.

Anderson, A., T and Gottfried, D., 1971. Contrasting behavior of P, Ti, and Nb in a differentiated high-alumina olivine tholeiite and a calc-alkaline andesitic suite. Geological Society of America Bulletin, 82(7): 1929-1942.

Applegarth, L.J., Tuffen, H., James, M.R., Pinkerton, H. and Cashman, K.V., 2013. Direct observations of degassing-induced crystallization in basalts. Geology, 41(2): 243-246.

Ariskin, A., 2003. The compositional evolution of differentiated liquids from the Skaergaard layered series as determined by geochemical thermometry. Russian Journal of Earth Sciences, 5(1): 1-29.

Ayele, A., Keir, D., Ebinger, C., Wright, T.J., Stuart, G.W., Buck, W.R., Jacques, E., Ogubazghi, G. and Sholan, J., 2009. September 2005 mega-dike emplacement in the Manda-Harraro nascent oceanic rift (Afar depression). Geophysical Research Letters, 36: L20306.

Baker, B.H. and McBirney, A.R., 1985. Liquid fractionation. Part III: Geochemistry of zoned magmas and the compositional effects of liquid fractionation. Journal of Volcanology and Geothermal Research, 24(1-2): 55-81.

Barth, G., Kleinrock, M. and Helz, R., 1994. The magma body at Kilauea Iki lava lake: Potential insights into mid-ocean ridge magma chambers. Journal of Geophysical Research: Solid Earth, 99(B4): 7199-7217.

Bateman, A.M., 1951. The formation of late magmatic oxide ores. Economic Geology, 46(4): 404-426.

Bergantz, G.W., 2000. On the dynamics of magma mixing by reintrusion: implications for pluton assembly processes. Journal of Structural Geology, 22(9): 1297-1309.

Bergantz, G.W. and Ni, J., 1999. A numerical study of sedimentation by dripping instabilities in viscous fluids. International Journal of Multiphase Flow, 25(2): 307-320.

Bergantz, G.W., Schleicher, J.M. and Burgisser, A., 2017. On the kinematics and dynamics of crystal-rich systems. Journal of Geophysical Research: Solid Earth, 122(8): 6131-6159.

Bigg, E.K., 1953. The supercooling of water. Proceedings of the Physical Society. Section B, 66(8): 688.

Biggar, G.M., 1979. Immiscibility in tholeiites. Mineralogical Magazine, 43: 543-544.

Bird, D.K., Brooks, C.K., Gannicott, R.A. and Turner, P.A., 1991. A gold-bearing horizon in the Skaergaard Intrusion. Economic Geology, 86(5): 1083-1092.

Bird, D.K., Rogers, R.D. and Manning, C.E., 1986. Mineralized fracture systems of the Skaergaard intrusion, East Greenland. Geoscience, 16. The Commission for Scientific Research in Greenland.

Bishop, F.C., 1980. The distribution of Fe2+ and Mg between coexisting ilmenite and pyroxene with applications to geothermometry. American Journal of Science, 280(1): 46-77.

Bogaerts, M. and Schmidt, M., 2006. Experiments on silicate melt immiscibility in the system Fe2SiO4–KAlSi3O8–SiO2–CaO–MgO–TiO2–P2O5 and implications for natural magmas. Contributions to Mineralogy and Petrology, 152(3): 257-274.
Boorman, S., Boudreau, A. and Kruger, F., 2004. The Lower Zone–Critical Zone transition of the Bushveld Complex: a quantitative textural study. Journal of Petrology, 45(6): 1209-1235.
Botcharnikov, R., Almeev, R., Koepke, J. and Holtz, F., 2008. Phase relations and liquid lines of descent in hydrous ferrobasalt—implications for the Skaergaard intrusion and Columbia River flood basalts. Journal of Petrology, 49(9): 1687-1727.
Bottinga, Y. and Weill, D.F., 1970. Densities of liquid silicate systems calculated from partial molar volumes of oxide components. American Journal of Science, 269(2): 169-182.
Boudreau, A., 2017. A personal perspective on layered intrusions. Elements, 13: 380-381.
Boudreau, A. and Meurer, W., 1999. Chromatographic separation of the platinum-group elements, gold, base metals and sulfur during degassing of a compacting and solidifying igneous crystal pile. Contributions to Mineralogy and Petrology, 134(2-3): 174-185.
Boudreau, A.E. and McBirney, A.R., 1997. The Skaergaard layered series. Part III. Non-dynamic layering. Journal of Petrology, 38(8): 1003-1020.
Bowen, N.L., 1928. The evolution of the igneous rocks. Princeton University Press, Princeton, New Jersey.
Boyes, X., 2018. Mush disaggregation in the Bardarbunga volcanic system, Iceland. MSci Thesis, University of Cambridge, Cambridge.
Brooks, C. and Gleadow, A., 1977. A fission-track age for the Skaergaard intrusion and the age of the East Greenland basalts. Geology, 5(9): 539-540.
Brooks, C.K. and Nielsen, T.F.D., 1978. Early stages in the differentiation of the Skaergaard magma as revealed by a closely related suite of dike rocks. Lithos, 11(1): 1-14.
Brown, P., Chambers, A. and Becker, S., 1987. A large soft-sediment fold in the Lilloise intrusion, East Greenland, Origins of Igneous Layering. Springer, pp. 125-143.
Brunet, F. and Chazot, G., 2001. Partitioning of phosphorus between olivine, clinopyroxene and silicate glass in a spinel lherzolite xenolith from Yemen. Chemical Geology, 176(1): 51-72.
Buddington, A.F. and Lindsley, D.H., 1964. Iron-Titanium Oxide Minerals and Synthetic Equivalents. Journal of Petrology, 5(2): 310-357.
Cahn, J.W., 1961. On spinodal decomposition. Acta Metallurgica, 9(9): 795-801.
Cahn, J.W., 1967. On the morphological stability of growing crystals. In: H.S. Peiser (Editor), Crystal Growth. Pergamon Press, Oxford, pp. 681.
Cahn, J.W., 1980. Surface stress and the chemical equilibrium of small crystals - I. The case of the isotropic surface. Acta Metallurgica, 28(10): 1333-1338.
Cameron, E.N., Jahns, R.H., McNair, A.H. and R, P.L., 1949. Internal structure of granitic pegmatites. Economic Geology Monograph, 2: 115.
Campbell, I.H., 1978. Some problems with the cumulus theory. Lithos, 11(4): 311-323.
Cashman, K.V., 1993. Relationship between plagioclase crystallization and cooling rate in basaltic melts. Contributions to Mineralogy and Petrology, 113(1): 126-142.
Cashman, K.V. and Ferry, J.M., 1988. Crystal size distribution (CSD) in rocks and the kinetics and dynamics of crystallization. Contributions to Mineralogy and Petrology, 99(4): 401-415.
Cashman, K.V., Sparks, R.S.J. and Blundy, J.D., 2017. Vertically extensive and unstable magmatic systems: A unified view of igneous processes. Science, 355(6331): 1-9.
Cawthorn, R., 2013. Rare earth element abundances in apatite in the Bushveld Complex—A consequence of the trapped liquid shift effect. Geology, 41(5): 603-606.
Cawthorn, R.G., 2015. The Bushveld Complex, South Africa. In: B. Charlier, O. Namur, R. Latypov and C. Tegner (Editors), Layered Intrusions. Springer, pp. 517-587.
Cawthorn, R.G. and Ashwal, L.D., 2009. Origin of Anorthosite and Magnetitite Layers in the Bushveld Complex, Constrained by Major Element Compositions of Plagioclase. Journal of Petrology, 50(9): 1607-1637.
Cawthorn, R.G., Harris, C. and Kruger, F.J., 2000. Discordant ultramafic pegmatoidal pipes in the Bushveld Complex. Contributions to Mineralogy and Petrology, 140(1): 119-133.
Cawthorn, R.G. and Walraven, F., 1998. Emplacement and Crystallization Time for the Bushveld Complex. Journal of Petrology, 39(9): 1669-1687.

Chambers, L.M. and Pringle, M.S., 2001. Age and duration of activity at the Isle of Mull Tertiary igneous centre, Scotland, and confirmation of the existence of subchrons during Anomaly 26r. Earth and Planetary Science Letters, 193(3-4): 333-345.
Charlier, B., 2015. Stable and metastable silicate liquid immiscibility in ferrobasalts. American Mineralogist, 100(11-12): 2367-2368.
Charlier, B. and Grove, T.L., 2012. Experiments on liquid immiscibility along tholeiitic liquid lines of descent. Contributions to Mineralogy and Petrology, 164(1): 27-44.
Charlier, B., Namur, O. and Grove, T.L., 2013. Compositional and kinetic controls on liquid immiscibility in ferrobasalt–rhyolite volcanic and plutonic series. Geochimica et Cosmochimica Acta, 113: 79-93.
Charlier, B., Namur, O., Toplis, M.J., Schiano, P., Cluzel, N., Higgins, M.D. and Vander Auwera, J., 2011. Large-scale silicate liquid immiscibility during differentiation of tholeiitic basalt to granite and the origin of the Daly gap. Geology, 39(10): 907-910.
Chen, H., Clark, A.H. and Kyser, T.K., 2010. The Marcona magnetite deposit, Ica, south-central Peru: A product of hydrous, iron oxide-rich melts? Economic Geology, 105(8): 1441-1456.
Chen, Y. and Zhang, Y., 2008. Olivine dissolution in basaltic melt. Geochimica et Cosmochimica Acta, 72(19): 4756-4777.
Chen, Y. and Zhang, Y., 2009. Clinopyroxene dissolution in basaltic melt. Geochimica et Cosmochimica Acta, 73(19): 5730-5747.
Chung, H.-Y. and Mungall, J.E., 2009. Physical constraints on the migration of immiscible fluids through partially molten silicates, with special reference to magmatic sulfide ores. Earth and Planetary Science Letters, 286(1-2): 14-22.
Coint, N. and Keiding, J., 2019. A microtextural record of silicate-liquid immiscibility in the 1800 Ma monzonitic Raftsund intrusion, Vesterålen-Lofoten archipelago, Northern Norway, EGU. EGU General Assembly 2019, Vienna, Austria.
Coint, N., Keiding, J. and Ihlen, P.M., 2017. Using bulk-rock and mineral chemistry to unravel the origin of FeTi-P mineralizations in the 1.8 Ga Raftsund monzosyenite, Lofoten, Northern Norway, Goldschmidt, Paris.
Crist, B. and Nesarikar, A.R., 1995. Coarsening in polyethylene-copolymer blends. Macromolecules, 28(4): 890-896.
Cygan, G. and Koster van Groos, A., 1978. Effects of Na2O and MgO on liquid immiscibility field in K2O-FeO-Al2O3-SiO2, American Geophysical Union, Washington DC, USA, pp. 401-401.
Daly, R.A., 1914. Igneous rocks and their origin. McGraw-Hill Book Company.
Danyushevsky, L.V., 2001. The effect of small amounts of H2O on crystallisation of mid-ocean ridge and backarc basin magmas. Journal of Volcanology and Geothermal Research, 110(3-4): 265-280.
Dare, S.A.S., Barnes, S.-J. and Beaudoin, G., 2015. Did the massive magnetite “lava flows” of El Laco (Chile) form by magmatic or hydrothermal processes? New constraints from magnetite composition by LA-ICP-MS. Mineralium Deposita, 50(5): 607-617.
Davis, M.J. and Ihinger, P.D., 1998. Heterogeneous crystal nucleation on bubbles in silicate melt. American Mineralogist, 83(9-10): 1008-1015.
De, A., 1974. Silicate liquid immiscibility in the Deccan Traps and its petrogenetic significance. Geological Society of America Bulletin, 85(3): 471-474.
DeHoff, R.T., 1991. A geometrically general theory of diffusion controlled coarsening. Acta Metallurgica et Materialia, 39(10): 2349-2360.
Deka, H., Biswas, G., Chakraborty, S. and Dalal, A., 2019. Coalescence dynamics of unequal sized drops. Physics of Fluids, 31(1): 012105.
Dingwell, D., Hess, K.-U. and Knoche, R., 1996. Granite and granitic pegmatite melts: volumes and viscosities. Earth and Environmental Science Transactions of the Royal Society of Edinburgh, 87(1-2): 65-72.
Dixon, S. and Rutherford, M., 1979. Plagiogranites as late-stage immiscible liquids in ophiolite and mid-ocean ridge suites: an experimental study. Earth and Planetary Science Letters, 45(1): 45-60.

Drouin, D., Réal Couture, A., Joly, D., Tastet, X., Aimez, V. and Gauvin, R., 2007. CASINO V2.42—A Fast and Easy-to-use Modeling Tool for Scanning Electron Microscopy and Microanalysis Users. Scanning, 29: 92-101.
Dufek, J., 2016. Multiphase Flow in Crustal Magmatic Processes, Melt in the Mantle: From Foundations to State-of-the-Art in Magma/Mantle Dynamics, Isaac Newton Institute for Mathematical Sciences, Cambridge, UK.
Dunbar, N.W., Jacobs, G.K. and Naney, M.T., 1995. Crystallization processes in an artificial magma: variations in crystal shape, growth rate and composition with melt cooling history. Contributions to Mineralogy and Petrology, 120(3): 412-425.
Durben, D.J. and Wolf, G.H., 1991. Raman spectroscopic study of the pressure-induced coordination change in GeO2 glass. Physical Review B, 43(3): 2355-2363.
Eales, H.V. and Cawthorn, R.G., 1996. The Bushveld Complex. In: R.G. Cawthorn (Editor), Developments in Petrology. Elsevier, pp. 181-229.
Elliott, C.M., 1989. The Cahn-Hilliard model for the kinetics of phase separation. In: R. J.F (Editor), Mathematical models for phase change problems. International Series of Numerical Mathematics. Birkhäuser Basel, pp. 35-73.
Elliott, M.T., Cheadle, M.J. and Jerram, D.A., 1997. On the identification of textural equilibrium in rocks using dihedral angle measurements. Geology, 25(4): 355-358.
Embree, G.F., Lowell, M.D. and Doherty, D.J., 1978. Drilling data from Sugar City exploration well, Madison County, Idaho. 2331-1258, USGS.
Eskin, D. and Katgerman, L., 2004. Mechanical properties in the semi-solid state and hot tearing of aluminium alloys. Progress in Materials Science, 49(5): 629-711.
Exertier, F., La Fontaine, A., Corcoran, C., Piazolo, S., Belousova, E., Peng, Z., Gault, B., Saxey, D.W., Fougerouse, D. and Reddy, S.M., 2018. Atom probe tomography analysis of the reference zircon gj-1: An interlaboratory study. Chemical Geology, 495: 27-35.
Farber, D.L. and Williams, Q., 1992. Pressure-induced coordination changes in alkali-germanate melts: An in situ spectroscopic investigation. Science, 256(5062): 1427-1430.
Farr, R.S., Honour, V.C. and Holness, M.B., 2017. Mean grain diameters from thin sections: matching the average to the problem. Mineralogical Magazine, 81(3): 515-530.
Fenner, C.N., 1929. The crystallization of basalts. American Journal of Science, 18(105): 225-253.
Findik, F., 2012. Improvements in spinodal alloys from past to present. Materials & Design, 42: 131-146.
Fischer, L.A., Wang, M., Charlier, B., Namur, O., Roberts, R.J., Veksler, I.V., Cawthorn, R.G. and Holtz, F., 2016. Immiscible iron- and silica-rich liquids in the Upper Zone of the Bushveld Complex. Earth and Planetary Science Letters, 443: 108-117.
Freestone, I., 1978. Liquid immiscibility in alkali-rich magmas. Chemical Geology, 23(1-4): 115-123.
Freestone, I. and Powell, R., 1983. The low temperature field of liquid immiscibility in the system K2O-Al2O3-FeO-SiO2 with special reference to the join fayalite-leucite-silica. Contributions to Mineralogy and Petrology, 82(2-3): 291-299.
Freestone, I.C., 1979. Immiscibility in tholeiites. Mineralogical Magazine, 43(328): 544-546.
Frietsch, R., 1978. On the magmatic origin of iron ores of the Kiruna type. Economic Geology, 73(4): 478-485.
Frost, B.R., Lindsley, D.H. and Andersen, D.J., 1988. Fe-Ti oxide-silicate equilibria; assemblages with fayalitic olivine. American Mineralogist, 73(7-8): 727-740.
Fujii, T., Kushiro, I., Nakamura, Y. and Koyaguchi, T., 1980. A note on silicate liquid immiscibility in Japanese volcanic rocks. The Journal of the Geological Society of Japan, 86(6): 409-412.
Ghiorso, M. and Carmichael, I., 1980. A regular solution model for metaluminous silicate liquids: Applications to geothermometry, immiscibility, and the source regions of basic magmas. Contributions to Mineralogy and Petrology, 71(4): 323-342.
Gill, R., 2010. Igneous rocks and processes: a practical guide. John Wiley & Sons Ltd.
Giordano, D., Nichols, A.R. and Dingwell, D.B., 2005. Glass transition temperatures of natural hydrous melts: a relationship with shear viscosity and implications for the welding process. Journal of Volcanology and Geothermal Research, 142(1-2): 105-118.
Giordano, D., Russell, J.K. and Dingwell, D.B., 2008. Viscosity of magmatic liquids: A model. Earth and Planetary Science Letters, 271(1): 123-134.

Govindaraju, K., 1994. Compilation of working values and sample description for 383 geostandards. Geostandards Newsletter, 18: 1-158.
Greig, J.W., 1927. Immiscibility in silicate melts. American Journal of Science, 13(73): 1-44.
Greig, J.W., 1928. On the evidence which has been presented for liquid silicate immiscibility in the laboratory and in the rocks of Agate Point, Ontario. American Journal of Science, 15(89): 375-402.
Grove, T.L., 1982. Use of FePt alloys to eliminate the iron loss problem in 1 atmosphere gas mixing experiments: Theoretical and practical considerations. Contributions to Mineralogy and Petrology, 78(3): 298-304.
Grove, T.L. and Baker, M.B., 1984. Phase equilibrium controls on the tholeiitic versus calc-alkaline differentiation trends. Journal of Geophysical Research: Solid Earth, 89(B5): 3253-3274.
Grove, T.L. and Bence, A., 1979. Crystallization kinetics in a multiply saturated basalt magma-an experimental study of Luna 24 ferrobasalt, Lunar and Planetary Science Conference Proceedings, pp. 439-478.
Grove, T.L., Kinzler, R.J. and Bryan, W.B., 1992. Fractionation of mid-ocean ridge basalt (MORB). In: J.P. Morgan, D.K. Blackman and J.M. Sinton (Editors), Mantle Flow and Melt Generation at Mid-Ocean Ridges. Geophysical Monograph Series. American Geophysical Union, pp. 281-310.
Guilbaud, M.N., Blake, S., Thordarson, T. and Self, S., 2007. Role of Syn-eruptive Cooling and Degassing on Textures of Lavas from the ad 1783–1784 Laki Eruption, South Iceland. Journal of Petrology, 48(7): 1265-1294.
Hamann, C., Hecht, L., Ebert, M. and Wirth, R., 2013. Chemical projectile–target interaction and liquid immiscibility in impact glass from the Wabar craters, Saudi Arabia. Geochimica et Cosmochimica Acta, 121: 291-310.
Hammer, J.E. and Rutherford, M.J., 2002. An experimental study of the kinetics of decompression-induced crystallization in silicic melt. Journal of Geophysical Research: Solid Earth, 107(B1).
Hammer, J.E., Sharp, T.G. and Wessel, P., 2010. Heterogeneous nucleation and epitaxial crystal growth of magmatic minerals. Geology, 38(4): 367-370.
Hanghøj, K., Rosing, M.T. and Brooks, C.K., 1995. Evolution of the Skaergaard magma: evidence from crystallized melt inclusions. Contributions to Mineralogy and Petrology, 120(3-4): 265-269.
Harker, A. and Clough, C.T., 1904. The Tertiary igneous rocks of Skye. Memoirs of the Geological Survey of the United Kingdom. J. Hedderwick & Sons, Glasgow.
Harker, D. and Parker, E.R., 1945. Grain shape and grain growth. Transactions of the American Society for Metals, 34: 156-201.
Hartlieb, P., Toifl, M., Kuchar, F., Meisels, R. and Antretter, T., 2016. Thermo-physical properties of selected hard rocks and their relation to microwave-assisted comminution. Minerals Engineering, 91: 34-41.
Hassanizadeh, S.M., 2016. Advanced theories of two-phase flow in deformable porous media, including fluid-fluid interfaces, Melt in the Mantle: From Foundations to State-of-the-Art in Magma/Mantle Dynamics, Isaac Newton Institute for Mathematical Sciences, Cambridge, UK.
Hele-Shaw, H.S., 1898. The Flow of Water. Nature, 58: 34-36.
Helz, R., 1980. Crystallization history of Kilauea Iki lava lake as seen in drill core recovered in 1967–1979. Bulletin Volcanologique, 43(4): 675-701.
Helz, R.T., 1987. Differentiation behavior of Kilauea Iki lava lake, Kilauea Volcano, Hawaii: an overview of past and current work. In: B.O. Mysen (Editor), Magmatic Processes: Physicochemical Principles. The Geological Society Special Publications, pp. 241-258.
Helz, R.T., Clague, D.A., Sisson, T.W. and Thornber, C.R., 2014. Petrologic Insights into Basaltic Volcanism at Historically Active Hawaiian Volcanoes. In: M.P. Poland, T.J. Takahashi and C.M. Landowski (Editors), Characteristics of Hawaiian volcanoes, USGS Professional Paper 1801, pp. 237-292.
Helz, R.T. and Thornber, C.R., 1987. Geothermometry of Kilauea Iki lava lake, Hawaii. Bulletin of Volcanology, 49(5): 651-668.
Helz, R.T. and Wright, T.L., 1992. Differentiation and magma mixing on Kilauea's east rift zone. Bulletin of Volcanology, 54(5): 361-384.

Heslop, M. and Smythe, J., 1910. On the Dyke at Crookdene (Northumberland) and its Relations to the Collywell, Tynemouth, and Morpeth Dykes. Quarterly Journal of the Geological Society, 66(1-4): 1-18.
Hess, H.H. and Smith, J.R., 1960. Stillwater Igneous Complex, Montana: A Quantitative Mineralogical Study, 80. The Geological Society of America, Baltimore.
Hess, P.C., 1995. Thermodynamic mixing properties and the structure of silicate melts. Structure, Dynamics and Properties of Silicate Melts, 32: 145-189.
Hickson, C.J. and Juras, S.J., 1986. Sample contamination by grinding. The Canadian Mineralogist, 24(3): 585-589.
Higgins, A.C. and Soper, N.J., 1981. Cretaceous-Palaeogene sub-basaltic and intrabasaltic sediments of the Kangerdlugssuaq area, Central East Greenland. Geological Magazine, 118(4): 337-354.
Higgins, M., 1994. Determination of crystal morphology and size from bulk measurements on thin sections: numerical modelling. American Mineralogist, 79: 113-119.
Higgins, M.D., 2000. Measurement of crystal size distributions. American Mineralogist, 85(9): 1105-1116.
Higgins, M.D., 2002. A crystal size-distribution study of the Kiglapait layered mafic intrusion, Labrador, Canada: evidence for textural coarsening. Contributions to Mineralogy and Petrology, 144(3): 314-330.
Hildebrand, R.S., 1986. Kiruna-type deposits; their origin and relationship to intermediate subvolcanic plutons in the Great Bear magmatic zone, Northwest Canada. Economic Geology, 81(3): 640-659.
Holgate, N., 1954. The Role of Liquid Immiscibility in Igneous Petrogenesis. The Journal of Geology, 62(5): 439-480.
Holmes, A. and Harwood, H., 1929. The tholeiite dikes of the north of England. Mineralogical Magazine, 22(124): 1-52.
Holness, M.B., 2006. Melt–Solid Dihedral Angles of Common Minerals in Natural Rocks. Journal of Petrology, 47(4): 791-800.
Holness, M.B., 2014. The effect of crystallization time on plagioclase grain shape in dolerites. Contributions to Mineralogy and Petrology, 168(5): 1076.
Holness, M.B., 2015. Plagioclase Growth Rates Control Three-grain Junction Geometry in Dolerites and Gabbros. Journal of Petrology, 56(11): 2117-2144.
Holness, M.B., Morse, S.A. and Tegner, C., 2009. Response to Comment by McBirney, Boudreau and Marsh. Journal of Petrology, 50(1): 97-102.
Holness, M.B., Neufeld, J.A., Gilbert, A.J. and Macdonald, R., 2017a. Orientation of Tabular Mafic Intrusions Controls Convective Vigour and Crystallization Style. Journal of Petrology, 58(10): 2035-2053.
Holness, M.B., Nielsen, T.F. and Tegner, C., 2017b. The Skaergaard Intrusion of East Greenland: Paradigms, Problems and New Perspectives. Elements, 13(6): 391-396.
Holness, M.B., Richardson, C. and Helz, R.T., 2012. Disequilibrium dihedral angles in dolerite sills: A new proxy for cooling rate. Geology, 40(9): 795-798.
Holness, M.B. and Sawyer, E.W., 2008. On the pseudomorphing of melt-filled pores during the crystallization of migmatites. Journal of Petrology, 49(7): 1343-1363.
Holness, M.B., Stripp, G., Humphreys, M., Veksler, I.V., Nielsen, T.F. and Tegner, C., 2011. Silicate liquid immiscibility within the crystal mush: late-stage magmatic microstructures in the Skaergaard intrusion, East Greenland. Journal of Petrology, 52(1): 175-222.
Holness, M.B., Tegner, C., Nielsen, T.F., Stripp, G. and Morse, S.A., 2007. A textural record of solidification and cooling in the Skaergaard intrusion, East Greenland. Journal of Petrology, 48(12): 2359-2377.
Holness, M.B., Tegner, C., Nielsen, T.F.D. and Charlier, B., 2017c. The Thickness of the Mushy Layer on the Floor of the Skaergaard Magma Chamber at Apatite Saturation. Journal of Petrology, 58(5): 909-932.
Honour, V.C., Holness, M.B., Partridge, J.L. and Charlier, B., 2019. Microstructural evolution of silicate immiscible liquids in ferrobasalts. Contributions to Mineralogy and Petrology, 174(9): 77.

Hoover, J.D., 1989. Petrology of the Marginal Border Series of the Skaergaard Intrusion. Journal of Petrology, 30(2): 399-439.
Hort, M., 1998. Abrupt change in magma liquidus temperature because of volatile loss or magma mixing: effects on nucleation, crystal growth and thermal history of the magma. Journal of Petrology, 39(5): 1063-1076.
Hou, T., Charlier, B., Holtz, F., Veksler, I., Zhang, Z., Thomas, R. and Namur, O., 2018. Immiscible hydrous Fe–Ca–P melt and the origin of iron oxide-apatite ore deposits. Nature Communications, 9(1): 1415.
Hou, T., Charlier, B., Namur, O., Schütte, P., Schwarz-Schampera, U., Zhang, Z. and Holtz, F., 2017. Experimental study of liquid immiscibility in the Kiruna-type Vergenoeg iron–fluorine deposit, South Africa. Geochimica et Cosmochimica Acta, 203: 303-322.
Hou, T. and Veksler, I.V., 2015. Experimental confirmation of high-temperature silicate liquid immiscibility in multicomponent ferrobasaltic systems. American Mineralogist, 100(5-6): 1304-1307.
Huang, H.-H., Lin, F.-C., Schmandt, B., Farrell, J., Smith, R.B. and Tsai, V.C., 2015. The Yellowstone magmatic system from the mantle plume to the upper crust. Science, 348(6236): 773-776.
Hudon, P. and Baker, D.R., 2002. The nature of phase separation in binary oxide melts and glasses. I. Silicate systems. Journal of Non-Crystalline Solids, 303(3): 299-345.
Hudon, P., Jung, I.H. and Baker, D.R., 2004. Effect of pressure on liquid-liquid miscibility gaps: A case study of the systems CaO-SiO2, MgO-SiO2, and CaMgSi2O6-SiO2. Journal of Geophysical Research: Solid Earth, 109.
Humphreys, M.C., 2009. Chemical evolution of intercumulus liquid, as recorded in plagioclase overgrowth rims from the Skaergaard intrusion. Journal of Petrology, 50(1): 127-145.
Humphreys, M.C., 2011. Silicate liquid immiscibility within the crystal mush: evidence from Ti in plagioclase from the Skaergaard intrusion. Journal of Petrology, 52(1): 147-174.
Humphreys, M.C.S. and Holness, M.B., 2010. Melt-rich segregations in the Skaergaard Marginal Border Series: Tearing of a vertical silicate mush. Lithos, 119(3): 181-192.
Hunter, R. and Sparks, R., 1987. The differentiation of the Skaergaard intrusion. Contributions to Mineralogy and Petrology, 95(4): 451-461.
Hunter, R. and Sparks, R., 1990. The differentiation of the Skaergaard intrusion. Contributions to Mineralogy and Petrology, 104(2): 248-251.
Irvine, T., 1983. Skaergaard trough-layering structures. Carnegie Institution of Washington Year Book, 82: 289-295.
Irvine, T., 1987. Layering and related structures in the Duke Island and Skaergaard intrusions: similarities, differences, and origins, Origins of igneous layering. Springer, pp. 185-245.
Irvine, T. and Stoeser, D., 1978. Structure of the Skaergaard trough bands. Carnegie Institution of Washington Year Book, 77: 725-732.
Irvine, T.N., 1982. Terminology for Layered Intrusions. Journal of Petrology, 23(2): 127-162.
Irvine, T.N., 1992. Emplacement of the Skaergaard intrusion. Carnegie Institution of Washington Year Book, 91: 91-96.
Irvine, T.N., Andersen, J.C.Ø. and Brooks, C.K., 1998. Included blocks (and blocks within blocks) in the Skaergaard intrusion: Geologic relations and the origins of rhythmic modally graded layers. Geological Society of America Bulletin, 110(11): 1398-1447.
Iwansson, K. and Landström, O., 2000. Contamination of rock samples by laboratory grinding mills. Journal of Radioanalytical and Nuclear Chemistry, 244(3): 609-614.
Jahns, R.H. and Burnham, C.W., 1969. Experimental studies of pegmatite genesis; l, A model for the derivation and crystallization of granitic pegmatites. Economic Geology, 64(8): 843-864.
Jakobsen, J.K., Veksler, I., Tegner, C. and Brooks, C.K., 2005. Immiscible iron-and silica-rich melts in basalt petrogenesis documented in the Skaergaard intrusion. Geology, 33(11): 885-888.
Jakobsen, J.K., Veksler, I.V., Tegner, C. and Brooks, C.K., 2011. Crystallization of the Skaergaard intrusion from an emulsion of immiscible iron-and silica-rich liquids: evidence from melt inclusions in plagioclase. Journal of Petrology, 52(2): 345-373.
James, G., Witten, D., Hastie, T. and Tibshirani, R., 2013. An introduction to statistical learning. Springer Texts in Statistics, 103. Springer, New York.

James, P.F., 1975. Liquid-phase separation in glass-forming systems. Journal of Materials Science, 10(10): 1802-1825.
Jang, Y.D., Naslund, H.R. and McBirney, A.R., 2001. The differentiation trend of the Skaergaard intrusion and the timing of magnetite crystallization: iron enrichment revisited. Earth and Planetary Science Letters, 189(3–4): 189-196.
Jaupart, C. and Tait, S., 1995. Dynamics of differentiation in magma reservoirs. Journal of Geophysical Research: Solid Earth, 100(B9): 17615-17636.
Jean, M.M., Christiansen, E.H., Champion, D.E., Vetter, S.K., Phillips, W.M., Schuth, S. and Shervais, J.W., 2018. Caldera Life-Cycles of the Yellowstone Hotspot Track: Death and Rebirth of the Heise Caldera. Journal of Petrology, 59(8): 1643-1670.
Jolly, R.J.H. and Sanderson, D.J., 1995. Variation in the form and distribution of dykes in the Mull swarm, Scotland. Journal of Structural Geology, 17(11): 1543-1557.
Jones, J.M., 1967. The Geology of the coast section from Tynemouth to Seaton Sluice. Transactions of the Natural History Society of Northumbria, 16(3): 1-52.
Jonsson, E., Troll, V.R., Högdahl, K., Harris, C., Weis, F., Nilsson, K.P. and Skelton, A., 2013. Magmatic origin of giant 'Kiruna-type' apatite-iron-oxide ores in Central Sweden. Scientific Reports, 3: 1644.
Juster, T.C., Grove, T.L. and Perfit, M.R., 1989. Experimental constraints on the generation of FeTi basalts, andesites, and rhyodacites at the Galapagos Spreading Center, 85 W and 95 W. Journal of Geophysical Research: Solid Earth, 94(B7): 9251-9274.
Kalikmanov, V.I., 2013. Classical nucleation theory, Nucleation Theory. Lecture Notes in Physics. Springer Dordrecht, pp. 17-41.
Kays, M., Goles, G. and Grover, T., 1989. Precambrian sequence bordering the Skaergaard Intrusion. Journal of Petrology, 30(2): 321-361.
Kays, M., McBirney, A. and Goles, G., 1981. Xenoliths of gneisses and the conformable, clot-like granophyres in the Marginal Border Group, Skaergaard intrusion, East Greenland. Contributions to Mineralogy and Petrology, 76(3): 265-284.
Kerr, A.C., Kent, R.W., Thomson, B.A., Seedhouse, J.K. and Donaldson, C.H., 1999. Geochemical Evolution of the Tertiary Mull Volcano, Western Scotland. Journal of Petrology, 40(6): 873-908.
Kersting, A.B., Arculus, R.J., Delano, J.W. and Loureiro, D., 1989. Electrochemical measurements bearing on the oxidation state of the Skaergaard Layered Intrusion. Contributions to Mineralogy and Petrology, 102(3): 376-388.
Kirkpatrick, R.J., 1975. Crystal growth from the melt: a review. American Mineralogist, 60(9-10): 798-814.
Kirkpatrick, R.J., 1977. Nucleation and growth of plagioclase, Makaopuhi and Alae lava lakes, Kilauea Volcano, Hawaii. Geological Society of America Bulletin, 88(1): 78-84.
Knipping, J.L., Bilenker, L.D., Simon, A.C., Reich, M., Barra, F., Deditius, A.P., Lundstrom, C., Bindeman, I. and Munizaga, R., 2015. Giant Kiruna-type deposits form by efficient flotation of magmatic magnetite suspensions. Geology, 43(7): 591-594.
Kohn, S., 2000. The dissolution mechanisms of water in silicate melts; a synthesis of recent data. Mineralogical Magazine, 64(3): 389-408.
Kolker, A., 1982. Mineralogy and geochemistry of Fe-Ti oxide and apatite (nelsonite) deposits and evaluation of the liquid immiscibility hypothesis. Economic Geology, 77(5): 1146-1158.
Kontak, D.J., De Young, M.Y.D.W. and Dostal, J., 2002. Late-stage crystallization history of the Jurassic North Mountain Basalt, Nova Scotia, Canada. I. Textural and chemical evidence for pervasive development of silicate-liquid immiscibility. The Canadian Mineralogist, 40(5): 1287-1311.
Kouchi, A., Sugawara, Y., Kashima, K. and Sunagawa, I., 1983. Laboratory growth of sector zoned clinopyroxenes in the system CaMgSi2O6-CaTiAl2O6. Contributions to Mineralogy and Petrology, 83(1): 177-184.
Krasov, N. and Clocchiatti, R., 1979. Immiscibility in silicate melts and its possible petrogenetic importance, as shown by study of melt inclusions, Transactions (Doklady) of the USSR Academy of Sciences, pp. 92-95.

Kubicki, J., Hemley, R. and Hofmeister, A., 1992. Raman and infrared study of pressure-induced structural changes in MgSiO3, CaMgSi2O6, and CaSiO3 glasses. American Mineralogist, 77(3-4): 258-269.
Kudo, A.M. and Weill, D.F., 1970. An igneous plagioclase thermometer. Contributions to Mineralogy and Petrology, 25(1): 52-65.
Land, D.H., 1974. Geology of the Tynemouth district. Memoirs of the Geological Survey of Great Britain, 15. The Stationery Office (TSO), London, 176 pp.
Larsen, R.B. and Brooks, C.K., 1994. Origin and Evolution of Gabbroic Pegmatites in the Skaergaard Intrusion, East Greenland. Journal of Petrology, 35(6): 1651-1679.
Larsen, R.B., Brooks, C.K. and Bird, D.K., 1992. Methane-bearing, aqueous, saline solutions in the Skaergaard intrusion, east Greenland. Contributions to Mineralogy and Petrology, 112(2): 428-437.
Larsen, R.B. and Tegner, C., 2006. Pressure conditions for the solidification of the Skaergaard intrusion: Eruption of East Greenland flood basalts in less than 300,000 years. Lithos, 92(1): 181-197.
Larson, D., Foord, D., Petford-Long, A., Liew, H., Blamire, M., Cerezo, A. and Smith, G., 1999. Field-ion specimen preparation using focused ion-beam milling. Ultramicroscopy, 79(1-4): 287-293.
Larson, D.J., Prosa, T., Ulfig, R.M., Geiser, B.P. and Kelly, T.F., 2013. Local Electrode Atom Probe Tomography. Springer Science, New York.
Lester, G., Clark, A., Kyser, T. and Naslund, H., 2013. Experiments on liquid immiscibility in silicate melts with H2O, P, S, F and Cl: implications for natural magmas. Contributions to Mineralogy and Petrology, 166(1): 329-349.
Levich, V.G., 1962. Motion and diffusion in thin liquid films, Physicochemical Hydrodynamics. Prentice-Hall International Series in the Physical and Chemical Engineering Sciences. Englewood Cliffs, N.J., Prentice-Hall, pp. 689-700.
Lifshitz, I.M. and Slyozov, V.V., 1961. The kinetics of precipitation from supersaturated solid solutions. Journal of Physics and Chemistry of Solids, 19(1-2): 35-50.
Lindsley, D., Brown, G.M. and Muir, I., 1969. Conditions of the ferrowollastonite-ferrohedenbergite inversion in the Skaergaard intrusion, East Greenland. Mineralogical Society of America Special Papers, 2: 193-201.
Lindsley, D.H. and Frost, B.R., 1992. Equilibria among Fe-Ti oxides, pyroxenes, olivine, and quartz: Part I. Theory. American Mineralogist, 77(9-10): 987-1003.
Loferski, P.J. and Arculus, R.J., 1993. Multiphase inclusions in plagioclase from anorthosites in the Stillwater Complex, Montana: implications for the origin of the anorthosites. Contributions to Mineralogy and Petrology, 114(1): 63-78.
Lofgren, G.E., 1983. Effect of heterogeneous nucleation on basaltic textures: a dynamic crystallization study. Journal of Petrology, 24(3): 229-255.
London, D., 2005. Granitic pegmatites: an assessment of current concepts and directions for the future. Lithos, 80(1-4): 281-303.
London, D., 2008. Pegmatites, 10. Canadian Mineralogist Special Publication, 368 pp.
London, D. and Morgan, G.B., VI, 2012. The Pegmatite Puzzle. Elements, 8(4): 263-268.
Longhi, J., 1990. Silicate liquid immiscibility in isothermal crystallization experiments, Lunar and Planetary Science Conference Proceedings, Houston, Texas, pp. 13-24.
Luais, B., 1987. Immiscibilité entre liquides silicatés dans les mésostases et les inclusions vitreuses des andésites basiques de Santorin (Arc Egéen). Bulletin de minéralogie, 110(1): 93-109.
Lundstrom, C., Boudreau, A. and Pertermann, M., 2005. Diffusion–reaction in a thermal gradient: Implications for the genesis of anorthitic plagioclase, high alumina basalt and igneous mineral layering. Earth and Planetary Science Letters, 237(3-4): 829-854.
Maaløes, S., 1976. The zoned plagioclase of the Skaergaard intrusion, East Greenland. Journal of Petrology, 17(3): 398-419.
Macdonald, R., Baginski, B., Upton, B., Pinkerton, H., MacInnes, D. and MacGillivray, J., 2010. The Mull Palaeogene dyke swarm: Insights into the evolution of the Mull igneous centre and dyke-emplacement mechanisms. Mineralogical Magazine, 74(4): 601-622.
Marsh, B.D., 1988. Crystal size distribution (CSD) in rocks and the kinetics and dynamics of crystallization. Contributions to Mineralogy and Petrology, 99(3): 277-291.

Marsh, B.D., 1996. Solidification fronts and magmatic evolution. Mineralogical Magazine, 60(1): 5-40.
Marsh, B.D., 2006. Dynamics of Magmatic Systems. Elements, 2(5): 287-292.
Marsh, B.D., 2015. Chapter 8 - Magma Chambers. In: H. Sigurdsson (Editor), The Encyclopedia of Volcanoes (Second Edition). Academic Press, Amsterdam, pp. 185-201.
Martin, B. and Kushiro, I., 1991. Immiscibility synthesis as an indication of cooling rates of basalts. Journal of Volcanology and Geothermal Research, 45(3-4): 289-310.
Martin, D., Griffiths, R.W. and Campbell, I.H., 1987. Compositional and thermal convection in magma chambers. Contributions to Mineralogy and Petrology, 96(4): 465-475.
McBirney, A., 1996. The Skaergaard intrusion, Developments in Petrology. Elsevier, pp. 147-180.
McBirney, A.R., 1975. Differentiation of the Skaergaard intrusion. Nature, 253: 691-694.
McBirney, A.R., 1989. The Skaergaard layered series: I. Structure and average compositions. Journal of Petrology, 30(2): 363-397.
McBirney, A.R., 1998. The Skaergaard Layered Series. Part V. Included Trace Elements. Journal of Petrology, 39(2): 255-276.
McBirney, A.R., 2008. Comments on: 'Liquid immiscibility and the evolution of basaltic magma' Journal of Petrology 48, 2187–2210. Journal of Petrology.
McBirney, A.R., 2009. Factors governing the textural development of Skaergaard gabbros: A review. Lithos, 111(1-2): 1-5.
McBirney, A.R. and Hunter, R.H., 1995. The Cumulate Paradigm Reconsidered. The Journal of Geology, 103(1): 114-122.
McBirney, A.R. and Nakamura, Y.S., 1974. Immiscibility in late-stage magmas of the Skaergaard intrusion. Carnegie Institution of Washington Yearbook, 73: 348-352.
McBirney, A.R. and Naslund, H., 1990. The differentiation of the Skaergaard intrusion. Contributions to Mineralogy and Petrology, 104(2): 235-240.
McBirney, A.R. and Noyes, R.M., 1979. Crystallization and Layering of the Skaergaard Intrusion. Journal of Petrology, 20(3): 487-554.
McBirney, A.R. and Sonnenthal, E.L., 1990. Metasomatic replacement in the Skærgaard Intrusion, East Greenland: Preliminary observations. Chemical Geology, 88(3): 245-260.
McCallum, I., Raedeke, L. and Mathez, E., 1980. Investigations of the Stillwater Complex: Part I. Stratigraphy and structure of the banded zone. American Journal of Science, 280(1): 59-87.
McKenzie, D., 2011. Compaction and crystallization in magma chambers: Towards a model of the Skaergaard intrusion. Journal of Petrology, 52(5): 905-930.
McKnight, T., 2016. Running on Cornstarch and Water 100 2857. https://www.youtube.com/watch?v=THkUB4ilDkU.
McNaught, A.D., 1997. Compendium of Chemical Terminology. International Union of Pure and Applied Chemistry, 1669. Blackwell Science, Oxford, 464 pp.
Mével, C., 1975. Les zonations chimiques dans les pillow-lavas spilitiques du Chenaillet et des Gets (Alpes françaises). Pétrologie, 1: 319-333.
Miller, M.K., Russell, K.F., Thompson, K., Alvis, R. and Larson, D.J., 2007. Review of atom probe FIB-based specimen preparation methods. Microscopy and Microanalysis, 13(6): 428-436.
Mills, R.D., Ratner, J.J. and Glazner, A.F., 2011. Experimental evidence for crystal coarsening and fabric development during temperature cycling. Geology, 39(12): 1139-1142.
Mitchell, J.G., Rands, P.N. and Ineson, P.R., 1989. Perturbation of the K-Ar age system in the Cleveland dyke, UK: evidence of an Early Eocene age for barite mineralisation in the Magnesian Limestone of County Durham. Chemical Geology, 79(1): 49-64.
Morse, S., Lindsley, D. and Williams, R., 1980. Concerning intensive parameters in the Skaergaard intrusion. American Journal of Science, 280: 159-170.
Morse, S.A., 1990. A discussion of Hunter and Sparks (Contrib Mineral Petrol 95:451–461). Contributions to Mineralogy and Petrology, 104(2): 240-244.
Morse, S.A., 1996. Kiglapait Mineralogy III: Olivine Compositions and Rayleigh Fractionation Models. Journal of Petrology, 37(5): 1037-1061.
Morse, S.A., 2008a. Compositional Convection Trumps Silicate Liquid Immisciblity in Layered Intrusions: a Discussion of 'Liquid immiscibility and the evolution of basaltic magma' by Veksler et al., Journal of Petrology 48, 2187–2210. Journal of Petrology, 49(12): 2157-2168.

Morse, S.A., 2008b. Toward a thermal model for the Skaergaard liquidus. American Mineralogist, 93(1): 248-251.
Morse, S.A. and Brady, J.B., 2017. Thermal History of the Upper Zone of the Kiglapait Intrusion. Journal of Petrology, 58(7): 1319-1332.
Mullis, A.M., 2003. A study of kinetically limited dendritic growth at high undercooling using phase-field techniques. Acta Materialia, 51(7): 1959-1969.
Mungall, J.E. and Su, S., 2005. Interfacial tension between magmatic sulfide and silicate liquids: Constraints on kinetics of sulfide liquation and sulfide migration through silicate rocks. Earth and Planetary Science Letters, 234(1): 135-149.
Mysen, B.O., 1983. The structure of silicate melts. Annual Review of Earth and Planetary Sciences, 11(1): 75-97.
Mysen, B.O. and Richet, P., 2018. Silicate glasses and melts. Elsevier, 692 pp.
Namur, O., Abily, B., Boudreau, A.E., Blanchette, F., Bush, J.W., Ceuleneer, G., Charlier, B., Donaldson, C.H., Duchesne, J.C., Higgins, M.D., Morata, D., Nielsen, T.F.D., O'Driscoll, B., Pang, K.N., Peacock, T., Spandler, C., Toramaru, A. and Veksler, I., 2015a. Igneous layering in basaltic magma chambers. In: B. Charlier, O. Namur, R. Latypov and C. Tegner (Editors), Layered Intrusions. Springer, pp. 75-152.
Namur, O., Charlier, B. and Holness, M.B., 2012. Dual origin of Fe–Ti–P gabbros by immiscibility and fractional crystallization of evolved tholeiitic basalts in the Sept Iles layered intrusion. Lithos, 154: 100-114.
Namur, O., Charlier, B., Toplis, M.J., Higgins, M.D., Hounsell, V., Liégeois, J.P. and Vander Auwera, J., 2011. Differentiation of tholeiitic basalt to A-type granite in the Sept Iles layered intrusion, Canada. Journal of Petrology, 52(3): 487-539.
Namur, O., Charlier, B., Toplis, M.J., Higgins, M.D., Liégeois, J.P. and Vander Auwera, J., 2010. Crystallization Sequence and Magma Chamber Processes in the Ferrobasaltic Sept Iles Layered Intrusion, Canada. Journal of Petrology, 51(6): 1203-1236.
Namur, O., Higgins, M.D. and Vander Auwera, J., 2015b. The Sept Iles intrusive suite, Quebec, Canada. In: B. Charlier, O. Namur, R. Latypov and C. Tegner (Editors), Layered Intrusions. Springer, pp. 465-515.
Namur, O. and Humphreys, M., 2018. Trace element constraints on the differentiation and crystal mush solidification in the Skaergaard intrusion, Greenland. Journal of Petrology, 59(3): 387-418.
Namur, O., Humphreys, M.C. and Holness, M.B., 2014. Crystallization of interstitial liquid and latent heat buffering in solidifying gabbros: Skaergaard intrusion, Greenland. Journal of Petrology, 55(7): 1389-1427.
Namur, O., Humphreys, M.C.S. and Holness, M.B., 2013. Lateral Reactive Infiltration in a Vertical Gabbroic Crystal Mush, Skaergaard Intrusion, East Greenland. Journal of Petrology, 54(5): 985-1016.
Naslund, H., 1976. Liquid immiscibility in the system KAlSi3O8-NaAlSi3O8-FeO-Fe2O3-SiO2 and its application to natural magmas. Year Book, Carnegie Institution of Washington, 75: 592-597.
Naslund, H., 1983. The effect of oxygen fugacity on liquid immiscibility in iron-bearing silicate melts. American Journal of Science, 283(10): 1034-1059.
Naslund, H., Turner, P. and Keith, D., 1991. Crystallization and layer formation in the middle zone of the Skaergaard Intrusion. Bulletin of the Geological Society of Denmark, 38: 165-171.
Naslund, H.R., 1984. Petrology of the Upper Border Series of the Skaergaard Intrusion. Journal of Petrology, 25(1): 185-212.
Neave, D.A., Buisman, I. and Maclennan, J., 2017. Continuous mush disaggregation during the long-lasting Laki fissure eruption, Iceland. American Mineralogist, 102(10): 2007-2021.
Neave, D.A., Passmore, E., Maclennan, J., Fitton, G. and Thordarson, T., 2013. Crystal–melt relationships and the record of deep mixing and crystallization in the AD 1783 Laki Eruption, Iceland. Journal of Petrology, 54(8): 1661-1690.
Nernst, W., 1891. Distribution of a substance between two solvents and between solvent and vapor. Zeitschrift für Physikalische Chemie, 163: 142-154.

Nielsen, T., Andersen, J. and Brooks, C., 2005. The Platinova reef of the Skaergaard intrusion. Exploration for platinum-group element deposits. Mineralogical Association of Canada Short Course Series, 35: 431-455.
Nielsen, T. and Brooks, C., 1981. The East Greenland rifted continental margin: An examination of the coastal flexure. Geological Society of London Journal, 138: 559-568.
Nielsen, T. and Brooks, C., 1995. Precious metals in magmas of East Greenland; factors important to the mineralization in the Skaergaard Intrusion. Economic Geology, 90(7): 1911-1917.
Nielsen, T., Brooks, C. and Keiding, J., in review. Bulk liquid for Skaergaard intrusion and its PGE-Au mineralisation: composition, correlation, liquid line of descent, and timing of sulphide saturation and silicate-silicate immiscibility. Journal of Petrology.
Nielsen, T. and Gannicot, R., 1993. The Au-PGM deposit of the Skaergaard intrusion, East Greenland, Terra Nova.
Nielsen, T.F., Andersen, J.Ø., Holness, M.B., Keiding, J.K., Rudashevsky, N., Rudashevsky, V., Salmonsen, L.P., Tegner, C. and Veksler, I.V., 2015. The Skaergaard PGE and gold deposit: the result of in situ fractionation, sulphide saturation, and magma chamber-scale precious metal redistribution by immiscible Fe-rich melt. Journal of Petrology, 56(8): 1643-1676.
Nielsen, T.F.D., 2004. The Shape and Volume of the Skaergaard Intrusion, Greenland: Implications for Mass Balance and Bulk Composition. Journal of Petrology, 45(3): 507-530.
Norton, D., Taylor, H. and Bird, D.K., 1984. The geometry and high-temperature brittle deformation of the Skaergaard Intrusion. Journal of Geophysical Research: Solid Earth, 89(B12): 10178-10192.
Norton, D. and Taylor Jr, H., 1979. Quantitative simulation of the hydrothermal systems of crystallizing magmas on the basis of transport theory and oxygen isotope data: An analysis of the Skaergaard intrusion. Journal of Petrology, 20(3): 421-486.
Nystroem, J.O. and Henriquez, F., 1994. Magmatic features of iron ores of the Kiruna type in Chile and Sweden; ore textures and magnetite geochemistry. Economic Geology, 89(4): 820-839.
O'Driscoll, B. and VanTongeren, J.A., 2017. Layered intrusions: From petrological paradigms to precious metal repositories. Elements, 13(6): 383-389.
Oberdorfer, R., 1904. Die vulkanischen tuffe des ries bei Nördlingen. Ph.D Thesis, C. Gruninger, K. Hofbuchdruckerei zu Gutenberg
Osborn, E.F., 1959. Role of oxygen pressure in the crystallization and differentiation of basaltic magma. American Journal of Science, 257(9): 609-647.
Ostwald, W., 1897. Studien über die Bildung und Umwandlung fester Körper. Zeitschrift für physikalische Chemie, 22(1): 289-330.
Passmore, E., Maclennan, J., Fitton, G. and Thordarson, T., 2012. Mush Disaggregation in Basaltic Magma Chambers: Evidence from the AD 1783 Laki Eruption. Journal of Petrology, 53(12): 2593-2623.
Paterson, S., Memeti, V., Mundil, R. and Žák, J., 2016. Repeated, multiscale, magmatic erosion and recycling in an upper-crustal pluton: Implications for magma chamber dynamics and magma volume estimates. American Mineralogist, 101(10): 2176-2198.
Paterson, S.R., Ardill, K., Vernon, R. and Žák, J., 2019. A review of mesoscopic magmatic structures and their potential for evaluating the hypersolidus evolution of intrusive complexes. Journal of Structural Geology, 125: 134-147.
Paulsen, J.D., Carmigniani, R., Kannan, A., Burton, J.C. and Nagel, S.R., 2014. Coalescence of bubbles and drops in an outer fluid. Nature Communications, 5: 3182.
Pearce, J.A. and Cann, J.R., 1973. Tectonic setting of basic volcanic rocks determined using trace element analyses. Earth and Planetary Science Letters, 19(2): 290-300.
Peltier, A., Ferrazzini, V., Staudacher, T. and Bachèlery, P., 2005. Imaging the dynamics of dyke propagation prior to the 2000–2003 flank eruptions at Piton de La Fournaise, Reunion Island. Geophysical Research Letters, 32: L22302.
Philpotts, A., 1967. Origin of certain iron-titanium oxide and apatite rocks. Economic Geology, 62(3): 303-315.
Philpotts, A., 1976. Silicate liquid immiscibility; its probable extent and petrogenetic significance. American Journal of Science, 276(9): 1147-1177.

Philpotts, A., 1977. Archean variolites—quenched immiscible liquids: Discussion. Canadian Journal of Earth Sciences, 14(1): 139-144.
Philpotts, A., 1981a. Liquid immiscibility in silicate melt inclusions in plagioclase phenocrysts. Bulletin de Minéralogie, 104(4): 317-324.
Philpotts, A., 1982. Compositions of immiscible liquids in volcanic rocks. Contributions to Mineralogy and Petrology, 80(3): 201-218.
Philpotts, A. and Ague, J., 2009. Principles of igneous and metamorphic petrology. Cambridge University Press.
Philpotts, A. and Doyle, C., 1980. Immiscibility in tholeiites: a discussion. Mineralogical Magazine, 43: 939-940.
Philpotts, A.R., 1978. Textural evidence for liquid immiscibility in tholeiites. Mineralogical Magazine, 42: 417-425.
Philpotts, A.R., 1979. Silicate Liquid Immiscibility in Tholeiitic Basalts. Journal of Petrology, 20(1): 99-118.
Philpotts, A.R., 1981b. A model for the generation of massif-type anorthosites. The Canadian Mineralogist, 19(2): 233-253.
Philpotts, A.R., 2008. Comments on: 'Liquid immiscibility and the evolution of basaltic magma' Journal of Petrology 48, 2187-2210. Journal of Petrology, 49(12): 2171-2175.
Philpotts, A.R. and Dickson, L.D., 2000. The formation of plagioclase chains during convective transfer in basaltic magma. Nature, 406(6791): 59-61.
Philpotts, A.R. and Doyle, C.D., 1983. Effect of magma oxidation state on the extent of silicate liquid immiscibility in a tholeiitic basalt. American Journal of Science, 283(9): 967-986.
Philpotts, A.R. and Philpotts, D.E., 2005. Crystal-mush compaction in the Cohassett flood-basalt flow, Hanford, Washington. Journal of Volcanology and Geothermal Research, 145(3): 192-206.
Pihler-Puzović, D., Périllat, R., Russell, M., Juel, A. and Heil, M., 2013. Modelling the suppression of viscous fingering in elastic-walled Hele-Shaw cells. Journal of Fluid Mechanics, 731: 162-183.
Pleše, P., Higgins, M.D., Mancini, L., Lanzafame, G., Brun, F., Fife, J.L., Casselman, J. and Baker, D.R., 2018. Dynamic observations of vesiculation reveal the role of silicate crystals in bubble nucleation and growth in andesitic magmas. Lithos, 296-299: 532-546.
Pratesi, G., Viti, C., Cipriani, C. and Mellini, M., 2002. Silicate-silicate liquid immiscibility and graphite ribbons in Libyan desert glass. Geochimica et Cosmochimica Acta, 66(5): 903-911.
Presnall, D., 1966. The join forsterite-diopside-iron oxide and its bearing on the crystallization of basaltic and ultramafic magmas. American Journal of Science, 264(10): 753-809.
Price, J.G., 1985. Ideal site mixing in solid solutions, with an application to two-feldspar geothermometry. American Mineralogist, 70(7-8): 696-701.
Pupier, E., Duchene, S. and Toplis, M.J., 2008. Experimental quantification of plagioclase crystal size distribution during cooling of a basaltic liquid. Contributions to Mineralogy and Petrology, 155(5): 555-570.
Putirka, K.D., 2008. Thermometers and Barometers for Volcanic Systems. Reviews in Mineralogy and Geochemistry, 69(1): 61-120.
Putnis, A. and Mauthe, G., 2001. The effect of pore size on cementation in porous rocks. Geofluids, 1(1): 37-41.
Raedeke, L. and McCallum, I., 1984. Investigations in the Stillwater complex: Part II. Petrology and petrogenesis of the ultramafic series. Journal of Petrology, 25(2): 395-420.
Raedeke, L.D., 1982. Petrogenesis of the Stillwater Complex. Ph.D Thesis, University of Washington.
Rahman, M.M., Lee, W., Iyer, A. and Williams, S.J., 2019. Viscous resistance in drop coalescence. Physics of Fluids, 31: 012104.
Reid, D. and Basson, I., 2002. Iron-rich ultramafic pegmatite replacement bodies within the upper critical zone, Rustenburg layered suite, Northam platinum mine, South Africa. Mineralogical Magazine, 66(6): 895-914.
Reynolds, I.M., 1985. The nature and origin of titaniferous magnetite-rich layers in the upper zone of the Bushveld Complex; a review and synthesis. Economic Geology, 80(4): 1089-1108.
Riegger, O. and Van Vlack, L., 1960. Dihedral angle measurement. Transactions of the Metallurgical Society of AIME, 218: 933-935.

Ripley, E.M., Severson, M.J. and Hauck, S.A., 1998. Evidence for sulfide and Fe-Ti-P-rich liquid immiscibility in the Duluth Complex, Minnesota. Economic Geology, 93(7): 1052-1062.
Roedder, E., 1951. Low Temperature liquid immiscibility in the system K2O-FeO-Al2O3-SiO2. American Mineralogist, 36: 282-286.
Roedder, E., 1978. Silicate liquid immiscibility in magmas and in the system K2O-FeO-AI2O3-SiO2: an example of serendipity. Geochimica et Cosmochimica Acta, 42(11): 1597-1617.
Roedder, E. and Weiblen, P., 1970a. Lunar petrology of silicate melt inclusions, Apollo 11 rocks. Geochimica et Cosmochimica Acta Supplement, 1: 801-837.
Roedder, E. and Weiblen, P.W., 1970b. Silicate liquid immiscibility found in lunar rocks. Geotimes, 15(3): 10-13.
Roedder, E. and Weiblen, P.W., 1970c. Silicate liquid immiscibility in lunar magmas, evidenced by melt inclusions in lunar rocks. Science, 167(3918): 641-644.
Roeder, P. and Osborn, E., 1966. Experimental data for the system MgO-FeO-Fe2O3-CaAl2Si2O8-SiO2 and their petrologic implications. American Journal of Science, 264(6): 428-480.
Rotenberg, Y., Boruvka, L. and Neumann, A.W., 1983. Determination of surface tension and contact angle from the shapes of axisymmetric fluid interfaces. Journal of Colloid and Interface Science, 93(1): 169-183.
Rutherford, M.J., Hess, P.C. and Daniel, G.H., 1974. Experimental liquid line of descent and liquid immiscibility for basalt 70017, Lunar and Planetary Science Conference Proceedings, pp. 569-583.
Ryabov, V.V., 1989. Immiscibility in Natural Glasses, Russia, Novosibirsk, 221 pp.
Ryan, M.P. and Sammis, C.G., 1981. The glass transition in basalt. Journal of Geophysical Research: Solid Earth, 86(B10): 9519-9535.
Ryerson, F. and Hess, P., 1978. Implications of liquid-liquid distribution coefficients to mineral-liquid partitioning. Geochimica et Cosmochimica Acta, 42(6): 921-932.
Saffman, P.G. and Taylor, G.I., 1958. The penetration of a fluid into a porous medium or Hele-Shaw cell containing a more viscous liquid. Proceedings of the Royal Society of London. Series A. Mathematical and Physical Sciences, 245(1242): 312-329.
Salmonsen, L.P. and Tegner, C., 2013. Crystallization sequence of the Upper Border Series of the Skaergaard Intrusion: revised subdivision and implications for chamber-scale magma homogeneity. Contributions to Mineralogy and Petrology, 165(6): 1155-1171.
Sato, H., 1995. Textural difference between pahoehoe and aa lavas of Izu-Oshima volcano, Japan--An experimental study on population density of plagioclase. Journal of Volcanology and Geothermal Research, 66(1): 101-114.
Sato, M. and Sumita, I., 2007. Experiments on gravitational phase separation of binary immiscible fluids. Journal of Fluid Mechanics, 591: 289-319.
Saunders, A., Fitton, J., Kerr, A., Norry, M. and Kent, R., 1997. The North Atlantic igneous province. In: J.J. Mahoney and M.F. Coffin (Editors), Large Igneous Provinces: Continental, Oceanic, and Planetary Flood Volcanism. Geophysical Monograph. American Geophysical Union, Washington DC, USA, pp. 45-93.
Saxey, D., Moser, D., Piazolo, S., Reddy, S. and Valley, J., 2018. Atomic worlds: Current state and future of atom probe tomography in geoscience. Scripta Materialia, 148: 115-121.
Scherer, G.W., 1999. Crystallization in pores. Cement and Concrete Research, 29(8): 1347-1358.
Schiavi, F., Walte, N. and Keppler, H., 2009. First in situ observation of crystallization processes in a basaltic-andesitic melt with the moissanite cell. Geology, 37(11): 963-966.
Schleicher, J.M. and Bergantz, G.W., 2017. The Mechanics and Temporal Evolution of an Open-system Magmatic Intrusion into a Crystal-rich Magma. Journal of Petrology, 58(6): 1059-1072.
Schmidt, M.W., Connolly, J.A.D., Günther, D. and Bogaerts, M., 2006. Element Partitioning: The Role of Melt Structure and Composition. Science, 312(5780): 1646-1650.
Scoon, R.N. and Mitchell, A.A., 1994. Discordant Iron-Rich Ultramafic Pegmatites in the Bushveld Complex and their Relationship to Iron-Rich Intercumulus and Residual Liquids. Journal of Petrology, 35(4): 881-917.
Sear, R.P., 2007. Nucleation: theory and applications to protein solutions and colloidal suspensions. Journal of Physics: Condensed Matter, 19(3): 033101.

Sensarma, S. and Palme, H., 2013. Silicate liquid immiscibility in the ~2.5 Ga Fe-rich andesite at the top of the Dongargarh large igneous province (India). Lithos, 170: 239-251.
Sheard, E.R., Williams-Jones, A.E., Heiligmann, M., Pederson, C. and Trueman, D.L., 2012. Controls on the concentration of zirconium, niobium, and the rare earth elements in the Thor Lake rare metal deposit, Northwest Territories, Canada. Economic Geology, 107(1): 81-104.
Shelby, J.E., 2005. Introduction to Glass Science and Technology. The Royal Society of Chemistry, Cambridge, 283 pp.
Sisson, T. and Grove, T., 1993. Experimental investigations of the role of H2O in calc-alkaline differentiation and subduction zone magmatism. Contributions to Mineralogy and Petrology, 113(2): 143-166.
Sloan, T., 1971. The structure of the Mull tertiary dyke swarm. Ph.D Thesis, University of London.
Snyder, D., Carmichael, I.S. and Wiebe, R., 1993. Experimental study of liquid evolution in an Fe-rich, layered mafic intrusion: constraints of Fe-Ti oxide precipitation on the T-fO2 and T-ϱ paths of tholeiitic magmas. Contributions to Mineralogy and Petrology, 113(1): 73-86.
Sonnenthal, E.L., 1992. Geochemistry of dendritic anorthosites and associated pegmatites in the Skaergaard Intrusion, East Greenland: Evidence for metasomatism by a chlorine-rich fluid. Journal of Volcanology and Geothermal Research, 52(1-3): 209-230.
Sørensen, L.L., Weatherley, S., Kokfelt, T. and Nielsen, T.F.D., 2016. Magmatic titanium-vanadium potential in Greenland, GEUS
Stewart, B.W. and DePaolo, D.J., 1990. Isotopic studies of processes in mafic magma chambers: II. The Skaergaard Intrusion, East Greenland. Contributions to Mineralogy and Petrology, 104(2): 125-141.
Stickels, C. and Hucke, E., 1964. Measurement of dihedral angles. Transactions of the Metallurgical Society of AIME, 230(4): 795-801.
Stolper, E. and Walker, D., 1980. Melt density and the average composition of basalt. Contributions to Mineralogy and Petrology, 74(1): 7-12.
Stripp, G.R., 2009. The Late-Stage Evolution of the Skaergaard Intrusion, East Greenland. Ph.D Thesis, University of Cambridge, Cambridge, 1-217 pp.
Tait, S. and Jaupart, C., 1992. Compositional convection in a reactive crystalline mush and melt differentiation. Journal of Geophysical Research: Solid Earth, 97(B5): 6735-6756.
Taylor Jr, H.P. and Forester, R.W., 1979. An oxygen and hydrogen isotope study of the Skaergaard intrusion and its country rocks: a description of a 55 my old fossil hydrothermal system. Journal of Petrology, 20(3): 355-419.
Teall, J., 1889. On the Amygdaloids of the Tynemouth Dyke. Geological Magazine 6(11): 481-483.
Teall, J.J.H., 1884. Petrological notes on some North of England dykes. Quarterly Journal of the Geological Society, 40(1-4): 209-247.
Tegner, C., 1997. Iron in plagioclase as a monitor of the differentiation of the Skaergaard intrusion. Contributions to Mineralogy and Petrology, 128(1): 45-51.
Tegner, C. and Cawthorn, R.G., 2010. Iron in plagioclase in the Bushveld and Skaergaard intrusions: implications for iron contents in evolving basic magmas. Contributions to Mineralogy and Petrology, 159(5): 719-730.
Tegner, C., Cawthorn, R.G. and Kruger, F.J., 2006. Cyclicity in the Main and Upper Zones of the Bushveld Complex, South Africa: Crystallization from a Zoned Magma Sheet. Journal of Petrology, 47(11): 2257-2279.
Tegner, C., Thy, P., Holness, M.B., Jakobsen, J.K. and Lesher, C.E., 2009. Differentiation and Compaction in the Skaergaard Intrusion. Journal of Petrology, 50(5): 813-840.
Thompson, A.B., Aerts, M. and Hack, A.C., 2007. Liquid Immiscibility in Silicate Melts and Related Systems. Reviews in Mineralogy and Geochemistry, 65(1): 99-127.
Thompson, K., Gorman, B., Larson, D., van Leer, B. and Hong, L., 2006. Minimization of Ga induced FIB damage using low energy clean-up. Microscopy and Microanalysis, 12(S02): 1736-1737.
Thy, P., Lesher, C.E. and Tegner, C., 2008. The Skaergaard liquid line of descent revisited. Contributions to Mineralogy and Petrology, 157(6): 735-747.
Thy, P., Tegner, C. and Lesher, C.E., 2009. Liquidus temperatures of the Skaergaard magma. American Mineralogist, 94(10): 1371-1376.

Tollari, N., Toplis, M.J. and Barnes, S.J., 2006. Predicting phosphate saturation in silicate magmas: an experimental study of the effects of melt composition and temperature. Geochimica et Cosmochimica Acta, 70(6): 1518-1536.
Toplis, M. and Carroll, M., 1995. An experimental study of the influence of oxygen fugacity on Fe-Ti oxide stability, phase relations, and mineral—melt equilibria in ferro-basaltic systems. Journal of Petrology, 36(5): 1137-1170.
Toplis, M. and Reynard, B., 2000. Temperature and time-dependent changes of structure in phosphorus containing aluminosilicate liquids and glasses: in-situ Raman spectroscopy at high temperature. Journal of Non-Crystalline Solids, 263: 123-131.
Toplis, M.J., Brown, W.L. and Pupier, E., 2008. Plagioclase in the Skaergaard intrusion. Part 1: Core and rim compositions in the layered series. Contributions to Mineralogy and Petrology, 155(3): 329-340.
Toplis, M.J. and Carroll, M.R., 1996. Differentiation of Ferro-Basaltic Magmas under Conditions Open and Closed to Oxygen: Implications for the Skaergaard Intrusion and Other Natural Systems. Journal of Petrology, 37(4): 837-858.
Toplis, M.J., Libourel, G. and Carroll, M.R., 1994. The role of phosphorus in crystallisation processes of basalt: An experimental study. Geochimica et Cosmochimica Acta, 58(2): 797-810.
Underhill, J.R., 2009. Role of intrusion-induced salt mobility in controlling the formation of the enigmatic 'Silverpit Crater', UK Southern North Sea. Petroleum Geoscience, 15(3): 197-216.
VanTongeren, J. and Mathez, E., 2012. Large-scale liquid immiscibility at the top of the Bushveld Complex, South Africa. Geology, 40(6): 491-494.
VanTongeren, J.A., 2018. Mixing and Unmixing in the Bushveld Complex Magma Chamber. In: S.K. Mondal and W.L. Griffin (Editors), Processes and Ore Deposits of Ultramafic-Mafic Magmas through Space and Time. Elsevier, pp. 113-138.
Veksler, I.V., 2004. Liquid immiscibility and its role at the magmatic–hydrothermal transition: a summary of experimental studies. Chemical Geology, 210(1): 7-31.
Veksler, I.V., 2009. Extreme iron enrichment and liquid immiscibility in mafic intrusions: Experimental evidence revisited. Lithos, 111(1): 72-82.
Veksler, I.V. and Charlier, B., 2015. Silicate liquid immiscibility in layered intrusions. In: B. Charlier, O. Namur, R. Latypov and C. Tegner (Editors), Layered Intrusions. Springer, pp. 229-258.
Veksler, I.V., Dorfman, A.M., Borisov, A.A., Wirth, R. and Dingwell, D.B., 2007. Liquid immiscibility and the evolution of basaltic magma. Journal of Petrology, 48(11): 2187-2210.
Veksler, I.V., Dorfman, A.M., Borisov, A.A., Wirth, R. and Dingwell, D.B., 2008a. Liquid Immiscibility and Evolution of Basaltic Magma: Reply to S. A. Morse, A. R. McBirney and A. R. Philpotts. Journal of Petrology, 49(12): 2177-2186.
Veksler, I.V., Dorfman, A.M., Danyushevsky, L.V., Jakobsen, J.K. and Dingwell, D.B., 2006. Immiscible silicate liquid partition coefficients: implications for crystal-melt element partitioning and basalt petrogenesis. Contributions to Mineralogy and Petrology, 152(6): 685-702.
Veksler, I.V., Dorfman, A.M., Rhede, D., Wirth, R., Borisov, A.A. and Dingwell, D.B., 2008b. Liquid unmixing kinetics and the extent of immiscibility in the system K2O–CaO–FeO–Al2O3–SiO2. Chemical Geology, 256(3): 119-130.
Veksler, I.V., Kähn, J., Franz, G. and Dingwell, D.B., 2010. Interfacial tension between immiscible liquids in the system K2O-FeO-Fe2O3-Al2O3-SiO2 and implications for the kinetics of silicate melt unmixing. American Mineralogist, 95(11-12): 1679-1685.
Vernon, R.H., 2004. A practical guide to Rock Microstructure. Cambridge University Press, Cambridge, 579 pp.
Viljoen, M.J. and Scoon, R.N., 1985. The distribution and main geologic features of discordant bodies of iron-rich ultramafic pegmatite in the Bushveld Complex. Economic Geology, 80(4): 1109-1128.
Villiger, S., Ulmer, P. and Müntener, O., 2006. Equilibrium and fractional crystallization experiments at 0.7 GPa; the effect of pressure on phase relations and liquid compositions of tholeiitic magmas. Journal of Petrology, 48(1): 159-184.

Villiger, S., Ulmer, P., Müntener, O. and Thompson, A.B., 2004. The liquid line of descent of anhydrous, mantle-derived, tholeiitic liquids by fractional and equilibrium crystallization—an experimental study at 1.0 GPa. Journal of Petrology, 45(12): 2369-2388.
Visser, W. and Koster Van Groos, A.F., 1976. Liquid immiscibility in K2O–FeO–Al2O3–SiO2. Nature, 264: 426-427.
Visser, W. and Van Groos, A.K., 1979a. Effect of pressure on liquid immiscibility in the system K2O-FeO-Al2O3-SiO2-P2O5. American Journal of Science, 279(10): 1160-1175.
Visser, W. and Van Groos, A.K., 1979b. Effects of P2O5 and TiO2 on liquid-liquid equilibria in the system K2O-FeO-Al2O3-SiO2. American Journal of Science, 279(8): 970-988.
Von Gruenewaldt, G., 1993. Ilmenite-apatite enrichments in the Upper Zone of the Bushveld Complex: a major titanium-rock phosphate resource. International Geology Review, 35(11): 987-1000.
Vukmanovic, Z., Holness, M.B., Monks, K. and Andersen, J., 2018. The Skaergaard trough layering: sedimentation in a convecting magma chamber. Contributions to Mineralogy and Petrology, 173: 1-18.
Wager, L. and Deer, W., 1939. Geological investigations in east Greenland. Part III. The petrology of the Skaergaard intrusion, Kangerdlugssuag, East Greenland. Meddelelser om Grønland, 105(4): 352.
Wager, L.R., 1960. The major element variation of the layered series of the Skaergaard intrusion and a re-estimation of the average composition of the hidden layered series and of the successive residual magmas. Journal of Petrology, 1(1): 364-398.
Wager, L.R. and Brown, G.M., 1968. Layered igneous rocks. WH Freeman, London.
Wagner, C., 1961. Theorie der alterung von niederschlägen durch umlösen (Ostwald-reifung). Zeitschrift für Elektrochemie, Berichte der Bunsengesellschaft für physikalische Chemie, 65(7-8): 581-591.
Wahl, S.M. and Militzer, B., 2015. High-temperature miscibility of iron and rock during terrestrial planet formation. Earth and Planetary Science Letters, 410: 25-33.
Wall, M., Cartwright, J., Davies, R. and McGrandle, A., 2010. 3D seismic imaging of a Tertiary Dyke Swarm in the Southern North Sea, UK. Basin Research, 22(2): 181-194.
Wang, M., Namur, O., Almeev, R., Holtz, F. and Charlier, B., in prep. Crystallization experiments on Snake River Plain ferrobasalts and the production of A-type rhyolites. Contributions to Mineralogy and Petrology.
Watson, E.B., 1976. Two-liquid partition coefficients: experimental data and geochemical implications. Contributions to Mineralogy and Petrology, 56(1): 119-134.
Whitney, D.L. and Evans, B.W., 2010. Abbreviations for names of rock-forming minerals. American Mineralogist, 95(1): 185-187.
Wiebe, R., 1979. Fractionation and liquid immiscibility in an anorthositic pluton of the Nain complex, Labrador. Journal of Petrology, 20(2): 239-269.
Wilke, M., Schmidt, C., Dubrail, J., Appel, K., Borchert, M., Kvashnina, K. and Manning, C.E., 2012. Zircon solubility and zirconium complexation in H2O+Na2O+SiO±Al2O3 fluids at high pressure and temperature. Earth and Planetary Science Letters, 349: 15-25.
Williams-Jones, A.E., Migdisov, A.A. and Samson, I.M., 2012. Hydrothermal mobilisation of the rare earth elements–a tale of "ceria" and "yttria". Elements, 8(5): 355-360.
Williams, Q. and Jeanloz, R., 1988. Spectroscopic evidence for pressure-induced coordination changes in silicate glasses and melts. Science, 239(4842): 902-905.
Williams, R.J., 1971. Reaction constants in the system Fe-MgO-SiO2-O2; intensive parameters in the Skaergaard intrusion, East Greenland. American Journal of Science, 271(2): 132-146.
Wilson, J.R. and Overgaard, G., 2005. Relationship between the Layered Series and the overlying evolved rocks in the Bjerkreim-Sokndal Intrusion, southern Norway. Lithos, 83(3): 277-298.
Wood, M.I. and Hess, P.C., 1980. The structural role of Al2O3 and TiO2 in immiscible silicate liquids in the system SiO2-MgO-CaO-FeO-TiO2-Al2O3. Contributions to Mineralogy and Petrology, 72(3): 319-328.
Wotzlaw, J.F., Bindeman, I.N., Schaltegger, U., Brooks, C.K. and Naslund, H.R., 2012. High-resolution insights into episodes of crystallization, hydrothermal alteration and remelting in the Skaergaard intrusive complex. Earth and Planetary Science Letters, 355-356: 199-212.

Wright, T.J., Ebinger, C., Biggs, J., Ayele, A., Yirgu, G., Keir, D. and Stork, A., 2006. Magma-maintained rift segmentation at continental rupture in the 2005 Afar dyking episode. Nature, 442: 291-294.

Yablonovitch, E. and Gmitter, T., 1984. Wetting Angles and Surface Tension in the Crystallization of Thin Liquid Films. Journal of the Electrochemical Society, 131(11): 2625-2630.

Yang, W.B., Niu, H.C., Shan, Q., Sun, W.D., Zhang, H., Li, N.B., Jiang, Y.H. and Yu, X.Y., 2014. Geochemistry of magmatic and hydrothermal zircon from the highly evolved Baerzhe alkaline granite: implications for Zr–REE–Nb mineralization. Mineralium Deposita, 49(4): 451-470.

Yao, W., Maris, H., Pennington, P. and Seidel, G., 2005. Coalescence of viscous liquid drops. Physical Review E, 71: 016309.

Yarger, J., Smith, K., Nieman, R., Diefenbacher, J., Wolf, G., Poe, B. and McMillan, P., 1995. Al coordination changes in high-pressure aluminosilicate liquids. Science, 270(5244): 1964-1967.

Yoder, H., Stewart, D. and Smith, J., 1957. Feldspars. Carnegie Institution Washington Yearbook, 56: 206-214.

Young, T., 1805. An essay on the cohesion of fluids. Philosophical Transactions of the Royal Society of London, 95: 65-87.

Yuan, Q., Namur, O., Fischer, L.A., Roberts, R.J., Lü, X. and Charlier, B., 2017. Pulses of plagioclase-laden magmas and stratigraphic evolution in the Upper Zone of the Bushveld Complex, South Africa. Journal of Petrology, 58(8): 1619-1643.

Žák, J. and Paterson, S.R., 2010. Magmatic erosion of the solidification front during reintrusion: the eastern margin of the Tuolumne batholith, Sierra Nevada, California. International Journal of Earth Sciences, 99(4): 801-812.

Zellmer, G.F., Sakamoto, N., Hwang, S.-L., Matsuda, N., Iizuka, Y., Moebis, A. and Yurimoto, H., 2016. Inferring the Effects of Compositional Boundary Layers on Crystal Nucleation, Growth Textures, and Mineral Chemistry in Natural Volcanic Tephras through Submicron-Resolution Imaging. Frontiers in Earth Science, 4(88): 1-7.

Zhang, Y., Ni, H. and Chen, Y., 2010. Diffusion data in silicate melts. Reviews in Mineralogy and Geochemistry, 72(1): 311-408.

Zhou, M.F., Chen, W.T., Wang, C.Y., Prevec, S.A., Liu, Patricia P. and Howarth, G.H., 2013. Two stages of immiscible liquid separation in the formation of Panzhihua-type Fe-Ti-V oxide deposits, SW China. Geoscience Frontiers, 4(5): 481-502.

Zieg, M. and Marsh, B., 2002. Crystal size distributions and scaling laws in the quantification of igneous textures. Journal of Petrology, 43(1): 85-101.

8 APPENDICES

Appendix Table 2.A Electron microprobe analyses using beams with different focuses on glass secondary standards of known composition.

SiO_2	TiO_2	Al_2O_3	FeO	MnO	MgO	CaO	Na_2O	K_2O	P_2O_5	Total
Basaltic glass A-99, Makaopuhi Lava Lake										
10 µm defocused beam, 4 nA, 15 kV										
50.13	3.86	12.17	13.54	0.14	4.97	9.19	2.63	0.86	0.59	98.13
50.60	4.19	11.94	13.36	0.17	4.89	9.20	2.70	0.88	0.56	98.50
51.04	4.09	12.11	13.21	0.27	4.85	9.07	2.76	0.78	0.56	98.74
50.82	3.99	12.05	12.89	0.13	4.80	9.30	2.99	0.90	0.56	98.47
49.90	4.02	12.27	12.98	0.28	4.98	9.24	2.70	0.91	0.55	97.67
50.01	3.92	11.64	13.03	0.17	4.90	9.05	2.91	0.90	0.57	96.97
52.03	4.04	11.79	13.82	0.19	4.63	9.09	2.66	0.83	0.56	99.61
50.80	4.13	12.19	13.51	0.23	4.97	9.31	2.84	0.91	0.55	99.40
50.36	4.11	11.09	13.52	0.25	5.08	9.09	2.84	0.80	0.53	97.71
50.09	4.02	11.66	13.75	0.23	4.60	9.09	2.73	0.82	0.55	97.50
50.30	4.21	12.26	13.23	0.21	4.73	9.07	2.87	0.81	0.57	98.27
51.22	3.95	11.88	13.29	0.32	4.92	9.15	2.77	0.83	0.57	98.82
51.31	3.97	11.13	13.61	0.26	4.94	9.07	2.83	0.85	0.56	98.42
50.23	4.00	12.01	13.52	0.26	4.92	9.17	2.97	0.81	0.57	98.37
2 µm focused beam, 4 nA, 15 kV										
50.39	4.13	12.14	13.70	0.16	4.77	9.15	2.71	0.89	0.58	98.57
50.76	3.98	11.82	13.78	0.08	5.10	8.95	2.76	0.83	0.56	98.58
50.31	4.12	12.38	13.58	0.21	4.77	9.05	2.63	0.93	0.58	98.52
50.97	4.09	12.31	13.82	0.25	4.84	9.18	2.79	0.78	0.60	99.64
50.34	4.10	11.70	13.55	0.15	4.83	9.17	2.55	0.83	0.53	97.71
50.28	4.00	12.11	13.48	0.20	5.02	9.36	2.70	0.83	0.59	98.55
51.13	3.96	12.00	13.53	0.17	5.85	8.96	2.75	0.87	0.57	99.76
50.17	4.14	12.08	13.76	0.23	4.98	9.22	2.80	0.88	0.56	98.75
50.55	4.17	11.50	13.82	0.09	5.08	8.94	2.75	0.87	0.56	98.35
51.21	4.04	11.85	13.26	0.17	4.80	9.26	2.71	0.83	0.57	98.69
51.30	3.80	11.96	13.73	0.26	5.06	9.18	2.44	0.83	0.60	99.10
50.75	4.01	11.92	13.89	0.16	5.01	9.19	2.76	0.85	0.58	99.08
50.28	3.93	12.12	13.57	0.29	5.10	9.47	2.47	0.82	0.58	98.68
50.78	4.11	11.58	13.56	0.28	4.91	8.90	2.87	0.82	0.54	98.33
50.14	3.91	13.14	13.27	0.20	4.91	9.18	2.66	0.91	0.55	98.95
Standard Deviation comparing 10 µm and 2 µm beam conditions										
0.49	0.10	0.38	0.26	0.06	0.22	0.13	0.13	0.04	0.02	-
Corning Glass Reference "D", NMNH 117218-3										
10 µm defocused beam, 4 nA, 15 kV										
SiO_2	TiO_2	Al_2O_3	FeO	MnO	MgO	CaO	Na_2O	K_2O	P_2O_5	Total
55.09	0.30	6.36	0.44	0.56	3.65	14.75	1.35	11.76	4.25	98.35
54.97	0.31	5.77	0.33	0.54	3.78	14.99	1.37	11.66	4.29	97.76
54.65	0.30	5.05	0.50	0.61	3.91	14.51	1.32	11.39	4.18	96.17
55.42	0.30	4.99	0.47	0.62	3.12	15.02	1.38	11.42	4.25	96.73
55.10	0.32	6.69	0.47	0.64	3.73	15.00	1.25	11.42	4.22	98.53
54.38	0.35	4.78	0.52	0.61	3.83	14.83	1.53	11.50	4.22	96.40
54.24	0.37	4.95	0.33	0.48	3.43	14.68	1.30	11.66	4.25	95.49
55.58	0.33	4.76	0.54	0.54	4.10	14.97	1.30	11.49	4.23	97.67
55.09	0.35	4.90	0.47	0.67	3.83	14.73	1.46	11.73	4.18	97.09
55.24	0.36	4.96	0.52	0.47	2.80	14.86	1.32	11.53	4.21	96.10
55.49	0.37	4.99	0.33	0.62	3.70	14.84	1.32	11.52	4.24	97.06
54.72	0.25	4.67	0.40	0.47	3.67	14.82	1.29	11.65	4.26	95.90
54.86	0.33	4.92	0.42	0.62	3.72	14.98	1.34	11.55	4.23	96.69
54.66	0.30	4.63	0.49	0.65	3.02	14.88	1.30	11.40	4.20	95.34

Continued from previous page

SiO_2	TiO_2	Al_2O_3	FeO	MnO	MgO	CaO	Na_2O	K_2O	P_2O_5	Total
54.77	0.35	4.98	0.46	0.63	3.23	14.88	1.23	11.67	4.23	96.07
2 µm focused beam, 4 nA, 15 kV										
54.29	0.32	4.70	0.57	0.61	3.99	15.35	1.21	11.12	4.30	96.22
55.05	0.30	4.43	0.37	0.73	3.99	15.13	1.29	11.03	4.37	96.24
54.92	0.31	5.07	0.48	0.56	3.82	15.19	1.30	10.84	4.37	96.67
54.96	0.37	4.69	0.37	0.65	3.87	15.07	1.37	11.23	4.24	96.47
55.61	0.42	5.15	0.45	0.57	3.44	15.35	1.27	11.00	4.34	97.23
55.45	0.40	5.09	0.48	0.60	3.91	15.23	1.44	11.07	4.32	97.67
55.26	0.37	4.97	0.47	0.68	3.82	15.48	1.32	11.30	4.33	97.74
55.01	0.32	5.21	0.46	0.46	3.88	15.25	1.32	11.18	4.26	97.23
54.71	0.41	4.68	0.47	0.64	3.76	15.53	1.27	11.42	4.27	96.86
54.95	0.42	5.05	0.43	0.70	3.73	15.16	1.27	11.30	4.35	97.10
55.11	0.36	4.39	0.48	0.55	3.78	15.05	1.25	11.54	4.28	96.75
54.93	0.30	5.03	0.39	0.62	3.73	15.24	1.41	11.12	4.34	96.81
54.25	0.29	4.26	0.47	0.57	3.94	15.36	1.36	11.54	4.24	96.13
54.95	0.36	5.18	0.52	0.76	3.63	15.10	1.33	11.28	4.36	97.23
Standard Deviation comparing 10 µm and 2 µm beam conditions										
0.37	0.04	0.50	0.06	0.07	0.30	0.24	0.07	0.24	0.06	-

Appendix Table 2.B Electron microprobe analyses of phases present. gl glass, pl plagioclase, ol olivine, aug augite, pig pigeonite, il ilmenite, tmt titanomagnetite, mt magnetite, wht whitlockite

Run	Phase (no. of grains analysed)	Oxide (wt.%)														An/Fo/Mg #	Density (g/cm^3)	Viscosity	NBO/T
		SiO_2	TiO_2	Al_2O_3	FeO	MnO	MgO	CaO	Na_2O	K_2O	P_2O_5	Y_2O_3	ZrO_2	Ce_2O_3	Total			log η (Pas)	
VIC08	gl(17)	58.59	1.81	13.45	10.46	0.10	2.00	4.77	4.28	3.01	1.16	0.17	0.14	0.00	99.93	25.1	2.56	4.67	0.41
1050	pl(9)	57.32	0.10	25.89	1.10	-	0.06	8.63	6.28	0.69	-	-	-	-	100.05	43.2	-		-
	aug(6)	50.48	0.85	2.03	16.62	-	16.03	13.36	0.28	0.03	-	-	-	-	99.69	45.9	-		-
	pig(5)	51.33	0.64	1.69	19.91	-	19.77	6.46	0.12	0.02	-	-	-	-	99.95	55.5	-		-
	mt(8)	0.32	17.21	2.54	72.39	0.27	2.76	0.17	0.02	0.05	-	-	-	-	95.74	-	-		-
VIC06	gl(17)	56.91	2.75	13.11	12.07	0.14	2.05	5.36	3.69	2.71	0.99	0.18	0.13	0.00	100.11	23.0	2.61	4.88	0.45
1030*	pl(8)	59.10	0.16	24.00	1.03	-	0.08	7.48	6.47	0.90	-	-	-	-	99.22	39.0	-		-
	ol(8)	34.08	0.14	-	41.68	0.55	22.82	0.43	0.03	0.04	-	-	-	-	99.77	49.4	-		-
	aug(7)	48.03	1.80	2.93	17.86	0.36	13.01	14.81	0.33	0.04	-	-	-	-	99.17	38.6	-		-
	pig(12)	49.77	1.10	2.01	22.70	0.45	17.54	6.08	0.13	0.03	-	-	-	-	99.81	50.6	-		-
	tmt(10)	4.17	40.91	1.05	47.19	0.45	2.54	0.38	0.25	0.26	-	-	-	-	97.21	-	-		-
	mt(9)	1.55	16.76	2.48	72.37	0.44	2.22	0.14	0.09	0.11	-	-	-	-	96.16	-	-		-
VIC08	gl Si(19)	61.97	1.60	13.47	8.37	0.10	1.43	3.63	4.07	3.50	1.25	0.14	0.17	0.00	99.70	23.0	2.51	5.50	0.30
1025	gl Fe(9)	38.28	6.28	6.43	21.74	0.33	3.97	10.03	1.97	0.88	5.69	1.42	0.48	0.46	97.97	24.3	2.93	3.63	1.31
	pl(9)	59.07	0.15	24.61	1.05	-	0.07	7.72	6.51	0.84	-	-	-	-	100.04	39.6	-		-
	aug(12)	49.25	1.01	1.80	15.88	-	15.98	14.56	0.31	0.05	-	-	-	-	98.85	45.2	-		-
	pig(4)	50.39	0.53	0.95	20.66	-	20.66	5.42	0.12	0.03	-	-	-	-	98.75	57.2	-		-
	mt(12)	0.96	17.06	2.08	72.96	0.59	2.18	0.26	0.10	0.07	-	-	-	-	96.26	-	-		-
VIC08	gl Si(18)	65.30	1.17	13.80	6.63	0.08	0.68	2.58	2.85	4.13	0.84	0.10	0.20	0.00	98.36	14.9	2.46	6.47	0.17
1010	gl Fe(9)	35.15	5.50	5.41	23.27	0.60	4.16	11.05	1.81	0.70	8.13	-	0.41	0.58	96.78	23.7	2.97	3.40	1.54
	pl(9)	58.77	0.16	23.68	1.04	-	0.06	7.13	6.27	0.90	-	-	-	-	98.02	38.6	-		-
	aug(12)	49.05	1.07	1.91	16.01	-	15.12	14.97	0.33	0.04	-	-	-	-	98.50	43.4	-		-
	pig(12)	50.23	0.62	1.09	20.28	-	19.91	6.42	0.13	0.03	-	-	-	-	98.70	55.4	-		-
	mt(13)	0.38	15.87	1.87	74.30	0.60	1.92	0.13	0.03	0.05	-	-	-	-	95.16	-	-		-
VIC06	gl Si(14)	59.47	2.15	13.09	9.59	0.12	1.36	4.73	2.92	3.33	1.19	0.19	0.22	0.00	98.36	19.9	2.55	5.74	0.34
1010*	gl Fe(10)	37.31	5.98	5.88	21.87	0.48	4.00	10.76	1.76	0.78	6.18	-	0.64	0.42	96.06	24.1	2.95	3.74	1.39
	pl(8)	59.37	0.15	23.54	1.06	-	0.08	6.91	6.55	0.89	-	-	-	-	98.55	36.8	-		-
	ol(11)	33.39	0.14	0.09	42.49	0.82	22.13	0.44	0.02	0.03	-	-	-	-	99.57	48.1	-		-

Continued from previous page

Run	Phase (no. of grains analysed)	Oxide (wt.%)														An/Fo/Mg #	Density (g/cm^3)	Viscosity	NBO/T
		SiO_2	TiO_2	Al_2O_3	FeO	MnO	MgO	CaO	Na_2O	K_2O	P_2O_5	Y_2O_3	ZrO_2	Ce_2O_3	Total			log η (Pas)	
	aug(9)	46.97	2.07	3.03	15.31	-	12.08	17.99	0.42	0.04	-	-	-	-	97.90	35.9	-		-
	pig(6)	49.15	1.04	1.48	23.60	-	18.07	4.87	0.10	0.02	-	-	-	-	98.33	51.9	-		-
	mt(12)	0.39	17.93	1.91	71.94	0.56	2.10	0.14	0.01	0.08	-	-	-	-	95.06	-	-		-
VIC07	gl Si(20)	66.96	1.14	13.74	5.82	0.09	0.47	2.13	2.66	4.24	0.69	0.06	0.26	0.00	98.24	15.8	2.44	6.84	0.13
1005	gl Fe(10)	34.01	6.28	4.94	23.38	0.67	4.38	10.79	1.80	0.67	7.83	-	0.49	0.94	96.19	24.5	3.00	3.57	1.59
	pl(8)	58.58	0.12	23.86	1.01	-	0.06	7.14	6.27	0.96	-	-	-	-	98.00	38.6	-		-
	aug(21)	49.83	0.86	1.67	16.27	0.54	15.07	14.27	0.33	0.06	-	-	-	-	98.90	43.7	-		-
	pig(8)	51.27	0.46	0.62	20.92	0.62	19.31	5.68	0.15	0.08	-	-	-	-	99.11	55.7	-		-
	mt(11)	0.20	17.52	1.85	72.68	0.54	2.09	0.13	0.03	0.05	-	-	-	-	95.09	-	-		-
VIC09	gl Si(21)	66.82	1.38	13.75	5.69	0.10	0.72	2.20	2.49	4.43	0.62	0.06	0.28	0.00	98.54	20.5	2.44	6.91	0.13
1000	gl Fe(10)	35.00	4.86	4.82	22.51	0.51	5.34	11.29	1.72	0.67	8.65	-	0.48	0.51	96.36	29.3	2.97	3.39	1.64
	pl(8)	58.47	0.18	23.91	1.16	-	0.07	7.21	6.52	0.96	-	-	-	-	98.48	37.9	-		-
	aug(17)	48.48	1.39	2.12	14.94	0.48	14.15	16.58	0.40	0.04	-	-	-	-	98.58	41.1	-		-
	pig(8)	51.47	0.61	1.26	19.56	0.53	20.98	5.08	0.10	0.02					99.61	58.9	-		-
	mt(8)	0.18	15.13	1.93	74.25	0.44	2.37	0.11	0.02	0.04	-	-	-	-	94.47	-	-		-
VIC09	gl Si(15)	68.27	1.28	14.08	4.41	0.10	0.39	1.60	2.48	4.74	0.53	0.04	0.26	0.00	98.18	17.4	2.41	7.50	0.08
980	gl Fe(8)	32.37	5.73	3.94	22.43	0.58	5.53	11.99	1.57	0.58	10.20	-	0.54	0.44	95.89	30.0	3.00	3.73	1.78
	pl(9)	58.96	0.14	23.63	1.05	-	0.07	6.83	6.88	1.05	-	-	-	-	98.61	35.4	-		-
	aug(17)	49.44	1.15	1.98	13.69	0.48	14.81	16.93	0.38	0.05	-	-	-	-	98.91	42.7	-		-
	pig(4)	51.47	0.56	1.37	19.72	0.66	21.14	4.75	0.20	0.04	-	-	-	-	99.91	59.4	-		-
	mt(10)	0.20	14.52	1.91	75.59	0.43	2.10	0.14	0.01	0.05	-	-	-	-	94.97	-	-		-
VIC09	gl Si(22)	69.92	1.02	14.54	3.86	0.06	0.29	1.38	2.42	5.30	0.49	0.05	0.21	0.00	99.53	15.2	2.40	7.94	0.06
955	gl Fe(8)	30.52	6.10	3.33	23.78	0.57	5.49	12.19	1.39	0.50	10.93	-	0.61	0.54	95.95	28.6	3.04	4.10	1.90
	pl(9)	62.56	0.05	22.84	0.57	-	0.01	5.06	6.94	1.63	-	-	-	-	99.65	28.7	-		-
	aug(23)	49.88	1.24	1.98	14.48	0.52	14.03	16.10	0.37	0.06	-	-	-	-	98.66	41.6	-		-
	pig(5)	51.18	0.69	1.15	18.85	0.66	18.84	7.69	0.16	0.03	-	-	-	-	99.25	53.9	-		-
	mt(9)	0.19	15.17	1.77	75.04	0.47	2.04	0.13	0.03	0.05	-	-	-	-	94.88	-	-		-
VIC10	gl Si(20)	65.87	1.05	13.53	6.96	0.11	0.80	2.59	2.79	3.95	0.81	0.10	0.21	0.03	98.79	16.1	2.46	6.29	0.18
1021+12	gl Fe(11)	35.32	5.00	5.43	21.56	0.56	4.52	11.47	1.84	0.81	8.90	-	0.39	0.82	96.62	26.7	2.93	3.21	1.53
	pl(8)	60.21	0.12	23.89	0.98	-	0.06	6.81	6.51	1.10	-	-	-	-	99.67	36.6	-		-
	aug(17)	50.29	0.93	1.74	16.21	0.36	14.45	14.41	0.28	0.03	-	-	-	-	98.70	42.6	-		-
	pig(8)	51.71	0.55	1.14	20.82	0.39	19.04	5.43	0.12	0.02	-	-	-	-	99.22	55.0	-		-
	mt(9)	0.33	16.14	2.11	74.20	0.42	2.02	0.12	0.03	0.06	-	-	-	-	95.42	-	-		-
VIC10	gl Si(12)	66.47	1.39	13.29	5.98	0.10	0.68	2.32	2.54	4.19	0.61	0.11	0.22	0.00	97.90	16.5	2.44	6.61	0.15
1021+40	gl Fe(11)	33.88	4.17	5.53	21.74	0.51	4.43	12.39	1.86	0.83	10.84	1.45	0.39	0.58	98.60	26.1	2.93	2.91	1.61
	pl(9)	58.85	0.14	23.09	1.01	-	0.05	6.58	6.68	1.15	-	-	-	-	97.54	35.2	-		-
	aug(7)	48.57	1.07	1.80	17.04	0.51	14.55	15.00	0.30	0.02	-	-	-	-	98.86	41.7	-		-
	pig(18)	49.74	0.67	1.26	21.50	0.62	19.35	5.89	0.12	0.02	-	-	-	-	99.17	54.3	-		-
	mt(12)	0.22	16.74	1.92	73.19	0.42	2.13	0.15	0.02	0.05	-	-	-	-	94.83	-	-		-
VIC10	gl Si(8)	68.92	1.32	13.81	4.66	0.06	0.62	1.77	2.85	4.38	0.32	0.07	0.28	0.00	99.06	18.6	2.42	6.84	0.10
1021+158	gl Fe(21)	30.78	4.32	4.55	20.61	0.62	5.00	13.86	1.72	0.63	13.33	1.37	0.63	0.60	98.02	29.5	2.93	2.78	1.79
	pl(9)	59.94	0.13	23.85	1.00	-	0.07	6.84	6.86	1.12	-	-	-	-	99.80	35.5	-		-
	aug(10)	48.71	1.64	2.88	15.85	0.35	12.92	17.12	0.35	0.02	-	-	-	-	99.84	37.9	-		-
	pig(7)	50.72	0.81	1.60	22.55	0.49	18.93	5.07	0.11	0.01	-	-	-	-	100.29	53.7	-		-
	mt(16)	0.18	17.23	2.24	73.12	0.44	2.32	0.09	0.02	0.04	-	-	-	-	95.68	-	-		-
VIC06	gl Si(13)	65.99	1.27	13.32	7.55	0.10	0.78	3.39	2.51	3.70	0.64	0.13	0.23	0.00	99.63	14.5	2.48	6.58	0.20
1000+18*	gl Fe(13)	38.70	5.45	5.96	23.47	0.61	3.68	11.39	1.58	0.72	5.89	-	0.59	0.30	98.34	21.4	2.96	3.78	1.42
	pl(10)	59.64	0.15	24.68	0.93	-	0.06	7.42	6.20	0.90	-	-	-	-	99.99	39.8	-		-
	ol(16)	34.84	0.17	0.53	42.80	0.67	18.16	0.68	0.09	0.10	-	-	-	-	98.05	43.1	-		-
	aug (12)	48.43	1.72	2.80	16.02	0.42	11.94	17.54	0.41	0.05	-	-	-	-	99.33	35.6	-		-

Continued from previous page

Run	Phase (no. of grains analysed)	Oxide (wt.%)														An/Fo/Mg #	Density (g/cm^3)	Viscosity log η (Pas)	NBO/T
		SiO_2	TiO_2	Al_2O_3	FeO	MnO	MgO	CaO	Na_2O	K_2O	P_2O_5	Y_2O_3	ZrO_2	Ce_2O_3	Total				
	pig(6)	50.50	1.02	1.84	23.36	0.55	18.07	5.19	0.11	0.01	-	-	-	-	100.65	51.8	-		-
	mt(9)	0.38	18.06	2.03	72.14	0.39	1.82	0.15	0.02	0.06	-	-	-	-	95.05	-	-		-
VIC07	gl Si(17)	69.75	1.20	13.94	4.41	0.08	0.42	1.52	2.42	4.54	0.49	0.05	0.19	0.00	99.01	13.6	2.41	7.31	0.07
1000+62	gl Fe(10)	29.91	5.81	4.21	22.25	0.51	5.00	12.59	1.519	0.57	11.91	-	0.61	0.88	94.28	28.1	3.00	3.34	1.82
	pl(10)	58.78	0.13	24.09	1.04	-	0.06	7.23	6.24	0.96	-	-	-	-	98.53	39.0	-		-
	aug(10)	49.85	0.94	1.83	13.93	0.37	15.23	16.31	0.35	0.04	-	-	-	-	98.85	43.8	-		-
	pig(6)	51.67	0.61	1.16	19.21	0.46	19.30	7.49	0.15	0.02	-	-	-	-	100.07	54.4	-		-
	mt(8)	0.20	14.79	1.75	75.14	0.34	2.04	0.14	0.03	0.05	-	-	-	-	94.48	-	-		-
VIC07	gl Si(16)	71.12	1.05	13.86	4.14	0.06	0.41	1.31	2.32	4.59	0.32	0.04	0.31	0.00	99.54	14.6	2.40	7.42	0.06
1000+182	gl Fe(9)	27.51	5.20	3.51	21.28	0.54	4.96	13.78	1.56	0.51	14.60	-	0.67	1.81	95.92	28.8	2.98	3.10	1.94
	pl(9)	59.68	0.14	24.19	1.06	-	0.06	6.94	6.48	1.09	-	-	-	-	99.64	37.1	-		-
	aug(9)	50.15	1.12	1.81	15.51	0.36	14.43	15.42	0.32	0.05	-	-	-	-	99.17	42.1	-		-
	pig(6)	52.11	0.69	1.14	18.99	0.46	20.58	6.04	0.12	0.02	-	-	-	-	100.15	57.8	-		-
	mt(14)	0.21	17.32	1.55	72.64	0.42	2.17	0.12	0.02	0.05	-	-	-	-	94.49	-	-		-

Run	Phase (no. of grains analysed)	Standard deviation of EPMA analyses population												
		SiO_2	TiO_2	Al_2O_3	FeO	MnO	MgO	CaO	Na_2O	K_2O	P_2O_5	Y_2O_3	ZrO_2	Ce_2O_3
VIC08	gl(17)	1.07	0.32	0.23	0.55	0.03	0.22	0.28	0.19	0.15	0.12	0.08	0.08	0.00
1050	pl(9)	0.63	0.02	0.46	0.03	-	0.05	0.49	0.25	0.07	-	-	-	-
	aug(6)	0.37	0.05	0.41	0.76	0.03	0.76	1.59	0.04	0.01	-	-	-	-
	pig(5)	0.27	0.08	0.33	0.46	0.03	1.23	1.79	0.05	0.01	-	-	-	-
	mt(8)	0.12	0.95	0.41	1.31	0.03	0.17	0.04	0.01	0.01	-	-	-	-
VIC06	gl(17)	0.65	0.19	0.56	0.66	0.04	0.16	0.30	0.16	0.12	0.08	0.04	0.08	0.00
1030*	pl(8)	0.68	0.02	0.27	0.12	-	0.02	0.36	0.16	0.11	-	-	-	-
	ol(8)	0.22	0.01	0.14	0.48	0.03	0.32	0.04	0.02	0.01	-	-	-	-
	aug(7)	0.30	0.23	0.35	1.53	0.03	1.28	2.75	0.06	0.01	-	-	-	-
	pig(12)	0.76	0.20	0.52	0.85	0.05	1.00	1.54	0.03	0.01	-	-	-	-
	tmt(10)	2.27	1.32	0.57	0.99	0.06	0.14	0.11	0.14	0.11	-	-	-	-
	mt(9)	1.34	0.94	0.48	1.06	0.06	0.12	0.08	0.10	0.08	-	-	-	-
VIC08	gl Si(19)	1.19	0.16	0.38	0.47	0.04	0.17	0.26	0.13	0.13	0.11	0.07	0.07	0.00
1025	gl Fe(9)	1.25	0.90	0.33	0.39	0.04	0.23	0.54	0.12	0.11	0.97	0.13	0.16	0.08
	pl(9)	0.73	0.03	0.64	0.09	-	0.03	0.46	0.20	0.09	-	-	-	-
	aug(12)	0.50	0.14	0.19	1.03	0.04	1.11	1.68	0.07	0.04	-	-	-	-
	pig(4)	0.63	0.05	0.13	0.48	0.07	0.57	0.88	0.01	0.01	-	-	-	-
	mt(12)	1.59	0.90	0.33	1.86	0.05	0.16	0.38	0.18	0.07	-	-	-	-
VIC08	gl Si(18)	0.88	0.18	0.43	0.52	0.04	0.27	0.31	0.23	0.19	0.14	0.04	0.04	0.00
1010	gl Fe(9)	0.74	1.17	0.26	0.37	0.04	0.27	0.46	0.14	0.08	1.03	-	0.14	0.10
	pl(9)	1.05	0.04	0.76	0.11	-	0.03	0.64	0.20	0.18	-	-	-	-
	aug(12)	0.40	0.17	0.25	1.19	0.05	1.02	2.02	0.05	0.02	-	-	-	-
	pig(12)	0.48	0.13	0.24	1.27	0.07	1.12	1.94	0.05	0.02	-	-	-	-
	mt(13)	0.22	0.61	0.11	0.63	0.06	0.08	0.03	0.02	0.02	-	-	-	-
VIC06	gl Si(14)	1.18	0.32	0.57	0.69	0.03	0.20	0.40	0.32	0.17	0.12	0.04	0.06	0.00
1010*	gl Fe(10)	1.01	0.85	0.36	0.32	0.08	0.29	0.44	0.13	0.07	0.90	-	0.09	0.12
	pl(8)	0.25	0.02	0.23	0.05	-	0.01	0.21	0.18	0.08	-	-	-	-
	ol(11)	0.25	0.02	0.04	0.62	0.03	0.43	0.05	0.01	0.02	-	-	-	-
	aug(9)	1.13	0.42	0.99	0.50	0.03	0.49	0.53	0.02	0.01	-	-	-	-
	pig(6)	0.52	0.17	0.70	1.01	0.04	0.66	0.80	0.03	0.01	-	-	-	-
	mt(12)	0.22	0.96	0.34	1.06	0.08	0.07	0.04	0.01	0.02	-	-	-	-

Continued from previous page

Run	Phase (no. of grains analysed)	Standard deviation of EPMA analyses population												
		SiO_2	TiO_2	Al_2O_3	FeO	MnO	MgO	CaO	Na_2O	K_2O	P_2O_5	Y_2O_3	ZrO_2	Ce_2O_3
VIC07	gl Si(20)	0.94	0.35	0.31	0.39	0.03	0.29	0.16	0.20	0.14	0.12	0.04	0.07	0.00
1005	gl Fe(10)	0.74	0.62	0.18	0.33	0.05	0.20	0.29	0.07	0.04	0.57	-	0.15	0.10
	pl(8)	0.45	0.03	0.23	0.10	-	0.02	0.24	0.08	0.04	-	-	-	-
	aug(21)	0.80	0.18	0.49	2.00	0.08	0.93	2.16	0.08	0.09	-	-	-	-
	pig(8)	0.35	0.11	0.40	1.01	0.04	1.39	1.46	0.10	0.07	-	-	-	-
	mt(11)	0.10	0.41	0.07	0.53	0.04	0.08	0.04	0.02	0.02	-	-	-	-
VIC09	gl Si(21)	1.14	0.31	0.72	0.43	0.04	0.32	0.23	0.22	0.14	0.16	0.05	0.09	0.00
1000	gl Fe(10)	1.28	0.55	0.35	0.35	0.06	0.26	0.43	0.09	0.09	0.80	-	0.09	0.19
	pl(8)	0.79	0.03	0.55	0.10	-	0.03	0.55	0.24	0.11	-	-	-	-
	aug(17)	0.73	0.18	0.17	0.67	0.06	0.90	1.28	0.05	0.03	-	-	-	-
	pig(8)	0.43	0.08	0.22	1.50	0.05	0.84	1.08	0.03	0.02	-	-	-	-
	mt(8)	0.05	0.85	0.13	0.97	0.05	0.04	0.01	0.01	0.01	-	-	-	-
VIC09	gl Si(15)	0.95	0.20	0.38	0.55	0.04	0.25	0.21	0.22	0.15	0.10	0.02	0.06	0.00
980	gl Fe(8)	1.88	0.86	0.63	1.04	0.07	0.56	0.92	0.20	0.12	1.60	-	0.06	0.22
	pl(9)	0.99	0.03	0.74	0.06	-	0.01	0.73	0.46	0.16	-	-	-	-
	aug(17)	0.62	0.27	0.35	0.82	0.05	0.90	1.48	0.10	0.04	-	-	-	-
	pig(4)	0.35	0.05	0.16	0.29	0.03	0.45	0.43	0.01	0.01	-	-	-	-
	mt(10)	0.06	0.63	0.13	0.90	0.04	0.11	0.04	0.01	0.02	-	-	-	-
VIC09	gl Si(22)	0.72	0.27	0.62	0.27	0.03	0.19	0.14	0.27	0.12	0.09	0.04	0.12	0.00
955	gl Fe(8)	1.48	1.64	0.27	0.92	0.06	0.86	1.10	0.11	0.08	2.37	-	0.14	0.22
	pl(9)	0.52	0.07	0.42	0.19	-	0.00	0.34	0.15	0.14	-	-	-	-
	aug(23)	1.19	0.32	0.35	0.82	0.07	1.12	1.59	0.08	0.05	-	-	-	-
	pig(5)	0.46	0.17	0.31	0.71	0.06	1.42	1.70	0.04	0.02	-	-	-	-
	mt(9)	0.07	0.30	0.25	0.54	0.06	0.21	0.05	0.02	0.01	-	-	-	-
VIC10	gl Si(20)	1.51	0.29	0.58	0.86	0.04	0.36	0.31	0.25	0.14	0.15	0.06	0.11	0.00
1021+12	gl Fe(11)	1.17	1.10	0.63	0.81	0.07	0.27	0.46	0.12	0.17	1.31	-	0.15	0.19
	pl(8)	0.75	0.01	0.43	0.05	-	0.01	0.50	0.24	0.12	-	-	-	-
	aug(17)	0.52	0.15	0.23	1.04	0.06	1.05	1.99	0.05	0.02	-	-	-	-
	pig(8)	0.48	0.10	0.31	1.08	0.07	1.11	1.19	0.04	0.02	-	-	-	-
	mt(9)	0.25	2.32	0.24	1.66	0.05	0.25	0.02	0.03	0.01	-	-	-	-
VIC10	gl Si(12)	1.15	0.26	0.33	0.58	0.04	0.23	0.29	0.31	0.13	0.14	0.04	0.07	0.00
1021+40	gl Fe(11)	3.09	1.26	1.23	1.21	0.10	0.59	1.16	0.29	0.19	2.28	0.14	0.09	0.08
	pl(9)	1.06	0.01	0.82	0.06	-	0.01	0.81	0.32	0.22	-	-	-	-
	aug(7)	0.44	0.24	0.23	1.24	0.05	1.02	2.20	0.06	0.01	-	-	-	-
	pig(18)	0.56	0.12	0.13	0.68	0.06	1.27	1.62	0.04	0.02	-	-	-	-
	mt(12)	0.07	0.48	0.13	0.47	0.04	0.14	0.04	0.02	0.03	-	-	-	-
VIC10	gl Si(8)	1.10	0.19	0.20	0.39	0.04	0.16	0.22	0.24	0.11	0.14	0.04	0.05	0.00
1021+158	gl Fe(21)	3.51	1.29	1.15	1.31	0.19	0.44	1.42	0.25	0.24	2.81	0.53	0.24	0.23
	pl(9)	0.98	0.03	0.74	0.06	-	0.01	0.76	0.28	0.23	-	-	-	-
	aug(10)	0.49	0.22	0.55	0.64	0.02	0.51	0.91	0.02	0.01	-	-	-	-
	pig(7)	0.61	0.16	0.36	0.74	0.07	0.98	0.74	0.03	0.01	-	-	-	-
	mt(16)	0.08	0.95	0.13	1.04	0.04	0.19	0.03	0.02	0.02	-	-	-	-
VIC06	gl Si(13)	1.06	0.12	0.55	0.92	0.04	0.43	0.55	0.13	0.22	0.10	0.03	0.05	0.00
1000+18*	gl Fe(13)	1.22	0.98	0.49	0.70	0.10	0.21	0.63	0.14	0.06	0.54	-	0.12	0.08
	pl(10)	1.02	0.02	0.73	0.06	-	0.01	0.58	0.26	0.13	-	-	-	-
	ol(16)	1.36	0.05	0.79	1.43	0.04	0.83	0.39	0.10	0.13	-	-	-	-
	aug (12)	0.71	0.34	0.46	0.76	0.04	1.04	1.59	0.08	0.05	-	-	-	-
	pig(6)	0.58	0.14	0.18	0.34	0.05	1.36	1.92	0.03	0.01	-	-	-	-
	mt(9)	0.31	1.05	0.36	0.93	0.04	0.12	0.10	0.01	0.02	-	-	-	-
VIC07	gl Si(17)	0.84	0.30	0.44	0.28	0.03	0.24	0.11	0.22	0.11	0.07	0.05	0.07	0.00

Continued from previous page

Run	Phase (no. of grains analysed)	Standard deviation of EPMA analyses population												
		SiO_2	TiO_2	Al_2O_3	FeO	MnO	MgO	CaO	Na_2O	K_2O	P_2O_5	Y_2O_3	ZrO_2	Ce_2O_3
1000+62	gl Fe(10)	3.01	0.70	2.46	0.74	0.06	0.29	1.24	0.07	0.13	2.61	-	0.13	0.28
	pl(10)	0.85	0.01	0.77	0.04	-	0.01	0.82	0.28	0.16	-	-	-	-
	aug(10)	1.20	0.09	0.16	1.23	0.04	0.69	1.47	0.06	0.01	-	-	-	-
	pig(6)	0.62	0.14	0.31	0.72	0.06	1.14	1.51	0.05	0.01	-	-	-	-
	mt(8)	0.19	0.64	0.16	0.32	0.03	0.12	0.08	0.03	0.01	-	-	-	-
VIC07	gl Si(16)	0.87	0.21	0.38	0.23	0.04	0.20	0.11	0.17	0.11	0.07	0.04	0.09	0.00
1000+182	gl Fe(9)	1.56	1.46	0.44	0.85	0.06	0.34	1.15	0.19	0.11	2.48	-	0.29	0.59
	pl(9)	0.83	0.02	0.91	0.12	-	0.03	0.80	0.31	0.23	-	-	-	-
	aug(9)	0.58	0.22	0.34	1.23	0.06	1.15	1.92	0.05	0.02	-	-	-	-
	pig(6)	0.55	0.26	0.26	1.18	0.04	1.28	1.72	0.04	0.01	-	-	-	-
	mt(14)	0.06	1.13	0.16	1.31	0.06	0.21	0.02	0.02	0.02	-	-	-	-

Appendix Table 3.A EPMA transects across large plagioclase phenocrysts in the centre of the Tynemouth Dyke (sample T7)

Plagioclase phenocryst transect	Oxide (wt.%)											3σ counting statistic uncertainties from EPMA							
	Na_2O	MgO	SiO_2	Al_2O_3	K_2O	TiO_2	FeO	CaO	Total	An#	Distance (μm)	Na	Mg	Si	Al	K	Ti	Fe	Ca
Transect 1	4.90	0.12	54.67	27.33	0.41	0.10	1.23	11.50	100.25	52.27	0	0.30	0.01	1.52	0.73	0.06	0.01	0.10	0.56
Transect 1	4.68	0.11	54.10	27.37	0.40	0.09	1.24	11.44	99.42	53.29	21	0.29	0.01	1.51	0.74	0.06	0.01	0.10	0.55
Transect 1	4.63	0.11	54.61	27.11	0.39	0.09	1.28	11.32	99.56	53.31	41	0.29	0.01	1.52	0.73	0.06	0.01	0.11	0.55
Transect 1	4.52	0.10	54.84	27.27	0.45	0.09	1.34	11.22	99.85	53.50	62	0.28	0.01	1.53	0.73	0.06	0.01	0.11	0.55
Transect 1	4.18	0.11	54.29	27.14	0.43	0.09	1.30	11.42	98.97	55.85	83	0.26	0.01	1.51	0.73	0.06	0.01	0.11	0.55
Transect 1	4.01	0.11	54.30	27.09	0.44	0.09	1.32	11.62	98.97	57.21	103	0.26	0.01	1.51	0.73	0.06	0.01	0.11	0.56
Transect 1	3.92	0.11	54.60	27.29	0.39	0.09	1.21	11.45	99.10	57.52	124	0.25	0.01	1.52	0.73	0.06	0.01	0.10	0.55
Transect 1	3.75	0.11	54.54	27.28	0.41	0.10	1.36	11.18	98.72	57.89	145	0.24	0.01	1.52	0.73	0.06	0.01	0.11	0.54
Transect 1	3.55	0.11	55.13	27.35	0.42	0.10	1.25	11.56	99.54	59.89	166	0.23	0.01	1.54	0.74	0.06	0.01	0.10	0.56
Transect 1	3.33	0.12	54.93	27.61	0.38	0.08	1.34	11.67	99.51	61.68	186	0.22	0.01	1.53	0.74	0.05	0.01	0.11	0.56
Transect 1	3.11	0.11	54.72	27.69	0.43	0.09	1.26	12.09	99.52	63.79	207	0.21	0.01	1.52	0.74	0.06	0.01	0.11	0.58
Transect 1	2.96	0.11	54.90	27.56	0.44	0.09	1.35	11.49	98.90	63.64	228	0.20	0.01	1.53	0.74	0.06	0.01	0.11	0.56
Transect 1	2.93	0.11	55.23	27.50	0.37	0.09	1.28	11.39	98.90	63.94	248	0.20	0.01	1.54	0.74	0.06	0.01	0.11	0.55
Transect 1	2.85	0.11	55.26	27.46	0.41	0.09	1.33	11.64	99.19	64.88	269	0.20	0.01	1.54	0.74	0.06	0.01	0.11	0.56
Transect 1	2.69	0.11	55.71	27.55	0.43	0.10	1.30	11.48	99.43	65.69	290	0.19	0.01	1.55	0.74	0.06	0.01	0.11	0.56
Transect 1	2.38	0.12	55.02	27.46	0.39	0.10	1.27	11.54	98.27	68.47	310	0.18	0.01	1.53	0.74	0.06	0.01	0.10	0.56
Transect 1	2.50	0.11	55.35	27.74	0.39	0.10	1.34	11.46	99.05	67.34	331	0.18	0.01	1.54	0.74	0.06	0.01	0.11	0.56
Transect 1	2.27	0.11	55.61	27.79	0.34	0.10	1.30	11.51	99.05	69.55	352	0.17	0.01	1.55	0.75	0.05	0.01	0.11	0.56
Transect 1	2.22	0.11	55.84	27.46	0.36	0.09	1.34	11.64	99.12	70.13	372	0.17	0.01	1.55	0.74	0.05	0.01	0.11	0.56
Transect 1	2.15	0.12	55.67	27.53	0.39	0.11	1.29	11.79	99.05	70.85	393	0.16	0.01	1.55	0.74	0.06	0.01	0.11	0.57
Transect 1	2.05	0.12	56.07	27.53	0.35	0.09	1.33	11.74	99.30	71.85	414	0.16	0.01	1.56	0.74	0.05	0.01	0.11	0.57
Transect 1	1.93	0.12	55.71	27.54	0.35	0.09	1.25	11.89	98.90	73.18	434	0.15	0.01	1.55	0.74	0.05	0.01	0.11	0.57
Transect 1	1.83	0.13	56.43	27.59	0.35	0.09	1.33	11.69	99.44	73.82	455	0.15	0.01	1.57	0.74	0.05	0.01	0.11	0.56
Transect 1	1.72	0.12	56.12	27.94	0.31	0.10	1.34	11.59	99.30	74.93	476	0.14	0.01	1.56	0.75	0.05	0.01	0.11	0.56
Transect 1	1.61	0.11	55.92	27.97	0.34	0.09	1.37	11.82	99.25	76.23	497	0.13	0.01	1.56	0.75	0.05	0.01	0.11	0.57
Transect 1	1.67	0.12	56.31	28.07	0.32	0.10	1.35	11.56	99.49	75.35	517	0.14	0.01	1.57	0.75	0.05	0.01	0.11	0.56
Transect 1	1.55	0.12	56.12	28.12	0.31	0.09	1.34	11.81	99.45	76.96	538	0.13	0.01	1.56	0.75	0.05	0.01	0.11	0.57
Transect 1	1.37	0.11	56.45	28.19	0.31	0.10	1.39	11.69	99.60	78.76	559	0.12	0.01	1.57	0.76	0.05	0.01	0.11	0.56
Transect 1	1.42	0.12	56.58	28.16	0.28	0.10	1.25	11.76	99.65	78.44	579	0.12	0.01	1.57	0.75	0.05	0.01	0.11	0.57
Transect 1	1.37	0.12	56.63	28.17	0.29	0.08	1.34	11.61	99.61	78.76	600	0.12	0.01	1.58	0.75	0.05	0.01	0.11	0.56
Transect 2	2.72	0.25	49.76	31.14	0.16	0.03	0.73	15.39	100.25	72.86	0	0.19	0.01	1.39	0.83	0.04	0.01	0.08	0.71

Continued from previous page

Plagioclase phenocryst transect	Oxide (wt.%)											3σ counting statistic uncertainties from EPMA							
	Na_2O	MgO	SiO_2	Al_2O_3	K_2O	TiO_2	FeO	CaO	Total	An#	Distance (μm)	Na	Mg	Si	Al	K	Ti	Fe	Ca
Transect 2	2.73	0.25	49.85	30.83	0.14	0.02	0.71	14.96	99.49	72.34	4	0.19	0.01	1.39	0.82	0.04	0.01	0.08	0.69
Transect 2	2.60	0.27	49.59	31.02	0.12	0.02	0.70	15.33	99.65	73.82	9	0.18	0.01	1.38	0.83	0.04	0.01	0.08	0.71
Transect 2	2.61	0.25	49.92	31.15	0.11	0.03	0.67	15.13	99.92	73.51	14	0.18	0.01	1.39	0.83	0.04	0.01	0.08	0.70
Transect 2	2.56	0.25	50.07	30.92	0.15	0.02	0.64	15.35	99.98	73.97	18	0.18	0.01	1.40	0.82	0.04	0.01	0.08	0.71
Transect 2	2.24	0.24	50.15	31.15	0.14	0.02	0.68	14.92	99.57	75.90	24	0.17	0.01	1.40	0.83	0.04	0.01	0.08	0.69
Transect 2	2.11	0.26	50.18	30.97	0.15	0.03	0.64	15.13	99.47	77.12	29	0.16	0.01	1.40	0.83	0.04	0.01	0.08	0.70
Transect 2	1.89	0.26	50.49	30.91	0.13	0.03	0.63	14.95	99.30	78.81	34	0.15	0.01	1.41	0.82	0.04	0.01	0.08	0.69
Transect 2	1.80	0.26	50.23	30.43	0.13	0.03	0.67	14.87	98.42	79.56	40	0.14	0.01	1.40	0.81	0.04	0.01	0.08	0.69
Transect 2	1.59	0.27	50.69	31.11	0.11	0.03	0.72	14.97	99.61	81.64	46	0.13	0.01	1.41	0.83	0.04	0.01	0.08	0.69
Transect 3	3.34	0.19	50.75	29.90	0.23	0.05	0.81	13.97	99.24	66.34	0	0.22	0.01	1.42	0.80	0.05	0.01	0.09	0.65
Transect 3	3.32	0.20	50.85	29.64	0.21	0.04	0.86	14.10	99.23	66.78	19	0.22	0.01	1.42	0.79	0.04	0.01	0.09	0.66
Transect 3	3.27	0.20	50.85	29.71	0.21	0.04	0.81	14.33	99.41	67.45	37	0.22	0.01	1.42	0.79	0.05	0.01	0.09	0.67
Transect 3	3.12	0.20	50.65	29.56	0.18	0.05	0.82	14.01	98.64	68.05	56	0.21	0.01	1.41	0.79	0.04	0.01	0.09	0.66
Transect 3	3.25	0.21	50.50	29.46	0.18	0.03	0.78	14.30	98.75	67.63	75	0.22	0.01	1.41	0.79	0.04	0.01	0.08	0.67
Transect 3	3.08	0.21	50.70	29.84	0.21	0.04	0.78	14.03	98.89	68.21	94	0.21	0.01	1.42	0.80	0.04	0.01	0.08	0.66
Transect 3	2.73	0.20	50.88	29.68	0.22	0.03	0.79	14.35	98.88	71.14	112	0.19	0.01	1.42	0.79	0.05	0.01	0.09	0.67
Transect 3	2.71	0.20	50.94	29.84	0.21	0.04	0.80	14.18	98.91	71.09	131	0.19	0.01	1.42	0.80	0.04	0.01	0.08	0.66
Transect 3	2.42	0.20	50.88	30.11	0.22	0.06	0.80	13.94	98.67	72.84	150	0.18	0.01	1.42	0.80	0.04	0.01	0.09	0.65
Transect 3	2.26	0.20	51.33	29.95	0.23	0.05	0.86	14.21	99.09	74.45	169	0.17	0.01	1.43	0.80	0.05	0.01	0.09	0.66
Transect 3	2.17	0.20	51.11	30.20	0.20	0.04	0.77	14.22	98.91	75.34	187	0.16	0.01	1.43	0.81	0.04	0.01	0.09	0.66
Transect 3	2.01	0.20	51.58	29.79	0.20	0.04	0.79	14.20	98.90	76.61	206	0.16	0.01	1.44	0.80	0.04	0.01	0.08	0.66

Appendix Table 4.A EPMA (wt.% oxide) of glass and minerals in samples from the 1976 and 1981 drill cores from the Kilauea Iki lava lake (KI); Snake River Plain (SRP) tholeiite in the USA and the Laki eruption in Iceland. The degree of polymerisation is parameterised as NBO/T, where T = Si + Al + P + Ti wt. %.

Samples (no. of analyses)	Sample depth from core top (m)	Temperature °C (Putrika 2008)	SiO_2	TiO_2	Al_2O_3	FeO	MnO	MgO	CaO	Na_2O	K_2O	P_2O_5	Total	NBO/T	Density (g/m^3)	Mg#/Fo#/An#
KI76 149 Si-rich glass (17)	45.4	1112	49.90 (0.3)	5.29 (0.1)	12.17 (0.1)	12.39 (0.1)	0.18 (0.1)	4.48 (0.1)	7.89 (0.1)	2.18 (0.3)	1.18 (0.1)	0.79 (0.1)	-	0.63	2.71	-
KI76 149 Fe-rich glass (5)	45.4	1112	40.42 (1.6)	10.18 (0.5)	3.96 (1.0)	21.41 (1.)	0.32 (0.02)	8.35 (0.3)	10.14 (0.3)	0.91 (0.1)	0.36 (0.2)	1.49 (0.1)	-	1.52	3.00	
KI76 149 Plagioclase (8)	45.4	-	48.08 (0.2)	0.13 (0.01)	30.46 (0.3)	0.94 (0.05)	-	0.10 (0.01)	15.12 (0.6)	2.80 (0.2)	0.12 (0.01)	-	-	-	-	83
KI76 149 Olivine (8)	45.4	-	37.53 (0.5)	0.23 (0.1)	-	22.71 (1.2)	-	38.11 (1.1)	0.19 (0.03)	-	-	-	-	-	-	57
KI76 149 Pyroxene (8)	45.4	-	50.544 (0.3)	9.10 (0.7)	2.27 (0.3)	7.15 (0.6)	-	16.29 (0.1)	12.67 (0.2)	0.11 (0.01)	-	-	-	-	-	64
KI76 147 Si-rich glass (45)	44.8	1090	54.22 (0.5)	3.99 (0.1)	12.55 (0.2)	11.88 (0.3)	0.19 (0.1)	3.62 (0.1)	6.94 (0.1)	2.87 (0.4)	1.60 (0.01)	0.91 (0.01)	-	0.54	2.61	
KI76 145 Plagioclase (8)	44.2	1073	51.67 (1.8)	0.14 (0.02)	28.09 (1.2)	0.89 (0.06)	-	0.09 (0.01)	12.26 (1.3)	4.17 (0.7)	0.23 (0.07)	-	-	-	-	73
KI76 145 Olivine (8)	44.2	1073	36.39 (0.7)	0.19 (0.06)	-	28.82 (3.4)	0.43 (0.04)	33.31 (2.6)	0.17 (0.02)	-	-	-	-	-	-	47
KI76 145 Pyroxene (8)	44.2	1073	50.52 (0.5)	9.73 (1.1)	2.21 (0.3)	7.98 (0.9)	-	16.11 (0.2)	12.32 (0.4)	0.11 (0.01)	-	-	-	-	-	61
KI76 143 Si-rich glass (9)	43.7	1054	56.29 (0.7)	2.16 (0.1)	12.93 (0.4)	10.27 (0.5)	-	2.26 (0.1)	5.17 (0.2)	2.84 (0.3)	2.30 (0.1)	1.59 (0.1)	-	0.40	2.54	
KI76 143 Plagioclase (8)	43.7	1054	50.19 (2.2)	0.10 (0.02)	29.57 (1.6)	0.89 (0.06)	-	0.09 (0.01)	13.96 (1.9)	3.34 (0.9)	0.19 (0.1)	-	-	-	-	79

Continued from previous page

Samples (no. of analyses)	Sample depth from core top (m)	Temperature °C (Putrika 2008)	SiO_2	TiO_2	Al_2O_3	FeO	MnO	MgO	CaO	Na_2O	K_2O	P_2O_5	Total	NBO/T	Density (g/m^3)	Mg#/Fo#/An#
KI76 143 Olivine (8)	43.7	1054	35.54 (0.5)	0.37 (0.08)	-	34.49 (1.8)	0.46 (0.01)	28.73 (1.3)	0.19 (0.01)	-	-	-	-	-	-	39
KI76 143 Pyroxene (8)	43.7	1054	51.19 (0.6)	8.65 (2.3)	1.78 (0.6)	10.41 (3.7)	-	17.06 (2.5)	10.55 (3.7)	0.10 (0.01)	-	-	-	-	-	56
KI76 140 Si-rich glass (8)	42.8	1017	63.43 (3.2)	1.25 (0.2)	14.14 (0.8)	5.47 (0.8)	-	0.87 (0.2)	2.78 (1.4)	3.05 (0.4)	3.35 (0.7)	0.79 (1.1)	-	0.15	2.45	
KI76 140 Fe-rich glass	42.8	1017	40.86	7.51	6.38	26.70	-	7.30	7.88	1.41	0.58	1.03	99.64	1.46	3.06	
KI76 140 Plagioclase (8)	42.8	1017	52.31 (3.1)	0.12 (0.03)	28.07 (1.87)	0.86 (0.07)	-	-	12.08 (2.29)	4.34 (1.1)	0.31 (0.18)	-	-	-	-	71
KI76 140 Olivine (8)	42.8	1017	36.28 (0.6)	0.30 (0.09)	-	31.61 (1.9)	0.39 (0.01)	31.54 (1.5)	0.17 (0.01)	-	-	-	-	-	-	44
KI76 140 Pyroxene (8)	42.8	1017	51.36 (0.3)	9.35 (0.8)	2.17 (0.3)	7.73 (0.9)	-	16.34 (0.1)	12.64 (0.4)	0.10 (0.01)	-	-	-	-	-	62
KI81 249.7 Plagioclase (8)	76.1	-	48.72 (0.7)	0.14 (0.1)	30.72 (0.8)	0.93 (0.3)	-	0.22 (0.19)	15.15 (0.5)	2.57 (0.3)	0.12 (0.02)	-	-	-	-	84
KI81 249.7 Olivine (8)	76.1	-	38.66 (0.3)	0.02 (0.01)	-	18.60 (0.1)	-	41.46 (0.1)	0.20 (0.02)	-	-	-	-	-	-	63
KI81 219.8 Plagioclase (8)	66.9	-	49.40 (1.0)	0.12 (0.01)	30.07 (0.5)	0.71 (0.04)	-	0.17 (0.01)	14.79 (0.6)	2.87 (0.4)	0.12 (0.02)	-	-	-	-	83
KI81 219.8 Olivine (8)	66.9	-	38.47 (0.3)	0.02 (0.01)	-	18.75 (0.1)	-	41.10 (0.2)	0.23 (0.02)	-	-	-	-	-	-	63
KI81 205.4 Plagioclase (8)	62.6	-	51.17 (0.3)	0.14 (0.01)	28.66 (0.1)	0.63 (0.1)	-	0.18 (0.01)	13.53 (0.1)	3.63 (0.1)	0.17 (0.01)	-	-	-	-	77
KI81 205.4 Olivine (8)	62.6	-	38.42 (0.4)	0.02 (0.01)	-	18.84 (0.2)	-	41.33 (0.2)	0.23 (0.01)	-	-	-	-	-	-	63
KI81 192.8 Plagioclase (8)	58.8	-	49.70 (1.9)	0.09 (0.02)	29.76 (1.1)	0.86 (0.1)	-	0.15 (0.1)	14.13 (1.3)	3.16 (0.7)	0.14 (0.03)	-	-	-	-	80
KI81 192.8 Olivine (8)	58.8	-	38.91 (0.3)	0.02 (0.01)	-	20.25 (0.3)	-	40.3 (0.4)	0.20 (0.01)	-	-	-	-	-	-	61
KI81 192.8 Pyroxene (8)	58.8	-	51.41 (0.4)	0.81 (0.1)	4.78 (0.5)	6.84 (0.6)	-	16.46 (0.1)	15.01 (0.1)	0.2 (0.01)	-	-	-	-	-	65
SRP 299 Si-rich glass (101)	91.3	1096	48.08 (0.5)	3.90 (0.1)	11.45 (0.2)	16.41 (0.3)	0.34 (0.1)	3.85 (0.2)	8.63 (0.2)	2.35 (0.1)	1.78 (0.1)	1.72 (0.03)	-	0.80	2.76	
SRP 299 Fe-rich glass (3)	91.3	1096	42.18 (3.8)	5.94 (1.1)	5.86 (2.5)	23.47 (3.6)	0.40 (0.1)	5.53 (0.9)	10.36 (1.3)	1.58 (0.5)	0.79 (0.5)	2.59 (0.6)	-	1.42	2.95	
SRP 298 Si-rich glass (92)	90.8	1093	48.25 (0.5)	3.94 (0.1)	11.43 (0.2)	16.45 (0.3)	0.33 (0.1)	3.77 (0.1)	8.68 (0.1)	2.45 (0.2)	1.82 (0.1)	1.74 (0.1)	-	0.80	2.75	
SRP 298 Fe-rich glass (9)	90.8	1093	43.81 (2.4)	5.33 (0.5)	7.17 (1.3)	21.33 (2.2)	0.48 (0.1)	4.77 (0.6)	10.02 (0.7)	1.94 (0.4)	1.17 (0.4)	2.38 (0.3)	-	1.23	2.89	
LAKI 04 Si-rich glass (181)	-	1114	49.24 (0.5)	3.94 (0.1)	11.46 (0.2)	15.92 (0.3)	0.27 (0.1)	4.55 (0.1)	9.07 (0.1)	2.79 (0.2)	0.58 (0.03)	0.55 (0.02)	98.37	0.80	2.76	
LAKI 04 Fe-rich glass (13)	-	1114	47.63 (1.2)	4.81 (0.5)	8.61 (1.1)	19.17 (1.5)	0.29 (0.04)	5.56 (0.6)	9.56 (0.4)	2.13 (0.3)	0.49 (0.1)	0.65 (0.1)	98.89	1.05	2.84	

Appendix Table 4.B Average measurements of Fe-rich CBL thickness and plagioclase outer rim thickness, made on BSE images. Note that the grains are randomly oriented, so these thicknesses are likely to be greater than the true 3D thickness.

Sample (no. of analyses)	Depth in drillcore (m)	Plag major axis (μm)	Plag minor axis (μm)	Aspect ratio	Fe-rich rim perpendicular to (001) (μm)	Fe-rich rim perpendicular to (010) (μm)	Ratio	Plag rim perpendicular to (001) (μm)	Plag rim perpendicular to (010) (μm)	Ratio
KI76 149 average (48)	45.4	65.5	17.2	4.2 (2.1)	1.0	0.5	2.0 (0.8)	1.3	0.6	2.5 (1.3)
KI76 147 average (51)	44.8	82.4	16.9	5.3 (2.8)	0.6	0.3	2.3 (1.2)	0.9	0.4	2.7 (1.6)
KI76 145 average (55)	44.3	79.2	14.3	6.0 (3.2)	0.4	0.2	2.5 (1.5)	0.7	0.3	2.1 (1.4)
KI81 250 average (58)	76.1	27.2	13.1	3.1 (1.5)	0.7	0.3	4.6 (1.5)	0.9	0.4	2.3 (0.9)
KI81 220 average (82)	67.0	12.6	11.0	3.6 (2.3)	0.8	0.5	1.7 (0.8)	0.9	0.5	1.9 (0.9)
KI81 205 average (41)	62.6	7.8	17.4	2.3 (0.3)	0.5	0.3	1.9 (0.7)	0.5	0.3	1.8 (0.6)
KI81 193 average (54)	58.8	18.4	19.4	4.4 (3.3)	0.5	0.3	2.0 (0.7)	0.5	0.3	1.7 (0.7)
SRP 314 average (79)	95.9	55.7	10.3	5.8 (3.3)	2.0	1.1	2.1 (1.2)	2.0	0.5	5.5 (1.4)
SRP 301 average (50)	91.7	52.9	9.5	6.2 (3.6)	1.9	1.0	2.2 (1.3)	1.9	0.4	5.4 (1.3)
SRP 300 average (97)	91.5	41.3	7.5	6.2 (3.5)	1.4	0.8	2.1 (1.5)	1.4	0.3	4.2 (2.1)
SRP 299 average (50)	91.3	42.4	7.7	6.0 (3.8)	1.2	0.6	2.1 (1.0)	0.9	0.4	3.1 (1.6)
SRP 298 average (73)	90.8	49.6	8.6	6.9 (3.9)	1.2	0.8	2.0 (1.3)	1.7	0.4	5.4 (1.3)
LAKI 04 average (67)	-	66.4	10.4	7.8 (4.0)	0.7	0.3	3.0 (1.5)	-	-	-

Appendix Table 4.C Line profiles of composition (obtained using EPMA), extending up to 50 μm outwards from the Fe-rich CBL around plagioclase, in samples from 44.8 m (KI 147) depth and 45.4 m (KI 149) depth (corresponding to quench temperatures of 1090°C and 1112°C, respectively).

Sample	Transect no.	Location relative to (010) plag face	SiO_2	SD	TiO_2	SD	Al_2O_3	SD	FeO	SD	MnO	SD	MgO	SD	CaO	SD	Na_2O	SD	K_2O	SD	P_2O_5	SD	Total	Distance (μm)
KI 149	1	Perp to (010)	48.88	0.65	5.22	0.08	11.94	0.35	11.93	0.45	0.20	0.04	4.52	0.20	7.71	0.18	2.60	0.14	1.14	0.08	0.78	0.04	94.91	0.0
KI 149	1	Perp to (010)	48.86	0.65	5.14	0.10	11.85	0.35	12.02	0.45	0.21	0.04	4.37	0.20	7.83	0.19	2.46	0.14	1.24	0.08	0.79	0.03	94.77	2.1
KI 149	1	Perp to (010)	49.21	0.65	5.24	0.10	12.04	0.35	12.07	0.45	0.19	0.04	4.37	0.20	7.75	0.18	2.28	0.13	1.21	0.08	0.79	0.04	95.12	4.3
KI 149	1	Perp to (010)	50.17	0.66	5.33	0.10	12.17	0.35	12.28	0.46	0.17	0.04	4.57	0.21	7.82	0.19	2.13	0.13	1.14	0.08	0.80	0.04	96.59	6.4
KI 149	1	Perp to (010)	49.89	0.66	5.29	0.10	12.43	0.35	12.21	0.45	0.19	0.04	4.53	0.21	7.98	0.19	2.03	0.12	1.22	0.08	0.80	0.04	96.57	8.6
KI 149	1	Perp to (010)	50.35	0.66	5.30	0.10	12.12	0.35	12.46	0.46	0.17	0.05	4.52	0.21	7.90	0.19	2.02	0.12	1.18	0.08	0.80	0.04	96.81	10.7
KI 149	1	Perp to (010)	50.22	0.66	5.26	0.10	12.37	0.35	12.54	0.46	0.18	0.05	4.56	0.21	7.93	0.19	2.04	0.12	1.20	0.08	0.78	0.04	97.07	12.9
KI 149	1	Perp to (010)	49.95	0.66	5.33	0.10	12.03	0.35	12.32	0.46	0.18	0.04	4.62	0.21	8.02	0.19	2.01	0.12	1.20	0.08	0.80	0.04	96.47	15.0
KI 149	1	Perp to (010)	49.94	0.66	5.35	0.10	12.03	0.35	12.60	0.46	0.17	0.04	4.55	0.21	7.93	0.19	1.99	0.12	1.22	0.08	0.80	0.04	96.58	17.2
KI 149	1	Perp to (010)	49.86	0.66	5.32	0.10	12.04	0.35	12.43	0.46	0.16	0.04	4.58	0.21	7.86	0.19	1.97	0.12	1.18	0.08	0.77	0.04	96.18	19.3
KI 149	1	Perp to (010)	49.92	0.66	5.34	0.10	11.95	0.35	12.30	0.46	0.20	0.04	4.55	0.21	7.84	0.19	1.92	0.12	1.26	0.08	0.82	0.04	96.10	21.4
KI 149	1	Perp to (010)	50.23	0.66	5.06	0.10	12.96	0.36	11.77	0.45	0.17	0.04	4.36	0.20	8.05	0.19	2.10	0.13	1.11	0.08	0.78	0.04	96.57	23.6
KI 149	1	Perp to (010)	50.27	0.66	4.60	0.10	14.90	0.39	10.79	0.42	0.16	0.04	3.84	0.19	8.58	0.19	2.20	0.13	1.01	0.07	0.71	0.03	97.06	25.7
KI 149	1	Perp to (010)	49.92	0.66	3.94	0.10	17.31	0.41	9.00	0.39	0.16	0.04	3.24	0.17	9.71	0.21	2.24	0.13	0.88	0.07	0.64	0.03	97.04	27.9
KI 149	1	Perp to (010)	49.89	0.66	3.31	0.10	19.71	0.44	7.77	0.36	0.14	0.04	2.69	0.16	10.39	0.21	2.51	0.14	0.77	0.07	0.59	0.03	97.77	30.0
KI 149	2	Parallel to (010)	50.31	0.66	4.02	0.09	17.20	0.41	8.71	0.38	0.11	0.04	2.98	0.17	9.60	0.21	3.59	0.17	0.68	0.06	0.66	0.03	97.87	0.0
KI 149	2	Parallel to (010)	49.34	0.66	5.26	0.09	13.37	0.37	11.53	0.44	0.15	0.04	4.21	0.20	8.62	0.19	3.00	0.15	0.95	0.07	0.83	0.04	97.27	2.1
KI 149	2	Parallel to (010)	49.20	0.65	5.79	0.10	11.45	0.34	12.83	0.47	0.20	0.04	4.86	0.21	8.33	0.19	2.61	0.14	1.04	0.08	0.88	0.04	97.20	4.1
KI 149	2	Parallel to (010)	48.71	0.65	6.11	0.10	10.01	0.32	13.56	0.48	0.18	0.04	5.06	0.22	8.34	0.19	2.16	0.13	1.18	0.08	0.92	0.04	96.23	6.2
KI 149	2	Parallel to (010)	49.23	0.65	6.02	0.10	10.20	0.32	13.38	0.48	0.21	0.05	5.08	0.22	8.11	0.19	1.99	0.12	1.21	0.08	0.92	0.04	96.36	8.3
KI 149	2	Parallel to (010)	49.97	0.66	5.67	0.10	10.78	0.33	12.62	0.46	0.20	0.04	4.94	0.21	7.95	0.19	1.94	0.12	1.24	0.08	0.87	0.04	96.19	10.4
KI 149	2	Parallel to (010)	50.25	0.66	5.41	0.10	11.21	0.34	12.48	0.46	0.20	0.04	4.73	0.21	7.74	0.18	1.96	0.12	1.33	0.09	0.83	0.04	96.14	12.4
KI 149	2	Parallel to (010)	50.19	0.66	5.37	0.10	11.58	0.34	12.32	0.46	0.24	0.04	4.62	0.21	7.76	0.18	1.98	0.12	1.25	0.08	0.80	0.04	96.11	14.5
KI 149	2	Parallel to (010)	49.97	0.66	5.27	0.10	11.84	0.35	12.74	0.47	0.19	0.04	4.48	0.20	7.87	0.19	1.95	0.12	1.21	0.08	0.78	0.04	96.29	16.6
KI 149	2	Parallel to (010)	49.66	0.66	5.23	0.10	11.88	0.35	12.61	0.46	0.19	0.05	4.54	0.21	7.92	0.19	2.05	0.13	1.19	0.08	0.78	0.04	96.05	18.6
KI 149	2	Parallel to (010)	50.03	0.66	5.31	0.10	12.16	0.35	12.51	0.46	0.21	0.04	4.66	0.21	7.82	0.19	1.94	0.12	1.24	0.08	0.83	0.04	96.71	20.7
KI 149	2	Parallel to (010)	50.11	0.66	5.31	0.09	12.27	0.35	12.43	0.46	0.19	0.04	4.49	0.20	7.86	0.19	1.90	0.12	1.19	0.08	0.80	0.04	96.58	22.8

Continued from previous page

Sample	Transect no.	Location relative to (010) plag face	SiO_2	SD	TiO_2	SD	Al_2O_3	SD	FeO	SD	MnO	SD	MgO	SD	CaO	SD	Na_2O	SD	K_2O	SD	P_2O_5	SD	Total	Distance (μm)
KI 149	2	Parallel to (010)	49.79	0.66	5.28	0.09	12.05	0.35	12.18	0.45	0.18	0.04	4.59	0.21	7.80	0.19	1.99	0.12	1.19	0.08	0.81	0.04	95.85	24.8
KI 149	2	Parallel to (010)	49.22	0.65	5.24	0.08	12.18	0.35	12.23	0.46	0.21	0.04	4.49	0.20	7.80	0.19	1.90	0.12	1.24	0.08	0.80	0.04	95.30	26.9
KI 149	2	Parallel to (010)	49.05	0.65	5.23	0.08	11.83	0.35	12.18	0.45	0.21	0.04	4.30	0.20	7.95	0.19	1.90	0.12	1.16	0.08	0.78	0.04	94.59	29.0
KI 149	3	Perp to (010)	50.21	0.67	0.12	0.03	29.99	0.54	0.81	0.14	-	-	-	-	13.26	0.24	3.63	0.16	0.15	0.04	0.16	0.02	98.51	0.0
KI 149	3	Perp to (010)	50.56	0.67	0.13	0.03	29.44	0.53	0.90	0.14	-	-	-	-	12.88	0.24	3.89	0.17	0.16	0.04	0.15	0.03	98.28	3.4
KI 149	3	Perp to (010)	51.12	0.68	0.14	0.03	29.52	0.53	0.92	0.14	-	-	0.17	0.05	12.61	0.24	4.06	0.18	0.16	0.04	0.14	0.02	98.84	6.9
KI 149	3	Perp to (010)	50.95	0.67	0.52	0.04	28.17	0.52	1.78	0.18	-	-	0.44	0.07	12.38	0.24	4.02	0.17	0.17	0.04	0.22	0.03	98.65	10.3
KI 149	3	Perp to (010)	49.34	0.66	5.34	0.05	11.73	0.49	12.42	0.24	0.19	0.04	4.53	0.10	7.74	0.22	2.59	0.17	1.20	0.05	0.80	0.03	95.88	13.7
KI 149	3	Perp to (010)	50.27	0.64	5.29	0.06	12.39	0.45	12.25	0.31	0.20	0.04	4.52	0.13	7.90	0.21	2.63	0.16	1.17	0.06	0.79	0.03	97.41	17.2
KI 149	3	Perp to (010)	50.08	0.63	5.23	0.07	12.30	0.41	12.12	0.35	0.17	0.04	4.43	0.15	7.79	0.20	2.46	0.16	1.20	0.06	0.82	0.03	96.60	20.6
KI 149	3	Perp to (010)	50.08	0.61	5.22	0.08	12.51	0.38	12.09	0.37	0.16	0.04	4.40	0.16	7.85	0.18	2.47	0.15	1.20	0.07	0.82	0.03	96.82	24.0
KI 149	3	Perp to (010)	50.38	0.58	5.25	0.09	12.36	0.31	12.01	0.42	0.20	0.04	4.48	0.18	7.90	0.17	2.36	0.13	1.21	0.07	0.81	0.03	96.96	27.5
KI 149	3	Perp to (010)	50.05	0.66	5.23	0.10	12.30	0.35	12.28	0.46	0.17	0.05	4.32	0.20	8.02	0.18	2.44	0.14	1.12	0.08	0.81	0.04	96.75	30.9
KI 149	3	Perp to (010)	49.81	0.66	5.25	0.10	12.21	0.35	12.20	0.46	0.18	0.04	4.41	0.21	7.96	0.19	2.41	0.14	1.13	0.08	0.80	0.04	96.36	34.4
KI 149	3	Perp to (010)	50.02	0.66	5.23	0.10	12.28	0.35	12.51	0.46	0.18	0.04	4.41	0.20	7.89	0.19	2.53	0.14	1.16	0.08	0.79	0.04	97.01	37.8
KI 149	3	Perp to (010)	50.12	0.66	5.30	0.10	12.17	0.36	12.30	0.45	0.19	0.04	4.38	0.20	7.89	0.19	2.62	0.14	1.14	0.08	0.79	0.04	96.91	41.2
KI 149	3	Perp to (010)	50.05	0.66	5.30	0.10	11.96	0.35	12.45	0.45	0.17	0.04	4.44	0.20	7.90	0.19	2.48	0.13	1.15	0.08	0.80	0.04	96.70	44.7
KI 149	3	Perp to (010)	49.82	0.66	5.28	0.10	12.17	0.35	12.45	0.46	0.19	0.04	4.28	0.20	7.99	0.19	2.51	0.14	1.14	0.08	0.81	0.04	96.64	48.1
KI 149	3	Perp to (010)	49.83	0.66	5.24	0.10	12.14	0.35	12.27	0.46	0.19	0.04	4.46	0.20	7.99	0.19	2.43	0.14	1.13	0.08	0.80	0.04	96.50	51.5
KI 149	3	Perp to (010)	49.87	0.66	5.27	0.10	12.17	0.35	12.25	0.46	0.18	0.04	4.38	0.20	7.97	0.19	2.56	0.14	1.13	0.08	0.79	0.04	96.57	55.0
KI 149	3	Perp to (010)	49.47	0.66	5.25	0.10	11.86	0.35	12.34	0.46	0.16	0.04	4.39	0.20	7.61	0.19	2.50	0.14	1.08	0.08	0.79	0.04	95.45	58.4
KI 149	3	Perp to (010)	48.88	0.66	5.10	0.10	11.82	0.35	12.14	0.46	0.21	0.04	4.40	0.21	7.52	0.19	2.42	0.14	1.07	0.08	0.77	0.04	94.32	61.8
KI 149	3	Perp to (010)	49.72	0.66	5.24	0.10	12.44	0.35	12.07	0.46	0.19	0.04	4.45	0.20	7.83	0.19	2.65	0.14	1.09	0.08	0.79	0.04	96.46	65.3
KI 149	3	Perp to (010)	50.33	0.66	5.19	0.10	11.46	0.35	12.15	0.45	0.20	0.04	4.83	0.20	8.26	0.19	2.53	0.14	1.05	0.08	0.76	0.04	96.76	68.7
KI 149	3	Perp to (010)	50.33	0.66	4.44	0.10	10.63	0.35	11.09	0.46	0.16	0.04	7.21	0.20	10.30	0.19	2.03	0.14	0.94	0.08	0.68	0.04	97.81	72.1
KI 149	3	Perp to (010)	50.03	0.66	3.93	0.10	7.73	0.35	10.30	0.46	0.20	0.04	9.83	0.20	13.08	0.18	1.37	0.14	0.59	0.08	0.60	0.04	97.66	75.6
KI 149	3	Perp to (010)	49.90	0.65	1.92	0.09	4.53	0.35	8.34	0.45	0.19	0.04	14.33	0.20	17.50	0.18	0.56	0.14	0.23	0.08	0.34	0.03	97.83	79.0
KI 149	3	Perp to (010)	50.24	0.65	1.54	0.09	2.49	0.35	7.95	0.45	0.20	0.04	15.68	0.20	18.60	0.18	0.32	0.14	0.02	0.08	0.28	0.04	97.33	82.4
KI 149	3	Perp to (010)	50.11	0.65	1.08	0.10	2.61	0.35	7.07	0.45	0.18	0.04	16.29	0.20	19.65	0.18	0.28	0.14	0.02	0.08	0.23	0.03	97.54	85.9
KI 149	3	Perp to (010)	49.83	0.66	1.04	0.10	2.76	0.36	6.66	0.45	0.16	0.04	16.26	0.20	19.87	0.19	0.30	0.14	0.01	0.08	0.22	0.04	97.11	89.3
KI 149	3	Perp to (010)	49.87	0.66	0.99	0.09	2.88	0.34	6.54	0.45	-	0.04	16.27	0.21	19.97	0.19	0.33	0.14	-	0.08	0.24	0.04	97.22	92.7
KI 147	1	Perp to (010)	53.77	2.20	4.01	0.23	12.62	0.60	11.74	0.96	0.17	0.08	3.76	0.32	7.02	0.39	3.18	0.38	1.61	0.13	0.91	0.07	98.79	0.0
KI 147	1	Perp to (010)	53.36	2.18	4.07	0.23	12.50	0.60	12.02	0.98	0.19	0.08	3.77	0.32	6.95	0.38	3.00	0.37	1.63	0.13	0.91	0.07	98.40	2.0
KI 147	1	Perp to (010)	54.03	2.20	3.98	0.23	12.43	0.59	11.76	0.97	0.18	0.08	3.61	0.31	6.91	0.38	2.39	0.33	1.58	0.13	0.87	0.07	97.74	3.9
KI 147	1	Perp to (010)	54.76	2.22	4.07	0.23	12.36	0.60	11.39	0.95	0.18	0.08	3.50	0.31	6.86	0.38	2.97	0.36	1.60	0.13	0.91	0.07	98.60	5.9
KI 147	1	Perp to (010)	53.60	2.19	4.07	0.23	12.24	0.59	12.05	0.98	0.19	0.08	3.63	0.32	7.24	0.39	3.32	0.39	1.52	0.13	0.89	0.07	98.76	7.9
KI 147	1	Perp to (010)	55.28	2.24	4.11	0.23	12.36	0.59	12.38	1.00	0.21	0.08	3.63	0.31	7.01	0.38	2.18	0.31	1.55	0.13	0.94	0.07	99.64	9.8
KI 147	1	Perp to (010)	54.47	2.21	4.09	0.23	12.70	0.60	12.08	0.98	0.31	0.08	3.84	0.32	6.96	0.38	3.09	0.38	1.58	0.13	0.95	0.07	100.06	11.8
KI 147	1	Perp to (010)	53.75	2.19	4.03	0.23	12.38	0.59	11.29	0.94	0.14	0.08	3.61	0.31	6.90	0.38	3.22	0.38	1.55	0.13	0.86	0.07	97.75	13.7
KI 147	1	Perp to (010)	54.37	2.21	4.00	0.23	12.61	0.60	12.51	1.01	0.18	0.08	3.74	0.32	6.97	0.38	2.85	0.36	1.55	0.13	0.92	0.07	99.68	15.7
KI 147	1	Perp to (010)	54.76	2.22	4.07	0.23	12.74	0.61	11.82	0.97	0.07	0.08	3.53	0.31	7.11	0.39	3.26	0.38	1.62	0.13	0.92	0.07	99.89	17.7
KI 147	1	Perp to (010)	54.98	2.23	4.06	0.23	12.49	0.60	11.53	0.95	0.17	0.08	3.43	0.30	6.91	0.38	2.43	0.33	1.54	0.13	0.91	0.07	98.45	19.6
KI 147	1	Perp to (010)	54.76	2.22	4.07	0.23	12.43	0.59	12.05	0.98	0.20	0.08	3.68	0.31	6.89	0.38	3.14	0.38	1.60	0.13	0.89	0.07	99.69	21.6
KI 147	1	Perp to (010)	54.04	2.20	3.98	0.23	12.99	0.61	12.12	0.98	0.21	0.09	3.69	0.31	6.80	0.38	3.02	0.37	1.60	0.13	0.96	0.07	99.40	23.6
KI 147	1	Perp to (010)	54.49	2.21	4.06	0.23	12.61	0.60	11.79	0.96	0.20	0.08	3.67	0.32	6.93	0.38	2.60	0.34	1.53	0.13	0.92	0.07	98.79	25.5
KI 147	1	Perp to (010)	54.52	2.22	3.98	0.23	12.81	0.61	11.90	0.97	0.13	0.08	3.47	0.30	7.03	0.39	3.20	0.38	1.58	0.13	0.93	0.07	99.54	27.5
KI 147	1	Perp to (010)	54.23	2.21	3.86	0.22	12.14	0.59	11.42	0.95	0.27	0.10	3.73	0.31	6.95	0.38	3.31	0.39	1.56	0.13	0.93	0.07	98.41	29.5
KI 147	1	Perp to (010)	53.72	2.19	3.91	0.22	12.59	0.60	12.24	0.99	0.22	0.09	3.48	0.31	6.72	0.38	2.63	0.34	1.66	0.13	0.91	0.07	98.08	31.4

Continued from previous page

Sample	Transect no.	Location relative to (010) plag face	SiO_2	SD	TiO_2	SD	Al_2O_3	SD	FeO	SD	MnO	SD	MgO	SD	CaO	SD	Na_2O	SD	K_2O	SD	P_2O_5	SD	Total	Distance (μm)
KI 147	1	Perp to (010)	53.92	2.20	3.87	0.22	12.66	0.60	11.90	0.98	0.30	0.08	3.70	0.32	6.77	0.38	2.54	0.34	1.65	0.13	0.93	0.07	98.24	33.4
KI 147	2	Parallel to (010)	54.43	2.21	4.09	0.23	12.47	0.59	12.03	0.98	0.25	0.08	3.67	0.31	7.04	0.39	3.27	0.39	1.53	0.13	0.92	0.07	99.69	0.0
KI 147	2	Parallel to (010)	53.85	2.19	4.05	0.23	12.43	0.60	11.62	0.96	0.19	0.08	3.71	0.32	6.91	0.38	3.19	0.38	1.59	0.13	0.93	0.07	98.47	1.8
KI 147	2	Parallel to (010)	53.89	2.19	4.11	0.23	12.54	0.60	11.99	0.97	0.15	0.08	3.51	0.31	7.00	0.39	3.19	0.38	1.55	0.13	0.93	0.07	98.87	3.7
KI 147	2	Parallel to (010)	53.69	2.19	4.09	0.23	12.65	0.60	11.96	0.97	0.15	0.08	3.58	0.31	6.90	0.38	3.32	0.38	1.60	0.13	0.94	0.07	98.87	5.5
KI 147	2	Parallel to (010)	53.62	2.18	4.05	0.23	12.72	0.60	11.93	0.97	0.22	0.09	3.46	0.32	6.90	0.38	2.30	0.32	1.56	0.13	0.88	0.07	97.64	7.4
KI 147	2	Parallel to (010)	54.53	2.21	4.06	0.23	12.24	0.59	11.83	0.97	0.23	0.09	3.50	0.31	7.02	0.39	3.16	0.38	1.51	0.13	0.91	0.07	98.99	9.2
KI 147	2	Parallel to (010)	54.19	2.20	4.01	0.23	12.28	0.59	12.13	0.98	0.18	0.08	3.61	0.31	7.09	0.39	2.55	0.34	1.63	0.13	0.91	0.07	98.59	11.0
KI 147	2	Parallel to (010)	53.78	2.19	3.94	0.22	12.70	0.60	11.80	0.97	0.23	0.08	3.55	0.31	6.94	0.38	3.09	0.37	1.59	0.13	0.89	0.07	98.51	12.9
KI 147	2	Parallel to (010)	53.73	2.19	4.02	0.23	12.47	0.59	12.06	0.98	0.19	0.08	3.69	0.31	6.96	0.38	3.02	0.37	1.61	0.13	0.91	0.07	98.66	14.7
KI 147	2	Parallel to (010)	53.87	2.19	4.07	0.23	12.78	0.60	11.89	0.97	0.23	0.09	3.67	0.31	6.67	0.37	3.17	0.37	1.65	0.13	0.90	0.07	98.90	16.6
KI 147	2	Parallel to (010)	53.70	2.19	3.99	0.23	12.47	0.59	11.60	0.95	0.11	0.08	3.69	0.31	7.07	0.39	2.42	0.33	1.62	0.13	0.92	0.07	97.60	18.4
KI 147	2	Parallel to (010)	54.07	2.20	3.99	0.23	12.50	0.60	11.86	0.97	0.25	0.09	3.61	0.31	6.88	0.38	3.08	0.37	1.63	0.13	0.90	0.07	98.77	20.2
KI 147	2	Parallel to (010)	53.73	2.19	4.03	0.23	12.50	0.59	12.34	0.99	0.21	0.09	3.68	0.31	6.82	0.38	2.76	0.35	1.60	0.13	0.92	0.07	98.58	22.1
KI 147	2	Parallel to (010)	53.99	2.20	3.99	0.23	12.35	0.59	11.51	0.95	0.25	0.09	3.75	0.32	6.83	0.38	2.98	0.36	1.57	0.13	0.91	0.07	98.13	23.9
KI 147	2	Parallel to (010)	53.78	2.19	3.96	0.22	12.74	0.60	12.20	0.99	0.24	0.09	3.74	0.32	7.11	0.39	3.20	0.38	1.60	0.13	0.91	0.07	99.48	25.8
KI 147	2	Parallel to (010)	54.05	2.20	3.89	0.22	12.63	0.60	11.74	0.96	0.27	0.10	3.48	0.30	6.85	0.38	2.73	0.35	1.67	0.13	0.91	0.07	98.21	27.6
KI 147	2	Parallel to (010)	54.83	2.22	3.88	0.22	12.55	0.60	11.96	0.97	0.20	0.09	3.45	0.30	6.99	0.38	2.53	0.33	1.59	0.13	0.88	0.07	98.85	29.4
KI 147	2	Parallel to (010)	53.42	2.18	3.83	0.22	12.64	0.60	11.55	0.95	0.17	0.08	3.58	0.31	6.74	0.38	3.22	0.38	1.66	0.13	0.90	0.07	97.70	31.3
KI 147	2	Parallel to (010)	53.96	2.19	3.83	0.22	12.31	0.59	11.51	0.95	0.24	0.09	3.73	0.31	6.74	0.38	2.97	0.36	1.71	0.14	0.91	0.07	97.91	33.1
KI 147	2	Parallel to (010)	53.37	2.18	3.74	0.21	11.49	0.57	12.09	0.98	0.17	0.09	3.78	0.32	6.47	0.37	2.62	0.34	1.68	0.13	0.89	0.07	96.31	35.0
KI 147	2	Parallel to (010)	55.96	2.25	4.11	0.23	10.81	0.55	12.47	1.00	0.10	0.09	3.90	0.33	6.59	0.37	2.21	0.31	1.72	0.14	0.96	0.07	98.82	36.8
KI 147	3	Parallel to (010)	54.97	2.23	3.85	0.22	12.63	0.60	12.19	0.99	0.21	0.09	3.78	0.32	6.92	0.38	3.07	0.38	1.66	0.13	0.92	0.07	100.20	0.0
KI 147	3	Parallel to (010)	54.37	2.21	3.97	0.23	12.79	0.60	11.97	0.97	0.27	0.10	3.52	0.31	6.99	0.38	2.17	0.31	1.57	0.13	0.90	0.07	98.51	1.7
KI 147	3	Parallel to (010)	54.15	2.20	3.82	0.22	12.29	0.59	11.85	0.97	0.20	0.08	3.96	0.32	6.62	0.37	2.53	0.33	1.62	0.13	0.91	0.07	97.95	3.4
KI 147	3	Parallel to (010)	54.25	2.21	3.88	0.22	12.80	0.61	11.80	0.96	0.20	0.08	3.60	0.31	6.84	0.38	3.12	0.38	1.61	0.13	0.92	0.07	99.03	5.1
KI 147	3	Parallel to (010)	54.55	2.21	3.85	0.22	12.50	0.60	11.65	0.96	0.12	0.05	3.86	0.32	6.79	0.38	3.21	0.38	1.63	0.13	0.95	0.07	99.09	6.8
KI 147	3	Parallel to (010)	53.76	2.19	3.90	0.22	12.66	0.60	11.70	0.96	0.13	0.05	3.59	0.31	6.94	0.38	3.26	0.38	1.62	0.13	0.92	0.07	98.47	8.5
KI 147	3	Parallel to (010)	55.71	2.25	3.92	0.22	12.44	0.59	11.76	0.96	0.24	0.09	3.77	0.32	7.07	0.39	2.04	0.30	1.50	0.13	0.89	0.07	99.34	10.1
KI 147	3	Parallel to (010)	55.15	2.23	3.83	0.22	12.72	0.60	11.45	0.94	-	-	3.83	0.32	6.77	0.38	2.69	0.34	1.64	0.13	0.94	0.07	99.04	11.8
KI 147	3	Parallel to (010)	54.08	2.20	3.92	0.22	12.43	0.60	11.61	0.96	0.24	0.09	3.39	0.30	6.95	0.38	2.73	0.34	1.69	0.14	0.91	0.07	97.97	13.5
KI 147	3	Parallel to (010)	53.75	2.19	3.85	0.22	12.81	0.60	11.52	0.95	0.19	0.08	3.87	0.32	6.83	0.38	3.30	0.39	1.64	0.13	0.89	0.07	98.64	15.2
KI 147	3	Parallel to (010)	53.96	2.20	3.92	0.22	12.62	0.60	11.73	0.97	0.19	0.08	3.61	0.31	6.88	0.38	3.11	0.37	1.62	0.13	0.94	0.07	98.58	16.9
KI 147	3	Parallel to (010)	54.60	2.22	3.97	0.22	12.53	0.60	12.00	0.98	0.19	0.08	3.64	0.31	6.81	0.38	2.22	0.31	1.47	0.13	0.93	0.07	98.36	18.6
KI 147	3	Parallel to (010)	54.54	2.21	3.88	0.22	12.63	0.60	12.10	0.98	0.21	0.08	3.65	0.31	6.80	0.38	2.64	0.34	1.62	0.13	0.93	0.07	98.99	20.3
KI 147	3	Parallel to (010)	53.85	2.20	3.93	0.22	12.80	0.61	11.65	0.96	0.25	0.09	3.65	0.31	6.94	0.38	3.24	0.38	1.57	0.13	0.92	0.07	98.80	22.0
KI 147	3	Parallel to (010)	54.27	2.21	3.93	0.22	12.49	0.60	11.81	0.97	-	-	3.56	0.31	6.65	0.37	3.28	0.38	1.65	0.13	0.94	0.07	98.63	23.7
KI 147	3	Parallel to (010)	54.15	2.21	3.86	0.22	12.59	0.60	12.23	0.99	0.18	0.08	3.65	0.31	6.79	0.38	3.08	0.37	1.56	0.13	0.91	0.07	99.00	25.4
KI 147	3	Parallel to (010)	54.51	2.22	3.91	0.22	12.73	0.60	12.30	0.99	0.18	0.08	3.56	0.31	6.83	0.38	2.34	0.32	1.55	0.13	0.91	0.07	98.81	27.0
KI 147	3	Parallel to (010)	54.38	2.21	3.82	0.22	12.36	0.60	11.69	0.96	0.24	0.09	3.45	0.30	7.03	0.39	2.53	0.34	1.60	0.13	0.91	0.07	98.01	28.7
KI 147	3	Parallel to (010)	54.53	2.21	3.92	0.22	12.42	0.59	11.60	0.96	0.09	0.04	3.54	0.31	6.99	0.38	2.94	0.36	1.61	0.13	0.90	0.07	98.54	30.4
KI 147	3	Parallel to (010)	53.94	2.20	4.01	0.23	12.71	0.60	11.67	0.96	0.23	0.09	3.65	0.31	6.81	0.38	3.17	0.38	1.59	0.13	0.92	0.07	98.70	32.1
KI 147	3	Parallel to (010)	54.57	2.22	3.93	0.22	12.73	0.60	12.24	0.99	0.25	0.09	3.58	0.31	6.93	0.38	3.32	0.39	1.68	0.13	0.93	0.07	100.16	33.8
KI 147	3	Parallel to (010)	54.88	2.22	3.99	0.23	12.71	0.60	11.64	0.96	0.15	0.06	3.51	0.31	6.81	0.38	2.05	0.30	1.53	0.13	0.95	0.07	98.22	35.5
KI 147	3	Parallel to (010)	55.05	2.23	3.90	0.22	12.78	0.60	11.87	0.97	0.18	0.06	3.52	0.31	6.77	0.38	2.81	0.35	1.57	0.13	0.94	0.07	99.38	37.2
KI 147	3	Parallel to (010)	55.08	2.23	3.94	0.22	12.81	0.60	12.45	1.00	0.09	0.04	3.66	0.31	7.02	0.39	3.05	0.37	1.62	0.13	0.90	0.07	100.63	38.9
KI 147	3	Parallel to (010)	54.19	2.20	3.99	0.23	12.42	0.59	11.83	0.97	0.24	0.09	3.68	0.31	6.87	0.38	2.25	0.31	1.58	0.13	0.92	0.07	97.97	40.6
KI 147	3	Parallel to (010)	53.70	2.19	3.87	0.22	12.66	0.60	11.81	0.97	0.18	0.08	3.61	0.31	6.99	0.38	3.27	0.39	1.62	0.13	0.90	0.07	98.62	42.3

Continued from previous page

Sample	Transect no.	Location relative to (010) plag face	SiO_2	SD	TiO_2	SD	Al_2O_3	SD	FeO	SD	MnO	SD	MgO	SD	CaO	SD	Na_2O	SD	K_2O	SD	P_2O_5	SD	Total	Distance (μm)
KI 147	3	Parallel to (010)	54.79	2.22	3.98	0.23	12.76	0.60	11.46	0.95	0.09	0.04	3.69	0.31	6.77	0.38	2.38	0.32	1.56	0.13	0.89	0.07	98.38	43.9
KI 147	3	Parallel to (010)	54.28	2.21	3.91	0.22	12.57	0.60	12.12	0.99	0.22	0.09	3.56	0.31	6.61	0.37	3.20	0.38	1.62	0.13	0.87	0.07	98.96	45.6
KI 147	3	Parallel to (010)	54.28	2.21	3.93	0.22	12.69	0.60	12.02	0.98	0.06	0.04	3.55	0.31	6.94	0.38	2.15	0.30	1.50	0.13	0.94	0.07	98.06	47.3
KI 147	3	Parallel to (010)	54.06	2.20	3.88	0.22	12.80	0.61	11.91	0.98	0.23	0.09	3.65	0.31	6.81	0.38	3.17	0.38	1.62	0.13	0.92	0.07	99.04	49.0
KI 147	3	Parallel to (010)	55.19	2.24	3.93	0.22	12.71	0.60	11.88	0.97	0.20	0.09	3.57	0.31	6.82	0.38	2.40	0.32	1.55	0.13	0.92	0.07	99.18	50.7
KI 147	3	Parallel to (010)	54.91	2.22	3.96	0.22	12.48	0.60	11.78	0.97	0.30	0.10	3.70	0.31	6.74	0.38	3.03	0.37	1.59	0.13	0.86	0.07	99.33	52.4
KI 147	3	Parallel to (010)	54.83	2.22	3.89	0.22	12.63	0.60	11.94	0.98	0.28	0.09	3.41	0.30	6.61	0.37	2.94	0.36	1.64	0.13	0.92	0.07	99.07	54.1
KI 147	3	Parallel to (010)	53.84	2.19	3.97	0.22	12.68	0.60	12.06	0.98	0.21	0.09	3.58	0.31	6.75	0.38	3.06	0.37	1.60	0.13	0.91	0.07	98.64	55.8
KI 147	3	Parallel to (010)	53.85	2.19	4.01	0.23	12.77	0.60	11.60	0.96	0.22	0.09	3.22	0.29	6.89	0.38	3.41	0.40	1.58	0.13	0.94	0.07	98.51	57.5
KI 147	3	Parallel to (010)	54.80	2.22	3.99	0.23	12.94	0.61	11.95	0.97	0.08	0.04	3.27	0.31	6.46	0.37	3.07	0.37	1.70	0.14	0.93	0.07	99.18	59.2
KI 147	3	Parallel to (010)	54.56	2.21	4.08	0.23	12.84	0.60	11.39	0.95	0.15	0.08	3.09	0.29	6.62	0.37	2.18	0.31	1.63	0.13	0.97	0.07	97.52	60.8
KI 147	3	Parallel to (010)	54.80	2.22	3.87	0.22	13.26	0.62	10.65	0.90	0.13	0.06	3.02	0.28	6.41	0.36	2.73	0.35	1.80	0.14	0.96	0.07	97.63	62.5
KI 147	3	Parallel to (010)	55.43	2.24	3.98	0.23	13.44	0.62	10.84	0.91	0.18	0.09	2.97	0.28	6.26	0.36	1.98	0.29	1.77	0.14	0.98	0.07	97.83	64.2
KI 147	4	Parallel to (010)	54.82	2.22	3.92	0.22	12.50	0.60	11.61	0.96	0.18	0.08	3.81	0.32	6.89	0.38	3.02	0.37	1.64	0.13	0.95	0.07	99.32	0.0
KI 147	4	Parallel to (010)	55.06	2.23	3.92	0.22	12.94	0.61	11.66	0.96	0.12	0.06	3.69	0.31	6.92	0.38	2.28	0.31	1.57	0.13	0.95	0.07	99.10	1.5
KI 147	4	Parallel to (010)	54.51	2.21	3.94	0.22	12.49	0.60	11.57	0.95	0.23	0.08	3.64	0.31	6.89	0.38	3.03	0.37	1.65	0.13	0.88	0.07	98.81	3.0
KI 147	4	Parallel to (010)	54.48	2.21	3.97	0.22	12.62	0.60	11.56	0.95	0.19	0.08	3.80	0.32	7.09	0.39	2.75	0.35	1.68	0.13	0.93	0.07	99.06	4.5
KI 147	4	Parallel to (010)	54.59	2.21	3.88	0.22	12.67	0.60	11.97	0.97	0.20	0.08	3.53	0.30	6.89	0.38	2.31	0.32	1.55	0.13	0.87	0.07	98.46	6.0
KI 147	4	Parallel to (010)	54.91	2.23	3.92	0.22	12.87	0.61	11.98	0.98	0.15	0.05	3.48	0.30	6.82	0.38	3.18	0.38	1.59	0.13	0.89	0.07	99.78	7.6
KI 147	4	Parallel to (010)	54.03	2.20	3.87	0.22	12.80	0.60	12.03	0.98	0.07	0.04	3.50	0.30	7.00	0.39	3.18	0.38	1.57	0.13	0.91	0.07	98.95	9.1
KI 147	4	Parallel to (010)	54.58	2.22	4.03	0.23	12.56	0.60	12.33	0.99	0.34	0.12	3.57	0.30	7.02	0.38	2.12	0.30	1.54	0.13	0.96	0.07	99.05	10.6
KI 147	4	Parallel to (010)	54.72	2.22	3.90	0.22	12.76	0.60	11.90	0.97	0.15	0.06	3.52	0.30	6.72	0.38	2.41	0.33	1.67	0.13	0.90	0.07	98.63	12.1
KI 147	4	Parallel to (010)	54.37	2.21	3.96	0.22	12.64	0.60	12.03	0.98	0.23	0.08	3.57	0.31	7.02	0.38	3.31	0.39	1.61	0.13	0.92	0.07	99.65	13.6
KI 147	4	Parallel to (010)	54.67	2.22	3.87	0.22	12.68	0.60	12.32	0.99	0.22	0.08	3.45	0.31	6.94	0.38	3.09	0.37	1.68	0.14	0.93	0.07	99.84	15.1
KI 147	4	Parallel to (010)	54.88	2.22	3.92	0.22	12.64	0.60	11.99	0.98	0.10	0.04	3.63	0.31	6.96	0.38	2.12	0.30	1.54	0.13	0.93	0.07	98.71	16.6
KI 147	4	Parallel to (010)	55.02	2.23	3.99	0.23	12.50	0.59	11.73	0.96	0.24	0.09	3.59	0.31	6.92	0.38	2.08	0.30	1.58	0.13	0.90	0.07	98.55	18.1
KI 147	4	Parallel to (010)	53.85	2.19	3.82	0.22	12.24	0.59	11.90	0.97	0.26	0.08	3.60	0.31	6.73	0.38	2.92	0.36	1.56	0.13	0.94	0.07	97.83	19.6
KI 147	4	Parallel to (010)	53.86	2.19	3.92	0.22	12.68	0.60	11.72	0.96	0.22	0.09	3.51	0.31	6.79	0.38	2.89	0.36	1.67	0.13	0.94	0.07	98.22	21.1
KI 147	4	Parallel to (010)	54.99	2.23	3.93	0.22	12.53	0.60	11.79	0.96	0.16	0.08	3.78	0.32	6.87	0.38	2.96	0.36	1.61	0.13	0.96	0.07	99.58	22.7
KI 147	4	Parallel to (010)	54.67	2.22	4.03	0.23	11.16	0.56	12.53	1.01	0.22	0.08	3.94	0.32	6.85	0.38	2.18	0.31	1.73	0.14	0.96	0.07	98.27	24.2
KI 147	5	Perp to (010)	54.40	2.21	3.86	0.22	12.60	0.60	11.75	0.96	0.18	0.08	3.82	0.32	6.96	0.38	3.32	0.39	1.65	0.13	0.88	0.07	99.42	0.0
KI 147	5	Perp to (010)	54.83	2.22	3.88	0.22	12.54	0.60	11.80	0.96	-	-	3.54	0.31	6.99	0.38	2.35	0.32	1.56	0.13	0.90	0.07	98.39	1.0
KI 147	5	Perp to (010)	54.50	2.21	3.92	0.22	12.62	0.60	11.95	0.98	0.15	0.08	3.67	0.31	7.01	0.38	2.84	0.35	1.68	0.13	0.89	0.07	99.22	2.0
KI 147	5	Perp to (010)	54.84	2.22	3.98	0.23	13.01	0.61	12.12	0.98	0.20	0.09	3.72	0.32	6.88	0.38	2.99	0.36	1.56	0.13	0.93	0.07	100.23	3.0
KI 147	5	Perp to (010)	54.07	2.20	4.00	0.23	12.58	0.60	11.91	0.97	0.05	0.02	3.63	0.31	6.96	0.38	2.29	0.32	1.61	0.13	0.89	0.07	98.00	4.0
KI 147	5	Perp to (010)	54.25	2.21	3.86	0.22	12.48	0.60	11.71	0.96	0.24	0.09	3.63	0.31	6.77	0.38	3.14	0.38	1.65	0.13	0.90	0.07	98.64	5.0
KI 147	5	Perp to (010)	54.22	2.21	3.87	0.22	12.66	0.60	11.63	0.95	0.11	0.05	3.41	0.30	6.73	0.38	2.48	0.33	1.63	0.13	0.93	0.07	97.68	6.0
KI 147	5	Perp to (010)	54.68	2.22	3.93	0.22	12.48	0.60	11.83	0.97	0.13	0.05	3.61	0.31	6.83	0.38	3.08	0.37	1.64	0.13	0.87	0.07	99.09	7.0
KI 147	5	Perp to (010)	55.02	2.23	3.90	0.22	12.57	0.60	11.73	0.96	0.12	0.05	3.65	0.31	7.04	0.39	2.49	0.33	1.67	0.13	0.93	0.07	99.11	8.0
KI 147	5	Perp to (010)	54.69	2.22	3.87	0.22	12.51	0.60	11.72	0.96	0.19	0.08	3.53	0.31	6.99	0.38	2.67	0.35	1.61	0.13	0.92	0.07	98.69	9.0
KI 147	5	Perp to (010)	54.19	2.20	3.92	0.22	12.52	0.59	11.60	0.96	0.28	0.09	3.60	0.31	6.98	0.38	1.96	0.30	1.60	0.13	0.89	0.07	97.54	10.0
KI 147	5	Perp to (010)	54.78	2.22	3.98	0.23	12.74	0.60	12.26	0.99	0.28	0.09	3.34	0.30	7.02	0.39	2.41	0.33	1.66	0.13	0.92	0.07	99.39	11.0
KI 147	5	Perp to (010)	55.07	2.23	3.98	0.23	12.42	0.59	11.46	0.95	0.13	0.04	3.70	0.31	7.08	0.39	2.44	0.33	1.57	0.13	0.91	0.07	98.75	12.0
KI 147	5	Perp to (010)	54.24	2.21	3.88	0.22	12.60	0.60	12.02	0.98	0.19	0.08	3.59	0.31	6.83	0.38	3.13	0.37	1.59	0.13	0.93	0.07	99.01	13.0
KI 147	5	Perp to (010)	54.99	2.23	3.87	0.22	12.82	0.60	11.99	0.98	0.24	0.09	3.64	0.31	6.95	0.38	2.03	0.30	1.55	0.13	0.93	0.07	99.01	14.0
KI 147	5	Perp to (010)	55.01	2.23	3.80	0.22	15.07	0.67	12.12	0.98	0.15	0.04	3.16	0.29	7.65	0.41	3.69	0.41	1.18	0.11	0.88	0.07	102.71	15.0
KI 147	5	Perp to (010)	53.44	2.19	0.28	0.05	27.60	0.96	0.87	0.26	-	-	0.27	0.10	11.62	0.54	4.58	0.45	0.27	0.05	0.20	0.04	99.12	16.0

Appendix Table 4.D Bulk chemical analyses for the specified phase from APT tips. Note that compositions are listed as atomic percent (at. %).

Sample	Si	Ti	Al	Fe	Mn	Mg	Ca	Na	K	P	O	Total
Average bulk analyses from the Plagioclase, Concentration (at %)												
178414	24.8	0.2	11.4	1.7	-	0.3	2.7	2.5	0.1	0.0	56.2	99.9
179197	23.0	0.0	12.6	2.6	0.0	0.6	3.2	3.0	0.2	0.1	53.6	98.9
179237	25.1	-	10.8	2.0	0.0	0.5	3.0	1.6	0.1	0.1	56.8	99.8
179377	23.8	0.0	11.0	1.9	0.0	0.5	3.0	2.1	0.1	0.0	57.5	99.9
173738	20.7	0.0	15.5	0.7	0.0	0.1	5.3	2.0	0.1	0.0	55.7	100.0
Average bulk analyses from the glass Compositional Boundary Layer, Concentration (at %)												
178414	17.6	0.8	2.1	12.6	0.2	7.8	7.3	0.4	0.0	1.5	49.7	99.9
179197	16.2	0.7	2.3	13.6	0.2	7.2	6.2	0.4	0.0	1.2	51.8	99.8
179237	17.2	0.7	2.2	13.0	0.2	7.9	6.7	0.3	0.0	1.6	50.1	100.0
179377	15.2	0.8	2.2	13.4	0.2	7.7	7.1	0.3	0.0	1.5	51.6	100.0
179526	15.7	0.7	2.4	13.5	0.2	7.9	7.1	0.5	0.0	1.2	50.9	100.0
173970	17.2	0.7	1.8	12.8	0.2	8.9	8.0	0.3	0.0	1.9	47.6	99.5
Average bulk analyses from the Fe-rich glass comprising the nanoemulsion, Concentration (at %)												
179523	16.5	1.5	3.9	12.3	0.12	9.2	7.4	0.3	0.1	0.9	47.4	99.7
179530	16.3	1.2	4.3	11.8	0.10	8.9	7.8	0.7	0.1	0.5	48.0	99.8
179484	16.6	1.4	4.1	11.5	0.16	8.5	7.8	0.8	0.1	1.4	47.6	99.8
179483	15.5	1.2	4.7	12.0	0.10	8.5	8.1	1.2	0.2	0.8	47.3	99.6
179534	16.3	1.2	4.0	11.6	0.06	9.2	8.3	0.6	0.1	0.4	47.5	99.1
173941	18.2	1.1	5.3	10.7	0.21	7.6	7.5	0.8	0.1	1.4	46.3	99.2
173974	18.4	1.4	5.5	10.5	0.04	7.6	6.4	0.5	0.1	1.4	47.6	99.5
173975	21.9	0.8	4.6	17.8	0.03	3.0	2.1	1.0	0.2	1.8	46.6	99.7
173967	20.7	0.9	5.5	10.8	0.10	6.1	5.8	0.6	0.1	1.5	48.1	100.1
173972	16.8	0.8	6.3	14.3	0.16	5.4	5.6	0.9	0.2	0.3	48.9	99.7
Average bulk analyses from the Si-rich glass comprising the nanoemulsion, Concentration (at %)												
179523	28.1	0.1	8.4	2.2	0.0	1.1	1.2	0.1	0.3	0.2	58.1	99.8
179530 (1)	27.4	0.1	8.1	2.3	0.0	0.7	0.9	1.5	0.7	0.1	57.8	99.6
179484 (1)	29.2	-	6.7	1.6	0.0	0.4	0.8	0.5	0.2	0.1	60.3	99.9
179522 (1)	28.7	0.0	7.5	2.1	0.0	0.7	0.8	1.7	0.6	0.1	57.5	99.6
179483	28.1	0.0	7.7	2.0	0.0	0.7	0.9	0.8	0.5	0.1	59.1	100.0
179534	28.5	0.0	8.3	2.2	0.0	0.7	0.9	2.3	0.7	0.1	56.1	99.9
179530 (2)	28.0	0.1	8.4	2.2	0.0	0.6	1.0	1.8	0.6	0.1	57.2	100.0
179484 (2)	28.1	0.2	7.9	2.1	0.0	0.7	1.1	0.5	0.4	0.0	58.9	100.0
179522 (2)	28.5	0.1	7.4	1.9	0.0	0.6	0.8	1.9	0.4	0.1	56.6	98.4
173941	26.2	0.1	8.9	2.3	0.0	0.9	1.4	1.4	0.5	0.1	57.6	99.4
173974	26.1	0.0	9.0	2.4	0.0	1.1	1.7	1.2	0.4	0.1	57.4	99.5
173773	26.6	0.0	8.9	2.1	0.0	0.8	1.6	1.1	0.4	0.2	58.3	100.0
173975	25.8	0.0	9.1	2.2	0.0	1.2	1.7	0.9	0.4	0.0	58.1	99.4
173967	25.3	0.0	8.9	2.5	0.0	1.2	1.8	1.5	0.5	0.2	57.5	99.3
173972	26.2	0.0	8.8	2.4	0.0	1.1	1.8	0.8	0.3	0.0	57.8	99.3
173770	26.5	0.0	8.8	2.3	0.0	0.8	1.4	0.9	0.3	0.1	58.8	100.0

Appendix Table 5.A Sample localities from fieldwork on the Skaergaard Intrusion. Processed samples are also indicated. LZ = Lower Zone; UZ = Upper Zone; (t) = trough layer; RZ = Roof Zone; MBS = Marginal Border Series.

Sample number	Longitude (decimal degrees)	Latitude (decimal degrees)	Height (m)	Unit	Description	Polished thin sections			Whole rock XRF analyses	
591121	31.7407	68.1869	870	LZC	Seepage of Fe-rich liquids associated with Ti-V layer 1	121 m (mafic-rich - gabbro contact)	121 f (felsic-rich)	-	121 WR (felsic-rich)	-
591122	31.7405833	68.18685	877	LZC	Seepage of Fe-rich liquids associated with Ti-V layer 3 (30m horizontal distance below layer 3)	122 f (felsic-rich – mafic-rich contact)	122 ga (mafic-average gabbro contact)	-	122 WR (mafic-rich)	-
591123	31.7404667	68.1868333	877	LZC	Seepage of Fe-rich liquids associated with Ti-V layer 3 (30m horizontal distance below layer 3)	123 (mafic-average gabbro contact)	-	-	-	-
591124	31.7401167	68.1866	887	LZC	Seepage of Fe-rich liquids associated with Ti-V layer 3	124 (mafic-rich-gabbro contact)	-	-	-	-
591125	31.7084167	68.13385			Granophyre cutting a boulder of plag, pyx and interstitial magnetite: Block A	125 (granophyre contact)	-	-	-	-
591126	31.7084167	68.13385			Granophyre with large amphiboles cutting a boulder of very CG pyx and plag: Block B	126	-	-	-	-
591127	31.7084167	68.13385			Granophyre with large amphiboles cutting a boulder of very CG pyx, ol and plag: Block C	127 (granophyre contact)	-	-	-	-
591128	31.7084167	68.13385			Granophyre with amphibole cutting a boulder of pyx, plag and ol: Block D	128 (granophyre from one edge to the other)	-	-	-	-
591129	31.7084167	68.13385			Two granophyre veins cross-cuts of a boulder of very CG pyx and plag: Block E	129 (granophyre contact)	-	-	-	-
591130	31.7084167	68.13385			Granophyre cross-cutting a felsic rich vein, with a selvage rich in magnetite: Block F	130 (granophyre contact)	-	-	-	-
591131	31.7084167	68.13385			Granophyre cutting a boulder: Block J	131 (felsic-rich)	-	-	131 WR (felsic-rich)	-
591132	31.7067833	68.1293167			Granophyre within 10m of Skaergaard roof contact	132 (granophyre)	-	-	-	-
591133	31.7067833	68.1293167			Granophyre within 10m of Skaergaard roof contact	133 (granophyre contact)	-	-	-	-
591134	31.7067833	68.1293167			Granophyre within 10m of Skaergaard roof contact	134 (felsic-rich)	-	-	134 WR (felsic-rich)	-
591150	31.7675667	68.1763333			Gabbroic pegmatite merging with wavy pyroxene rock	150 (boundary of gabbroic pegmatite)	-	-	-	-
591151	31.7675667	68.1763333			Gabbroic pegmatite merging with wavy pyroxene rock	151 (boundary of pegmatite)	-	-	-	-
591152	31.7675667	68.1763333			Gabbroic pegmatite merging with wavy pyroxene rock	152 (boundary of pegmatite)	-	-	-	-
591153	31.7675667	68.1763333			Olivine pyroxenite with interstitial plag parallel to gabbroic pegmatite	153 (mafic-rich)	-		153 WR (mafic-rich)	-
591616	31.7258667	68.193	400	LZB	Olivine pyroxenite adjacent to gabbroic pegmatite; plagioclase-rich sample adjacent to olivine pyroxenite	696 F (felsic-rich)	696 M (mafic-rich)	-	696 WR (mafic-rich)	-
591154	31.73195	68.1996167			Segregated melt sample, above gabbroic pegmatite: both silicic and mafic fraction - cross-bedded belt	154 (felsic-rich)	-	-	-	-
591155	31.73195	68.1996167			Segregated melt sample, above gabbroic pegmatite: mafic fraction - cross-bedded belt	155 (mafic-rich)	-	-	-	-
591156	31.7222667	68.2049333	44	LZA	Plag with pyroxene and magnetite; Olivine pyroxenite with interstitial magnetite; Plag with amphibole and some pyroxene	156 A (gabbroic pegmatite)	156 B (mafic-rich)	156 C (felsic-rich)	156 B WR (mafic-rich)	156 A WR (gabbroic pegmatite)

Continued from previous page

Sample number	Longitude (decimal degrees)	Latitude (decimal degrees)	Height (m)	Unit	Description	Polished thin sections			Whole rock XRF analyses	
591157	31.7222	68.2044833	57	LZA	Segregated melt sample above gabbroic pegmatite: both silicic and mafic fraction	157 F (felsic-rich)	157mg (mafic-rich - average gabbro contact)	157mF (mafic-rich - felsic-rich contact)	157 M WR (mafic-rich)	157 F WR (felsic-rich)
591158	31.7006	68.2022167	746	LZB	Gabbroic pegmatite: felsic-rich segregation contact with mafic-rich segregation	158 g (felsic-rich)	158 m (gabbroic pegmatite)	-	158 WR (felsic-rich)	-
591159	31.7006	68.2022167	746	LZB	Gabbroic pegmatite	159 (gabbroic pegmatite)	-	-	159 WR (gabbroic peg)	-
591160	31.6965333	68.2077	768	LZB	Segregated melt sample: both felsic-rich and mafic-rich segregations	160 F (felsic-rich)	160 M (mafic-rich)	-	160 F WR (felsic-rich)	160 M WR (mafic-rich)
591161	31.7251167	68.1643333	1350	UZA(t)	Segregated melt samples adjacent to dendritic anorthosites: felsic-rich and mafic-rich segregations	161 F (felsic-rich)	161 M (mafic-rich)	-	161 F WR (felsic-rich)	161 M WR (mafic-rich)
591162	31.7231	68.1645667	1405	UZA(t)	Segregated melt samples adjacent to dendritic anorthosites: felsic-rich and mafic-rich segregations	162 B (felsic-rich)	162 A (mafic-rich)	162 A-B (contact)	162 B WR (felsic-rich)	162 A WR (mafic-rich)
591163	31.7229833	68.1644333	1455	UZA(t)	Segregated melt samples adjacent to dendritic anorthosites: felsic-rich and mafic-rich segregations	-	-	-	163 B WR (felsic-rich)	163 A WR (mafic-rich)
591164	31.7228	68.1644	1470	UZA(t)	Segregated melt samples adjacent to dendritic anorthosites: felsic-rich and mafic-rich segregations	164 A-B (mafic-rich - felsic-rich contact)	-	-	164 WR (mafic-rich)	-
591165	31.7228167	68.1646667	1405	UZA(t)	Dendritic anorthosites with mafic-rich segregations at the down-dip tips of the dendritic texture	165 FT (mafic-rich dendritic tip cut through)	165 FT2 (mafic-rich dendritic fingertip cut through)	-	-	-
591166	31.7238667	68.1645	1375	UZA(t)	Gabbroic pegmatite	166 F (felsic-rich)	166 G (gabbroic pegmatite)	-	166 F WR (felsic-rich)	166 G WR (gabbroic pegmatite)
591167	31.7225167	68.1647	1430	UZA(t)	Gabbroic pegmatite with felsic- and mafic-rich segregations	167 F (felsic-rich)	167 M (mafic-rich)	-	167 F WR (felsic-rich)	167 M WR (mafic-rich)
591168	31.7036667	68.16175	1767	UZB	Segregated melt sample: mafic-rich segregation within a slumped modal packet	168 (mafic-rich)	-	-	168 WR (mafic-rich)	-
591169	31.7037333	68.1616667	1767	UZB	Segregated melt sample: felsic-rich segregation within a slumped modal packet	169 (felsic-rich)	-	-	-	-
591170	31.7036667	68.16175	1767	UZB	Segregated melt sample: felsic-rich segregation	170 (felsic-rich)	-	-	170 WR (felsic-rich)	-
591171	31.72285	68.1681333	1232	UZA	Gabbroic pegmatite dyke, which feeds a sill - sample of the centre of the dyke and the dyke-host rock contact	171 DC (dyke centre) - gabbroic pegmatite	171 (gabbroic pegmatite-host rock contact)	-	171 WR (centre of dyke) - gabbroic pegmatite	-
591172	31.72285	68.1681333	1232	UZA	Gabbroic pegmatite sill, which is fed by a dyke - sample of the centre of the dyke and the dyke-host rock contact	172 (gabbroic pegmatite-host rock contact)	-	-	-	-
591173	31.7198	68.1688	1232	UZA	Gabbroic pegmatite sill which runs parallel to model layering	173 (gabbroic pegmatite)	-	-	173 WR (gabbroic pegmatite)	-
591174	31.7191667	68.16835	1268	UZA	Gabbroic pegmatite sill which runs parallel to model layering, both top and bottom of sill, the sample is a full transect	174 (gabbroic pegmatite-host rock contact)	-	-	174 WR (gabbroic pegmatite)	-
591175	31.68845	68.1625	2050	UZC	Melanogranophyre sill: A is the base; B is the top	175 A (base of sill) - gabbroic pegmatite	175 B (top of sill) - gabbroic pegmatite	-	-	-
591176	31.6877	68.1624167	2055	UZC	Melanogranophyre sill: sample from the centre of the sill in plan view	176 C (gabbroic pegmatite - felsic-rich segregation contact)	176 M (gabbroic pegmatite)	-	176 WR (gabbroic pegmatite)	-

Continued from previous page

Sample number	Longitude (decimal degrees)	Latitude (decimal degrees)	Height (m)	Unit	Description	Polished thin sections			Whole rock XRF analyses	
591177	31.687	68.16225	2060	UZC	Felsic-rich segregation	177 C (felsic-rich - host gabbro contact)	177 (felsic-rich segregation)	-	177 WR (felsic-rich)	-
591178	31.6867667	68.1623833	2060	UZC	Melanogranophyre; felsic-rich segregation above the gabbroic pegmatite	178 A (felsic-rich)	178 B (gabbroic pegmatite)	-	178 WR (felsic-rich)	-
591179	31.6839333	68.1632333	2055	UZC	Melt segregation: Mafic-rich and felsic segregations	179 F (felsic-rich)	179 M (mafic-rich)	-	179 WR (felsic-rich)	-
591180	31.6874833	68.1625667	2055	UZC	Melt segregation: felsic-rich	180 (felsic-rich)	-	-	180 WR (felsic-rich)	-
591181	31.6878167	68.1627333	2053	UZC	Melt segregation: felsic-rich	181 (felsic-rich)	-	-	181 WR (felsic-rich)	-
591182	31.6880333	68.1628167	2050	UZC	Melanogranophyre: gabbroic pegmatite and felsic-rich segregation	182 F (gabbroic pegmatite)	182 F2 (felsic-rich)	-	-	-

Appendix Table 5.B Whole rock XRF analyses for major elements in wt.%. LZ = Lower Zone; UZ = Upper Zone; (t) = trough layer; RZ = Roof Zone; MBS = Marginal Border Series. * denotes sample triplicates to assess analytical precision.

Sample	Unit	Height (m)	Lithology	SiO_2	Al_2O_3	Fe_2O_3	MgO	CaO	Na_2O	K_2O	TiO_2	MnO	P_2O_5	LOI	Total	Mg#	Density
				wt. %													g/cm^3
156A	LZA	44	Gabbroic peg	51.4	19.5	7.7	4.2	11.0	2.8	0.7	1.4	0.1	0.4	0.3	99.5	32	2.6
159	LZB	746	Gabbroic peg	46.1	14.9	13.5	1.6	11.2	3.2	0.8	4.1	0.2	3.9	0.5	99.9	9	2.7
171	UZA	1232	Gabbroic peg	64.0	12.9	10.3	0.8	3.8	3.7	2.4	1.2	0.2	0.4	0.1	99.7	6	2.5
173	UZA	1232	Gabbroic peg	53.5	11.8	17.4	1.9	6.3	3.3	1.1	2.3	0.2	1.1	0.5	99.5	9	2.6
174 F*	UZA	1268	Gabbroic peg	50.6	12.2	18.7	3.2	7.4	3.2	0.4	3.1	0.3	0.7	-0.1	99.5	13	2.7
166G	UZA	1375	Gabbroic peg	46.5	10.2	25.3	2.9	7.1	2.8	0.7	2.7	0.4	2.0	-0.7	99.9	9	2.8
176*	UZC	2055	Gabbroic peg	38.7	3.2	41.4	0.6	10.5	1.0	0.2	3.7	1.1	2.1	-2.8	99.8	1	3.0
134	RZ	-	Felsic-rich seg	65.6	13.2	6.0	2.3	3.0	3.9	2.2	1.3	0.1	0.3	1.3	99.0	25	2.5
131	RZ	-	Felsic-rich seg	76.7	11.9	2.0	0.1	2.5	5.9	0.1	0.5	0.0	0.0	0.1	99.8	5	2.4
157F	LZA	57	Felsic-rich seg	49.6	20.0	5.5	3.1	12.4	3.1	1.2	2.4	0.1	0.0	2.0	99.5	33	2.6
160F	LZB	768	Felsic-rich seg	58.9	19.4	6.9	n.d.	6.7	5.6	0.8	0.6	0.1	0.2	0.2	99.5	n.d.	2.5
121	LZC	870	Felsic-rich seg	53.8	23.6	3.9	1.1	6.8	4.9	1.9	0.6	0.0	0.3	2.6	99.5	19	2.5
166F	UZA(t)	1375	Felsic-rich seg	62.1	11.8	12.2	0.9	4.0	4.5	2.0	1.2	0.2	0.5	0.4	99.6	6	2.5
161F	UZA(t)	1350	Felsic-rich seg	57.9	22.5	4.7	0.2	6.6	5.9	0.6	0.5	0.1	0.1	0.5	99.6	4	2.5
162B	UZA(t)	1405	Felsic-rich seg	57.3	23.0	3.9	0.4	7.9	5.4	0.6	0.5	0.1	0.2	0.4	99.7	8	2.5
163B*	UZA(t)	1455	Felsic-rich seg	57.8	24.1	2.8	0.0	7.9	5.7	0.5	0.3	0.1	0.1	0.4	99.2	0	2.5
167F	UZA(t)	1430	Felsic-rich seg	68.8	12.3	8.4	0.3	2.2	5.6	0.4	1.0	0.1	0.3	0.5	99.9	3	2.4
170	UZB	1767	Felsic-rich seg	55.6	19.7	10.0	0.8	6.7	5.2	0.6	0.9	0.1	0.1	0.1	99.7	6	2.6
181	UZC	2053	Felsic-rich seg	60.0	17.9	7.5	n.d.	6.2	5.3	1.1	0.8	0.1	0.6	0.3	99.7	n.d.	2.5
179	UZC	2055	Felsic-rich seg	61.6	18.7	6.3	n.d.	5.5	5.7	1.0	0.6	0.1	0.1	0.3	99.7	n.d.	2.5
180	UZC	2055	Felsic-rich seg	61.0	19.5	4.9	n.d.	5.9	5.8	1.3	0.4	0.1	0.2	0.4	99.3	n.d.	2.5
177	UZC	2060	Felsic-rich seg	52.9	23.1	5.9	1.5	10.4	4.0	0.5	0.9	0.1	0.3	0.1	99.6	18	2.6
153	MBS	-	Mafic-rich seg	42.5	4.9	23.9	14.6	9.3	0.1	0.1	3.6	0.3	0.1	0.7	100.0	35	2.9
156B	LZA	44	Mafic-rich seg	43.4	7.8	20.1	14.6	8.6	0.8	0.1	5.1	0.3	0.1	-0.8	100.0	39	2.9
157M	LZA	57	Mafic-rich seg	44.9	12.7	16.5	15.2	7.1	1.6	0.2	1.7	0.2	0.2	-0.5	99.6	44	2.8
696	LZB	400	Mafic-rich seg	35.5	3.7	34.8	15.3	4.1	0.5	0.1	7.6	0.4	0.1	-2.4	99.6	27	3.1
160M	LZB	768	Mafic-rich seg	37.7	1.4	34.7	25.3	1.9	n.d.	0.0	1.1	0.4	0.0	-2.6	99.9	39	3.1
122*	LZC	877	Mafic-rich seg	6.3	1.8	62.5	5.4	0.6	n.d.	0.0	24.7	0.4	0.0	-1.4	100.1	7	3.8
161M	UZA(t)	1350	Mafic-rich seg	18.8	3.3	58.2	5.6	1.4	0.3	0.1	14.3	0.5	0.1	-3.2	99.4	8	3.5
162A	UZA(t)	1405	Mafic-rich seg	32.0	3.6	42.5	9.8	3.3	0.5	0.1	9.7	0.5	0.1	-2.7	99.6	17	3.2
167M	UZA(t)	1430	Mafic-rich seg	35.7	6.0	40.9	8.7	3.8	1.1	0.2	5.5	0.5	0.2	-2.6	99.9	15	3.1
163A	UZA(t)	1455	Mafic-rich seg	25.4	1.2	52.3	9.7	3.2	n.d.	0.0	10.6	0.6	0.1	-3.5	99.6	14	3.4
164	UZA(t)	1470	Mafic-rich seg	11.4	3.7	61.6	1.7	0.9	0.5	0.3	21.7	0.4	0.1	-2.8	99.5	2	3.7
168	UZB	1767	Mafic-rich seg	33.1	3.5	42.5	5.5	9.1	0.5	0.1	5.5	0.6	2.0	-2.4	99.9	10	3.1

Appendix Table 5.C Whole rock XRF analyses for trace elements in ppm. LZ = Lower Zone; UZ = Upper Zone; (t) = trough layer; RZ = Roof Zone; MBS = Marginal Border Series. * denotes sample triplicates to assess analytical precision.

Sample	Unit	Height (m)	Lithology	V	Cr	Ni	Cu	Zn	Sr	Y	Zr	Nb	Ba	Sc	La	Ce	Nd	Rb
				ppm														
156A	LZA	44	Gab peg	234	13	42	135	62	363	55	232	15	182	25	24	71	45	16
159	LZB	746	Gab peg	87	1	10	627	128	331	154	332	51	221	26	68	189	141	22
171	UZA	1232	Gab peg	7	4	n.d.	382	100	217	116	741	39	474	16	65	158	88	58
173	UZA	1232	Gab peg	18	4	n.d.	721	146	275	109	492	37	332	28	53	141	91	22
174 F*	UZA	1268	Gab peg	121	1	1	766	144	295	59	274	18	129	33	23	73	47	8
166G	UZA	1375	Gab peg	21	4	4	722	207	274	96	284	22	174	26	38	108	80	17
176*	UZC	2055	Gab peg	n.d.	7	8	656	318	140	101	111	25	51	31	14	65	60	6
134	RZ	-	Felsic-rich seg	146	25	24	37	41	249	35	215	17	995	16	31	70	32	32
131	RZ	-	Felsic-rich seg	19	5	n.d.	85	42	204	155	798	86	16	1	87	209	113	0
157F	LZA	57	Felsic-rich seg	322	13	58	33	26	706	32	279	21	375	26	7	37	23	36
160F	LZB	768	Felsic-rich seg	114	6	12	145	38	439	27	124	9	125	13	10	37	23	7
121	LZC	870	Felsic-rich seg	131	16	10	89	10	690	16	87	3	204	8	14	41	21	38
161F	UZA(t)	1350	Felsic-rich seg	16	5	n.d.	78	51	562	23	110	4	156	7	10	37	20	5
166F	UZA(t)	1375	Felsic-rich seg	n.d.	4	n.d.	239	147	204	134	675	38	385	24	63	158	97	41
162B	UZA(t)	1405	Felsic-rich seg	6	4	n.d.	289	31	531	20	88	4	145	9	8	33	19	5
167F	UZA(t)	1430	Felsic-rich seg	0	4	n.d.	596	60	199	120	805	41	134	11	63	156	92	6
163B*	UZA(t)	1455	Felsic-rich seg	3	3	n.d.	311	19	548	16	79	4	122	6	6	28	15	3
170	UZB	1767	Felsic-rich seg	n.d.	4	n.d.	177	69	459	16	108	6	158	21	3	23	14	6
177	UZC	2060	Felsic-rich seg	2	5	n.d.	155	85	603	48	213	14	220	9	17	56	36	10
179	UZC	2055	Felsic-rich seg	n.d.	4	n.d.	141	107	597	70	340	23	304	4	29	84	55	15
180	UZC	2055	Felsic-rich seg	n.d.	4	n.d.	158	51	683	53	282	15	1681	8	19	61	38	16
181	UZC	2053	Felsic-rich seg	n.d.	4	n.d.	200	84	488	78	345	21	255	7	30	88	59	15
153	MBS	-	Mafic-rich seg	515	225	259	444	174	60	26	96	13	39	58	n.d.	18	14	3
156B	LZA	44	Mafic-rich seg	615	27	312	138	142	119	21	125	15	41	49	n.d.	17	12	3
157M	LZA	57	Mafic-rich seg	205	20	465	154	120	206	21	107	10	60	17	4	24	16	5
160M	LZB	768	Mafic-rich seg	115	31	587	125	253	24	9	46	6	6	17	n.d.	11	6	1
696	LZB	400	Mafic-rich seg	822	46	284	159	252	68	17	104	19	21	36	n.d.	15	9	3
122*	LZC	877	Mafic-rich seg	5256	1045	357	85	430	13	2	106	23	n.d.	36	n.d.	n.d.	n.d.	1
161M	UZA(t)	1350	Mafic-rich seg	564	n.d.	24	181	457	60	9	107	18	n.d.	23	n.d.	6	6	3
162A	UZA(t)	1405	Mafic-rich seg	40	7	13	3575	264	83	11	92	28	7	33	n.d.	9	6	2
167M	UZA(t)	1430	Mafic-rich seg	132	4	15	501	273	142	15	70	13	34	24	n.d.	11	10	6
163A	UZA(t)	1455	Mafic-rich seg	314	n.d.	19	1557	385	12	10	61	15	n.d.	41	n.d.	8	5	2
164	UZA(t)	1470	Mafic-rich seg	807	1	20	406	483	48	21	220	29	12	27	n.d.	22	18	15
168	UZB	1767	Mafic-rich seg	4	10	6	1290	281	101	45	48	7	21	69	4	40	34	2

Appendix Table 5.D Average EPMA results for plagioclase core major elements (wt.%). LZ = Lower Zone; UZ = Upper Zone; (t) = trough layer.

Sample	Unit	Height (m)	Lithology	No. of analyses	Oxides (wt.%) average concentrations						An# (mol. %)	Standard deviation of population					
					Na_2O	CaO	K_2O	SiO_2	Al_2O_3	Total		Na_2O	CaO	K_2O	SiO_2	Al_2O_3	An#
156A	LZA	44	Gabbroic peg	14	4.9	11.0	0.4	53.6	28.0	97.9	55	0.3	0.4	0.0	0.8	0.3	2
159	LZB	746	Gabbroic peg	4	6.8	7.8	0.6	59.9	25.1	100.2	39	0.4	0.9	0.2	1.3	0.7	4
158M	LZB	746	Gabbroic peg	5	7.0	7.1	0.6	58.9	24.6	98.1	36	0.0	0.2	0.1	0.5	0.3	1
171	UZA	1232	Gabbroic peg	14	6.5	8.5	0.4	58.2	25.6	99.2	42	0.1	0.1	0.0	0.5	0.3	1
173	UZA	1687	Gabbroic peg	9	7.0	7.4	0.5	59.0	24.9	98.8	37	0.1	0.4	0.0	0.5	0.4	1
172	UZA	1687	Gabbroic peg	17	6.1	8.9	0.5	57.0	25.7	98.3	45	0.2	0.3	0.1	0.6	0.5	2
174	UZA	1723	Gabbroic peg	17	6.4	8.1	0.4	58.6	25.4	99.0	41	0.7	1.4	0.1	2.0	1.0	7
166G	UZA(t)	1375	Gabbroic peg	5	7.0	8.1	0.4	57.0	24.7	97.2	39	0.1	0.3	0.1	0.4	0.4	1
176M	UZC	2055	Gabbroic peg	6	7.3	6.6	0.4	60.7	23.9	99.0	33	0.1	0.1	0.0	0.3	0.1	1
175A	UZC	2050	Gabbroic peg	19	7.5	6.6	0.4	59.9	24.2	98.5	33	0.2	0.3	0.1	0.4	0.4	1
175B	UZC	2050	Gabbroic peg	16	7.3	6.8	0.5	59.5	23.9	97.9	34	0.2	0.3	0.1	0.5	0.3	2
178B	UZC	2060	Gabbroic peg	15	7.3	6.6	0.4	60.3	23.9	98.6	33	0.1	0.1	0.1	0.5	0.2	1
156C	LZA	44	Felsic-rich	5	5.4	10.1	0.4	55.7	26.8	98.5	51	0.1	0.2	0.0	0.4	0.1	1
157mf F	LZA	57	Felsic-rich	18	4.5	12.0	0.3	53.1	29.0	98.8	60	0.3	0.5	0.1	0.9	0.4	2
696F	LZB	400	Felsic-rich	3	5.5	9.4	1.1	56.9	26.5	99.4	49	0.6	0.8	0.9	0.5	0.5	4
158g	LZB	746	Felsic-rich	5	6.9	7.5	0.5	59.1	24.9	98.9	37	0.2	0.1	0.0	0.4	0.2	1
160F	LZB	768	Felsic-rich	17	4.6	11.7	0.3	54.2	28.3	99.2	59	0.3	0.5	0.0	0.7	0.5	3
121F	LZC	870	Felsic-rich	8	5.5	10.0	0.5	55.2	26.9	98.0	50	0.3	0.6	0.1	0.9	0.6	3
122F	LZC	877	Felsic-rich	30	5.4	10.2	0.4	55.5	27.0	98.5	51	0.2	0.4	0.0	0.7	0.3	2
166F	UZA(t)	1375	Felsic-rich	10	7.5	7.4	0.5	57.9	24.3	97.6	36	0.2	0.3	0.1	0.6	0.3	1
162B	UZA(t)	1405	Felsic-rich	14	6.2	8.9	0.5	58.0	26.1	99.7	44	0.2	0.3	0.1	0.5	0.3	2
167F	UZA(t)	1430	Felsic-rich	15	7.2	6.9	0.6	60.5	24.3	99.5	35	0.2	0.2	0.1	0.5	0.2	1
169	UZB	1767	Felsic-rich	13	6.8	7.6	0.6	58.8	24.6	98.5	38	0.1	0.2	0.1	0.3	0.3	1
170	UZB	1767	Felsic-rich	24	6.7	7.7	0.6	58.5	24.8	98.4	39	0.1	0.3	0.1	0.6	0.3	1
181	UZC	2053	Felsic-rich	12	7.2	6.8	0.5	60.1	24.1	98.7	35	0.2	0.2	0.0	0.4	0.3	1
179F	UZC	2055	Felsic-rich	12	7.2	6.8	0.5	60.5	24.4	99.4	34	0.2	0.4	0.0	0.6	0.4	2
180	UZC	2055	Felsic-rich	17	7.4	6.7	0.4	59.9	24.2	98.6	33	0.2	0.3	0.0	0.7	0.3	1
178A	UZC	2060	Felsic-rich	17	7.1	6.9	0.4	59.7	24.1	98.2	35	0.1	0.2	0.0	0.4	0.3	1
177	UZC	2060	Felsic-rich	17	7.4	6.8	0.5	59.6	23.9	98.2	34	0.2	0.2	0.0	0.5	0.4	1
156B	LZA	44	Mafic-rich	14	4.6	11.6	0.4	54.1	28.3	99.0	58	0.3	0.6	0.1	0.8	0.4	2
157mf M	LZA	57	Mafic-rich	12	4.1	12.5	0.3	52.1	29.3	98.4	63	0.5	0.9	0.1	1.2	0.9	4
696M	LZB	400	Mafic-rich	14	5.6	10.0	0.5	56.1	27.1	99.2	50	0.2	0.3	0.2	0.6	0.2	2
160M	LZB	768	Mafic-rich	14	5.4	10.5	0.3	55.1	26.9	98.2	52	0.3	0.5	0.1	0.8	0.4	3
124	LZC	887	Mafic-rich	13	5.3	10.5	0.3	55.3	27.1	98.4	52	0.1	0.2	0.0	0.4	0.2	1
121M	LZC	870	Mafic-rich	25	5.5	10.2	0.5	55.5	27.2	98.8	51	0.2	0.3	0.0	0.5	0.4	2
165FT	UZA(t)	1405	Mafic-rich	20	6.2	8.7	0.5	57.5	25.9	98.9	44	0.2	0.3	0.1	0.7	0.3	2
162A	UZA(t)	1405	Mafic-rich	16	6.2	8.9	0.5	58.0	26.1	99.7	44	0.1	0.2	0.1	0.4	0.3	1
167M	UZA(t)	1430	Mafic-rich	7	6.5	8.2	0.5	58.6	25.3	99.0	41	0.3	0.6	0.1	0.7	0.5	3
168	UZB	1767	Mafic-rich	17	6.6	7.8	0.6	59.6	24.9	99.5	39	0.2	0.2	0.1	0.5	0.2	1
182F2	UZC	2050	Mafic-rich	16	7.1	7.0	0.5	60.2	24.3	99.1	35	0.1	0.2	0.0	0.6	0.3	1
182F	UZC	2050	Mafic-rich	15	7.2	6.9	0.5	59.5	24.1	98.2	35	0.2	0.3	0.0	0.4	0.3	1
179M	UZC	2055	Mafic-rich	18	7.0	7.0	0.5	60.1	24.3	98.9	36	0.1	0.2	0.0	0.4	0.3	1

Appendix Table 5.E Average EPMA results for plagioclase rim major elements (wt.%). LZ = Lower Zone; UZ = Upper Zone; (t) = trough layer.

Sample	Unit	Height (m)	Lithology	No. of analyses	Oxides (wt.%) average concentrations						An# (mol. %)	Standard deviation of population					
					Na_2O	CaO	K_2O	SiO_2	Al_2O_3	Total		Na_2O	CaO	K_2O	SiO_2	Al_2O_3	An#
156A	LZA	44	Gabbroic peg	15	5.0	10.8	0.4	54.0	27.9	98.6	54	0.2	0.3	0.1	0.7	0.3	2
159	LZB	746	Gabbroic peg	3	8.6	3.6	1.3	64.9	21.9	100.4	19	0.4	0.3	0.3	0.7	0.3	2
158M	LZB	746	Gabbroic peg	4	6.9	7.0	0.6	59.2	24.3	98.6	36	0.1	0.2	0.0	0.3	0.3	1
171	UZA	1232	Gabbroic peg	14	6.7	8.1	0.4	58.9	25.5	100.1	40	0.4	0.6	0.1	0.9	0.5	3
173	UZA	1687	Gabbroic peg	8	7.3	6.7	0.5	59.7	24.1	98.7	34	0.3	0.6	0.1	0.8	0.4	3
172	UZA	1687	Gabbroic peg	18	6.3	8.6	0.5	57.3	25.7	98.8	43	0.3	0.6	0.1	0.9	0.6	3
174	UZA	1723	Gabbroic peg	12	6.2	8.6	0.4	57.8	25.8	99.3	43	0.2	0.6	0.1	1.0	0.5	2
166G	UZA(t)	1375	Gabbroic peg	5	7.2	7.9	0.4	57.0	24.7	97.9	38	0.2	0.4	0.0	0.8	0.3	2
176M	UZC	2055	Gabbroic peg	6	7.3	6.7	0.4	60.8	24.1	99.9	34	0.0	0.2	0.1	0.4	0.3	1
175A	UZC	2050	Gabbroic peg	19	7.4	6.6	0.4	59.7	24.3	99.1	33	0.2	0.3	0.1	0.4	0.4	1
175B	UZC	2050	Gabbroic peg	15	7.3	6.7	0.4	59.6	23.9	98.6	34	0.2	0.2	0.0	0.3	0.1	1
178B	UZC	2060	Gabbroic peg	15	7.4	6.5	0.4	60.0	24.0	98.9	33	0.1	0.2	0.1	0.6	0.2	1
156C	LZA	44	Felsic-rich	3	5.8	9.6	0.4	55.9	26.7	98.6	48	0.3	0.5	0.1	0.4	0.4	3
157mf F	LZA	57	Felsic-rich	16	4.4	12.0	0.4	52.8	29.0	99.1	60	0.5	0.9	0.1	1.0	0.7	4
696F	LZB	400	Felsic-rich	3	8.5	4.1	1.2	63.6	22.4	99.9	21	0.3	0.7	0.1	1.0	0.5	3
158g	LZB	746	Felsic-rich	5	6.9	7.5	0.6	59.1	24.8	99.4	38	0.2	0.2	0.1	0.4	0.2	1
160F	LZB	768	Felsic-rich	33	4.9	11.0	0.3	55.3	27.8	99.9	55	0.3	0.6	0.0	0.8	0.6	3
121F	LZC	870	Felsic-rich	7	5.5	9.9	0.5	55.3	27.0	98.6	50	0.3	0.7	0.1	1.0	0.5	3
122F	LZC	877	Felsic-rich	30	5.6	9.9	0.4	56.0	26.7	99.1	50	0.3	0.5	0.1	0.7	0.5	3
166F	UZA(t)	1375	Felsic-rich	11	8.2	6.3	0.5	59.1	23.5	98.1	30	0.5	0.8	0.1	1.0	0.5	4
162B	UZA(t)	1405	Felsic-rich	10	6.4	8.4	0.5	58.5	26.1	100.4	42	0.2	0.6	0.1	0.7	0.5	3
167F	UZA(t)	1430	Felsic-rich	12	8.0	5.5	0.6	62.0	23.2	99.7	28	0.4	0.7	0.1	1.2	0.6	3
169	UZB	1767	Felsic-rich	13	6.8	7.6	0.6	58.7	24.9	99.0	38	0.2	0.4	0.1	0.6	0.3	2
170	UZB	1767	Felsic-rich	22	6.7	7.8	0.6	58.4	25.0	99.1	39	0.2	0.2	0.1	0.5	0.3	1
181	UZC	2053	Felsic-rich	9	7.4	6.6	0.4	60.4	24.0	99.3	33	0.4	0.4	0.1	0.4	0.4	2
179F	UZC	2055	Felsic-rich	11	7.2	6.8	0.4	60.5	24.3	99.8	34	0.3	0.3	0.1	0.7	0.3	2
180	UZC	2055	Felsic-rich	17	7.3	6.7	0.4	59.6	24.4	99.0	34	0.1	0.2	0.1	0.6	0.3	1
178A	UZC	2060	Felsic-rich	17	7.3	6.7	0.4	60.0	24.0	98.9	34	0.2	0.3	0.1	0.4	0.3	1
177	UZC	2060	Felsic-rich	13	7.6	6.6	0.4	59.8	23.9	98.9	33	0.2	0.3	0.1	0.5	0.3	2
156B	LZA	44	Mafic-rich	14	4.7	11.4	0.3	54.4	28.2	99.4	57	0.2	0.5	0.1	0.8	0.4	2
157mf M	LZA	57	Mafic-rich	12	4.7	11.7	0.3	53.5	28.8	99.5	58	0.3	0.6	0.1	1.0	0.5	3
696M	LZB	400	Mafic-rich	14	5.5	10.0	0.5	56.3	27.2	99.9	50	0.3	0.4	0.2	0.7	0.3	2
160M	LZB	768	Mafic-rich	15	5.6	10.0	0.3	55.4	26.7	98.9	49	0.3	0.6	0.1	0.8	0.5	3
124	LZC	887	Mafic-rich	15	5.3	10.5	0.3	55.3	27.2	99.2	52	0.1	0.3	0.0	0.5	0.3	1
121M	LZC	870	Mafic-rich	24	5.6	10.0	0.5	55.8	27.0	99.3	50	0.3	0.5	0.1	0.9	0.5	2
165FT	UZA(t)	1405	Mafic-rich	20	6.3	8.6	0.5	57.7	25.8	99.5	43	0.2	0.3	0.1	0.5	0.3	1
162A	UZA(t)	1405	Mafic-rich	15	6.3	8.8	0.4	57.8	26.2	100.0	44	0.1	0.2	0.1	0.4	0.2	1
167M	UZA(t)	1430	Mafic-rich	7	6.5	8.2	0.5	58.6	25.4	99.5	41	0.2	0.3	0.1	0.7	0.4	1
168	UZB	1767	Mafic-rich	16	6.6	7.7	0.6	59.1	25.0	99.6	39	0.1	0.2	0.2	0.6	0.3	1
182F2	UZC	2050	Mafic-rich	14	7.2	6.9	0.5	60.0	24.2	99.4	35	0.2	0.2	0.0	0.5	0.2	1
182F	UZC	2050	Mafic-rich	15	7.2	7.0	0.5	59.3	24.3	98.9	35	0.1	0.2	0.0	0.5	0.3	1
179M	UZC	2055	Mafic-rich	18	7.1	7.0	0.5	59.9	24.2	99.4	35	0.1	0.2	0.1	0.3	0.3	1